Mixed Metal-Based Materials for Electrocatalytic Oxygen Evolution Reaction in Aqueous Alkaline Media

Inaugural thesis presented to the Faculty of Mathematics and Natural Sciences of Heinrich Heine University of Düsseldorf

for degree of

Doctor of Philosophy (Ph.D.) in Natural Science

presented by

Soheil Abdpour
From Iran, Nowdesheh

Düsseldorf, November 2023

from the Institute of Inorganic Chemistry and Structural Chemistry I
of the Heinrich-Heine-University Düsseldorf

Published by permission of the
Faculty of Mathematics and Natural Sciences at
Heinrich Heine University Düsseldorf

Supervisor: Prof. Dr. Christoph Janiak
Co-supervisor: Prof. Dr. Christian Ganter

Date of oral examination: 24.11.2023

To my Parents

Eidesstattliche Erklärung

Ich versichere an Eides statt, dass die vorliegende Dissertation von mir selbstständig und ohne unzulässige fremde Hilfe unter der Beachtung der „Grundsätze zur Sicherung guter wissenschaftlicher Praxis“ an der Heinrich-Heine-Universität Düsseldorf erstellt worden ist. Die aus fremden Quellen direkt oder indirekt übernommenen Inhalte sowie Ergebnisse sind als solche kenntlich gemacht. Die Arbeit wurde bisher weder im Inland noch im Ausland in gleicher oder ähnlicher Form einer anderen Prüfungsbehörde vorgelegt. Es wurden keine früheren erfolglosen Promotionsversuche unternommen.

…………………………… ……………………………

Ort, Datum Unterschrift

Acknowledgments

First and foremost, I would like to express my heartfelt appreciation to my esteemed supervisor, Prof. Dr. Christoph Janiak, for graciously affording me the invaluable opportunity to join and collaborate with his research group. I am profoundly grateful for his unwavering guidance, patience, and the continuous inspiration that he provided throughout my research work. I would also like to extend my gratitude to Prof. Dr. Christian Ganter for being my co-supervisor.

My sincere thanks go to Dr. Ishtvan Boldog for his unwavering scientific support and his invaluable assistance in elucidating the structures of the newly synthesized MOFs during my tenure at Heinrich Heine University Düsseldorf. I appreciate Birgit Tommes's contributions to the IR measurements, Anette Ricken's expertise in AAS measurements, and Marcell Demandt's technical support. A special acknowledgment is due to Mr. Marcus Fetzer's assistance in conducting several SEM-EDX measurements.

Furthermore, I thank Lars Rademacher for his guidance in measurements with the Gamry potentiostat/galvanostat and TEM measures. I thank Takin Haj Hassani Sohi and Tobias Heinen for their assistance with single crystal X-ray measurements and Robert Oestreich's expertise in gas-sorption measurements using the BELSORP device. I also appreciate Thi Hai Yen Beglau's contributions to XPS analysis. In addition, I extend my thanks to Jutta Bourgeois for her invaluable assistance with all organizational matters.

I sincerely appreciate my colleagues Takin Haj Hassani Sohi, Abdulrahman Mohabbat, Dr. Daniel Komisarek, and Dr. Stefanie Bügel's support during administrative challenges in Düsseldorf. My gratitude also goes out to the entire AC1 group for their warm welcome, unwavering support, and the friendly atmosphere they provided. I am thankful to a multitude of individuals within the working group, with special recognition for Philipp Seiffert, Lea Pongratz, Marilyn Kaul, Till Strothmann, Linda Sondermann, Hanibal Othman, Dennis Woitassek, Dennis Woschko, Tim Müller, Aysenur Limon, Dustin Jordan, Vasily Gvilava, Dietrich Püschel, Annette Vollrath, Lukas Eisenhuth, David Geller, Jonas Fabrizi, Dr. Tobie Matemb Ma Ntep, Dr. Gündoğ Yücesan and Peter Ferber. Your contributions have impacted my journey, and I am truly grateful for your support and camaraderie.

List of publications

1- **S. Abdpour**, M. N.A. Fetzer, I. Boldog, R. Oestreich, T. H. Y. Beglaua, C. Janiak, *Dalton Trans.*, submitted

2- **S. Abdpour**, L Rademacher, MNA Fetzer, THY Beglau, C Janiak, Iron-Containing Nickel Cobalt Sulfides, Selenides, and Sulfoselenides as Active and Stable Electrocatalysts for the Oxygen Evolution Reaction in an Alkaline Solution, *Solids,* **2023**, *4* ,181–200. https://doi.org/10.3390/solids4030012

3- H. T. Dzoujo, V. O. Shikuku, S. Tome, S. Akiri, N. M. Kengne, **S. Abdpour**, C. Janiak, M. A. Etoh, D. Dina, *J. Environ. Manage.,* **2022**, *318*, 115533. https://doi.org/10.1016/j.jenvman.2022.115533

4- **S. Abdpour**, E. Kowsari, B. Bazri, M. R. A. Moghaddam, S. Sarabadani Tafreshi, N. H. de Leeuw, I. Simon, L. Schmolke, D. Dietrich, S. Ramakrishna, C. Janiak, Amino-functionalized MIL-101(Cr) photodegradation enhancement by sulfur-enriched copper sulfide nanoparticles: An experimental and DFT study, *J. Mol. Liq.,* **2020**, *319*, 114341. https://doi.org/10.1016/j.molliq.2020.114341

Kurze Zusammenfassung

Diese Doktorarbeit erforschte fortschrittliche elektrokatalytische Materialien für die Sauerstoffentwicklungsreaktion (OER), eine wichtige Komponente erneuerbarer Energietechnologien. Die Forschung unterteilt sich in zwei verschiedene Bereiche, die wertvolle Einblicke in die Entwicklung effizienter und nachhaltiger OER-Katalysatoren bieten.

Im ersten Teil wurde die Synthese von eisenhaltigen Nickel-Kobalt-Sulfiden, Seleniden und Sulfoseleniden durch einen einfachen zweistufigen Hydrothermieprozess untersucht. Diese Materialien wurden als Elektrokatalysatoren für die OER in einer alkalischen Lösung verwendet. Die Schlüsselrolle von Eisen bei der Verbesserung der elektrokatalytischen Leistung von Nickel-Kobalt-basierten Elektrokatalysatoren wurde in der Studie betont, in der alle eisenhaltigen Nickel-Kobalt-Sulfide, Selenide und Sulfoselenide eine verbesserte OER-Leistung im Vergleich zu eisenfreien Proben zeigten. Die folgende OER-Leistung wurde für eisenhaltige Nickel-Kobalt-Sulfid-, und Selenidproben beobachtet: $Fe_{0,1}Ni_{1,4}Co_{2,9}(S_{0,87}O_{0,13})_4$, (318 mV bei 50 mA cm^{-2}); $Fe_{0,2}Ni_{1,5}Co_{2,8}(S_{0,9}O_{0,1})_4$, (310 mV bei 50 mA cm^{-2}); $Fe_{0,3}Ni_{1,2}Co_{2,5}(S_{0,9}O_{0,1})_4$, (294 mV bei 50 mA cm^{-2}); $Fe_{0,6}Ni_{1,2}Co_{2,5}(S_{0,83}O_{0,17})_4$, (294 mV bei 50 mA cm^{-2}); $Fe_{0,4}Ni_{0,7}Co_{1,6}(Se_{0,81}O_{0,19})_4$, (306 mV bei 50 mA cm^{-2}), zeigten eine überlegene OER-Leistung im Vergleich zu eisenfreien Gegenstücken, $Ni_{1,0}Co_{2,1}(S_{0,9}O_{0,1})_4$, (346 mV bei 50 mA cm^{-2}) und $Ni_{0,7}Co_{1,4}(Se_{0,85}O_{0,15})_4$, (355 mV bei 50 mA cm^{-2}).

Bemerkenswerterweise wurde eine außergewöhnliche OER-Leistung von trimetallischen Eisen-, Nickel- und Kobalt-Sulfoselenidproben mit geringen Überpotenzialen und herausragender Stabilität demonstriert. Das eisenhaltige Nickel-Kobalt-Sulfoselenid, $Fe_{0,5}Ni_{1,0}Co_{2,0}(S_{0,57}Se_{0,25}O_{0,18})_4$, stach mit einem Überpotenzial von 277 mV hervor und übertraf die RuO_2 Benchmarkelektrode ,299 mV, bei 50 mA cm^{-2}. Darüber hinaus wurde durch $Fe_{0,5}Ni_{1,0}Co_{2,0}(S_{0,57}Se_{0,25}O_{0,18})_4$ eine bemerkenswerte Stabilität gezeigt, mit nur einer minimalen Erhöhung des Überpotenzials von 277 mV auf 279 mV bei 50 mA cm^{-2} nach einem 20-stündigen Chronopotentiometrie-Test.

Im zweiten Teil wurden gemischte Nickel-Eisen-Metallorganische Gerüst Verbindungen (MOF), speziell bimetallische CPM-37(Ni,Fe) mit variierendem

Eisengehalt, erstmals als Vorstufen für Elektrodenmaterialien in der OER synthetisiert. Die bimetallischen CPM-37(Ni,Fe)-Proben zeigten beachtliche spezifische Oberflächen (BET), mit Werten von 2039, 1955 und 2378 $m^2\,g^{-1}$ für CPM-37(Ni_2Fe), CPM-37(NiFe) und CPM-37($NiFe_2$). Im Gegensatz dazu wiesen die monometallischen Pendants, CPM-37(Ni) und CPM-37(Fe), deutlich geringere Oberflächenbereiche von 87 bzw. 368 $m^2\,g^{-1}$ auf.

Die aus den bimetallischen CPM-37(Ni,Fe)-Proben abgeleiteten gemischten Nickel- und Eisenhydroxide/-oxide zeigten während der OER eine überlegene Leistung, wobei CPM-37(Ni_2Fe) (Ni/Fe ~ 2) als herausragender Katalysator hervortrat. Es wurde ein geringes Überpotenzial von 290 mV bei 50 mA cm^{-2} gezeigt, zusammen mit einem niedrigen Tafel-Slope von 39 mV dec^{-1} und guter elektrochemischer Leistungsstabilität (eine Erhöhung des Überpotenzials von 290 auf 304 mV bei 50 mA cm^{-2} nach 20 Stunden Chronopotentiometrie), was die RuO_2 Benchmark-Elektrode übertraf (deren Überpotenzial nach 20 Stunden Chronopotentiometrie von 300 auf 386 mV anstieg).

Short summary

This PhD thesis explored advanced electrocatalytic materials for the oxygen evolution reaction (OER), a vital component of renewable energy technologies. The research was conducted in two distinct parts, each offering valuable insights into developing efficient and sustainable OER catalysts.

In the first part, the synthesis of iron-containing nickel-cobalt sulfides, selenides, and sulfoselenide was investigated via a straightforward two-step hydrothermal process. These materials were used as electrocatalysts for the OER in an alkaline solution. The pivotal role of iron in enhancing the electrocatalytic performance of nickel-cobalt-based electrocatalysts was underscored by the study, where all iron-containing nickel-cobalt sulfides, selenide, and sulfoselenide showed enhanced OER performance compared to iron-free samples. The following OER performance was observed for iron-containing nickel-cobalt sulfide and selenide samples: $Fe_{0.1}Ni_{1.4}Co_{2.9}(S_{0.87}O_{0.13})_4$, (318 mV at 50 mA cm^{-2}); $Fe_{0.2}Ni_{1.5}Co_{2.8}(S_{0.9}O_{0.1})_4$, (310 mV at 50 mA cm^{-2}); $Fe_{0.3}Ni_{1.2}Co_{2.5}(S_{0.9}O_{0.1})_4$, (294 mV at 50 mA cm^{-2}); $Fe_{0.6}Ni_{1.2}Co_{2.5}(S_{0.83}O_{0.17})_4$, (294 mV at 50 mA cm^{-2}); $Fe_{0.4}Ni_{0.7}Co_{1.6}(Se_{0.81}O_{0.19})_4$, (306 mV at 50 mA cm^{-2}) exhibit superior OER performance compared to iron-free counterparts, $Ni_{1.0}Co_{2.1}(S_{0.9}O_{0.1})_4$, (346 mV at 50 mA cm^{-2}) and $Ni_{0.7}Co_{1.4}(Se_{0.85}O_{0.15})_4$, (355 mV at 50 mA cm^{-2}).

Notably, exceptional OER performance was demonstrated by trimetallic iron, nickel, and cobalt sulfoselenide sample, with low overpotentials and outstanding stability. The iron-containing nickel cobalt sulfoselenide, $Fe_{0.5}Ni_{1.0}Co_{2.0}(S_{0.57}Se_{0.25}O_{0.18})_4$, was found to stand out with an overpotential of 277 mV, surpassing benchmark RuO_2 electrodes, 299 mV, at 50 mA cm^{-2}. Moreover, remarkable stability was exhibited by $Fe_{0.5}Ni_{1.0}Co_{2.0}(S_{0.57}Se_{0.25}O_{0.18})_4$, with only a minimal increase in overpotential from 277 mV to 279 mV at 50 mA cm^{-2} after a 20 h chronopotentiometry test.

In the second part, mixed metal nickel-iron metal-organic framework (MOF), specifically bimetallic CPM-37(Ni,Fe) with varying iron content, were synthesized for the first time as precursors for electrode materials in OER. Noteworthy high specific surface areas (BET) were exhibited by the bimetallic CPM-37(Ni,Fe) samples, with values of 2039, 1955, and 2378 $m^2\ g^{-1}$ for CPM-37(Ni_2Fe), CPM-37(NiFe), and CPM-37($NiFe_2$), respectively. Conversely, the monometallic counterparts, CPM-

37(Ni) and CPM-37(Fe), were characterized by markedly lower surface areas, 87 and 368 $m^2 g^{-1}$, respectively.

The mixed-phase nickel and iron hydroxide/oxides derived from bimetallic CPM-37(Ni,Fe) samples during OER showed superior performance, with CPM-37(Ni_2Fe) (Ni/Fe ~ 2) emerging as the standout catalyst. A small overpotential of 290 mV at 50 mA cm^{-2} was exhibited, along with a low Tafel slope of 39 mV dec^{-1} and good electrochemical performance stability (an overpotential increase from 290 to 304 mV at 50 mA cm^{-2} after 20 h chronopotentiometry), outperforming the benchmark RuO_2 electrode (which experienced an overpotential increase from 300 to 386 mV after 20 h chronopotentiometry).

List of abbreviations

°C	Degree Celsius
η	Overpotential
Å	Ångstrom
a.u.	Arbitrary unit
AAS	Atomic absorption spectrometry
BET	Brunauer-Emmett-Teller
Calc.	Calculated
Cm	Centimeter
CP	Chronopotentiometry
CV	Cyclic voltammetry
DMF	N, N’-Dimethylformamide
EDX	Energy-dispersive X-ray spectroscopy
EIS	Electrochemical impedance spectroscopy
Fig.	Figure
FT-IR	Fourier transform infrared
g	Gram
h	Hour
H_2BPCDA	Biphenyl-4,4'-dicarboxylic acid
LSV	Linear sweep voltammetry
min	Minute
mL	Milliliter
MOFs	Metal-organic frameworks
nm	Nanometer
NMP	N-methyl-2-pyrrolidone
PVDF	Polyvinylidene fluoride
PXRD	Powder X-ray diffraction
RHE	Reversible hydrogen electrode
SBU	Secondary building unit
SEM	Scanning electron microscopy
TEM	Transmission electron microscopy
TGA	Thermogravimetric analysis
TPAMA	N,N',N''-tris-(pyrid-4-yl)-trimesamide (TPAMA) ligand

wt%	Weight percentage
XPS	X-ray photoelectron microscopy
θ, Theta	Angle of diffracted wave in Bragg's equation

Table of Contents

1 Introduction

1.1 Electrochemical water splitting

Global energy demand is expected to significantly increase in the coming decades, primarily driven by the rapid growth of the global population and widespread industrial development in various parts of the world.[1] The overwhelming majority of current energy resources are come from fossil fuels, such as natural gas, oil, and coal. These resources are categorized as non-renewable energy sources, leading to significant environmental challenges.[2] Therefore, addressing the need for alternative, sustainable, and clean energy resources is paramount in ensuring the sustainable development of human society in the coming years. Pioneering revolutionary technologies for converting and storing eco-friendly and renewable energy sources, such as solar and wind power, represents the most promising approach to resolving the impending energy crisis in the future.[3]

However, solar and wind energy encounter intermittent functionality, limiting their practical applicability. To tackle the sporadic nature of renewable energy sources like wind and solar, electrocatalytic water splitting, which enables the production of clean H_2 energy, has garnered considerable attention over the past few decades.[4] Electrochemical water splitting was first introduced by Troostwijk and Deiman in Amsterdam during the 18th century, marking a significant milestone in electrochemistry.[5] However, the development of the process was primarily accomplished in the 20th century when scientists could reach about 50% efficiency in water electrolysis.[6] Electrocatalytic water splitting consists of two reactions: the anodic reaction, oxygen evolution reaction (OER), and the cathodic reaction, hydrogen evolution reaction (HER). These reactions are conventionally conducted in alkaline or acidic electrolytes to mitigate charge transport losses during water splitting.[7] Depending on whether an alkaline or acidic electrolyte is used, distinct half-reactions occur at the anode and cathode, which can be summarized as the following equations:[8–10]

In acidic electrolyte

$2H_2O\ (l) \rightarrow 4H^+(aq) + 4e^- + O_2(g)$ at anode (1)

$4e^- + 4H^+(aq) \rightarrow 2H_2(g)$ at cathode (2)

In alkaline electrolyte

$4OH^-(aq) \rightarrow 2H_2O(l) + 4e^- + O_2(g)$ at anode (3)

$4e^- + 4\ H_2O(l) \rightarrow 4OH^-(aq) + 2H_2(g)$ at cathode (4)

According to the anodic and cathodic half-reactions in both acidic and alkaline electrolytes, the overall water splitting reaction can be expressed as follows:

$2H_2O(l) \rightarrow 2H_2(g) + O_2(g)$ $E° = 1.23\ V$ (5)

In both acidic and alkaline media, a thermodynamic potential of 1.23 V (equivalent to an energy input of $\Delta G = 237.1\ kJ\ mol^{-1}$) is required to drive the water splitting reaction.[1] However, due to the sluggish kinetics of both the anodic and cathodic reactions, a higher overpotential is necessary to achieve a significant current density during water splitting. Consequently, in practical applications, the required potential for water splitting exceeds the theoretical value of 1.23 V. As depicted in Figure 1, conventional water electrolysis in acidic electrolytes employs a proton exchange membrane (PEM), whereas, in alkaline electrolytes, a diaphragm is used to separate the anode and cathode electrodes.[2]

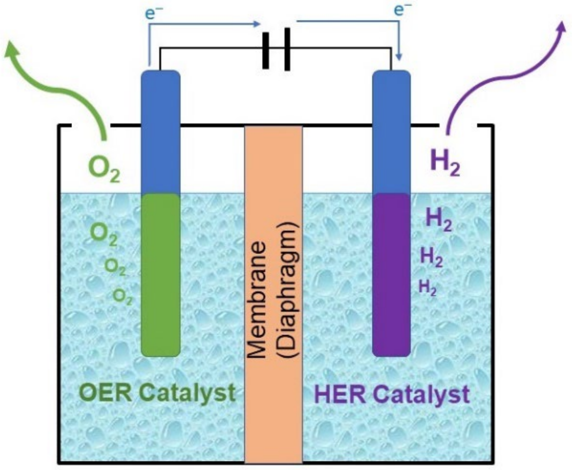

Figure 1 Scheme of conventional water electrolysis.

Despite enormous efforts and significant budget allocations aimed at developing an efficient water-splitting process, the practical application of this technology still needs to be improved. The most critical challenges are as follows:

1- Incompatibility or complex integration of HER and OER electrocatalysts.[11]

2- The potential for forming explosive H_2/O_2 gas mixtures in coupled HER and OER half-cells.[12]

3- The OER exhibits a higher overpotential for the four-electron process compared to HER to generate the same current density.[13]

4- Challenges in the development of cost-effective H_2 storage and transportation systems.[14]

To address the issues mentioned above, different strategies have been developed, including:

a) decoupled water electrolysis,

b) hybrid water electrolysis,

c) tandem water electrolysis,

and d) overall water splitting.

Among these innovative approaches, overall water splitting using earth abundance electrocatalysts received more attention mainly due to reducing the overall cost of water electrolysis through simplifying the electrolyzer configuration.[2]

1.2 Oxygen evolution reaction

The oxygen evolution reaction (OER) is one of the most critical electrocatalytic reactions, and it is often coupled with various cathodic responses, such as hydrogen evolution (HER), carbon dioxide reduction (CO_2RR), ammonia synthesis (NRR), and electrocatalytic hydrogenation. This coupling has empowered numerous electrocatalytic applications.[15] However, OER is considered a bottleneck of water splitting, mainly due to its inherently glacial kinetics[16] with a four-proton (H^+) coupled (e^-) transfer process.[17]

Depending on using alkaline or acidic electrolytes, two different theoretical models have been developed for OER, described in the following equations (6-13), where * denotes a surface adsorption site.[16–19]

OER In alkaline media

$$4OH^- \rightleftarrows OH^* + 3OH^- + e^- \tag{6}$$

$$OH^* + 3OH^- \rightleftarrows O^* + 2OH^- + H_2O + e^- \tag{7}$$

$$O^* + 2OH^- + H_2O \rightleftarrows OOH^* + OH^- + H_2O + e^- \tag{8}$$

$$OOH^* + OH^- + H_2O \rightleftarrows O_2 + 2H_2O + e^- \tag{9}$$

OER In acidic media

$$2H_2O \rightleftarrows OH^* + H_2O + H^+ + e^- \tag{10}$$

$$OH^* + H_2O \rightleftarrows O^* + H_2O + H^+ + e^- \tag{11}$$

$$O^* + H_2O \rightleftarrows OOH^* + H^+ + e^- \tag{12}$$

$$OOH^* \rightleftarrows O_2 + H^+ + e^- \tag{13}$$

In alkaline and acidic electrolytes, the OER process occurs on catalytically active sites involving intermediate species such as OH^*, O^*, and OOH^*. These species are formed through four thermodynamically uphill processes, which constitute the OER reactions. The step with a higher energy barrier is the rate-limiting step which determines the efficiency of the OER process.[19,20] According to the scaling relation[i] (which is in line with the Sabatier Principle[ii]) between the energy demand for producing O^* and HOO^* species, the sum of energies required for $OH^* \rightarrow O^*$ is approximately the same as the required energy for $O^* \rightarrow OOH^*$, which is equal to 3.2 eV.[20] Therefore, by increasing the energy barrier for $OH^* \rightarrow O^*$, the energy barrier for $O^* \rightarrow OOH^*$ should decreased and vice versa.

In catalyst science, the conventional approach to represent scaling relations is through the utilization of volcano plots, a methodology that is also extensively employed in electrocatalysis.[21] Figure 2 displays the typical volcano plot for metal oxides, illustrating the OER in alkaline solution.

---

[i] Scaling relations in catalyst science refer to the relationships between various properties of catalysts and their catalytic activities. These properties can include adsorption energies, reaction barriers, and other parameters relevant to the catalytic process.

[ii] According to Sabatier Principle, optimal catalytic activity is achieved when the interaction between reactants and catalysts maintains a delicate balance, with neither excessively strong nor excessively weak interactions.

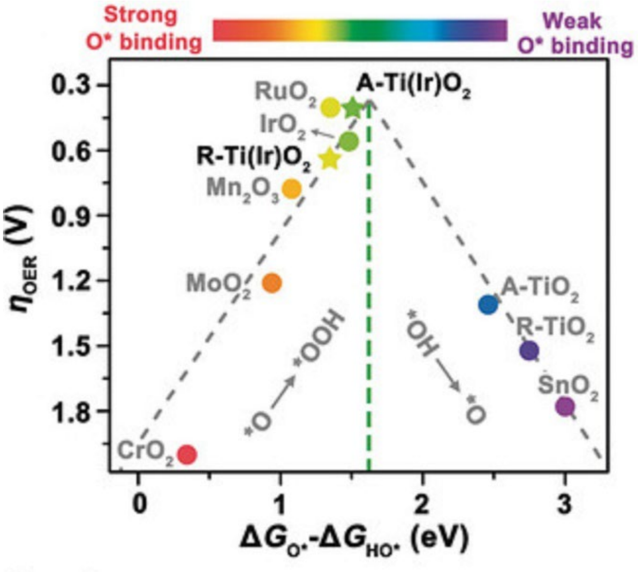

Figure 2 OER volcano plot for metal oxides in alkaline solution. Reproduced with permission from ref 22 Copyright 2020 John Wiley and Sons.

At the summit of the volcano plot, the energies associated with the OH* → O* and O* → OOH* steps attain equilibrium, leading to the lowest overpotential. Consequently, the catalyst demonstrates maximum efficiency when its adsorption sites align closely with the peak of the volcano plot.[21]

1.3 Oxygen evolution reaction criteria and methods

To assess the electrocatalytic performance of the OER, it is essential to employ benchmarking methodologies that facilitate more effective comparisons across diverse research groups and institutions.[23] The assessment of the OER performance for each electrocatalyst necessitates the consideration of several essential electrochemical parameters. These key factors include overpotential (η), Tafel slope, Exchange Current Density (j_0), Electrochemically Active Surface Area (ECSA), Turnover Frequency (TOF), Mass and Specific Activities, Electrochemical impedance analysis (EIS), and the long-term stability of the electrocatalyst in practical applications. A concise discussion of each of the parameters is provided in the subsequent sections.

1.3.1 Overpotential (η)

Overpotential at defined current density (x mA cm^{-2}, x is selected current density) (η_x) considered the most important parameter to evaluate the performance of catalysts in electrocatalytic processes such as OER, HER, and ORR.[24] Overpotential (η) is defined as the difference in potential between the potential at a specific current density and the equilibrium potential (1.23 V vs RHE).[23] The applied potential through an electrochemical cell can be calculated using Nernest equation[25] (equation 14)

$$E = E^{0'} + \frac{RT}{nF} Ln \frac{C_{ox}}{C_{red}} \tag{14}$$

Where $E^{0'}$ is the formal potential of the overall reaction, R is the ideal gas constant, T is temperature in Kelvin (K), n refers to the numbers of electrons transferring during the electrocatalytic reaction, F[i] is faraday constant, and C_{ox} and C_{red} are the concentration of oxidized and reduced reagents, respectively. Thus, the operational voltage cell can be described as follows:

$$E_{OP} = E_{eq} + \eta_a + \eta_c + IR \tag{15}$$

Herein, E_{eq} represents the potential observed at equilibrium conditions. η_a and η_c denote the overpotentials essential for surmounting the kinetic barriers associated with the OER at the anode and the HER at the cathode, respectively. IR represents the potential drop to compensate for the internal resistance within the system.[19,26] The current density of 10 mA cm^{-2} is a widely reported value in the literature, primarily attributed to its alignment with the photoelectrochemical water splitting efficiency of 12.3%. Nevertheless, electrocatalysts incorporating Ni and Co exhibit distinctive redox peaks beyond 1.23 V vs. RHE. Consequently, higher current density conditions, such as 50 or 100 mA cm^{-2}, were employed to assess the OER performance of these catalysts.[27,28]

1.3.2 Tafel slope and exchange current density

Tafel analysis constitutes one of the fundamental methodologies for assessing electrocatalysts intended for water electrolysis applications. Tafel analysis is a powerful means to extract essential insights regarding the intrinsic kinetics of the investigated electrocatalyst by examining the OER and HER processes.[29] The Tafel

---

[i] F= $9.64853321233100184\times10^{4}$ C·mol^{-1}

equation establishes a logarithmic relationship between the overpotential and the current density, mathematically represented as Equation (16).[27]

$$\eta = a + b \times \log(j) \qquad (16)$$

$$a = 2.303\, RT\, log \frac{j_0}{\propto nF} \qquad (17) \qquad\qquad b = 2.303\, \frac{RT}{\propto nF} \qquad (18)$$

In equations (16) – (18), the symbol "b" signifies the Tafel slope, j denotes the current density, j_0 represents the exchange current density, R stands for the ideal gas constant, the temperature in Kelvin (K), n signifies the number of electrons transferred during the redox reaction, F represents the Faraday constant, and α corresponds to the charge transfer coefficient.

Exchange current density (j_0) represents the current density in the absence of net electrolysis when η is equal to zero. The direct measurement of j_0 is not feasible using electrochemical techniques. Therefore, the exchange current density is derived by extending the linear regression of the Tafel plot until it intersects with the corresponding logarithmic current density at the reversible potential of the electrocatalytic investigation. Typically, a proficient electrocatalyst demonstrates a substantial j_0 value.[30]

1.3.3 Electrochemically active surface area (ECSA)

While numerous researchers have presented ECSA as a parameter for catalytic activity and justifying the current density trend in their studied catalysts, its true significance is that the electrochemically accessible or active surface area is subject to variation across different electrochemical processes and materials. As a result, ECSA cannot be regarded as a fundamental activity parameter for evaluating or screening materials as electrocatalysts in water splitting. Recently, Anantharaj et al. suggested that EIS parameters obtained under catalytic turnover conditions, including Rct[i], phase angle, RC[ii] time constant, and admittance at the lowest frequency, can serve as reliable indicators to explain activity variations, irrespective of the source of these differences in activity levels.[31]

---

[i] Charge transfer resistance

[ii] Resistor–capacitor

1.3.4 Turnover frequency (TOF)

An electrocatalyst's turnover frequency (TOF) in a specific electrochemical reaction is an essential kinetic parameter that quantifies the rate at which the catalyst can facilitate the desired electrochemical process. In other words, It quantifies the rate at which desired product production occurs, normalized to the number of active sites present.[32] TOF can be calculated through the following equation for electrocatalytic reactions involving gas production.

$$TOF = \frac{j\,N_A}{NF\Gamma} \qquad (19)$$

In the preceding equation, the symbol j represents the current density (expressed in A cm^{-2}. The variable N_A corresponds to Avogadro's number, while n denotes the number of electrons involved in the molecular evolution of a product (e.g., n = 2 for H_2 and n = 4 for O_2). The term F denotes the Faraday constant, and Γ represents the surface concentration of active sites or the count of participating atoms within the catalyst material.[33,34]

1.3.5 Faradic efficiency (FE)

The Faradic efficiency (FE) denotes the electron conversion efficiency for producing specific products, such as molecular O_2 and H_2. In the case of the OER, the FE is determined as the ratio between the experimental and theoretical values of oxygen production. Following equation is used to calculate the FE. The subsequent Equation (20) provides a means for computing the FE.

$$FE = \frac{I_R n_D}{I_D n_R N_{CL}} \qquad (20)$$

I_R and I_D correspond to the currents acquired from the ring and disc sections, respectively. The parameters n_R and n_D signify the number of electrons transferred at the ring and disc regions. N_{CL} represents the collection efficiency of the Rotating Ring-Disk Electrode (RRDE).[35]

1.3.6 Mass and specific activities

In electrocatalysis, two other quantitative parameters, mass activity, and specific activity, are used to define an electrocatalyst's catalytic activity. The mass activity is represented by the current normalized concerning the catalyst loading and is typically expressed in amperes per gram (A/g). On the other hand, the specific activity is determined by normalizing the current for the electrochemical surface area (ECSA) or the Brunauer−Emmett−Teller (BET) surface area.[35]

1.3.7 Electrochemical impedance analysis (EIS)

Electrochemical impedance spectroscopy (EIS) is a reliable technique for uncovering the electrochemical properties of catalysts, surfaces, interfaces, coatings, and similar materials.[36] EIS parameters (such as charge transfer resistance, Rct, phase angle, RC time constant, and admittance determined at the lowest frequency) obtained during catalytic turnover circumstances can serve as a dependable means to substantiate variations in the activity of electrocatalyst.[31]

1.3.8 Long-term stability of the electrocatalyst

The stability of a catalyst constitutes a pivotal factor in the realm of practical applications. The enduring nature of a tailored electrode hinges not solely upon the durability of the catalytic substance but also upon the capacity of the binding agent to endure corrosive electrochemical circumstances, techniques employed in catalyst ink preparation, and subsequent drying conditions.[30] Two prevalent approaches for assessing the durability of electrocatalysts encompass expeditious cyclic coltammetry (CV), recognized as the 'accelerated degradation' (AD) assessment, alongside extended water electrolysis conducted within potentiostatic or galvanostatic mode.[37,38] When comparing these two approaches, utilizing either potentiostatic or galvanostatic techniques may offer enhanced dependability in ascertaining the enduring viability of electrocatalysts over extended durations during genuine water electrolysis. An electrocatalyst that exhibits consistent stability and sustains an unvarying current density (when employed in potentiostatic mode, chronoamperometry technique) or maintains a constant potential (when operated under galvanostatic conditions, chronopotentiometry technique) without detrimental alterations for a duration exceeding 10 hours can be deemed adequately robust for potential upscaling in prototype water electrolysis systems.[38]

1.4 Mixed metal sulfides for electrochemical oxygen evolution reaction

Metal sulfides are chemical compounds where metal or semi-metal ions combine with sulfur anions, resulting in compositions denoted as M_xS_y. The most common metals used for synthesis of metal sulfides are shown in Figure 3. The combination of different metals with sulfur leads to of mono-metal sulfides with stoichiometries like MS, M_2S, M_3S_4, and MS_2, as observed in various cases.[39] Following a comparable methodology, the synthesis of bimetallic sulfides results in the generation of compounds designated as $A_{1-x}B_xS_y$, wherein the values of integers x and y are employed to define the precise proportions of the components. This strategy of combining different metallic elements with sulfur enables the creation of a diverse range of materials with tailored properties, extending their potential use in many fields such as energy storage, catalysis, and electronics.[40,41]

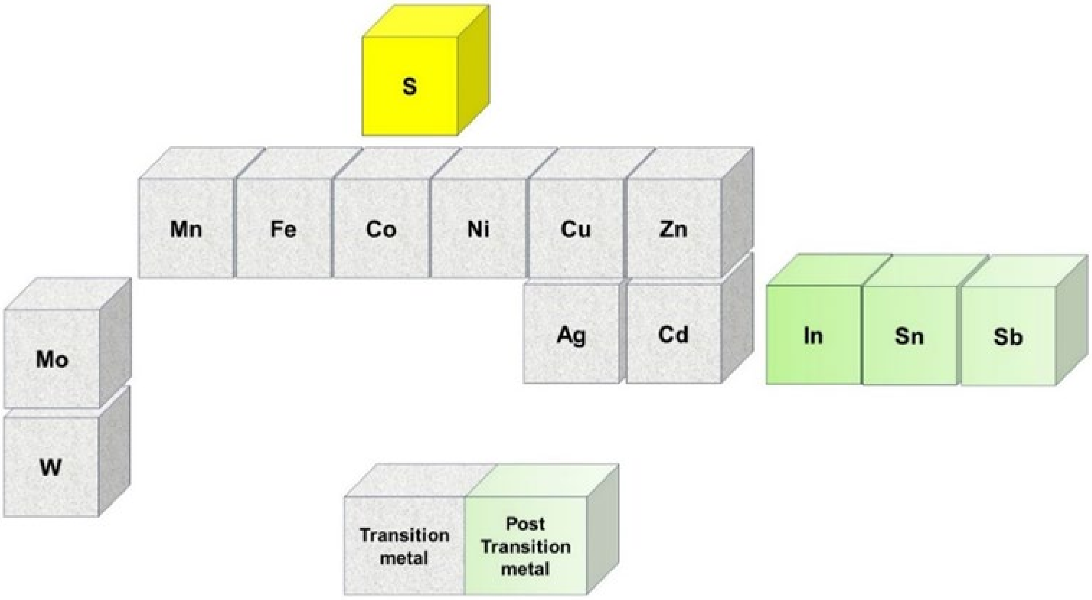

Figure 3 Typical metals that have been used for the synthesis of metal sulfides.[42]

The atomic arrangements of metals and sulfur within metal sulfides encompass intricate combinations governed by a close-packed system delineated by ionic size and charge distribution considerations.[43] Based on the arrangement of metal and sulfur atoms, several distinct structures can be identified for metal sulfides, as follows:[42]

a. The predominant and highly symmetrical structural configuration is the simple sodium chloride (NaCl) arrangement, wherein each ion occupies a position within an octahedral framework encompassing six nearest neighbours bearing opposite charges. This structural motif is exemplified by compounds like lead sulfide (PbS), commonly referred to as galena. Notably, the crystalline arrangement transitions into high-symmetry pyrite when the crystal structure accommodates two sulfide ions within each octahedral position of the NaCl arrangement.
b. The subsequent structural archetype involves sphalerite (ZnS), wherein each metal ion is enveloped by six oppositely charged ions arranged tetrahedrally.
c. The third pivotal structural configuration is represented by the fluorite form, wherein the metal cation is encircled by eight anions, and each anion, in turn, is surrounded by four metal cations. This arrangement is exemplified by calcium fluoride (CaF_2). Conversely, a reversal of atomic positions results in the formation of the anti-fluorite structure, wherein the metal cation is encompassed by four anions, and each anion is bordered by eight metal cations. This structure primarily observed in alkali metal sulfides such as K_2S, Rb_2S, Li_2S, Na_2S.

Moreover, metal sulfides can be classified into two structural categories: layered and non-layered configurations like the cubic spinel structure. Layered metal sulfides, including MoS_2, WS_2, and CuS, exhibit stacked atomic layers that contribute to distinctive electronic and mechanical properties, finding utility in fields such as electronics and lubrication. Conversely, non-layered metal sulfides, such as $CdIn_2S_4$,[44] $LiTi_2S_4$,[45] and $CuCr_2S_4$,[46] adopt the cubic spinel structure, with a general formula AB_2S_4. Within this arrangement, metal cations find their place in two distinct interstitial sites: the tetrahedral A cations (divalent cations, e.g., Mg, Fe, Ni, Mn, Zn) and the octahedral B cations (trivalent cations, e.g., Al, Fe, Cr, Mn, Ti). The spinel structure's adaptability emerges from the array of metal combinations that can occupy these sites, thereby shaping the material's properties and potential applications. This structural diversity underscores the profound versatility of metal sulfides as a compound class, wielding multifaceted utility across a spectrum of scientific domains.[42] The most common reported transition metal sulfides and sulfur source for synthesis metal sulfides are summarized in Table 1.

Table 1 common transition metal sulfides reported in literature and sulfur sources used for the synthesis metal sulfides.[42]

Frequently encountered transition monometallic sulfides documented in various publications
FeS, Fe_3S_4, FeS_2, Co_4S_3, Co_9S_8, CoS, Co_3S_4, Co_2S_3, CoS_2, CuS_2, CuS, $Cu_{1.12}S$, Cu_2S, WS_2, NiS_2, Ni_3S_2, Ni_6S_5, Ni_7S_6, Ni_9S_8, NiS, Ni_3S_4
Frequently encountered transition multi-metallic sulfides documented in various publications
$NiCo_2S_4$, $CuFeS_2$, $Fe_{0.5}Co_{0.5}S_2$, $CoMoS_2$, $FeMoS_2$, $NiMoS_2$, $NiCr_2S_4$, $FeNi_2S_4$, FeV_2S_4, $CuCoS_4$, $W_{1-x}Mo_xS_2$, VMo_2S_4, $FeMo_4S_6$, $CoNi_2S_4$, NiCoMoS, $Co_{0.4}Ru_{0.6}S_2$, Ag_2WS_4, Ag_3CuS_2, $CuIr_2S_4$, $Ag(Fe,Ni)_8S_8$, $Co_{0.5}MoS_2$, $CoMoS_4$
Frequently employed source materials for sulfur in the synthesis of nanomaterials of metal sulfides
Sulphur (powder) Thioacetamide Thiocarbamide Na_2S, H_2S Thiourea ($CS(NH_2)_2$) tert-Dodecanethiol Diethyl sulfide Ammonium persulfate Dithiooxamide Sodium diethyl Dithiocarbamate Carbon disulfide 1-Dodecanethiol Sodium hydrosulfide Trifluoromethanesulfonate L-Cysteine Dimethyl sulfoxide Thiobenzoate Glutathione Thioglycolic acid, 1-Butyl-3-methlyimidazole Thiocyanate

Metal sulfides have been proven to exhibit superior electrical conductivity, mechanical durability, thermal resilience, and heightened electrochemical reactivity compared to their corresponding counterparts comprised of metal oxides.[47,48] The notable abilities of metal sulfides can be attributed to the sulfur atoms' capacity to establish S−S linkages via a swiftly reversible redox mechanism. This gives rise to a pliable phase configuration, enhancing charge capacity and facilitating electron transfer. By employing intrinsic and extrinsic surface engineering modifications, regulating composition, and meticulously designing phase and structure controls, certain transition-metal sulfides have achieved activity levels that rival those of specific noble-metal catalysts.[22,49]

Compared with monometallic sulfides, mixed metal sulfides (MMSs) unveil more intricate redox mechanisms and elevated electronic conduction capabilities, yielding a marked enhancement in the electrochemical performance.[50–52] As a case in point, consider $NiCo_2S_4$; it showcases significantly elevated specific capacitance when compared to its corresponding singular metal sulfides (NiS_x and CoS_x), boasting an electrical conductivity approximately 100 times greater than that of $NiCo_2O_4$.[50] MMSs have displayed favorable electrochemical performance concerning ORR, OER, and HER. Enhanced redox processes have resulted in the utilization of MMS in a wide array of applications, encompassing hybrid supercapacitors (HSCs),[53] metal–air batteries (MABs),[54] water electrolysis,[55] as well as lithium-ion batteries (LIBs)[56] and sodium-ion batteries (SIBs).[57]

Extensive records highlight the substantial impact of crystalline phases, compositions, structural attributes, morphological characteristics, electroactive material dimensions, and electrode architecture on the efficacy of electrochemical energy storage and conversion systems.[58–60] As a result, researchers have invested immense efforts in enhancing MMSs for diverse energy storage and conversion applications, aiming for greater efficiency.

Diverse techniques have been employed to synthesize mixed metal sulfides, encompassing solid-state approaches,[61,62] precipitation,[52] hot injection,[63,64] refluxing,[65] hydro/solvothermal processes,[66] electrodeposition,[67] as well as self-template methods.[51] The hydro/solvothermal technique stands out as the predominant strategy for producing nanostructured MMSs. Within this process, a pair of metal salts alongside a sulfur source (such as sulfur powder, Na_2S, thiourea (TU), or thioacetamide (TAA) are dissolved in either water, an organic solvent, or a combination of both. Subsequently, this solution is subjected to controlled heating at a predetermined temperature and maintained at that level for a specific duration.[68]

A variety of mixed metal sulfides have been employed for energy conversion and storage purposes. These categories encompass M–Co–S (where M = Ni, Cu, Zn, and Mn),[50,69–73] M–Fe–S (where M = Co and Ni),[65,74–76] M–Mo(W)–S,[62,77–79] as well as M–Sb–S (where M = Cu, Co, and Bi),[80–82] and M–Sn–S (where M = Cu and Co), [61,83,84] systems.

1.5 Metal-organic frameworks for electrochemical oxygen evolution reaction

As an emerging and distinctive class of porous materials, porous coordination polymers (PCPs) or metal–organic frameworks (MOFs) represent crystalline structures characterized by well-defined, long-range arrangements of metal ions and organic ligands. These intricate frameworks are intricately linked through coordination bonds, creating a three-dimensional network that exhibits unique properties and offers extensive potential for various applications.[85–87] The adaptability in altering its components' geometries, sizes, and functionalities has resulted in the documentation and examination of over 20,000 distinct MOFs in the past ten years.[88] MOF structures incorporate organic carboxylates, functioning as ditopic or polytopic units. Their coupling with metal-containing elements yields robust MOFs with porosity exceeding 50% of the crystal volume. MOFs demonstrate surface areas from 1000 to 10,000 $m^2\,g^{-1}$, surpassing traditional materials like zeolites.[88]

The unique feature of MOFs lies in their remarkable structural versatility, pore size, and chemical functionality, making them exceptionally adaptable for various purposes, which opens up a diverse spectrum of potential applications. Based on the reported applications primarily found in scientific journals and patents, several key applications for MOFs in recent years can be highlighted, including: gas storage, separations,[88] catalysis,[89] sensor,[90] separation membrane,[91] water and air purification,[92] and their significance extends energy-related domains such as heat transfer,[93] supercapacitors,[94] electrochemical application,[95] and catalytic conversions,[96] which has led to thorough investigation, industrial-scale manufacturing, and widespread utilization.[97] The most frequently employed applications of MOFs are depicted in Figure 4.

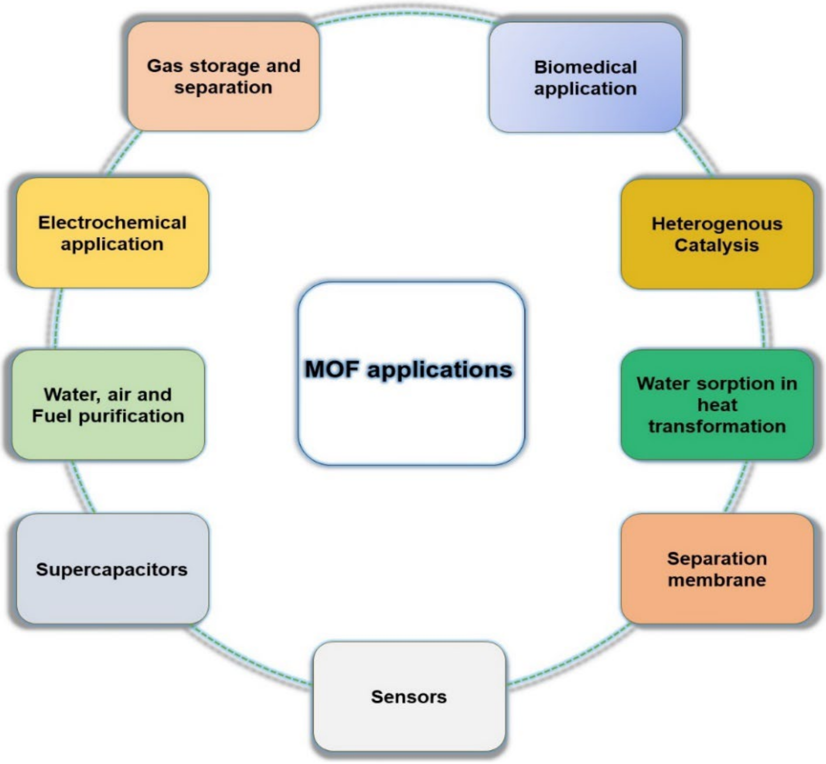

Figure 4 Metal-organic frameworks (MOFs) applications.[98]

Synthesis of MOFs typically begins with the selection of metal ions or clusters, which act as the nodes in the framework of MOFs. These metal nodes must be able to create coordination bonds with the organic linkers. Commonly used metal ions include zinc (Zn), copper (Cu), chromium (Cr), Nickel (Ni), Iron (Fe), Cobalt (Co), and so on, depending on the desired properties of the MOF. Organic linkers are molecules with multiple functional groups capable of coordinating with the metal nodes. These organic linkers can be chosen based on their shape, size, and the preferred properties of the resulting MOF. Common organic linkers include carboxylate groups (e.g., terephthalic acid, 4 4'-biphenyl dicarboxylic acid) and nitrogen-containing groups (e.g., pyridine or imidazole). Metal nodes and organic linkers are usually mixed in water or organic solvents such as dimethylformamide (DMF) or dimethyl sulfoxide (DMSO). The formation of MOFs involves the coordination of metal nodes with organic linkers, resulting in the self-assembly of a highly ordered, porous crystalline structure.[99– 103]

Figure 5 illustrates well-known MOF architectures alongside their respective metal nodes and organic linkers.

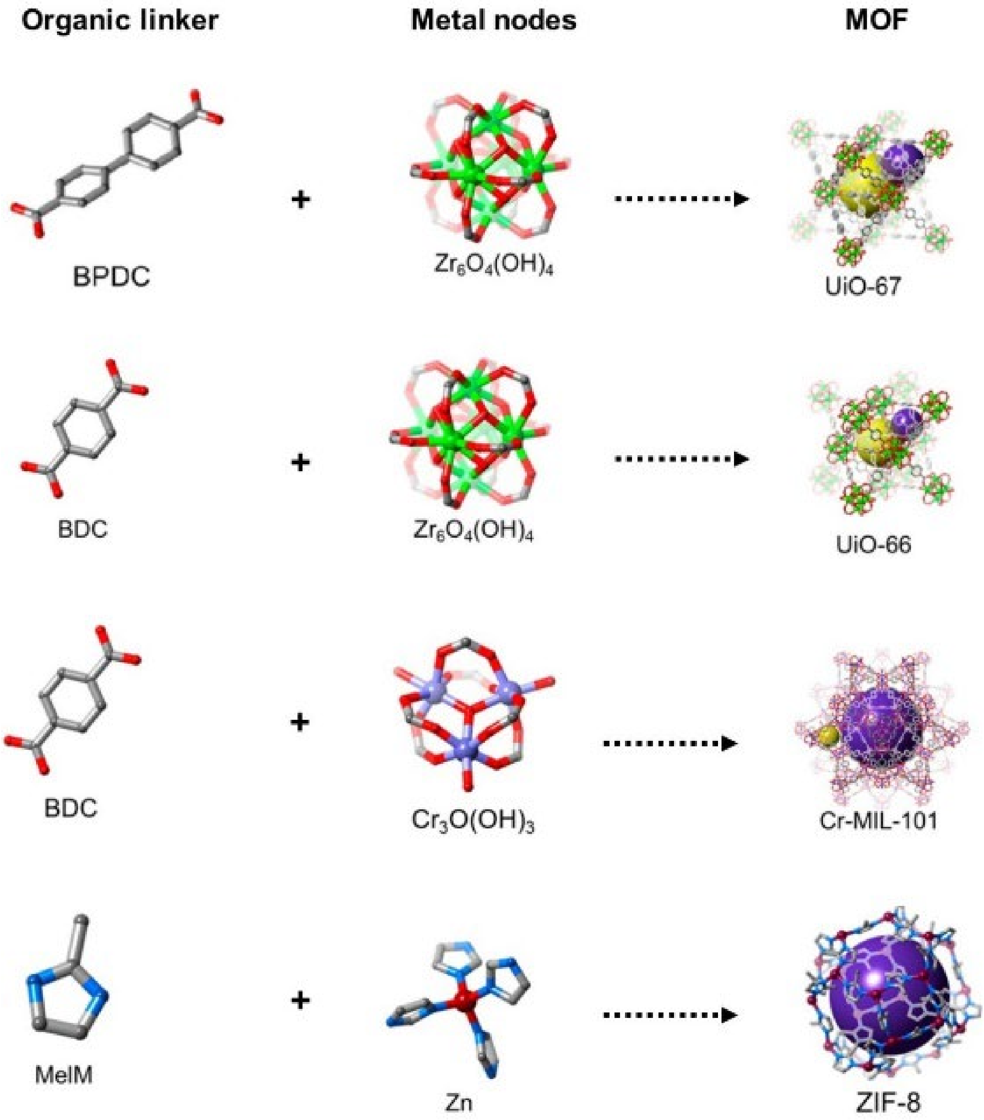

Figure 5 Depictions of renowned metal-organic frameworks (MOFs) structures alongside their corresponding node and linker constituents. Reprinted with permission from ref 100. Copyright 2017 American Chemical Society.

The array of techniques utilized for synthesizing metal-organic frameworks (MOFs) over the past few decades is succinctly depicted in Figure 6. In tandem with conventional room temperature synthesis, diverse approaches, including conventional electric (CE) heating, microwave (MW) heating, electrochemistry (EC), mechanochemistry (MC), and ultrasonic (US) methods, have found application. Both traditional step-by-step procedures and high-throughput methodologies have been harnessed in specific investigations.[103]

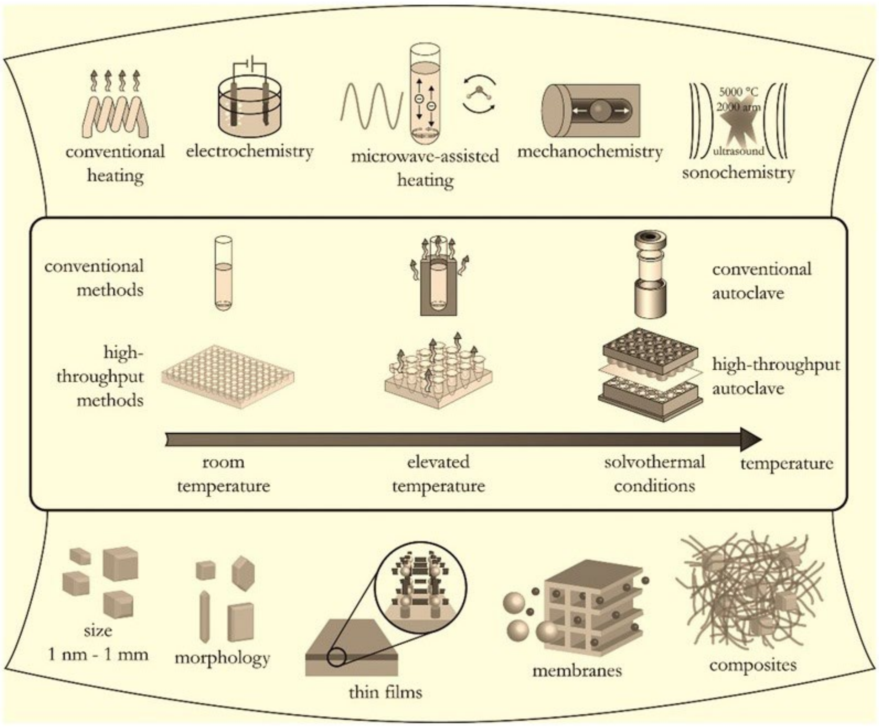

Figure 6 Summary of fabrication techniques, potential reaction heat levels, and ultimate reaction outcomes in the production of MOFs. Reprinted with permission from ref 103. Copyright 2012 American Chemical Society.

Given the clearly defined chemical and physical attributes characterizing, ranging from regulated pore architectures to abundant unsaturated active metal ion sites, along with their notably specific surface area and readily modifiable surfaces, MOFs have earned roles as catalysts, precursors, and templates for crafting non-precious metal catalysts for OER, HER, ORR, as well as for diverse applications in energy storage and conversion.[104] MOFs exhibit distinct attributes that render them an intriguing foundation for crafting exceptional electrocatalyst materials. Primarily, the versatility of MOF precursors allows for the facile generation of multi-metallic compounds by fine-tuning the composition. Secondly, MOFs, which possess uniform nanostructures like nanospheres, nanopolyhedrons, and nanorods, can ingeniously give rise to multiscale materials with both microstructural and nanostructural characteristics. The resultant materials inherit and preserve the advantages that augment electrocatalytic activity.[104–107]

In the electrocatalysis procedure, the plentiful metal sites within MOFs emerge as promising active sites where reaction intermediates' adsorption and release occur. The extensive surface area and an abundance of pores facilitate efficient mass transfer. Moreover, manipulating the morphology and structure of MOFs aids in the exposure of additional active sites, consequently enhancing their utilization. The distinctive advantages of using MOFs as precursors starkly contrast conventional methods. These characteristics align perfectly with the criteria for an efficient electrocatalyst in processes like HER, OER, and ORR.[108]

Previously, many unmodified MOFs or MOF composites have been directly employed as electrocatalysts, benefiting from their substantial specific surface area, plentiful micropores, and the numerous active sites provided by unsaturated metal ions within MOFs. However, unaltered MOFs' intrinsic activity and conductivity limitations have restricted their broader utilization in electrocatalytic applications. Consequently, extensive efforts have been dedicated to enhancing the intrinsic activity of metal sites and expanding the pool of accessible active sites through compositional and morphological adjustments.[109] Three primary approaches have been utilized to boost the electrocatalytic capabilities of MOFs, and these efforts center around augmenting the availability of exposed active sites and fine-tuning the electronic configuration of MOFs to optimize the properties related to intermediate adsorption and desorption, elucidated in the ensuing paragraphs.

a) Controlling the growth parameters of MOFs to yield ultra-thin MOF nanosheets or nanoarrays is advantageous for facilitating efficient electron transfer, and amplifying the number of catalytically active sites, swift mass transport.[110,111]
b) Combining MOFs with functional materials or any other active component.[112]
c) Altering the coordination surroundings of MOFs through metal centers adjustment, lattice structure modulation, and linker modification.[113]

Researchers have also explored the use of MOFs as sacrificial templates for generating various types of electrocatalytically active substances such as MOF-derived porous carbon supported with metals or alloys,[114] metal sulfides,[115] metal oxides,[116] metal phosphides.[117]

Various types of MOFs have been employed as precatalysts for the OER. These encompass monometallic MOFs based on Cobalt (e.g., ZIF-67),[118] Nickel (e.g., MOF-74(Ni)),[119] Copper (e.g., Cu-BDC),[120] and Zinc (e.g., ZIF-8).[121] Additionally, bimetallic MOFs have also been utilized, spanning Co-M bimetallic

MOFs (with M representing metals such as Ni, Fe, Cu, Zn, Ir, Mo),[104,122–125] as well as Ni-M bimetallic MOFs (where M can be Ni, Fe, Cu, Zn, Ir, Mo),[126] and even trimetallic MOFs such as Ni-Co-Fe Prussian blue analog.[127]

The role of pristine MOFs in electrocatalytic reactions remains a subject of ongoing debate. Nevertheless, as illustrated in Figure 7, it is worth noting that the coordinate bonding between metal nodes and organic linkers in MOFs is inherently weaker than the ionic bonding found in inorganic solids. This inherent weakness makes these bonds susceptible to degradation under the harsh conditions encountered during electrocatalysis.[128]

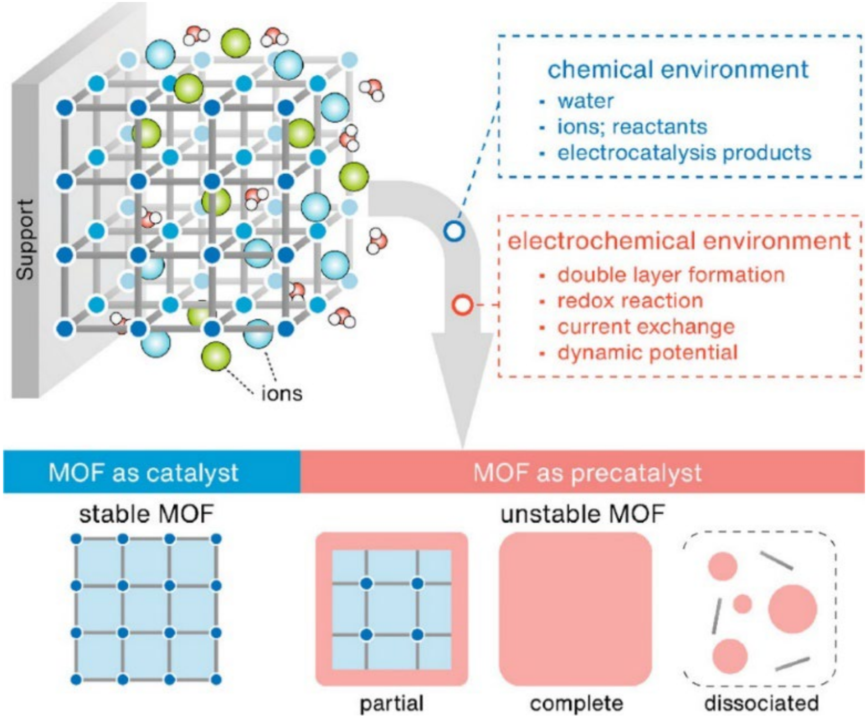

Figure 7 Chemical and electrochemical environment during the electrocatalysis process, leading to complete conversion for stable MOFs or destruction for unstable MOFs. Reprinted with permission from ref 128. Copyright 2021 American Chemical Society.

Furthermore, water facilitates the hydrolysis of the coordination sites between metal and linker, leading to the irreversible breakdown of the framework. This process generates hydroxide/hydrated metal species in alkaline electrolytes or protonated linkers in acidic electrolytes, which subsequently diffuse into the electrolyte.[129] In the context of electrocatalysis, MOFs are exposed to an electrochemical environment. Therefore, even though MOFs may exhibit stability in a chemical environment, the electrochemical conditions can be considerably more severe, leading to the potential degradation of MOF structures. For example, it would be misleading to assert that a MOF is a stable electrocatalyst for CO_2RR in neutral environments solely based on its stability. This is because the actual chemical environment of the MOF becomes highly alkaline during the electrocatalytic process, which facilitates MOF structural degradation.[128]

Hence, in recent years, extensive research endeavors have been undertaken by scientists to unravel the transformations occurring within MOFs during electrocatalytic processes. These efforts aim to uncover the active sites responsible for the electrocatalytic performance of MOFs when utilized as precatalysts. For example, Tian et al. have shown that when a potential is applied, a three nm-thick oxyhydroxide layer rapidly forms on the surface of the MOFs (FJI-H25Fe and FJI-H25FeCo). Furthermore, they observed that within just 20 seconds, the MOFs could undergo complete conversion into metal oxyhydroxide nanosheets through the applied CV potential sequence.[130] Utilizing operando X-ray absorption spectroscopy (XAS), Tang and co-authors provided insights into the structural changes occurring in a $Ni_{0.5}Co_{0.5}$-MOF-74 during OER. Their findings suggest that $Ni_{0.5}Co_{0.5}$-MOF-74 undergoes a transformation into $Ni_{0.5}Co_{0.5}OOH_{0.75}$ during this electrocatalytic process.[131] These investigations have revealed that MOFs transform into hydroxides and oxyhydroxides species under the harsh conditions of the OER. These transformed species then play a crucial role as active sites in facilitating the OER reaction.

2 Motivation and objectives

The quest for sustainable energy sources and environmentally friendly technologies has emerged as one of the most critical challenges of our time. Among the various possible ways to address this challenge, developing efficient and cost-effective electrocatalysts for the Oxygen Evolution Reaction (OER) stands out as a critical milestone in advancing renewable energy systems. In this context, synthesizing and characterizing novel materials that can drive the OER with high activity and stability are paramount. This motivation section outlines the rationale behind our research on two distinct classes of earth-abundant transition metal materials, including earth-abundant mixed metal sulfides (containing Co, Ni, and Fe) and bimetallic metal-organic frameworks (MOFs) featuring Fe and Ni as potential electrocatalysts for OER.

Mixed metal sulfides, consisting of cobalt (Co), nickel (Ni), and iron (Fe), hold great promise in catalyzing the OER due to their unique electronic structures and abundant elemental composition. Our research endeavors have led to the successful synthesis and modification of iron-containing nickel-cobalt sulfides. We have created iron-containing nickel cobalt sulfoselenide by introducing selenium (Se) into the structure. These novel materials exhibited exceptional electrocatalytic activity and stability towards OER, a significant breakthrough in the field. The utilization of Earth-abundant elements contributes to sustainability which addresses the issues associated with the scarcity of precious metals, such as Ir and Ru, traditionally used in electrocatalysis.

In parallel, our research has also focused on bimetallic MOFs containing iron (Fe) and nickel (Ni) as potential electrocatalysts for OER. Specifically, we targeted CPM-37(Ni), a promising but chemically unstable MOF, and undertook to enhance its chemical stability. Our efforts have led to the development of stable Fe, Ni bimetallic CPM-37(Ni, Fe), representing the first successful synthesis of such a material. These stable bimetallic MOFs have shown remarkable potential as effective precatalysts for OER. The introduction of iron into the MOF structure enhances its stability and improves its catalytic activity. Moreover, our approach of stabilizing unstable MOF by introducing a second metal into its structure could serve as a blueprint for stabilizing other chemically unstable MOFs, expanding the applicability of this exciting class of materials in various catalytic applications.

In conclusion, our research is driven by the urgent need for sustainable and efficient catalysts for the oxygen evolution reaction. Through synthesizing and modifying earth-abundant mixed metal sulfides and developing bimetallic MOFs as precursors, we aim to contribute to the advancement of clean energy technologies.

The obtained results for this research are provided in the cumulative section as scientific articles.

3 Cumulative part

Sections 3.1 and 3.2 herein encompass the findings of this doctoral dissertation, which have been disseminated and published/submitted in international scholarly journals. The publications are arranged chronologically, commencing with the initial publication where the author served as the primary contributor. Each published work includes a brief introduction and a concise overview of the research, along with a clear delineation of the roles and responsibilities of the authors involved. The figures, tables, and diagrams are not indexed according to the main text but adhere to the specific numbering system established within each publication. Additionally, each publication maintains its distinct list of references.

3.1 Iron-Containing nickel cobalt sulfides, selenides, and sulfoselenides as active and stable electrocatalysts for the oxygen evolution reaction in an alkaline solution

Soheil Abdpour, Lars Rademacher, Marcus N. A. Fetzer, Thi Hai Yen Beglau and Christoph Janiak

Solids, **2023**, *4*, 181–200.

doi: 10.3390/solids4030012

Pursuing efficient and sustainable electrocatalysts for the oxygen evolution reaction (OER) in alkaline solutions is crucial to renewable energy technology. This study presents a novel approach to synthesizing of iron-containing nickel-cobalt sulfides, selenides, and sulfoselenides, engineered through a straightforward two-step hydrothermal process at temperatures not exceeding 160 °C. These materials were evaluated for their electrocatalytic potential in OER, conducted in a 1 mol L^{-1} KOH aqueous alkaline environment.

The investigation unveiled a striking enhancement in OER performance when iron was introduced into nickel-cobalt sulfides and selenides, as evidenced by substantially reduced overpotentials compared to their iron-free counterparts. The iron-containing catalysts demonstrated exceptional OER activity at a current density of 50 mA cm^{-2}, with particularly noteworthy examples including $Fe_{0.6}Ni_{1.2}Co_{2.5}(S_{0.83}O_{0.17})_4$, $Fe_{0.5}Ni_{1.0}Co_{2.0}(S_{0.57}Se_{0.25}O_{0.18})_4$ showcasing overpotentials of 294 mV and 277 mV, respectively.

Intriguingly, the iron-containing nickel cobalt sulfoselenide, $Fe_{0.5}Ni_{1.0}Co_{2.0}(S_{0.57}Se_{0.25}O_{0.18})_4$, emerged as a standout performer, surpassing the industry benchmark, RuO_2 electrode (299 mV at 50 mA cm^{-2}), with an overpotential of 277 mV at 50 mA cm^{-2}. This remarkable performance can be attributed to its low charge transfer resistance (Rct) of 0.8 Ω at 1.5 V vs. RHE. Equally significant is its stability, as evidenced by a minimal increase in overpotential from 277 mV to 279 mV after a rigorous 20 h chronopotentiometry test to reach 50 mA cm^{-2} current density.

These results underscore the potential of trimetallic iron, nickel, cobalt sulfide, selenide, and sulfoselenide materials as high-performance, cost-effective, and durable electrocatalysts for sustainable OER reactions. The study presents a valuable strategy for developing efficient electrocatalytic materials, contributing to advancing renewable energy technologies.

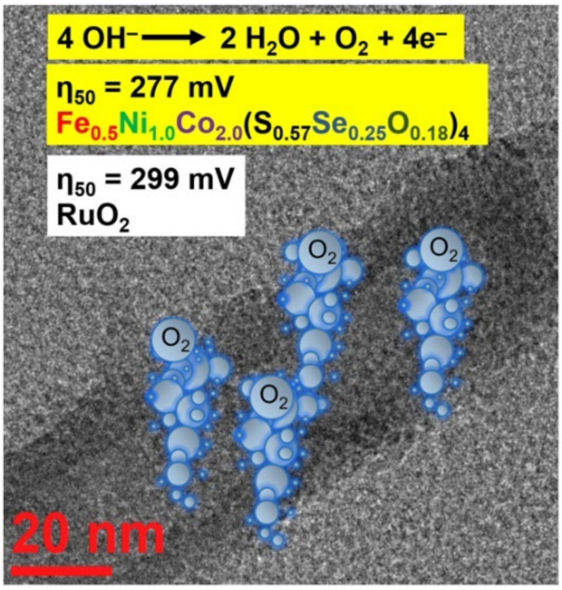

Author`s contribution to the publication:

- Concept and fabrication process.
- Synthesize all materials, encompassing sulfides, selenides, and sulfoselenide samples.
- Characterization of the materials (except EDX-SEM, TEM)
- Illustration of all figures, charts, and tables.
- Assessment of all findings and the initial composition of the manuscript's preliminary draft.
- Revising the manuscript in response to the reviewer's feedback.
- The initial manuscript and its subsequent revised version were rectified and formally submitted to the international journal "Solids" under the auspices of Prof. Dr. Christoph Janiak.

solids

Article

Iron-Containing Nickel Cobalt Sulfides, Selenides, and Sulfoselenides as Active and Stable Electrocatalysts for the Oxygen Evolution Reaction in an Alkaline Solution

Soheil Abdpour, Lars Rademacher, Marcus N. A. Fetzer, Thi Hai Yen Beglau and Christoph Janiak *

Institut für Anorganische Chemie und Strukturchemie, Heinrich-Heine-Universität Düsseldorf, 40204 Düsseldorf, Germany; soheil.abdpour@hhu.de (S.A.); larad101@hhu.de (L.R.); marcus.fetzer@uni-duesseldorf.de (M.N.A.F.); beglau@uni-duesseldorf.de (T.H.Y.B.)

* Correspondence: janiak@hhu.de

Abstract: Iron-containing nickel sulfides, selenides, and sulfoselenides were synthesized via a simple two-step hydrothermal reaction (temperature ≤ 160 °C) for their application as electrocatalysts in the oxygen evolution reaction (OER) in an alkaline solution (1 mol L^{-1} KOH). The study demonstrated that iron-containing nickel cobalt sulfides and selenides exhibit superior OER performance with lower overpotentials compared to iron-free nickel cobalt sulfide and selenide, which highlights the significant role of iron in enhancing OER nickel cobalt electrocatalysts: $Fe_{0.1}Ni_{1.4}Co_{2.9}(S_{0.87}O_{0.13})_4$, η_{50} = 318 mV; $Fe_{0.2}Ni_{1.5}Co_{2.8}(S_{0.9}O_{0.1})_4$, η_{50} = 310 mV; $Fe_{0.3}Ni_{1.2}Co_{2.5}(S_{0.9}O_{0.1})_4$, η_{50} = 294 mV; $Fe_{0.6}Ni_{1.2}Co_{2.5}(S_{0.83}O_{0.17})_4$, η_{50} = 294 mV; $Fe_{0.4}Ni_{0.7}Co_{1.6}(Se_{0.81}O_{0.19})_4$, η_{50} = 306 mV compared to $Ni_{1.0}Co_{2.1}(S_{0.9}O_{0.1})_4$, η_{50} = 346 mV; and $Ni_{0.7}Co_{1.4}(Se_{0.85}O_{0.15})_4$, η_{50} = 355 mV (all values at current densities η_{50} of 50 mA cm^{-2}). Furthermore, the iron-containing nickel cobalt sulfoselenide $Fe_{0.5}Ni_{1.0}Co_{2.0}(S_{0.57}Se_{0.25}O_{0.18})_4$ displayed exceptional OER performance with η_{50} = 277 mV, surpassing the benchmark RuO_2 electrode with η_{50} = 299 mV. The superior performance of the sulfoselenide was attributed to its low charge transfer resistance (Rct) of 0.8 Ω at 1.5 V vs. the reversible hydrogen electrode (RHE). Moreover, the sulfoselenide demonstrated remarkable stability, with only a minimal increase in overpotential (η_{50}) from 277 mV to 279 mV after a 20 h chronopotentiometry test. These findings suggest that trimetallic iron, nickel and cobalt sulfide, selenide, and especially sulfoselenide materials hold promise as high-performance, cost-effective, and durable electrocatalysts for sustainable OER reactions. This study provides a valuable approach for the development of efficient electrocatalytic materials, contributing to the advancement of renewable energy technologies.

Keywords: iron-containing material; nickel cobalt sulfide; nickel cobalt selenide; sulfoselenide; oxygen evolution reaction (OER)

Citation: Abdpour, S.; Rademacher, L.; Fetzer, M.N.A.; Beglau, T.H.Y.; Janiak, C. Iron-Containing Nickel Cobalt Sulfides, Selenides, and Sulfoselenides as Active and Stable Electrocatalysts for the Oxygen Evolution Reaction in an Alkaline Solution. *Solids* **2023**, *4*, 181–200. https://doi.org/10.3390/solids4030012

Academic Editor: Stefano Agnoli

Received: 11 June 2023
Revised: 4 July 2023
Accepted: 12 July 2023
Published: 16 July 2023

1. Introduction

According to the US Energy Information Administration (EIA) report, the total world energy consumption will rise to 815 quadrillion Btu (British thermal units) in 2040, a 29% increase compared to 2020 [1], demonstrating the increasing demand for energy in the near future. Using clean and renewable energy is one of the main issues for societies. Green hydrogen (H_2), produced with renewable energy, is seen as an alternative fuel and energy storage resource in the future [2]. Water splitting is one of the most studied ways to produce H_2. With electrocatalysis, this process includes the hydrogen evolution reaction (HER) and the oxygen evolution reaction (OER) [3]. The anodic reaction (OER) involves a sluggish four-electron/four-proton-coupled transfer reaction. It is the main obstacle to an economic water-splitting process since it requires a much higher potential (1.6–2 V vs. the reversible hydrogen electrode, RHE) than the theoretical equilibrium potential of E° = 1.23 V vs. RHE [4–8].

The well-known benchmark materials for OER are the oxides of iridium and ruthenium (IrO_2 and RuO_2), while Pt-based materials are used as benchmarks for HER [9]. However, the high cost, scarcity, and low stability of these precious noble metals limit their practical large-scale application for water electrolysis [10,11]. Sustainable water splitting requires utilizing non-precious metals as a catalyst. Using non-precious metals with high abundance, durability, and catalytic activity, especially in OER, can effectively improve the scalability of electrocatalytic hydrogen production. Therefore, in recent years, there has been an impetus to develop high-performance, stable, and low-cost (non-noble) transition metal-based electrocatalysts such as transition metal sulfides [12], hydroxides, oxides, oxide-hydroxides [13–16], phosphides [17], nitrides [18], perovskites [19,20], and spinels [21] for OER.

Transition metal sulfides possess good conductivity and excellent mechanical and thermal stability, making them promising electrocatalysts for OER and HER and the oxygen reduction reaction (ORR) [22]. Moreover, mixed-metal sulfides, MMSs, show even higher electric conductivity and richer redox reactions through the synergistic effect of multi-transition metal ions, leading to a notable enhancement in electrocatalytic performance compared to monometallic sulfides [23,24].

Bimetallic nickel cobalt sulfide is one of the most studied and promising MMSs, and is extensively studied for electrocatalytic energy conversion and storage devices [25]. For example, the thiospinel $NiCo_2S_4$ with Ni(II) on tetrahedral (T_d) sites and Co(III) ions on octahedral (O_h) sites receives much attention in many electrocatalysis applications, including water splitting, supercapacitors, and zinc-air batteries [26–29]. However, the electrocatalytic activity and stability of $NiCo_2S_4$ remains lower than IrO_2 and RuO_2 in OER and lower than Pt-based catalysts for HER [30]. To improve the electrocatalytic performance of nickel cobalt sulfides, researchers have applied many different strategies, including making composites with carbon materials [31–33], metal oxides [34,35], oxyhydroxides [15], layer double hydroxide [15], metal sulfides [36,37], incorporating other active metals such as Ru, Ir, and Pt in the structure [38,39] and also partially replacing sulfur ions with nitrogen [40], phosphorous [41] or selenium ions [42].

The improved electrocatalytic performance of nickel cobalt sulfide in the presence of anions such as Se and P can be attributed to effectively altering the surface electron density by modulating the compound's d-band [42–44]. Increased electrocatalytic activity in the presence of other cations is mainly related to improving exposed active sites, reducing the charge transfer resistance, enhancing structural stability, and synergistic interactions between host and guest cations [45,46].

Although replacing anions or cations is widely used to upgrade the water-splitting performance of nickel cobalt sulfides, only a few reports applied a simultaneous cation and anion replacement to evaluate a possible synergistic effect. Recently, Deng et al. synthesized the polymetallic sulfoselenide, $Co_{0.31}Ni_{0.22}Ru_{0.05}S_{0.46}Se_{0.41}$, which showed an overpotential of η_{10} = 261 mV (1.491 V vs. RHE) at 10 mA cm^{-2}, while RuO_2 needed η_{10} = 254 mV (1.484 V vs. RHE) under the same conditions [47]. However, ruthenium limits its classification as a completely non-precious metal electrocatalyst.

Here, we establish a facile two-step hydrothermal strategy to synthesize iron-containing nickel cobalt sulfides, selenides, and sulfoselenide as non-precious polymetallic compounds. A series of mixed-metal iron nickel cobalt carbonate hydroxide hydrates, (Fe_xNi_{1-x})CoCH-(y), were synthesized and used as a precursor for sulfurization, selenization, and sulfoselenization.

2. Materials and Methods

2.1. Materials

All commercial chemicals were used as received without any purification: cobalt chloride hexahydrate $CoCl_2 \cdot 6H_2O$ (CAS: 7791-13-1 98% abcr GmbH, Karlsruhe, Germany), nickel chloride hexahydrate $NiCl_2 \cdot 6H_2O$ (CAS: 7791-20-0 98%, ACS reagent, Roth, Karlsruhe, Germany), ammonium iron(II) sulfate hexahydrate $(NH_4)_2Fe(SO_4)_2 \cdot 6H_2O$ (CAS: 7783-85-9 BioUltra, 99% Sigma–Aldrich, St. Louis, MO, USA), sodium sulfide nonahydrate $Na_2S{\cdot}9H_2O$ (CAS: 1313-84-4 98% Acros Organics, New Dehli, India), selenium dioxide SeO_2 (CAS: 7446-08-4 98%, Sigma–Aldrich, St. Louis, MO, USA), urea $OC(NH_2)_2$ (CAS: 57-13-6 ACS reagent 99.5%, Sigma–Aldrich, St. Louis, MO, USA), potassium hydroxide KOH (CAS: 1310-58-3,1N, Roth, Karlsruhe, Germany), N-methyl-2-pyrrolidone NMP (CAS: 872-32-2 95%, abcr, Karlsruhe, Germany), hydrazine monohydrate $N_2H_4{\cdot}H_2O$ (CAS: 7803-57-8, Thermo Scientific, Kandel, Germany), polyvinylidene fluoride PVDF (CAS: 24937-79-9, Sigma–Aldrich, Karlsruhe, Germany), and carbon black Vulcan XC-72R (Fuelcellstore, Bryan, TX, USA). Nickel foam NF was purchased from Recemat BV, Cell Material Engineering, The Netherlands. Ultrapure water was produced using the Sartorius Arium mini device. Before using NF, it was cut into 1 × 2 cm^2 pieces and cleaned with acetone (CAS: 67-64-1, ACS reagent, ≥99.5%, Sigma–Aldrich, St. Louis, MO, USA), hydrochloric acid (CAS: 7647-01-0, 1 mol L^{-1}, Geel, Belgium), ultrapure water, and ethanol (CAS: 64-17-5, 98%, Th. Geyer, Renningen, Germany) for 15 min in an ultrasonic bath and then dried at 100 °C in a vacuum oven for 15 min.

2.2. Preparation of Nickel Cobalt Carbonate Hydroxide (NiCoCH) and Iron Nickel Cobalt Carbonate Hydroxide (Fe_xNi_{1-x})CoCH-(y) Precursors

The NiCoCH sample was prepared according to the previously reported method by Chen et al. [20]. The amount of 950 mg (4.00 mmol) $CoCl_2{\cdot}H_2O$, 475 mg (2.00 mmol) $NiCl_2{\cdot}6H_2O$, and 1.1 g (18 mmol) urea was added to 40 mL of ultrapure water and stirred for 10 min. Then, the obtained solution was transferred into a Teflon-lined stainless-steel autoclave and heated to 120 °C for 6 h. The product was washed five times with ultrapure water (50 mL each) and two times with ethanol (25 mL each), then dried in a vacuum oven at 60 °C overnight. Yield = 860 mg. (Fe_xNi_{1-x})CoCH-(y) precursors were synthesized by the same method except that the amounts of 98, 196, 294, or 392 mg (0.25, 0.50, 0.75, 1.0 mmol) of $(NH_4)_2Fe(SO_4)_2{\cdot}6H_2O$ were added. Yields = 875 mg, 900 mg, 917 mg, and 930 mg, respectively.

Thereafter, (Fe_xNi_{1-x})CoCH-(y) was used to refer to the iron-containing nickel cobalt carbonate hydroxide with y = 0.25, 0.50, 0.75, and 1.0 mmol of $(NH_4)_2Fe(SO_4)_2{\cdot}6H_2O$ added to the reaction mixture; (Fe_xNi_{1-x})CoCH-(y) refers to all samples.

2.3. Preparation of Iron Nickel Cobalt Sulfides, Selenide, and Sulfoselenide

Iron-containing nickel cobalt sulfide samples were prepared by hydrothermal sulfidation of the (Fe_xNi_{1-x})CoCH-(y) precursors. A chosen amount of iron-containing precursor (125 mg) was dispersed in 40 mL of ultrapure water in an 80 mL Teflon-lined autoclave and stirred for 20 min. After that, 750 mg (3.125 mmol) of $Na_2S{\cdot}9H_2O$ was added. The resultant suspension was transferred to the oven, and the temperature was kept at 160 °C for 12 h. The obtained product was washed five times with ultrapure water (50 mL each) and two times with ethanol (20 mL each), then dried in a vacuum oven at 60 °C overnight. Yield was about 90 mg.

The iron-containing nickel cobalt sulfoselenide sample, $Fe_{0.5}Ni_{1.0}Co_{2.0}(S_{0.57}Se_{0.25}O_{0.18})_4$, was synthesized via sulfidation and selenization of (Fe_xNi_{1-x})CoCH-(1.0) in one step. (Fe_xNi_{1-x})CoCH-(1.0) (125 mg) was dispersed in ultrapure water and stirred for 20 min. Then, 680 mg (2.70 mmol) of $Na_2S{\cdot}9H_2O$ and 50 mg (0.425 mmol) of SeO_2 were added to the suspension. Finally, 10 mL of $N_2H_4{\cdot}H_2O$ was slowly added to the suspension. The Teflon-lined stainless-steel autoclave was kept at 160 °C for 12 h. The resulting powder was washed five times with ultrapure water (50 mL each time) and two times with ethanol (20 mL each time) and dried at 60 °C overnight. Yield was 100 mg.

Iron-containing nickel cobalt selenide, $Fe_{0.4}Ni_{0.7}Co_{1.6}(Se_{0.81}O_{0.19})_4$ was synthesized by selenization of (Fe_xNi_{1-x})CoCH-(1.0). (Fe_xNi_{1-x})CoCH-(1.0) (125 mg) was dispersed in 30 mL of ultrapure water and stirred for 20 min followed by adding 100 mg (0.9 mmol) SeO_2. Then, 10 mL of N_2H_4 was added to abovementioned suspension and stirred for another 10 min. The resulting suspension was transferred to a stainless autoclave and heated at 160 °C for 12 h. The obtained black powder was washed five times with ultrapure water (50 mL each) and three times with absolute ethanol (20 mL each), then dried at 60 °C in the vacuum oven overnight. Yield was 110 mg.

For comparison, nickel cobalt sulfide, $Ni_{1.0}Co_{2.1}(S_{0.9}O_{0.1})_4$ and nickel cobalt selenide, $Ni_{0.7}Co_{1.4}(Se_{0.85}O_{0.15})_4$, and were synthesized by sulfidation or selenization of NiCoCH (Supplementary Materials, Section S1). The schematic illustration of the synthesis is shown in Scheme 1.

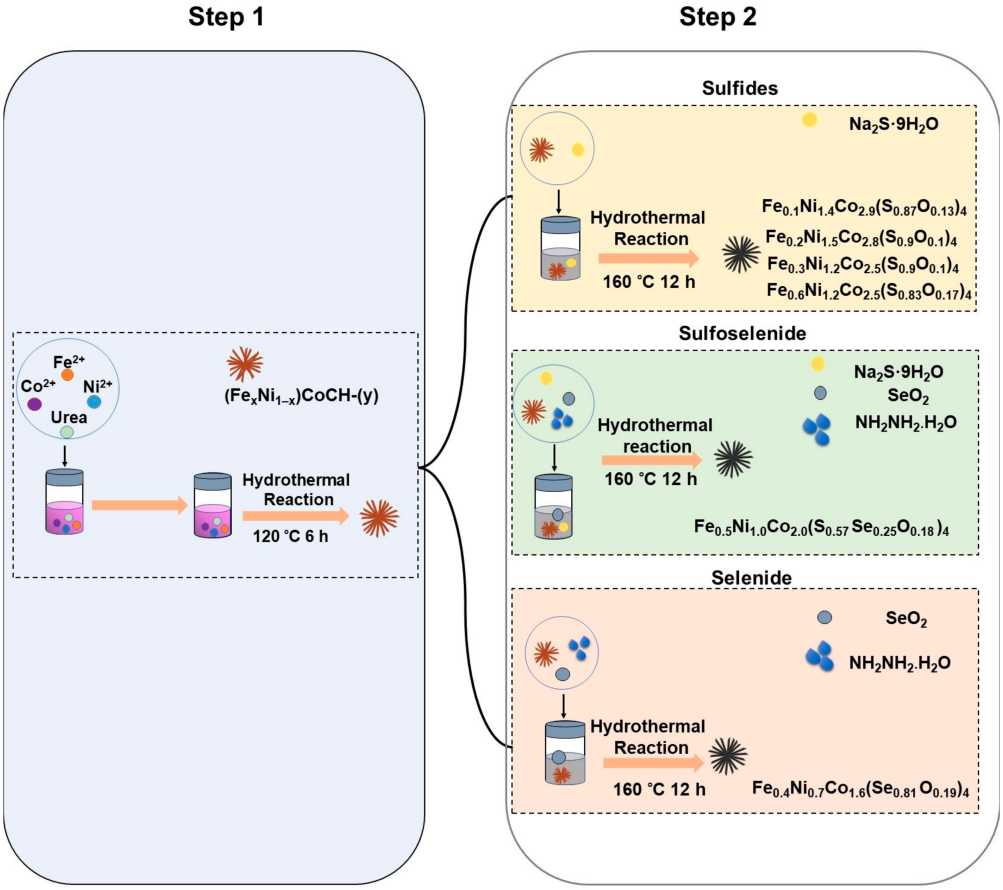

Scheme 1. Schematic illustration of the preparation process for iron-containing Ni-Co sulfide, sulfoselenide, and selenide. $(Fe_xNi_{1-x})CoCH$-(y) represents the precursor iron-containing nickel cobalt carbonate hydroxide hydrate.

2.4. Material Characterization

Powder X-ray diffraction (PXRD) analysis was conducted at ambient temperature on a Rigaku Miniflex 600 powder diffractometer (Rigaku, Tokyo, Japan) using Cu Kα1 radiation with λ = 1.5406 Å (40 kV, 15 mA, 600 W) and a flat silicon low background with a small indent in the range of $2\theta = 5°–100°$. The obtained PXRD data were evaluated with the Match v3.11 software.

Scanning electron microscopy (SEM) was performed with Jeol JSM-6510LV QSEM (Jeol, Akishima, Japan) advanced electron microscope (LaB_6 cathode at 20 kV) equipped with a Bruker Xflash 410 silicon drift detector for energy-dispersive X-ray (EDX) spectroscopy.

Transmission electron microscopy (TEM) with energy-dispersive X-ray spectroscopy (TEM-EDX) was carried out with a FEI Tecnai G2 F20 electron microscope (FEI Co., Hillsboro, OR, USA) operated at 200 kV accelerating voltage.

A Quantachrome Autosorb-6 automatic adsorption analyzer (Quantachrome Gmbh; Odelzhausen, Germany) was used to determine nitrogen sorption isotherms for the BET surface area determination of the samples at 77 K. The samples were degassed at 90 °C in a 10^{-2} mbar vacuum for 15 h before the gas sorption measurement.

X-ray photoelectron spectroscopy (XPS) data were collected using a ULVAC-PHI VersaProbe II microfocus X-ray photoelectron spectrometer (ULVAC-PHI, Chigasaki, Japan). The spectra were recorded using a polychromatic aluminum Kα X-ray source (1486.8 eV) and referenced to the carbon 1s orbital with a binding energy of 284.8 eV.

Quantification of the metal content of the samples was performed using a Perkin-Elmer PinaAcle 900T atomic absorption spectrometer (Perkin Elmer LAS GmbH, Rodgau-Jügesheim, Germany) (sample preparation described in Supplementary Materials, Section S2).

The sulfur content was determined with a VarioMICRO CHNS microanalyzer (Elementar Analysensysteme, Langenselbold, Germany).

2.5. Electrochemical Measurements

All electrochemical analyses were conducted on a three-electrode cell using an Interface 1010E potentiostat from Gamry Instruments at ambient temperature. The reversible hydrogen electrode, RHE, and Pt foil were used as a reference and counter electrode. Coated nickel foam, NF, was the working electrode. A slurry containing 8:1:1 mass portions of the active materials (mixed-metal sulfide, selenide, or sulfoselenide material), carbon black, Vulcan XC-72R, and polyvinylidene fluoride, PVDF, respectively, in *N*-methyl-2-pyrrolidone, NMP was prepared and carefully dropped on a 1 cm^2 area of the NF surface, and dried at 60 °C for 12 h in a vacuum oven to prepare the coated NF electrode. To prepare the slurry, a weighted mass of 5 mg of the mixed-metal sulfide, selenide, or sulfoselenide material was utilized. Additionally, the weight of the electrode before and after loading the slurry was measured. The slurry was accurately applied to a 1 cm^2 area of the electrode surface. Throughout the OER, we ensured the presence of a 1 cm^2 electrode immersed in the KOH solution. Before starting the electrochemical analysis, an N_2 gas flow was passed through the electrolyte to remove dioxygen from the 1 mol L^{-1} KOH electrolyte.

Linear sweep voltammetry LSV measurement was applied to determine the catalytic performance of the coated NF electrode at a scan rate of 5 mV s^{-1}. Before starting the LSV measurement, 20 cycles of cyclic voltammetry at a scan rate of 100 mV s^{-1} were run to reach a stable electrocatalytic performance. The potentials of the LSV polarization curves were corrected by iR compensation. The chronopotentiometry at the current density of 50 mA cm^{-2} for 20 h was used to evaluate the stability of the selected electrocatalyst in long-term performance. Moreover, to understand the electrode/electrolyte interface behavior, electrochemical impedance spectroscopy, EIS, was performed in the frequency range of 0.1–100 kHz at 1.5 V vs. RHE.

3. Result and Discussion

3.1. Synthesis and Analysis

Nickel cobalt carbonate hydroxide (NiCoCH) and iron-containing nickel cobalt carbonate hydroxides (Fe_xNi_{1-x})CoCH-(y) were synthesized from $CoCl_2{\cdot}6H_2O$, $NiCl_2{\cdot}6H_2O$, $(NH_4)_2Fe(SO_4)_2{\cdot}6H_2O$ and urea as precursors in hydrothermal reactions (Step 1 in Scheme 1). Four different amounts of $(NH_4)_2Fe(SO_4)_2{\cdot}6H_2O$ were used to synthesize (Fe_xNi_{1-x})CoCH-(y), while keeping the $NiCl_2{\cdot}6H_2O$ and $CoCl_2{\cdot}6H_2O$ amounts constant. The samples were named (Fe_xNi_{1-x})CoCH-(0.025), (Fe_xNi_{1-x})CoCH-(0.05), (Fe_xNi_{1-x})CoCH-(0.075), and (Fe_xNi_{1-x})CoCH-(0.1), representing the use of 0.025, 0.05, 0.075, and 1.0 mmol of the iron precursor. The sulfidation and selenization of the metal carbonate hydroxide precursors were achieved through a hydrothermal sulfidation process with $Na_2S{\cdot}9H_2O$ and a selenization process with SeO_2 (Step 2 in Scheme 1). For the sulfoselenide sample, a mixture of $Na_2S{\cdot}9H_2O$ and SeO_2 was employed in the hydrothermal reaction.

Two different methods were used to determine the chemical formula of the as-prepared samples, a combination of AAS for the metal and CHNS analysis for the sulfur content (method 1) and SEM-EDX (method 2) (Supplementary Materials, Tables S2–S6). Method 1 provides more precise atomic ratios of metal and S content in the samples than EDX. In EDX, the emitted X-rays give a 1–2 µm depth analysis but EDX as an X-ray spectroscopy experiences matrix effects and would need standards of similar composition as the sample for peak identification and accurate quantification. For the sulfoselenide and selenide sample, AAS for the metal content was combined with EDX for the Se content. Moreover, the chemical formulae obtained from AAS + CHNS + EDX were much closer to charge balance than the EDX-derived formulae. Based on the metal-to-sulfur ratios obtained from method 1 and the charge balance calculation of the samples, oxygen should also be incorporated into the structure of the samples. The presence of oxygen in the structure of samples was also proven from the EDX and XPS spectrum. Therefore, the chemical formulae are given here with their estimated oxygen content. The chemical formulas resulting from methods 1 and 2 are provided in Table S6. The measured SEM-EDX data of the samples are provided in Figures S1–S8.

The crystallinity of all sulfide samples was low, as evidenced by broad peaks of low intensity in the powder X-ray diffractograms, PXRDs (Figure 1a). The crystalline phases in the iron-containing nickel cobalt samples were verified as spinels by matching to the known diffractograms of $NiCo_2S_4$ (ICDD no. 43-1477) and Co_3S_4 (ICDD no. 75-1561) (Figure 1). The prominent diffraction peaks located at 26.8°, 31.5°, 38.1°, 50.4°, and 55.2° can be attributed to the (220), (311), (400), (511), and (440) planes of the spinel lattice [24]. In addition, in the PXRD patterns of $NiCo_2S_4$ and iron-containing nickel cobalt samples, the diffraction peaks at 29.9° and 52.1° can be attributed to the (311) and (440) planes, respectively, of Co_9S_8 (ICDD no. 73-1442). It should be mentioned that the presence of an Co_9S_8 impurity in $NiCo_2S_4$ is reported in much of the previous literature, including the work of Chen et al. [24], who first reported the formation of sea-urchin-like $NiCo_2S_4$ using metal carbonate hydroxide as a precursor [33,40,47–51].

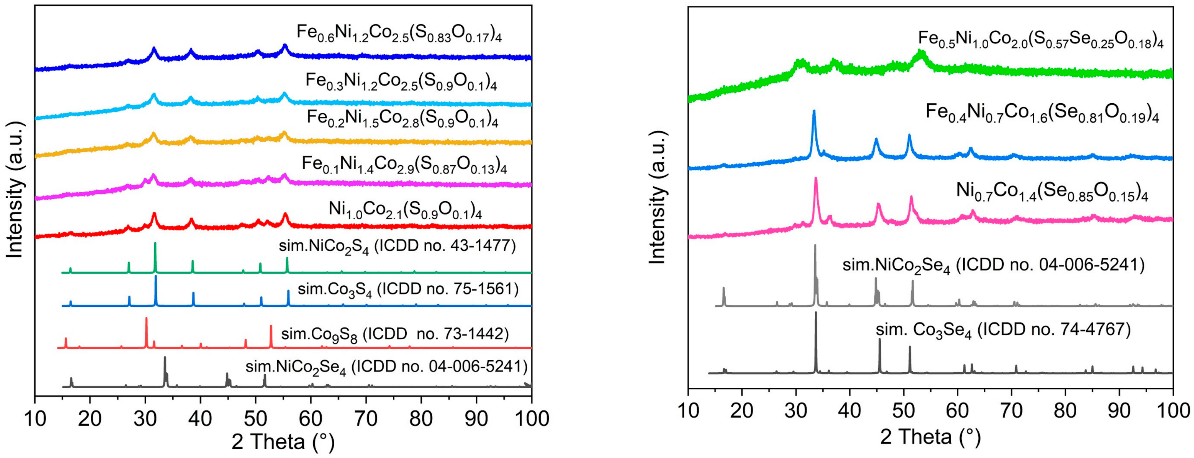

(**a**) (**b**)

Figure 1. PXRD patterns of (**a**) as-prepared sulfide and (**b**) selenide and sulfoselenide samples compared to simulated (sim.) patterns of different metal sulfides and selenides.

The content of the crystalline Co_9S_8 impurity decreases with increasing iron content and is only barely visible in $Fe_{0.3}Ni_{1.2}Co_{2.5}(S_{0.9}O_{0.1})_4$ and no longer visible in $Fe_{0.6}Ni_{1.2}Co_{2.5}(S_{0.83}O_{0.17})_4$. The corresponding selenides are of higher crystallinity (Figure 1b). The prominent reflection peaks of $NiCo_2Se_4$ and $Fe_{0.4}Ni_{0.7}Co_{1.6}(Se_{0.81}O_{0.19})_4$ match the simulation for $NiCo_2Se_4$ (ICDD no. 04-006-5241), where they correspond to the (002), (311), and (−313) crystal plane located at 33.3°, 44.9°, and 51.4°, respectively [52]. By incorporating both sulfur and selenium in the structure, the crystallinity of $Fe_{0.5}Ni_{1.0}Co_{2.0}(S_{0.57}Se_{0.25}O_{0.18})_4$ from the PXRD pattern became too low and no clear crystalline phase analysis was possible anymore. Such low crystallinity was also seen in the literature for nickel sulfoselenide, oxygen-containing cobalt sulfide, and nickel sulfide nanoparticles, which were reported with excellent OER properties [53–55]. Previous reports have demonstrated that incorporating or doping transition metal sulfides, such as nickel cobalt sulfides with iron, induces lattice strain which results in peak broadening [56]. A small shift towards lower angles of the experimental diffractograms of selenium-containing samples versus the simulated diffractograms of the sulfur-only analogues can be ascribed to a larger lattice spacing which is caused by the larger radius of selenium compared to sulfur [57]. A shift in the peak positions between experimental and simulated diffractograms is also obtained if the sample is not properly aligned with the goniometer axis, e.g., by placing too thick a sample on the sample holder in the Bragg–Brentano geometry [58].

The morphology of the as-prepared samples was studied using scanning electron microscopy, SEM. As shown in Figure 2a, $Ni_{1.0}Co_{2.1}(S_{0.9}O_{0.1})_4$ consists of needle-like structures combining parts with a sea urchin-like morphology. By increasing the iron content, the morphology became more sea urchin-like (Figure 2b–f). In the selenides and the sulfoselenide $Fe_{0.6}Ni_{1.2}Co_{2.5}(S_{0.83}O_{0.17})_4$ sample, Figure 2e,f, agglomerations of needle-like primary particles can be seen. The SEM-energy dispersive X-ray (EDX) mappings (Supplementary Materials, Figure S9) support the AAS- and CHNS-based elemental analysis for the chemical formulae, and SEM-EDX was the analysis of choice to determine the selenium content.

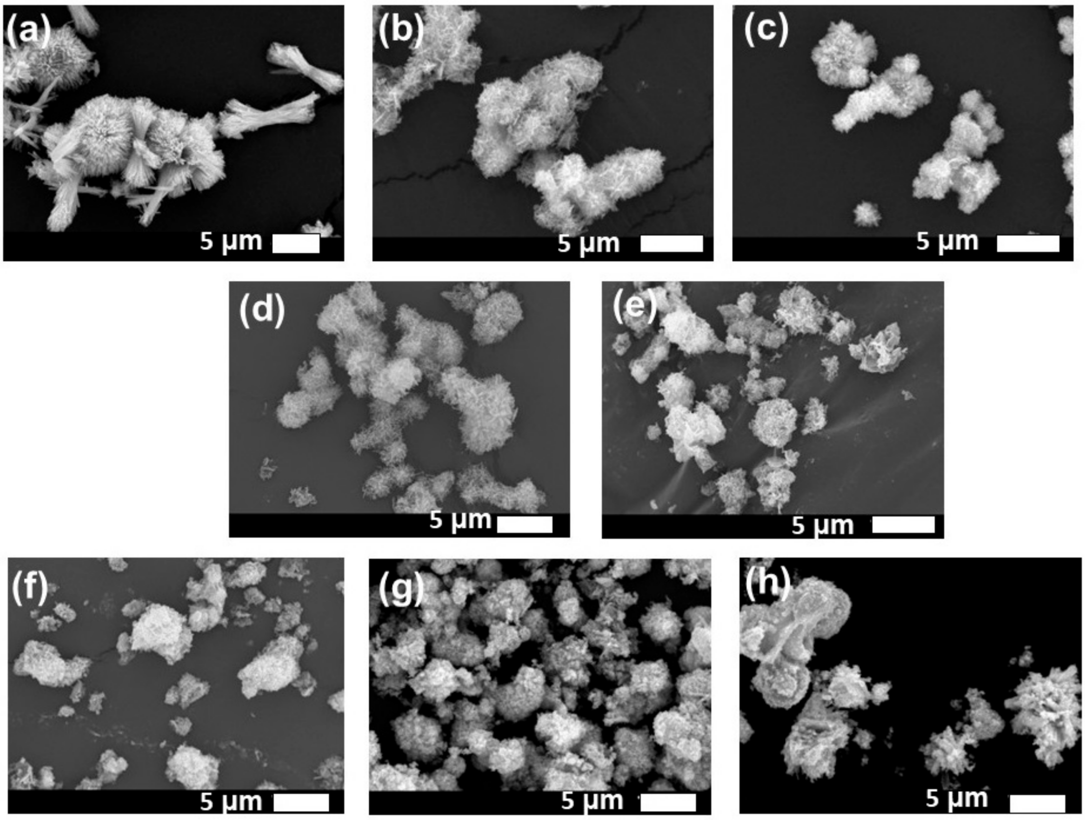

Figure 2. SEM images of the as-prepared samples: (**a**) $Ni_{1.0}Co_{2.1}(S_{0.9}O_{0.1})_4$, (**b**) $Fe_{0.1}Ni_{1.4}Co_{2.9}(S_{0.87}O_{0.13})_4$, (**c**) $Fe_{0.2}Ni_{1.5}Co_{2.8}(S_{0.9}O_{0.1})_4$, (**d**) $Fe_{0.3}Ni_{1.2}Co_{2.5}(S_{0.9}O_{0.1})_4$, (**e**) $Fe_{0.6}Ni_{1.2}Co_{2.5}(S_{0.83}O_{0.17})_4$, (**f**) $Fe_{0.5}Ni_{1.0}Co_{2.0}(S_{0.57}Se_{0.25}O_{0.18})_4$, (**g**) $Fe_{0.4}Ni_{0.7}Co_{1.6}(Se_{0.81}O_{0.19})_4$, and (**h**) $Ni_{0.7}Co_{1.4}(Se_{0.85}O_{0.15})_4$.

To further investigate the sulfoselenide $Fe_{0.5}Ni_{1.0}Co_{2.0}(S_{0.57}Se_{0.25}O_{0.18})_4$, transition electron microscopy, TEM-EDX, was performed. The TEM images, Figure 3, confirmed the needle-like microstructure. EDX-mapping also proved the uniform presence of Fe, Ni, Co, S, and Se in the sulfoselenide sample (see Supplementary Materials, Table S1 for atom ratios).

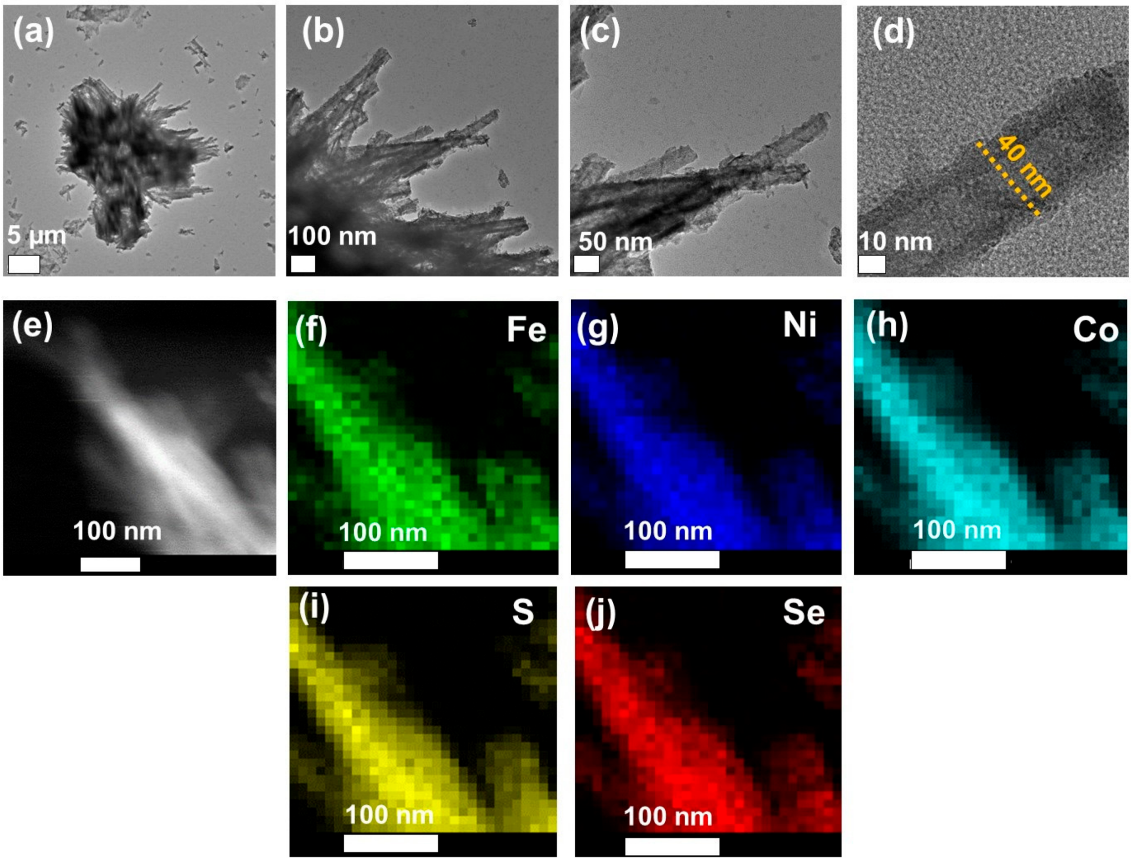

Figure 3. TEM images (**a**–**e**) of $Fe_{0.5}Ni_{1.0}Co_{2.0}(S_{0.57}Se_{0.25}O_{0.18})_4$ and (**f**–**j**) HAADF STEM-EDX mapping results of Fe, Ni, Co, S, and Se, recorded from a nano needle section (**e**) of $Fe_{0.5}Ni_{1.0}Co_{2.0}(S_{0.57}Se_{0.25}O_{0.18})_4$.

Nitrogen adsorption–desorption isotherms, and specific surface area (BET) of the samples are given in Figure S10 and Table S7.

X-ray photoelectron spectroscopy (XPS) was conducted to determine the valence state of the elements in $Ni_{1.0}Co_{2.1}(S_{0.9}O_{0.1})_4$ and $Fe_{0.5}Ni_{1.0}Co_{2.0}(S_{0.57}Se_{0.25}O_{0.18})_4$. As shown in Figure S11, X-ray survey spectra indicate the existence of Ni, Co, and S in $Ni_{1.0}Co_{2.1}(S_{0.9}O_{0.1})_4$ and of Fe, Ni, Co, S, and Se in $Fe_{0.5}Ni_{1.0}Co_{2.0}(S_{0.57}Se_{0.25}O_{0.18})_4$. The high-resolution spectra of the metal atoms and of Se are shown in Figure 4 and those of S 2p and O1s of $Ni_{1.0}Co_{2.1}(S_{0.9}O_{0.1})_4$ in Figures S12a and S13a, respectively. The positions of the XPS peaks are summarized in Tables S8 and S9. It should be noted that the analysis depth of XPS is only 0.7–11 nm as the detected photoelectrons can only escape from such a thin surface layer of the sample.

The metal ratios and the ratios between different oxidation states of nickel and cobalt (Table 1) were calculated by integrating the fitted peak area for each metal valence state using the Ni $2p_{3/2}$ and Co $2p_{3/2}$ regions. In $Ni_{1.0}Co_{2.1}(S_{0.9}O_{0.1})_4$, Ni^{2+} and Co^{3+} are the prevalent oxidation states.

Based on element ratios obtained from AAS and CHNS analysis and also the metal valence states for nickel and cobalt in the $Ni_{1.0}Co_{2.1}(S_{0.9}O_{0.1})_4$ sample, the chemical formula can be given as $((Ni^{2+})_{0.72}(Ni^{3+})_{0.28})_{1.0}((Co^{2+})_{0.27}(Co^{3+})_{0.72})_{2.1}(S_{0.9}O_{0.1})_4$ which is anion-cation charge-balanced within rounding errors.

In contrast to the $Ni_{1.0}Co_{2.1}(S_{0.9}O_{0.1})_4$ sample, Ni^{3+} and Co^{2+} are the dominant valence states in $Fe_{0.5}Ni_{1.0}Co_{2.0}(S_{0.57}Se_{0.25}O_{0.18})_4$, which might be one of the reasons for the improved OER performance of this catalyst. It is believed that Ni^{3+} can improve electrophilicity and oxygen adsorption, which can increase the amount of NiOOH active sites during the OER reaction [59].

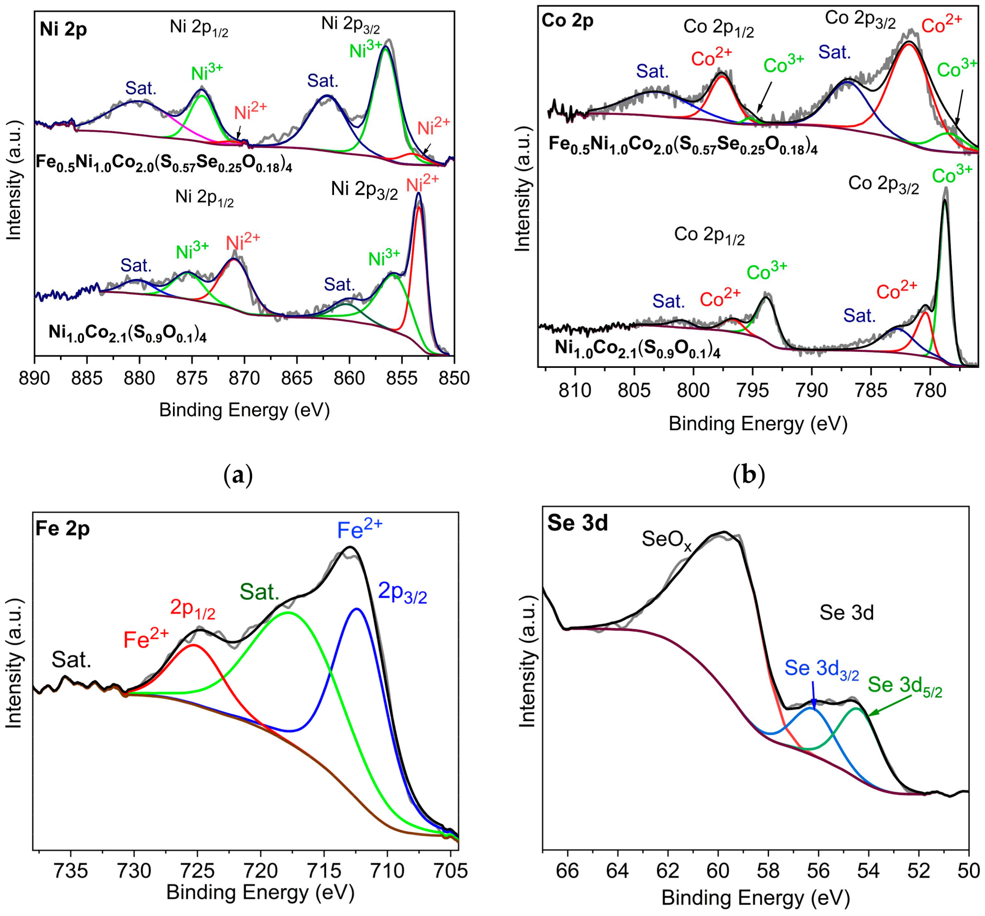

(**a**) (**b**)

(**c**) (**d**)

Figure 4. High-resolution XPS spectra of (**a**) Ni 2p region and (**b**) Co 2p region of $Ni_{1.0}Co_{2.1}(S_{0.9}O_{0.1})_4$ and $Fe_{0.5}Ni_{1.0}Co_{2.0}(S_{0.57}Se_{0.25}O_{0.18})_4$, (**c**) Fe 2p region and (**d**) Se 3d region of $Fe_{0.5}Ni_{1.0}Co_{2.0}(S_{0.57}Se_{0.25}O_{0.18})_4$.

Table 1. The metal ratios and the ratios between different oxidation states of nickel and cobalt in $Ni_{1.0}Co_{2.1}(S_{0.9}O_{0.1})_4$ and $Fe_{0.5}Ni_{1.0}Co_{2.0}(S_{0.57}Se_{0.25}O_{0.18})_4$.

Sample		At% [(a)]	Ni/Co [(a)]		At% [(b)]	Position (eV)	M^{2+}/M^{3+}
$Ni_{1.0}Co_{2.1}(S_{0.9}O_{0.1})_4$ [(c)]	Ni	6.90	1/2	Ni^{2+}	35.6	853.3	2.59
				Ni^{3+}	13.7	856.0	
	Co	13.90		Co^{2+}	17.0	780.3	0.37
				Co^{3+}	45.9	778.7	
			Fe/Ni/Co [(a)]				
$Fe_{0.5}Ni_{1.0}Co_{2.0}(S_{0.57}Se_{0.25}O_{0.18})_4$ [(d)]	Fe	2.30	1.0/2.5/4.1				
	Ni	5.70		Ni^{2+}	3.3	854.5	0.10
				Ni^{3+}	32.9	856.5	
	Co	9.40		Co^{2+}	46.7	781.9	6.65
				Co^{3+}	7.0	779.1	

[(a)] From XPS survey spectrum (Figure S11, Supplementary Materials). [(b)] Based on the Ni $2p_{3/2}$ and Co $2p_{3/2}$ regions in XPS. [(c)] Element composition from AAS-CHNS. [(d)] Element composition from AAS-CHNS-EDX(Se) (Tables S3–S6, Supplementary Materials).

The Fe 2p spectrum (Figure 4c) for $Fe_{0.5}Ni_{1.0}Co_{2.0}(S_{0.57}Se_{0.25}O_{0.18})_4$ represents two broad peaks at 712.5 eV and 725.0 eV, which can be assigned to Fe $2p_{3/2}$ and Fe $2p_{1/2}$, respectively [60]. Furthermore, two satellite peaks were detected at 717.5 and 734.5 eV [61,62]. The $2p_{3/2}$ spectrum range is 710 to 720 eV including the satellite peak, while the $2p_{1/2}$ spectrum range is 720−735 eV with the satellite peak. For iron, it should be noted that the Fe 2p spectral background is contributed to from the Co_{LMM} and Ni_{LMM} Auger peaks, making an unequivocal deconvolution and peak assignment difficult [63,64]. The Se 3d XPS spectra of $Fe_{0.5}Ni_{1.0}Co_{2.0}(S_{0.57}Se_{0.25}O_{0.18})_4$ (Figure 4d) consist of two peaks centered at 55.0 and 57.0 eV, representing Se $3d_{5/2,}$ and Se $3d_{3/2}$, respectively. The peak at 59.5 eV was attributed to the SeO_X forming on the surface due to exposure to air, and to the overlap with the Co 3p signal [42]. The high-resolution spectrum of S 2p and O 1s of $Fe_{0.5}Ni_{1.0}Co_{2.0}(S_{0.57}Se_{0.25}O_{0.18})_4$ are shown in Figures S12b and S13b (Supplementary Materials), respectively. Based on the elemental ratios obtained from AAS, CHNS, and EDX(Se) analysis, and also metal valence states for iron, nickel, and cobalt in the $Fe_{0.5}Ni_{1.0}Co_{2.0}(S_{0.57}Se_{0.25}O_{0.18})_4$ sample, the chemical formula can be given as $(Fe^{2+})_{0.5}((Ni^{2+})_{0.1}(Ni^{3+})_{0.9})_{1.0}((Co^{2+})_{0.87}(Co^{3+})_{0.13})_{2.0}(S_{0.57}Se_{0.25}O_{0.18})_4$.

3.2. Oxygen Evolution Reaction Performance

The OER activity of the mixed-metal sulfides, selenides, and the sulfoselenide was evaluated by a three-electrode setup in 1.0 mol L^{-1} KOH solution. The working electrode was prepared according to a method used by Li et al. [33], a slurry containing 8:1:1 mass portions of the active materials (mixed-metal sulfide, selenide, or sulfoselenide material), carbon black, Vulcan XC-72R, and polyvinylidene fluoride, PVDF, respectively, in *N*-methyl-2-pyrrolidone, NMP (further details in experimental section). As is shown in Figure 5a, the polarization curves of the as-prepared electrodes revealed that the presence of iron could reduce the overpotential of the $Ni_{1.0}Co_{2.1}(S_{0.9}O_{0.1})_4$ parent compound. In the polarization curves, the peaks around 1.3–1.4 eV are attributed to the oxidation of Ni^{2+}/Ni^{3+} [65].

The overpotential for $Ni_{1.0}Co_{2.1}(S_{0.9}O_{0.1})_4$ of 346 mV at 50 mA cm^{-2} was reduced with increasing iron content in $Fe_{0.1}Ni_{1.4}Co_{2.9}(S_{0.87}O_{0.13})_4$, $Fe_{0.2}Ni_{1.5}Co_{2.8}(S_{0.9}O_{0.1})_4$, $Fe_{0.3}Ni_{1.2}Co_{2.5}(S_{0.9}O_{0.1})_4$, and $Fe_{0.6}Ni_{1.2}Co_{2.5}(S_{0.83}O_{0.17})_4$ to 318, 310, 294, and 294 mV, respectively (Figure 5a,b). The electronic interaction between Fe, Ni, and Co in the iron-containing samples alters the electronic structure, making Ni^{2+} oxidation more difficult, resulting in a positive shift in the Ni^{2+}/Ni^{3+} anodic peak at 1.3–1.4 eV [33,40]. The reduction in the OER overpotential in iron-containing samples can be attributed to reducing the charge transfer resistance through the synergistic electronic interaction between Fe, Co and Ni from a charge redistribution between active sites within the samples. Density functional theory (DFT) calculations in the literature traced the synergy to a decrease in the Gibbs free energy for the formation of a MOOH intermediate, which not only enhanced the intrinsic OER activity, but also significantly improved the intrinsic conductivity of iron-containing samples, greatly facilitating the charge transfer process [66].

In the next step, the effect of the coexistence of sulfur and selenium was investigated. The overpotential of $Fe_{0.5}Ni_{1.0}Co_{2.0}(S_{0.57}Se_{0.25}O_{0.18})_4$ (green line) of 277 mV at 50 mA cm^{-2} presents a 17 mV and 22 mV reduction compared to $Fe_{0.6}Ni_{1.2}Co_{2.5}(S_{0.83}O_{0.17})_4$ (294 mV) and RuO_2 (299 mV) (Figure 5c,d), indicating that the insertion of selenium improves the performance of the transition metal sulfide. Moreover, the OER performance of $Fe_{0.5}Ni_{1.0}Co_{2.0}(S_{0.57}Se_{0.25}O_{0.18})_4$ at 100 mA cm^{-2} only needed 299 mV while RuO_2 required 341 mV overpotential, which demonstrates the excellent electrocatalytic activity of $Fe_{0.5}Ni_{1.0}Co_{2.0}(S_{0.57}Se_{0.25}O_{0.18})_4$ even under a high current density. The boost of the OER activity of $Fe_{0.5}Ni_{1.0}Co_{2.0}(S_{0.57}Se_{0.25}O_{0.18})_4$ can be attributed to the effect of selenide incorporation that reduces the energy barrier of the OER reaction, optimizes the electronic structure of active sites via modulating of the d-band of the compound, and also accelerates the kinetics of the reaction [67].

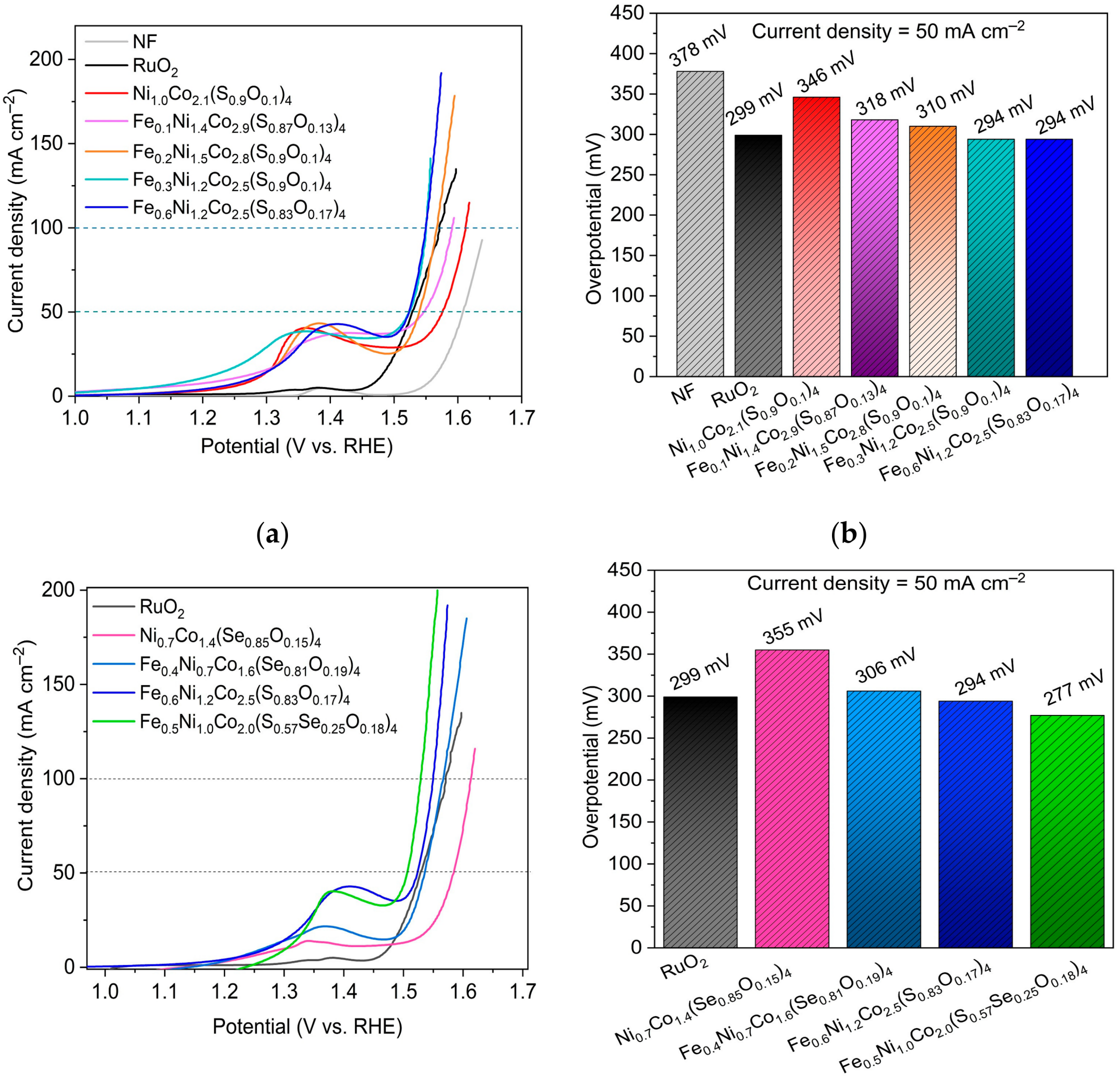

(**a**) (**b**)

(**c**) (**d**)

Figure 5. (**a**) OER LSV polarization curves and (**b**) bar chart of corresponding overpotentials at 50 mA cm^{-2} of iron-containing sulfides. (**c**) OER LSV polarization curves and (**d**) bar chart of corresponding overpotentials at 50 mA cm^{-2} of different iron-containing sulfides, selenides, and sulfoselenide.

The Tafel slopes of the samples were obtained from LSV polarization curves at a scan rate of 5 mV s^{-1} using the Tafel Equation (1) [68]:

$$\eta = a + b \times \log(j) \quad (1)$$

η is the overpotential, b is the Tafel slope, j is the current density, and c is the intercept with the y-axis. The value of the Tafel slope is one of the most useful kinetic parameters and is inversely proportional to the kinetics of the OER reaction. Hence, as demonstrated in Figure 6a,b, $Fe_{0.5}Ni_{1.0}Co_{2.0}(S_{0.57}Se_{0.25}O_{0.18})_4$, with the lowest value of the Tafel slope, presents the most favorable OER kinetics among the investigated samples. Furthermore, according to Krasil'shchikov's mechanistic paths (Equations (2)–(5), M = active site, b = Tafel slope) [68,69] with their corresponding Tafel slope values, the rate-determining step of the OER reaction for $Ni_{1.0}Co_{2.1}(S_{0.9}O_{0.1})_4$ (b = 125 mV dec^{-1}) is metal oxidation with hydroxide formation (reaction (2)). By increasing the iron content in the samples, the Tafel slope decreased and reached 85 mV dec^{-1} for $Fe_{0.6}Ni_{1.2}Co_{2.5}(S_{0.83}O_{0.17})_4$, suggesting that metal oxidation with hydroxide formation (2), and deprotonation of a metal hydroxide (3), both present rate-determining steps.

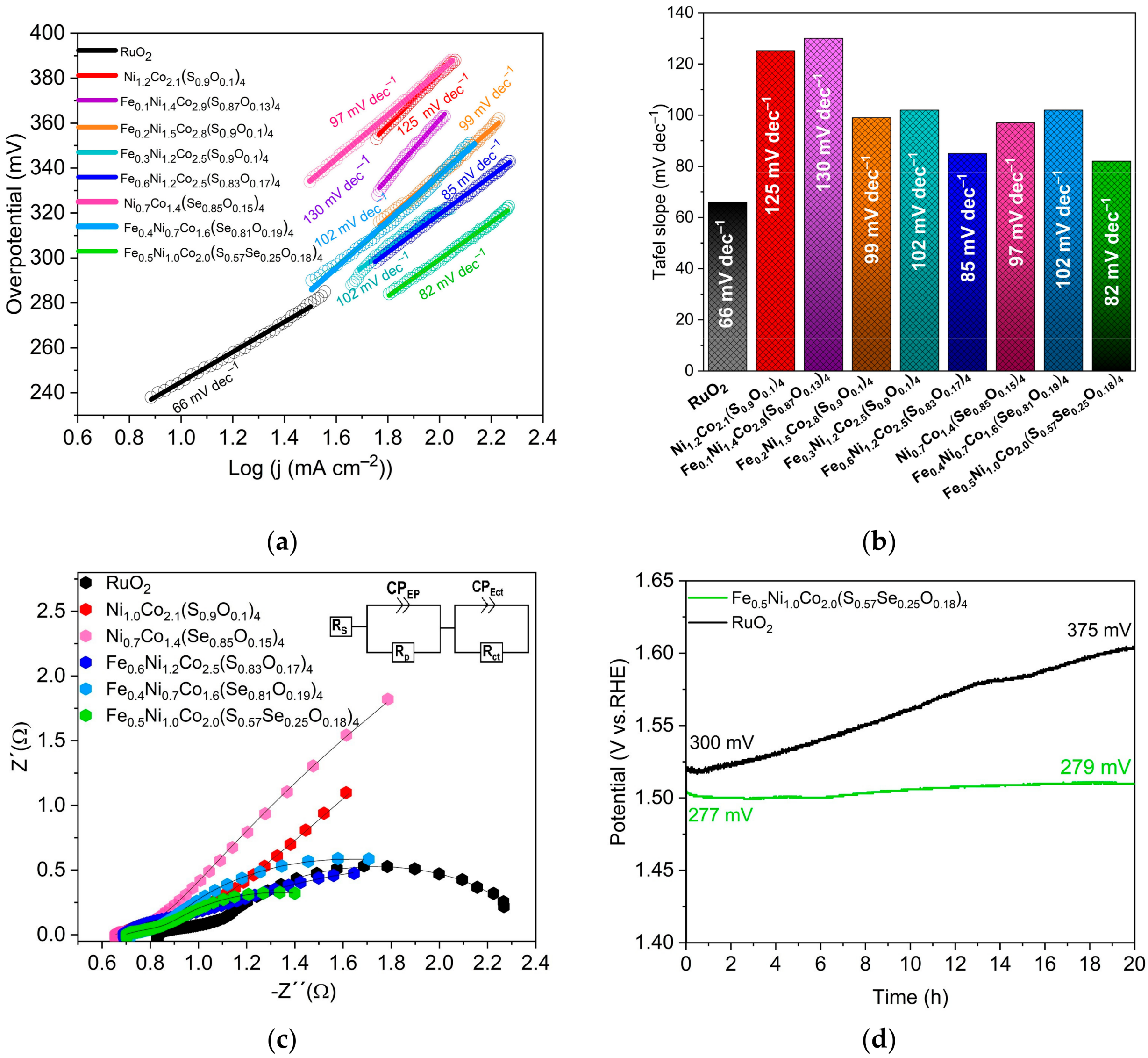

(**a**) (**b**)

(**c**) (**d**)

Figure 6. (**a**) Tafel plots and (**b**) bar chart of Tafel slopes of the samples. (**c**) Nyquist plots of selected samples and Voigt circuit model. (**d**) Chronopotentiometry test of $Fe_{0.5}Ni_{1.0}Co_{2.0}(S_{0.57}Se_{0.25}O_{0.18})_4$ and RuO_2.

The lowest Tafel slope among the samples belongs to the sulfoselenide $Fe_{0.5}Ni_{1.0}Co_{2.0}(S_{0.57}Se_{0.25}O_{0.18})_4$ with 82 mV dec^{-1}, which is again evidence for the role of selenium in enhancing the kinetics of the OER reaction. The Tafel value of 82 mV dec^{-1} of $Fe_{0.5}Ni_{1.0}Co_{2.0}(S_{0.57}Se_{0.25}O_{0.18})_4$ is close to reaction (3) (b = 60 mV dec^{-1}), being, then, rate-determining in the overall OER process.

$$M + OH^- \leftrightarrows MOH + e^-,\ b = 120\ \text{mV dec}^{-1} \tag{2}$$

$$MOH + OH^- \leftrightarrows MO^- + H_2O,\ b = 60\ \text{mV dec}^{-1} \tag{3}$$

$$MO^- \rightarrow MO + e^-,\ b = 45\ \text{mV dec}^{-1} \tag{4}$$

$$2MO \rightarrow 2M + O_2, b = 19 \text{ mV dec}^{-1} \quad (5)$$

Electrochemical impedance spectroscopy (EIS) was conducted for the electron-transfer kinetics during the OER reaction and to justify the obtained overpotentials [70]. Figure 6c shows Nyquist plots of the samples at the potential of 1.5 V vs. RHE. The semicircle diameter of Nyquist plots is inversely proportional to the charge transfer rate across the electrode and the electrolyte that accelerates reaction kinetics. Hence, a smaller semicircle diameter represents more favorable charge transfer kinetics [27].

The smaller semicircle diameter of the $Fe_{0.5}Ni_{1.0}Co_{2.0}(S_{0.57}Se_{0.25}O_{0.18})_4$ Nyquist plot indicates that the coexistence of iron and selenium in $Fe_{0.5}Ni_{1.0}Co_{2.0}(S_{0.57}Se_{0.25}O_{0.18})_4$ can reduce the charge transfer resistance (Rct). Furthermore, a Voigt circuit model was applied to the Nyquist plots to evaluate the specific value for the charge resistance in the OER process. As shown in Table 2, the value of charge resistance for $Fe_{0.5}Ni_{1.0}Co_{2.0}(S_{0.57}Se_{0.25}O_{0.18})_4$ is the lowest (0.8 Ω) compared to the other investigated samples. The results from the Rct values are in line with the recorded OER overpotentials of the samples and the electrocatalytic performance.

Table 2. Overpotential at 50 mA cm^{-2}, Tafel slopes, and estimated charge transfer resistance of selected samples at 1.5 V vs. RHE.

Sample	**Overpotential (mV)**	**Tafel Slope (mV dec^{-1})**	**Charge Transfer Resistance Rct (Ω)**
$Ni_{1.0}Co_{2.1}(S_{0.9}O_{0.1})_4$	346	125	1.8
$Ni_{0.7}Co_{1.4}(Se_{0.85}O_{0.15})$	355	97	1.7
$Fe_{0.6}Ni_{1.2}Co_{2.5}(S_{0.83}O_{0.17})_4$	294	85	2.2
$Fe_{0.4}Ni_{0.7}Co_{1.6}(Se_{0.81}O_{0.19})_4$	306	102	1.4
$Fe_{0.5}Ni_{1.0}Co_{2.0}(S_{0.57}Se_{0.25}O_{0.18})_4$	277	82	0.8
(Fe_xNi_{1-x})CoCH-(1.0)	330	98	2.5
RuO_2	299	66	1.2

To elucidate the importance of sulfur and selenium in the OER electrocatalysis performance, the (Fe_xNi_{1-x})CoCH-(1.0) precursor for $Fe_{0.6}Ni_{1.2}Co_{2.5}(S_{0.83}O_{0.17})_4$ and $Fe_{0.5}Ni_{1.0}Co_{2.0}(S_{0.57}\ Se_{0.25}O_{0.18})_4$ was investigated and found to have an OER LSV polarization curve with a higher overpotential of 330 mV vs. RHE to reach 50 mA cm^{-2} and a Tafel slope of 98 mV dec^{-1}, higher than the iron-containing sulfide and sulfoselenide (Table 2, Figure S14). Furthermore, the larger Nyquist plot semicircle diameter and higher charge transfer resistance (R_{ct} = 2.5 Ω) of (Fe_xNi_{1-x})CoCH-(1.0) imply the importance of S and Se in facilitating the charge transfer through the electrode–electrolyte interface in sulfide, selenides, and sulfoselenide samples (Figure S15).

One of the critical parameters to evaluate the performance of electrocatalysts in practical applications is their long-term stability. Hence, a chronopotentiometry test, at a current density of 50 mA cm^{-2} for 20 h, was conducted to evaluate the long-term stability performance of the $Fe_{0.5}Ni_{1.0}Co_{2.0}(S_{0.57}Se_{0.25}O_{0.18})_4$ [50].

Figure 6d illustrates that, after 20 h of OER reaction, the overpotential for obtaining 50 mA cm^{-2} only increased from 277 mV to 279 mV, which is essentially constant and supports the excellent electrocatalyst stability of $Fe_{0.5}Ni_{1.0}Co_{2.0}(S_{0.57}Se_{0.25}O_{0.18})_4$ for practical applications. Especially since for RuO_2 the overpotential increased from 300 mV to 375 mV during the same chronopotentiometry test for 20 h, at 50 mA cm^{-2}. A recent study by Jiang et al. [70,71] proved that a SeO_x film on the surface could improve the catalyst stability in the OER reaction, which can be the reason behind the high stability of $Fe_{0.5}Ni_{1.0}Co_{2.0}(S_{0.57}\ Se_{0.25}O_{0.18})_4$ during the OER reaction (the overpotential increased from 277 to only 279 at 50 mA cm^{-1} after 20 h OER reaction).

The superior OER activity and stability of $Fe_{0.5}Ni_{1.0}Co_{2.0}(S_{0.57}Se_{0.25}O_{0.18})_4$ material can be attributed to several effects resulting from introducing Fe and Se^{2-} in the structure of the nickel cobalt sulfide base material; introducing Fe sites can enhance OER performance (a) by optimizing bond energies for OER intermediates adsorbing on the electrode surface, which facilitates the OER kinetics [72], (b) by overcoming the metal oxidation step and facilitating O_2 evolution [73], or (c) by improving the conductivity of the electrode film [74]. However, it is known that the surface of electrodes containing iron, nickel, and cobalt is oxidized and amorphized in the course of oxygen evolution occurring at high positive electrode potentials [75–77].

For comparison, the overpotential values of several high performance electrocatalysts at a current density of 50 mA cm^{-2} using nickel foam as substrate are presented in Table 3. Notably, the results demonstrate that the OER performance of the sulfoselenide $Fe_{0.5}Ni_{1.0}Co_{2.0}(S_{0.57}Se_{0.25}O_{0.18})_4$ is on par with the best electrocatalysts reported in the literature, highlighting its comparable effectiveness.

Table 3. Comparison of nickel- and cobalt-based electrocatalysts for OER.

Catalyst	Overpotential (mV)	Current Density (mA cm^{-2})	Electrode Substrate [(a)]	Ref.
$Fe_{0.5}Ni_{1.0}Co_{2.0}(S_{0.57}Se_{0.25}O_{0.18})_4$	277	50	NF	This work
$Co_3O_4/NiCo_2O_4$	407	50	NF	[78]
$NiO/\alpha\text{-}Fe_2O_3$	244	50	NF	[79]
$P\text{-}Ni_3S_2/CoFe_2O_4$	254	50	NF	[79,80]
PANI [(b)]/NiFe–OH	260	50	NF	[81]
$LaCoO_3$	420	50	NF	[82]
Ce-doped Ni_3S_2	257	50	NF	[83]
Porous Ni_3S_2	291	50	NF	[84]
$(Co_{1.2}MoO_{4.21}\cdot 3H_2O)/Ni_3S_2$	290	50	NF	[85]
$CoHPO_4\cdot H_2O$	350	50	NF	[86]
NiSe@NiOOH	300	50	NF	[87]
P-containing $NiCo_2S_4$	300	50	NF	[41]
NiFe-LDH [(c)]/Co_3O_4	274	50	NF	[88]

[(a)] NF = nickel foam; as we used a nickel foam electrode and current densities of 50 mA cm^{-2}, this comparative listing is restricted to the same conditions. [(b)] PANI = polyaniline. [(c)] LDH = layered double hydroxides.

During the course of our studies, we realized the number of parameters and that an orthogonal experimental design would be beneficial [89]. We have suggested a theoretical orthogonal experimental design for future work on iron-containing sulfides, selenides, and sulfoselenides (Section S8, Supplementary Materials).

4. Conclusions

A novel trimetallic sulfoselenide, $Fe_{0.5}Ni_{1.0}Co_{2.0}(S_{0.57}Se_{0.25}O_{0.18})_4$, electrocatalyst was synthesized via a two-step hydrothermal method. The mixed-metal sulfoselenide possessed higher OER activity than the bimetallic nickel cobalt sulfide $Ni_{1.0}Co_{2.1}(S_{0.9}O_{0.1})_4$, the bimetallic nickel cobalt selenide $Ni_{0.7}Co_{1.4}(Se_{0.85}O_{0.15})_4$, the trimetallic iron-containing nickel cobalt sulfides, $Fe_{0.1}Ni_{1.4}Co_{2.9}(S_{0.87}O_{0.13})_4$, $Fe_{0.2}Ni_{1.5}Co_{2.8}(S_{0.9}O_{0.1})_4$, $Fe_{0.3}Ni_{1.2}Co_{2.5}(S_{0.9}O_{0.1})_4$, and $Fe_{0.6}Ni_{1.2}Co_{2.5}(S_{0.83}O_{0.17})_4$, and the iron-containing nickel cobalt selenide, $Fe_{0.4}Ni_{0.7}Co_{1.6}(Se_{0.81}O_{0.19})_4$. The trimetallic sulfoselenide required an overpotential of only 277 mV at 50 mV cm^{-2} and had favorable OER kinetics, manifested by a Tafel slope of 82 mV dec^{-1}. The OER performance of $Fe_{0.5}Ni_{1.0}Co_{2.0}(S_{0.57}Se_{0.25}O_{0.18})_4$ surpassed the well-known RuO_2 benchmark material where the required overpotential (300 mV to generate 50 mA cm^{-2}) was 23 mV higher under the same condition (1 mol L^{-1} KOH). The 20 h chronopotentiometry analysis revealed that $Fe_{0.5}Ni_{1.0}Co_{2.0}(S_{0.57}Se_{0.25}O_{0.18})_4$ has remarkable stability during long-term operation in alkaline media (the overpotential increased only from 277 to 279 mV) while, under the same conditions, RuO_2 showed a considerable loss in activity (such that the overpotential increasing from 300 to 375 mV during the generation of the 50 mA cm^{-2} current density).

Furthermore, the incorporation of selenium also significantly affected the OER activity and stability by reducing the energy barrier of the OER reaction, optimizing the electronic structure of active sites by modifying the d-band of the materials. Indeed, a SeO_x film on the surface of $Fe_{0.5}Ni_{1.0}Co_{2.0}(S_{0.57}Se_{0.25}O_{0.18})_4$ can enhance the long-term stability of the catalyst. Considering the improvements in OER performance, this simple two-step hydrothermal synthesis of trimetallic sulfoselenides, from transition metal carbonate hydroxide, (Fe_xNi_{1-x})CoCH-(y), as precursors can be used as a facile and practical approach to produce the next generation of non-precious polymetallic polychalcogenide materials for the oxygen evolution reaction.

Supplementary Materials: The following supporting information can be downloaded at: https://www.mdpi.com/article/10.3390/solids4030012/s1, Section S1: preparation of $Ni_{0.7}Co_{1.4}(Se_{0.85}O_{0.15})_4$ and $Ni_{1.0}Co_{2.1}(S_{0.9}O_{0.1})_4$; Section S2: Sample preparation for AAS; Section S3: Scanning electron microscopy and energy dispersive X-ray spectroscopy (SEM/EDX) and TEM/EDX; Section S4: Elemental analysis and atomic spectroscopy measurements; Section S5: Nitrogen sorption measurement; Section S6: X-ray photoelectron spectroscopy; Section S7: Electrochemical characterization; Section S8: Theoretical orthogonal experimental design. References [90–128] are cited in the Supplementary Materials.

Author Contributions: Conceptualization: S.A. and C.J.; methodology: S.A.; validation: S.A.; formal analysis: S.A., L.R., M.N.A.F. and T.H.Y.B.; writing—original draft preparation: S.A.; writing—review and editing: S.A. and C.J.; supervision: C.J.; project administration: C.J.; funding acquisition: C.J. All authors have read and agreed to the published version of the manuscript.

Funding: This research was funded by the joint National Natural Science Foundation of China–Deutsche Forschungsgemeinschaft (NSFC-DFG) project (DFG JA466/39-1).

Institutional Review Board Statement: Not applicable.

Informed Consent Statement: Not applicable.

Data Availability Statement: The data presented in this study are available on request from the corresponding author.

Acknowledgments: The authors also thank Annette Ricken for the AAS measurements.

Conflicts of Interest: The authors declare no conflict of interest.

References

1. Conti, J.; Holtberg, P.; Diefenderfer, J.; LaRose, A.; Turnure, J.T.; Westfall, L. *International Energy Outlook 2016 with Projections to 2040*; Report number: DOE/EIA--0484; U.S. Energy Information Administration, U.S. Department of Energy: Washington, DC, USA, 2016; Volume 20585, pp. 7–16.
2. Wu, D.; Kusada, K.; Yoshioka, S.; Yamamoto, T.; Toriyama, T.; Matsumura, S.; Chen, Y.; Seo, O.; Kim, J.; Song, C.; et al. Efficient Overall Water Splitting in Acid with Anisotropic Metal Nanosheets. *Nat. Commun.* **2021**, *12*, 1145. [CrossRef]
3. Huang, W.; Zhang, J.; Liu, D.; Xu, W.; Wang, Y.; Yao, J.; Tan, H.T.; Dinh, K.N.; Wu, C.; Kuang, M.; et al. Tuning the Electronic Structures of Multimetal Oxide Nanoplates to Realize Favorable Adsorption Energies of Oxygenated Intermediates. *ACS Nano* **2020**, *14*, 17640–17651. [CrossRef] [PubMed]
4. Jiao, Y.; Zheng, Y.; Jaroniec, M.; Qiao, S.Z. Design of Electrocatalysts for Oxygen- and Hydrogen-Involving Energy Conversion Reactions. *Chem. Soc. Rev.* **2015**, *44*, 2060–2086. [CrossRef]
5. Du, P.; Eisenberg, R. Catalysts Made of Earth-Abundant Elements (Co, Ni, Fe) for Water Splitting: Recent Progress and Future Challenges. *Energy Environ. Sci.* **2012**, *5*, 6012. [CrossRef]
6. Yu, Y.; Li, P.; Wang, X.; Gao, W.; Shen, Z.; Zhu, Y.; Yang, S.; Song, W.; Ding, K. Vanadium Nanobelts Coated Nickel Foam 3D Bifunctional Electrode with Excellent Catalytic Activity and Stability for Water Electrolysis. *Nanoscale* **2016**, *8*, 10731–10738. [CrossRef] [PubMed]
7. Sondermann, L.; Jiang, W.; Shviro, M.; Spieß, A.; Woschko, D.; Rademacher, L.; Janiak, C. Nickel-Based Metal-Organic Frameworks as Electrocatalysts for the Oxygen Evolution Reaction (OER). *Molecules* **2022**, *27*, 1241. [CrossRef]
8. Öztürk, S.; Moon, G.; Spieß, A.; Budiyanto, E.; Roitsch, S.; Tüysüz, H.; Janiak, C. A Highly-Efficient Oxygen Evolution Electrocatalyst Derived from a Metal-Organic Framework and Ketjenblack Carbon Material. *ChemPlusChem* **2021**, *86*, 1106–1115. [CrossRef] [PubMed]

9. Wei, C.; Rao, R.R.; Peng, J.; Huang, B.; Stephens, I.E.L.; Risch, M.; Xu, Z.J.; Shao-Horn, Y. Recommended Practices and Benchmark Activity for Hydrogen and Oxygen Electrocatalysis in Water Splitting and Fuel Cells. *Adv. Mater.* **2019**, *31*, 1806296. [CrossRef]
10. Kong, D.; Cha, J.J.; Wang, H.; Lee, H.R.; Cui, Y. First-Row Transition Metal Dichalcogenide Catalysts for Hydrogen Evolution Reaction. *Energy Environ. Sci.* **2013**, *6*, 3553. [CrossRef]
11. Qu, M.; Jiang, Y.; Yang, M.; Liu, S.; Guo, Q.; Shen, W.; Li, M.; He, R. Regulating Electron Density of NiFe-P Nanosheets Electrocatalysts by a Trifle of Ru for High-Efficient Overall Water Splitting. *Appl. Catal. B* **2020**, *263*, 118324. [CrossRef]
12. Guo, Y.; Park, T.; Yi, J.W.; Henzie, J.; Kim, J.; Wang, Z.; Jiang, B.; Bando, Y.; Sugahara, Y.; Tang, J.; et al. Nanoarchitectonics for Transition-Metal-Sulfide-Based Electrocatalysts for Water Splitting. *Adv. Mater.* **2019**, *31*, 1807134. [CrossRef] [PubMed]
13. Jiang, F.; Choy, W.C.H.; Li, X.; Zhang, D.; Cheng, J. Post-Treatment-Free Solution-Processed Non-Stoichiometric NiO_x Nanoparticles for Efficient Hole-Transport Layers of Organic Optoelectronic Devices. *Adv. Mater.* **2015**, *27*, 2930–2937. [CrossRef] [PubMed]
14. Wang, N.; Cao, Z.; Kong, X.; Liang, J.; Zhang, Q.; Zheng, L.; Wei, C.; Chen, X.; Zhao, Y.; Cavallo, L.; et al. Activity Enhancement via Borate Incorporation into a NiFe (Oxy)Hydroxide Catalyst for Electrocatalytic Oxygen Evolution. *J. Mater. Chem. A* **2018**, *6*, 16959–16964. [CrossRef]
15. Li, X.; Kou, Z.; Xi, S.; Zang, W.; Yang, T.; Zhang, L.; Wang, J. Porous $NiCo_2S_4$/FeOOH nanowire arrays with rich sulfide/hydroxide interfaces enable high OER activity. *Nano Energy* **2020**, *78*, 105230. [CrossRef]
16. Subbaraman, R.; Tripkovic, D.; Chang, K.-C.; Strmcnik, D.; Paulikas, A.P.; Hirunsit, P.; Chan, M.; Greeley, J.; Stamenkovic, V.; Markovic, N.M. Trends in Activity for the Water Electrolyser Reactions on 3d M(Ni,Co,Fe,Mn) Hydr(Oxy)Oxide Catalysts. *Nat. Mater.* **2012**, *11*, 550–557. [CrossRef]
17. Wang, C.; Chen, W.; Yuan, D.; Qian, S.; Cai, D.; Jiang, J.; Zhang, S. Tailoring the Nanostructure and Electronic Configuration of Metal Phosphides for Efficient Electrocatalytic Oxygen Evolution Reactions. *Nano Energy* **2020**, *69*, 104453. [CrossRef]
18. Denny, S.R.; Tackett, B.M.; Tian, D.; Sasaki, K.; Chen, J.G. Exploring Electrocatalytic Stability and Activity of Unmodified and Platinum-Modified Tungsten and Niobium Nitrides. *Int. J. Hydrogen Energy* **2020**, *45*, 22883–22892. [CrossRef]
19. Zhang, H.; Guan, D.; Gao, X.; Yu, J.; Chen, G.; Zhou, W.; Shao, Z. Morphology, crystal structure and electronic state one-step co-tuning strategy towards developing superior perovskite electrocatalysts for water oxidation. *J. Mater. Chem. A* **2019**, *7*, 19228–19233. [CrossRef]
20. Zhang, H.; Guan, D.; Hu, Z.; Huang, Y.-C.; Wu, X.; Dai, J.; Dong, C.-L.; Xu, X.; Lin, H.-J.; Chen, C.-T.; et al. Exceptional lattice-oxygen participation on artificially controllable electrochemistry-induced crystalline-amorphous phase to boost oxygen-evolving performance. *Appl. Catal.* **2021**, *297*, 120484. [CrossRef]
21. Ma, N.; Chen, G.; Zhu, Y.; Sun, H.; Dai, J.; Chu, H.; Ran, R.; Zhou, W.; Cai, R.; Shao, Z. A Self-Assembled Hetero-Structured Inverse-Spinel and Anti-Perovskite Nanocomposite for Ultrafast Water Oxidation. *Small* **2020**, *16*, 2002089. [CrossRef]
22. Ibrahim, K.B.; Tsai, M.C.; Chala, S.A.; Berihun, M.K.; Kahsay, A.W.; Berhe, T.A.; Su, W.-N.; Hwang, B.-J. A review of transition metal-based bifunctional oxygen electrocatalysts. *J. Chin. Chem. Soc.* **2019**, *66*, 829–865. [CrossRef]
23. Fu, G.; Lee, J.-M. Ternary Metal Sulfides for Electrocatalytic Energy Conversion. *J. Mater. Chem. A* **2019**, *7*, 9386–9405. [CrossRef]
24. Chen, H.; Jiang, J.; Zhang, L.; Wan, H.; Qi, T.; Xia, D. Highly Conductive $NiCo_2S_4$ Urchin-like Nanostructures for High-Rate Pseudocapacitors. *Nanoscale* **2013**, *5*, 8879–8883. [CrossRef] [PubMed]
25. Shen, L.; Yu, L.; Wu, H.B.; Yu, X.-Y.; Zhang, X.; Lou, X.W. Formation of Nickel Cobalt Sulfide Ball-in-Ball Hollow Spheres with Enhanced Electrochemical Pseudocapacitive Properties. *Nat. Commun.* **2015**, *6*, 6694. [CrossRef]
26. Kulkarni, P.; Nataraj, S.K.; Balakrishna, R.G.; Nagaraju, D.H.; Reddy, M.V. Nanostructured Binary and Ternary Metal Sulfides: Synthesis Methods and Their Application in Energy Conversion and Storage Devices. *J. Mater. Chem. A* **2017**, *5*, 22040–22094. [CrossRef]
27. Liu, W.; Zhang, J.; Bai, Z.; Jiang, G.; Li, M.; Feng, K.; Yang, L.; Ding, Y.; Yu, T.; Chen, Z.; et al. Controllable Urchin-Like $NiCo_2S_4$ Microsphere Synergized with Sulfur-Doped Graphene as Bifunctional Catalyst for Superior Rechargeable Zn-Air Battery. *Adv. Funct. Mater.* **2018**, *28*, 1706675. [CrossRef]
28. Zhu, W.; Ren, M.; Hu, N.; Zhang, W.; Luo, Z.; Wang, R.; Wang, J.; Huang, L.; Suo, Y.; Wang, J. Traditional $NiCo_2S_4$ Phase with Porous Nanosheets Array Topology on Carbon Cloth: A Flexible, Versatile and Fabulous Electrocatalyst for Overall Water and Urea Electrolysis. *ACS Sustain. Chem. Eng.* **2018**, *6*, 5011–5020. [CrossRef]
29. Feng, X.; Jiao, Q.; Liu, T.; Li, Q.; Yin, M.; Zhao, Y.; Li, H.; Feng, C.; Zhou, W. Facile Synthesis of Co_9S_8 Hollow Spheres as a High-Performance Electrocatalyst for the Oxygen Evolution Reaction. *ACS Sustain. Chem. Eng.* **2018**, *6*, 1863–1871. [CrossRef]
30. Chauhan, M.; Reddy, K.P.; Gopinath, C.S.; Deka, S. Copper Cobalt Sulfide Nanosheets Realizing a Promising Electrocatalytic Oxygen Evolution Reaction. *ACS Catal.* **2017**, *7*, 5871–5879. [CrossRef]
31. Liu, Q.; Jin, J.; Zhang, J. $NiCo_2S_4$@graphene as a Bifunctional Electrocatalyst for Oxygen Reduction and Evolution Reactions. *ACS Appl. Mater. Interfaces* **2013**, *5*, 5002–5008. [CrossRef]
32. Xu, X.; Liu, X.; Zhong, W.; Zhang, L.; Liu, G.; Du, Y. Nanostructured $NiCo_2S_4$@$NiCo_2O_4$-Reduced Graphene Oxide as an Efficient Hydrogen Evolution Electrocatalyst in Alkaline Electrolyte. *J. Colloid Interface Sci.* **2021**, *601*, 570–580. [CrossRef]
33. Li, H.; Chen, L.; Jin, P.; Li, Y.; Pang, J.; Hou, J.; Peng, S.; Wang, G.; Shi, Y. $NiCo_2S_4$ Microspheres Grown on N, S Co-Doped Reduced Graphene Oxide as an Efficient Bifunctional Electrocatalyst for Overall Water Splitting in Alkaline and Neutral PH. *Nano Res.* **2022**, *15*, 950–958. [CrossRef]

34. He, B.; Song, J.-J.; Li, X.-Y.; Xu, C.-Y.; Li, Y.-B.; Tang, Y.-W.; Hao, Q.-L.; Liu, H.-K.; Su, Z. A nitrogen-doped $NiCo_2S_4$/CoO hollow multi-layered heterostructure microsphere for efficient oxygen evolution in Zn–air batteries. *Nanoscale* **2021**, *13*, 810–818. [CrossRef] [PubMed]
35. Fereja, S.L.; Li, P.; Zhang, Z.; Guo, J.; Fang, Z.; Li, Z.; Chen, W. Construction of $NiCo_2S_4$/Fe_2O_3 Hybrid Nanostructure as a Highly Efficient Electrocatalyst for the Oxygen Evolution Reaction. *Electrochim. Acta* **2022**, *405*, 139793. [CrossRef]
36. Liu, J.; Wang, J.; Zhang, B.; Ruan, Y.; Lv, L.; Ji, X.; Xu, K.; Miao, L.; Jiang, J. Hierarchical $NiCo_2S_4$@NiFe LDH Heterostructures Supported on Nickel Foam for Enhanced Overall-Water-Splitting Activity. *ACS Appl. Mater. Interfaces* **2017**, *9*, 15364–15372. [CrossRef] [PubMed]
37. Huang, Y.; Ge, S.; Chen, X.; Xiang, Z.; Zhang, X.; Zhang, R.; Cui, Y. Hierarchical $FeCo_2S_4$@$FeNi_2S_4$ Core/Shell Nanostructures on Ni Foam for High-Performance Supercapacitors. *Chem. Eur. J.* **2019**, *25*, 14117–14122. [CrossRef]
38. Su, H.; Song, S.; Gao, Y.; Li, N.; Fu, Y.; Ge, L.; Song, W.; Liu, J.; Ma, T. In Situ Electronic Redistribution Tuning of $NiCo_2S_4$ Nanosheets for Enhanced Electrocatalysis. *Adv. Funct. Mater.* **2022**, *32*, 2109731. [CrossRef]
39. Zhu, X.; Nguyen, D.C.; Prabhakaran, S.; Kim, D.H.; Kim, N.H.; Lee, J.H. Activating catalytic behavior of binary transition metal sulfide-shelled carbon nanotubes by iridium incorporation toward efficient overall water splitting. *Mater. Today Nano* **2023**, *21*, 100296. [CrossRef]
40. Wu, Y.; Liu, X.; Han, D.; Song, X.; Shi, L.; Song, Y.; Niu, S.; Xie, Y.; Cai, J.; Wu, S.; et al. Electron Density Modulation of $NiCo_2S_4$ Nanowires by Nitrogen Incorporation for Highly Efficient Hydrogen Evolution Catalysis. *Nat. Commun.* **2018**, *9*, 1425. [CrossRef]
41. Min, K.; Yoo, R.; Kim, S.; Kim, H.; Shim, S.E.; Lim, D.; Baeck, S.-H. Facile Synthesis of P-Doped $NiCo_2S_4$ Nanoneedles Supported on Ni Foam as Highly Efficient Electrocatalysts for Alkaline Oxygen Evolution Reaction. *Electrochim. Acta* **2021**, *396*, 139236. [CrossRef]
42. Liang, T.; Lenus, S.; Liu, Y.; Chen, Y.; Sakthivel, T.; Chen, F.; Ma, F.; Dai, Z. Interface and M^{3+}/M^{2+} Valence Dual-Engineering on Nickel Cobalt Sulfoselenide/Black Phosphorus Heterostructure for Efficient Water Splitting Electrocatalysis. *Energy Environ. Mater.* **2023**, *6*, e12332. [CrossRef]
43. Gu, H.; Fan, W.; Liu, T. Phosphorus-doped $NiCo_2S_4$ nanocrystals grown on electrospun carbon nanofibers as ultra-efficient electrocatalysts for the hydrogen evolution reaction. *Nanoscale Horiz.* **2017**, *2*, 277–283. [CrossRef] [PubMed]
44. Gong, Q.; Cheng, L.; Liu, C.; Zhang, M.; Feng, Q.; Ye, H.; Zeng, M.; Xie, L.; Liu, Z.; Li, Y. Ultrathin $MoS_{2(1-x)}Se_{2x}$ Alloy Nanoflakes For Electrocatalytic Hydrogen Evolution Reaction. *ACS Catal.* **2015**, *5*, 2213–2219. [CrossRef]
45. Zhou, Y.; Wang, Y.; Zhao, H.; Su, J.; Zhang, H.; Wang, Y. Investigation of Anion Doping Effect to Boost Overall Water Splitting. *J. Catal.* **2020**, *381*, 84–95. [CrossRef]
46. Liu, R.; Xu, S.; Shao, X.; Wen, Y.; Shi, X.; Huang, L.; Hong, M.; Hu, J.; Yang, Z. Defect-Engineered NiCo-S Composite as a Bifunctional Electrode for High-Performance Supercapacitor and Electrocatalysis. *ACS Appl. Mater. Interfaces* **2021**, *13*, 47717–47727. [CrossRef]
47. Deng, W.; Xie, W.; Li, D.; Gai, Y.; Chen, Z.; Yu, J.; Yang, R.; Bao, X.; Jiang, F. Controllable Tuning of Polymetallic Co-Ni-Ru-S-Se Ultrathin Nanosheets to Boost Electrocatalytic Oxygen Evolution. *NPG Asia Mater.* **2022**, *14*, 25. [CrossRef]
48. Sarawutanukul, S.; Tomon, C.; Duangdangchote, S.; Phattharasupakun, N.; Sawangphruk, M. Rechargeable Photoactive Zn-Air Batteries Using $NiCo_2S_4$ as an Efficient Bifunctional Photocatalyst towards OER/ORR at the Cathode. *Batter. Supercaps* **2020**, *3*, 541–547. [CrossRef]
49. Cai, D.; Wang, D.; Wang, C.; Liu, B.; Wang, L.; Liu, Y.; Li, Q.; Wang, T. Construction of Desirable $NiCo_2S_4$ Nanotube Arrays on Nickel Foam Substrate for Pseudocapacitors with Enhanced Performance. *Electrochim. Acta* **2015**, *151*, 35–41. [CrossRef]
50. Song, Y.; Wang, Z.; Yan, Y.; Zhao, W.; Bakenov, Z. $NiCo_2S_4$ Nanoparticles Embedded in Nitrogen-Doped Carbon Nanotubes Networks as Effective Sulfur Carriers for Advanced Lithium–Sulfur Batteries. *Microporous Mesoporous Mater.* **2021**, *316*, 110924. [CrossRef]
51. Huang, Z.; He, W.; Shen, H.; Han, G.; Wang, H.; Su, P.; Song, J.; Yang, Y. $NiCo_2S_4$ Microflowers as Peroxidase Mimic: A Multi-Functional Platform for Colorimetric Detection of Glucose and Evaluation of Antioxidant Behavior. *Talanta* **2021**, *230*, 122337. [CrossRef]
52. Guo, Z.; Diao, Y.; Han, X.; Liu, Z.; Ni, Y.; Zhang, L. Mesoporous $NiCo_2Se_4$ Tube as an Efficient Electrode Material with Enhanced Performance for Asymmetric Supercapacitor Applications. *CrystEngComm* **2021**, *23*, 2099–2112. [CrossRef]
53. Meng, A.; Yuan, X.; Shen, T.; Zhao, J.; Song, G.; Lin, Y.; Li, Z. Amorphous Nickel Sulfide Nanoparticles Anchored on N-Doped Graphene Nanotubes with Superior Properties for High-Performance Supercapacitors and Efficient Oxygen Evolution Reaction. *Nanoscale* **2020**, *12*, 4655–4666. [CrossRef] [PubMed]
54. Cai, P.; Huang, J.; Chen, J.; Wen, Z. Oxygen-Containing Amorphous Cobalt Sulfide Porous Nanocubes as High-Activity Electrocatalysts for the Oxygen Evolution Reaction in an Alkaline/Neutral Medium. *Angew. Chem.* **2017**, *129*, 4936–4939. [CrossRef]
55. Chen, N.; Du, Y.-X.; Zhang, G.; Lu, W.-T.; Cao, F.-F. Amorphous Nickel Sulfoselenide for Efficient Electrochemical Urea-Assisted Hydrogen Production in Alkaline Media. *Nano Energy* **2021**, *81*, 105605. [CrossRef]
56. Guan, D.; Shi, C.; Xu, H.; Gu, Y.; Zhong, J.; Sha, Y.; Hu, Z.; Ni, M.; Shao, Z. Simultaneously mastering operando strain and reconstruction effects via phase-segregation strategy for enhanced oxygen-evolving electrocatalysis. *J. Energy Chem.* **2023**, *82*, 572–580. [CrossRef]
57. Shi, Z.; Qi, X.; Zhang, Z.; Song, Y.; Zhang, J.; Guo, C.; Zhu, Z. Porous Cobalt Sulfide Selenium Nanorods for Electrochemical Hydrogen Evolution. *ACS Omega* **2021**, *6*, 23300–23310. [CrossRef]

58. Pecharsky, V.K.; Zavalij, P.Y. *Fundamentals of Powder Diffraction and Structural Characterization of Materials*, 2nd ed.; ch. 12.1.5; Springer Science & Business Mediaz: New York, NY, USA, 2005; p. 313. Available online: https://link.springer.com/chapter/10.1007/0-387-24567-7_2 (accessed on 2 July 2023).
59. Wang, H.-Y.; Hsu, Y.-Y.; Chen, R.; Chan, T.-S.; Chen, H.M.; Liu, B. Ni^{3+}-Induced Formation of Active NiOOH on the Spinel Ni-Co Oxide Surface for Efficient Oxygen Evolution Reaction. *Adv. Energy Mater.* **2015**, *5*, 1500091. [CrossRef]
60. Wang, Q.; Shang, L.; Shi, R.; Zhang, X.; Zhao, Y.; Waterhouse, G.I.N.; Wu, L.-Z.; Tung, C.-H.; Zhang, T. NiFe Layered Double Hydroxide Nanoparticles on Co,N-Codoped Carbon Nanoframes as Efficient Bifunctional Catalysts for Rechargeable Zinc-Air Batteries. *Adv. Energy Mater.* **2017**, *7*, 1700467. [CrossRef]
61. Biesinger, M.C.; Payne, B.P.; Grosvenor, A.P.; Lau, L.W.M.; Gerson, A.R.; Smart, R.S.C. Resolving Surface Chemical States in XPS Analysis of First Row Transition Metals, Oxides and Hydroxides: Cr, Mn, Fe, Co and Ni. *Appl. Surf. Sci.* **2011**, *257*, 2717–2730. [CrossRef]
62. Yamashita, T.; Hayes, P. Analysis of XPS Spectra of Fe^{2+} and Fe^{3+} Ions in Oxide Materials. *Appl. Surf. Sci.* **2008**, *254*, 2441–2449. [CrossRef]
63. Yin, L.I.; Yellin, E.; Adler, I. X-Ray Excited LMM Auger Spectra of Copper, Nickel, and Iron. *J. Appl. Phys.* **1971**, *42*, 3595–3600. [CrossRef]
64. He, Y.; Liu, X.; Chen, G.; Pan, J.; Yan, A.; Li, A.; Lu, X.; Tang, D.; Zhang, N.; Qiu, T.; et al. Synthesis of Co(II)-Fe(III) Hydroxide Nanocones with Mixed Octahedral/Tetrahedral Coordination toward Efficient Electrocatalysis. *Chem. Mater.* **2020**, *32*, 4232–4240. [CrossRef]
65. Akbari, M.S.A.; Bagheri, R.; Song, Z.; Najafpour, M.M. Oxygen-evolution reaction by nickel/nickel oxide interface in the presence of ferrate(VI). *Sci. Rep.* **2020**, *10*, 8757. [CrossRef] [PubMed]
66. Li, J.; Cui, H.; Du, X.; Zhang, X. The Controlled Synthesis of Nitrogen and Iron Co-Doped Ni_3S_2@NiP_2 Heterostructures for the Oxygen Evolution Reaction and Urea Oxidation Reaction. *Dalton Trans.* **2022**, *51*, 2444–2451. [CrossRef] [PubMed]
67. Huang, H.; Ning, S.; Xie, Y.; He, Z.; Teng, J.; Chen, Z.; Fan, Y.; Shi, J.; Barboiu, M.; Wang, D.; et al. Synergistic Modulation of Electronic Interaction to Enhance Intrinsic Activity and Conductivity of Fe–Co–Ni Hydroxide Nanotube for Highly Efficient Oxygen Evolution Electrocatalyst. *Small* **2023**, *19*, 2302272. [CrossRef]
68. Yang, L.; Qin, H.; Dong, Z.; Wang, T.; Wang, G.; Jiao, L. Metallic S-CoTe with Surface Reconstruction Activated by Electrochemical Oxidation for Oxygen Evolution Catalysis. *Small* **2021**, *17*, 2102027. [CrossRef] [PubMed]
69. Shinagawa, T.; Garcia-Esparza, A.T.; Takanabe, K. Insight on Tafel Slopes from a Microkinetic Analysis of Aqueous Electrocatalysis for Energy Conversion. *Sci. Rep.* **2015**, *5*, 13801. [CrossRef]
70. Li, G.; Anderson, L.; Chen, Y.; Pan, M.; Abel Chuang, P.-Y. New Insights into Evaluating Catalyst Activity and Stability for Oxygen Evolution Reactions in Alkaline Media. *Sustain. Energy Fuels.* **2018**, *2*, 237–251. [CrossRef]
71. Shang, X.; Chen, W.; Jiang, Z.-J.; Song, C.; Jiang, Z. In Situ Growth of SeO_x Films on the Surface of Ni–Fe–Selenide Nanosheets as Highly Active and Stable Electrocatalysts for the Oxygen Evolution Reaction. *Mater. Adv.* **2022**, *3*, 2546–2557. [CrossRef]
72. Zhang, K.; Zou, R. Advanced Transition Metal-Based OER Electrocatalysts: Current Status, Opportunities, and Challenges. *Small* **2021**, *17*, 2100129. [CrossRef]
73. Anantharaj, S.; Kundu, S.; Noda, S. "The Fe Effect": A Review Unveiling the Critical Roles of Fe in Enhancing OER Activity of Ni and Co Based Catalysts. *Nano Energy* **2021**, *80*, 105514. [CrossRef]
74. Kuai, C.; Xi, C.; Hu, A.; Zhang, Y.; Xu, Z.; Nordlund, D.; Sun, C.-J.; Cadigan, C.A.; Richards, R.M.; Li, L.; et al. Revealing the Dynamics and Roles of Iron Incorporation in Nickel Hydroxide Water Oxidation Catalysts. *J. Am. Chem. Soc.* **2021**, *143*, 18519–18526. [CrossRef] [PubMed]
75. Lopes, P.P.; Chung, D.Y.; Rui, X.; Zheng, H.; He, H.; Martins, P.F.B.D.; Strmcnik, D.; Stamenkovic, V.R.; Zapol, P.; Mitchell, J.F.; et al. Dynamically stable active sites from surface evolution of perovskite materials during the oxygen evolution reaction. *J. Am. Chem. Soc.* **2021**, *143*, 2741–2750. [CrossRef]
76. Friebel, D.; Louie, M.W.; Bajdich, M.; Sanwald, K.E.; Cai, Y.; Wise, A.M.; Cheng, M.-J.; Sokaras, D.; Weng, T.-C.; Alonso-Mori, R.; et al. Identification of Highly Active Fe Sites in (Ni,Fe)OOH for Electrocatalytic Water Splitting. *J. Am. Chem. Soc.* **2015**, *137*, 1305–1313. [CrossRef]
77. Sinitsyn, P.A.; Kuznetsov, V.V.; Filatova, E.A.; Levchenko, S.V. Ruddlesden–Popper Oxides $LaSrM1_{1-x}M2_xO_{4\pm\delta}$ (M1, M2—Fe, Co, Ni) Synthesized by the Spray-Pyrolysis Method as Promising Electrocatalysts for Oxygen Evolution Reaction. *Energies* **2022**, *15*, 8315. [CrossRef]
78. Yang, M.; Lu, W.; Jin, R.; Liu, X.-C.; Song, S.; Xing, Y. Superior Oxygen Evolution Reaction Performance of Co_3O_4/$NiCo_2O_4$/Ni Foam Composite with Hierarchical Structure. *ACS Sustain. Chem. Eng.* **2019**, *14*, 12214–12221. [CrossRef]
79. Chuah, X.F.; Hsieh, C.-T.; Huang, C.-L.; Raja, D.S.; Lin, H.-W.; Lu, S.-Y. In-Situ Grown, Passivator-Modulated Anodization Derived Synergistically Well-Mixed Ni–Fe Oxides from Ni Foam as High-Performance Oxygen Evolution Reaction Electrocatalyst. *ACS Appl. Energy Mater.* **2019**, *2*, 743–753. [CrossRef]
80. Duan, J.-J.; Zhang, R.-L.; Feng, J.-J.; Zhang, L.; Zhang, Q.-L.; Wang, A.-J. Facile Synthesis of Nanoflower-like Phosphorus-Doped Ni_3S_2/$CoFe_2O_4$ Arrays on Nickel Foam as a Superior Electrocatalyst for Efficient Oxygen Evolution Reaction. *J. Colloid Interface Sci.* **2021**, *581*, 774–782. [CrossRef]

81. Xue, Z.; Wang, Y.; Yang, M.; Wang, T.; Zhu, H.; Rui, Y.; Wu, S.; An, W. In-Situ Construction of Electrodeposited Polyaniline/Nickel-Iron Oxyhydroxide Stabilized on Nickel Foam for Efficient Oxygen Evolution Reaction at High Current Densities. *Int. J. Hydrogen Energy.* **2022**, *47*, 34025–34035. [CrossRef]
82. Zhao, T.; Wang, Y.; Chen, X.; Li, Y.; Su, Z.; Zhao, C. Vertical Growth of Porous Perovskite Nanoarrays on Nickel Foam for Efficient Oxygen Evolution Reaction. *ACS Sustain. Chem. Eng.* **2020**, *8*, 4863–4870. [CrossRef]
83. Gao, W.; Ma, F.; Wang, C.; Wen, D. Ce Dopant Significantly Promotes the Catalytic Activity of Ni Foam-Supported Ni_3S_2 Electrocatalyst for Alkaline Oxygen Evolution Reaction. *J. Power Sources* **2020**, *450*, 227654. [CrossRef]
84. Kim, D.Y.; Lee, H.; Choi, S.R.; Choi, S.; An, W.Y.; Cho, H.-S.; Choi, M.; Park, J.-Y. Synthesis of Hierarchically Porous Ni Foam-Supported Heazlewoodite Ni_3S_2 Nanorod Electrocatalysts for Highly Efficient Oxygen Evolution Reaction. *J. Alloys Compd.* **2022**, *914*, 165305. [CrossRef]
85. Tao, K.; Gong, Y.; Zhou, Q.; Lin, J. Nickel Sulfide Wrapped by Porous Cobalt Molybdate Nanosheet Arrays Grown on Ni Foam for Oxygen Evolution Reaction and Supercapacitor. *Electrochim. Acta* **2018**, *286*, 65–76. [CrossRef]
86. Sun, Z.; Yuan, M.; Lin, L.; Yang, H.; Li, H.; Sun, G.; Yang, X.; Ma, S. Needle Grass-like Cobalt Hydrogen Phosphate on Ni Foam as an Effective and Stable Electrocatalyst for the Oxygen Evolution Reaction. *Chem. Commun.* **2019**, *55*, 9729–9732. [CrossRef]
87. Li, X.; Han, G.-Q.; Liu, Y.-R.; Dong, B.; Hu, W.-H.; Shang, X.; Chai, Y.-M.; Liu, C.-G. NiSe@NiOOH Core–Shell Hyacinth-like Nanostructures on Nickel Foam Synthesized by in Situ Electrochemical Oxidation as an Efficient Electrocatalyst for the Oxygen Evolution Reaction. *ACS Appl. Mater. Interfaces* **2016**, *8*, 20057–20066. [CrossRef]
88. Zhang, Y.; Guo, P.; Niu, S.; Wu, J.; Wang, W.; Song, B.; Wang, X.; Jiang, Z.; Xu, P. Magnetic Field Enhanced Electrocatalytic Oxygen Evolution of NiFe-LDH/Co_3O_4 P-n Heterojunction Supported on Nickel Foam. *Small Methods* **2022**, *6*, 2200084. [CrossRef]
89. Ji, L.; Si, Y.; Liu, H.; Song, X.; Zhu, W.; Zhu, A. Application of orthogonal experimental design in synthesis of mesoporous bioactive glass. *Microporous Mesoporous Mater.* **2014**, *184*, 122–126. [CrossRef]
90. Mohamed, S.G.; Hussain, I.; Shim, J.-J. One-Step Synthesis of Hollow C-$NiCo_2S_4$ Nanostructures for High-Performance Supercapacitor Electrodes. *Nanoscale* **2018**, *10*, 6620–6628. [CrossRef]
91. Pu, J.; Cui, F.; Chu, S.; Wang, T.; Sheng, E.; Wang, Z. Preparation and Electrochemical Characterization of Hollow Hexagonal $NiCo_2S_4$ Nanoplates as Pseudocapacitor Materials. *ACS Sustain. Chem. Eng.* **2014**, *2*, 809–815. [CrossRef]
92. Zou, J.; Xie, D.; Zhao, F.; Wu, H.; Niu, Y.; Li, Z.; Zou, Q.; Deng, F.; Zhang, Q.; Zeng, X. Microwave Rapid Synthesis of Nickel Cobalt Sulfides/CNTs Composites as Superior Cycling Ability Electrode Materials for Supercapacitors. *J. Mater. Sci.* **2021**, *56*, 1561–1576. [CrossRef]
93. Bao, Y.; Zhang, W.; Yun, T.; Dai, J.; Li, G.; Mao, W.; Guan, M.; Zhuang, Y. The Application of Transition Metal Sulfide Ni_3S_4/CNFs in Rechargeable Ni–Zn Batteries. *New J. Chem.* **2021**, *45*, 22491–22496. [CrossRef]
94. Kung, C.-W.; Chen, H.-W.; Lin, C.-Y.; Huang, K.-C.; Vittal, R.; Ho, K.-C. CoS Acicular Nanorod Arrays for the Counter Electrode of an Efficient Dye-Sensitized Solar Cell. *ACS Nano* **2012**, *6*, 7016–7025. [CrossRef]
95. Khani, H.; Wipf, D.O. Iron Oxide Nanosheets and Pulse-Electrodeposited Ni–Co–S Nanoflake Arrays for High-Performance Charge Storage. *ACS Appl. Mater. Interfaces* **2017**, *9*, 6967–6978. [CrossRef]
96. Matoba, M.; Anzai, S.; Fujimori, A. Thermal Expansion, Thermoelectric Power, and XPS Study of the Nonmetal-Metal Transition in $Ni_{1-x}S_{1-y}Se_y$. *J. Phys. Soc. Jpn.* **1991**, *60*, 4230–4244. [CrossRef]
97. Shi, Z.-T.; Kang, W.; Xu, J.; Sun, L.-L.; Wu, C.; Wang, L.; Yu, Y.-Q.; Yu, D.Y.W.; Zhang, W.; Lee, C.-S. In Situ Carbon-Doped $Mo(Se_{0.85}S_{0.15})_2$ Hierarchical Nanotubes as Stable Anodes for High-Performance Sodium-Ion Batteries. *Small* **2015**, *11*, 5667–5674. [CrossRef]
98. Danilson, M.; Altosaar, M.; Kauk, M.; Katerski, A.; Krustok, J.; Raudoja, J. XPS Study of CZTSSe Monograin Powders. *Thin Solid Films* **2011**, *519*, 7407–7411. [CrossRef]
99. Zou, X.; Wu, Y.; Liu, Y.; Liu, D.; Li, W.; Gu, L.; Liu, H.; Wang, P.; Sun, L.; Zhang, Y. In Situ Generation of Bifunctional, Efficient Fe-Based Catalysts from Mackinawite Iron Sulfide for Water Splitting. *Chem* **2018**, *4*, 1139–1152. [CrossRef]
100. Sahoo, M.K.; Samantara, A.K.; Behera, J.N. In Situ Transformed Cobalt Metal–Organic Framework Electrocatalysts for the Electrochemical Oxygen Evolution Reaction. *Inorg. Chem.* **2020**, *59*, 12252–12262. [CrossRef]
101. Beamson, G.; Briggs, D. *High Resolution XPS of Organic Polymers: The Scienta ESCA300 Database*; Wiley: New York, NY, USA, 1992.
102. Shen, Y.; Zhu, Y.; Sunarso, J.; Guan, D.; Liu, B.; Liu, H.; Zhou, W.; Shao, Z. New Phosphorus-Doped Perovskite Oxide as an Oxygen Reduction Reaction Electrocatalyst in an Alkaline Solution. *Chem. Eur. J.* **2018**, *24*, 6950–6957. [CrossRef]
103. Yang, H.; Li, F.; Zhan, S. Intramolecular hydroxyl nucleophilic attack pathway by a polymeric water oxidation catalyst with single cobalt sites. *Nat. Catal.* **2022**, *5*, 414–429. [CrossRef]
104. Feng, C.; Wang, F.; Liu, Z. A self-healing catalyst for electrocatalytic and photoelectrochemical oxygen evolution in highly alkaline conditions. *Nat. Commun.* **2021**, *12*, 5980. [CrossRef]
105. Garcés-Pineda, F.A.; Blasco-Ahicart, M.; Nieto-Castro, D. Direct magnetic enhancement of electrocatalytic water oxidation in alkaline media. *Nat. Energy* **2019**, *4*, 519–525. [CrossRef]
106. Zhang, S.L.; Guan, B.Y.; Lu, X.F.; Xi, S.; Du, Y.; Lou, X.W.D. Metal Atom-Doped Co_3O_4 Hierarchical Nanoplates for Electrocatalytic Oxygen Evolution. *Adv. Mater.* **2020**, *32*, 2002235. [CrossRef] [PubMed]
107. Sundivich, J.; May, K.J.; Gasteiger, H.A.; Goodenough, G.B.; Horn, Y.S. A Perovskite Oxide Optimized for Oxygen Evolution Catalysis from Molecular Orbital Principles. *Science* **2011**, *334*, 1383–1385. [CrossRef]

108. Shan, Z.; Archana, P.S.; Shen, G.; Gupta, A.; Bakker, M.G.; Pan, S. NanoCOT: Low-Cost Nanostructured Electrode Containing Carbon, Oxygen, and Titanium for Efficient Oxygen Evolution Reaction. *J. Am. Chem. Soc.* **2015**, *137*, 11996–12005. [CrossRef] [PubMed]
109. Lee, S.; Ji, L.; De Palma, A.C. Scalable highly stable Si-based metal-insulator-semiconductor photoanodes for water oxidation fabricated using thin-film reactions and electrodeposition. *Nat. Commun.* **2021**, *12*, 3982. [CrossRef] [PubMed]
110. Chen, R.; Zhang, Z.; Wang, Z.; Wu, W.; Du, S.; Zhu, W.; Lv, H.; Cheng, N. Constructing Air-Stable and Reconstruction-Inhibited Transition Metal Sulfide Catalysts via Tailoring Electron-Deficient Distribution for Water Oxidation. *ACS Catal.* **2022**, *12*, 13234–13246. [CrossRef]
111. Shit, S.; Chhetri, S.; Jang, W.; Murmu, N.C.; Koo, H.; Samanta, P.; Kuila, T. Cobalt Sulfide/Nickel Sulfide Heterostructure Directly Grown on Nickel Foam: An Efficient and Durable Electrocatalyst for Overall Water Splitting Application. *ACS Appl. Mater. Interfaces* **2018**, *10*, 27712–27722. [CrossRef]
112. Zhang, K.; Min, X.; Zhang, T.; Si, M.; Jiang, J.; Chai, L.; Shi, Y. Biodeposited Nano-CdS Drives the In Situ Growth of Highly Dispersed Sulfide Nanoparticles during Pyrolysis for Enhanced Oxygen Evolution Reaction. *ACS Appl. Mater. Interfaces* **2020**, *12*, 54553–54562. [CrossRef]
113. Tiwari, A.; Yoon, Y.; Novak, T.G.; An, K.S.; Jeon, S. Continuous Network of Phase-Tuned Nickel Sulfide Nanostructures for Electrocatalytic Water Splitting. *ACS Appl. Nano Mater.* **2019**, *2*, 5061–5070. [CrossRef]
114. Ji, Q.; Kong, Y.; Tan, H.; Duan, H.; Li, N.; Tang, B.; Wang, Y.; Feng, S.; Lv, L.; Wang, C.; et al. Operando Identification of Active Species and Intermediates on Sulfide Interfaced by Fe_3O_4 for Ultrastable Alkaline Oxygen Evolution at Large Current Density. *ACS Catal.* **2022**, *12*, 4318–4326. [CrossRef]
115. Xie, M.; Ai, S.; Yang, J.; Yang, Y.; Chen, Y.; Jin, Y. In-Situ Generation of Oxide Nanowire Arrays from AgCuZn Alloy Sulfide with Enhanced Electrochemical Oxygen-Evolving Performance. *ACS Appl. Mater. Interfaces* **2015**, *7*, 17112–17121. [CrossRef]
116. Shit, S.; Bolar, S.; Murmu, N.C.; Kuila, T. Design Principle of Monoclinic $NiCo_2Se_4$ and Co_3Se_4 Nanoparticles with Opposing Intrinsic and Geometric Electrocatalytic Activity toward the OER. *ACS Sustain. Chem. Eng.* **2019**, *7*, 18015–18026. [CrossRef]
117. Swathi, S.; Yuvakkumar, R.; Ravi, G.; Thambidurai, M.; Nguyen, H.D.; Velauthapillai, D. Ternary Copper Iron Sulfide Microflowers Anchored on Reduced Graphene Oxide for Water Splitting. *ACS Appl. Nano Mater.* **2023**, *6*, 6538–6549. [CrossRef]
118. Waqas, M.; Younis, J.; Awais, M.; Nazar, N.; Hussain, S.; Murtaza, S.; Yasmin, N.; Ashiq, M.N.; Mirza, M.; Safdar, M. CrS_2-Modulated Enhanced Catalytic Properties of CdS/MoS_2 Heterostructures Toward Photodegradation and Electrochemical OER Kinetics. *Energy Fuels* **2022**, *36*, 8391–8401. [CrossRef]
119. Jayaramulu, K.; Masa, J.; Tomanec, O.; Peeters, D.; Ranc, V.; Schneemann, A.; Zboril, R.; Schuhmann, W.; Fischer, R.A. Nanoporous Nitrogen-Doped Graphene Oxide/Nickel Sulfide Composite Sheets Derived from a Metal-Organic Framework as an Efficient Electrocatalyst for Hydrogen and Oxygen Evolution. *Adv. Funct. Mater.* **2017**, *27*, 1700451. [CrossRef]
120. Ganesan, P.; Sivanantham, A.; Shanmugam, S. Inexpensive electrochemical synthesis of nickel iron sulphides on nickel foam: Super active and ultra-durable electrocatalysts for alkaline electrolyte membrane water electrolysis. *J. Mater. Chem. A* **2016**, *4*, 16394–16402. [CrossRef]
121. Gervas, C.; Khan, M.D.; Zhang, C.; Zhao, C.; Gupta, R.K.; Carleschi, E.; Doyle, B.P.; Revaprasadu, N. Effect of cationic disorder on the energy generation and energy storage applications of $Ni_xCo_{3-x}S_4$ thiospinel. *RSC Adv.* **2018**, *8*, 24049–24058. [CrossRef]
122. Wu, H.; Lu, Q.; Zhang, J. Thermal Shock-Activated Spontaneous Growing of Nanosheets for Overall Water Splitting. *Nano-Micro Lett.* **2020**, *12*, 162. [CrossRef] [PubMed]
123. Wang, X.; Yang, Y.; Wang, R.; Li, L.; Zhao, X.; Zhang, W. Porous Ni_3S_2–Co_9S_8 Carbon Aerogels Derived from Carrageenan/NiCo-MOF Hydrogels as an Efficient Electrocatalyst for Oxygen Evolution in Rechargeable Zn–Air Batteries. *Langmuir* **2022**, *38*, 7280–7289. [CrossRef] [PubMed]
124. Li, M.; Xu, Z.; Li, Y.; Wang, J.; Zhong, Q. In situ fabrication of cobalt/nickel sulfides nano hybrid based on various sulfur sources as highly efficient bifunctional electrocatalysts for overall water splitting. *Nano Select* **2022**, *3*, 147–156. [CrossRef]
125. Guo, M.-L.; Wu, Z.-Y.; Zhang, M.-M.; Huang, Z.-J.; Zhang, K.-X.; Wang, B.-R.; Tu, J.-C. Coupling interface constructions of $FeOOH/NiCo_2S_4$ by microwave-assisted method for efficient oxygen evolution reaction. *Rare Met.* **2023**, *42*, 1847–1857. [CrossRef]
126. Jin, C.; Hou, M.; Li, X.; Liu, D.; Qu, D.; Dong, Y.; Xie, Z.; Zhang, C. Rapid electrodeposition of Fe-doped nickel selenides on Ni foam as a bi-functional electrocatalyst for water splitting in alkaline solution. *J. Electroanal.* **2022**, *906*, 116014. [CrossRef]
127. Guo, Y.; Zhou, X.; Tang, J.; Tanaka, S.; Kaneti, Y.V.; Na, J.; Jiang, B.; Yamauchi, Y.; Bando, Y.; Sugahara, Y. Multiscale structural optimization: Highly efficient hollow iron-doped metal sulfide heterostructures as bifunctional electrocatalysts for water splitting. *Nano Energy* **2020**, *75*, 104913. [CrossRef]
128. Wang, C.-Y.; Dong, W.-D.; Zhou, M.-R.; Wang, L.; Hu, Z.-Y.; Chen, L.; Li, Y.; Su, B.-L. Gradient selenium-doping regulating interfacial charge transfer in zinc sulfide/carbon anode for stable lithium storage. *J. Colloid Interface Sci.* **2022**, *619*, 42–50. [CrossRef] [PubMed]

Iron-Containing Nickel Cobalt Sulfides, Selenides, and Sulfoselenides as Active and Stable Electrocatalysts for the Oxygen Evolution Reaction in an Alkaline Solution

Table of Contents

Section S1 Preparation of $Ni_{1.0}Co_{2.1}(S_{0.9}O_{0.1})_4$ and $Ni_{0.7}Co_{1.4}(Se_{0.85}O_{0.15})_4$

The nickel cobalt sulfide sample $Ni_{1.0}Co_{2.1}(S_{0.9}O_{0.1})_4$ was prepared through the hydrothermal sulfidation of the precursor (NiCoCH). An amount of 125 mg of the NiCoCH precursor was dispersed in 40 mL of ultrapure water within an 80 mL Teflon-lined autoclave and stirred for 20 minutes. Subsequently, 750 mg (3.125 mmol) of $Na_2S\cdot9H_2O$ was added. The resulting suspension was transferred to an oven and maintained at 160 °C for 12 hours. The obtained product was washed five times with ultrapure water (50 mL each) and twice with ethanol (20 mL each), followed by drying in a vacuum oven at 60 °C overnight. The yield was approximately 95 mg.

Nickel cobalt selenide sample $Ni_{0.7}Co_{1.4}(Se_{0.85}O_{0.15})_4$: The amount of 125 mg of NiCoCH was dispersed in 30 mL of ultrapure water, followed by addition of 100 mg (0.9 mmol) of SeO_2 and stirring for 10 min. Then 10 mL of N_2H_4 was added to the suspension and stirred for another 10 min. The resulting suspension was transferred to a stainless-steel autoclave and heated at 160 °C for 12 h. The obtained black powder was washed five times with ultrapure water (50 mL each) and three times with absolute ethanol (20 mL each), then dried at 60 °C in the vacuum oven overnight. Yield 105 mg.

Section S2 Sample preparation for atomic absorption spectroscopy

A precisely weighted dried sample of approx. 5 mg was suspended in 10 mL of aqua regia solution (3:1 conc. HCl and HNO_3 mixture) and the liquid was slowly boiled under stirring under the fume-hood until evaporation of the liquid. The treatment by 10 mL aqua regia solution was repeated two times, which yielded a clear solution prior to the final evaporation. Finally, the obtained residue was dissolved in a fresh portion of aqua regia solution (5 mL aqua regia + 10 mL ultrapure water) and stirred overnight. The solution was filtered, the filter was carefully washed multiple times with ultrapure water, and the filtrate was diluted precisely to 50 mL in a volumetric flask to yield the solution used for the determination of the Fe, Ni, and Co content in the samples.

Section S3 Scanning electron microscopy and energy dispersive X-ray spectroscopy (SEM/EDX) and TEM/EDX

The print-out data of the SEM-EDX analysis, which were used to calculate the chemical formula of as-prepared catalysts, are provided in Figures S1–S8.

Because of overlapping sulfur and gold peaks, no gold sputtering was applied to the samples, except for $Ni_{0.7}Co_{1.4}(Se_{0.85}O_{0.15})_4$ which was Au-sputtered.

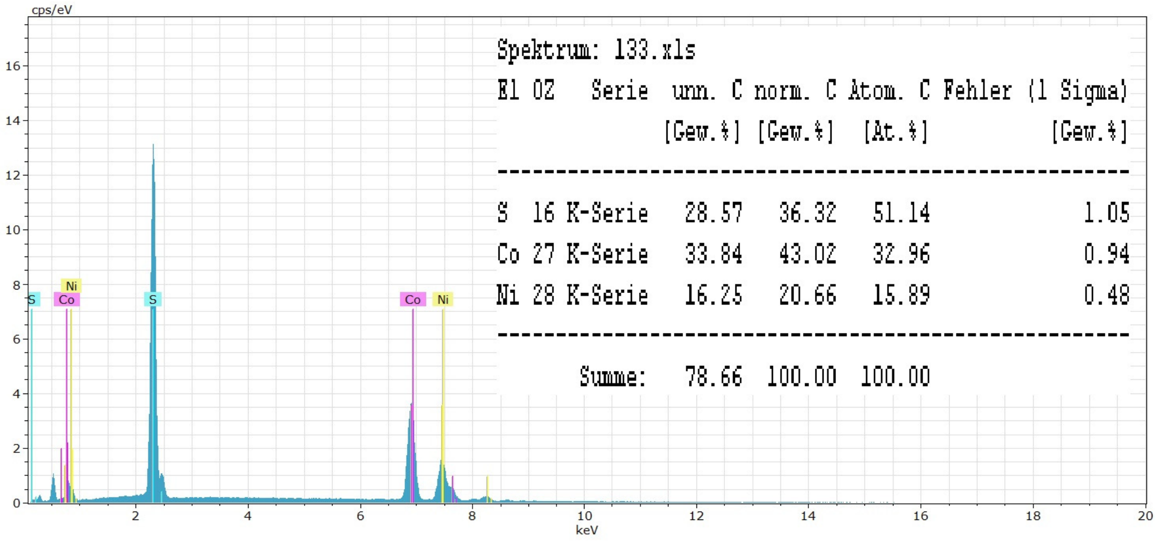

```
Spektrum: 133.xls
El OZ    Serie  unn. C norm. C Atom. C Fehler (1 Sigma)
                [Gew.%] [Gew.%]  [At.%]           [Gew.%]
---------------------------------------------------------
S  16 K-Serie   28.57   36.32   51.14              1.05
Co 27 K-Serie   33.84   43.02   32.96              0.94
Ni 28 K-Serie   16.25   20.66   15.89              0.48
---------------------------------------------------------
        Summe:  78.66  100.00  100.00
```

Figure S1. Energy dispersive X-ray analysis of $Ni_{1.0}Co_{2.1}(S_{0.9}O_{0.1})_4$.

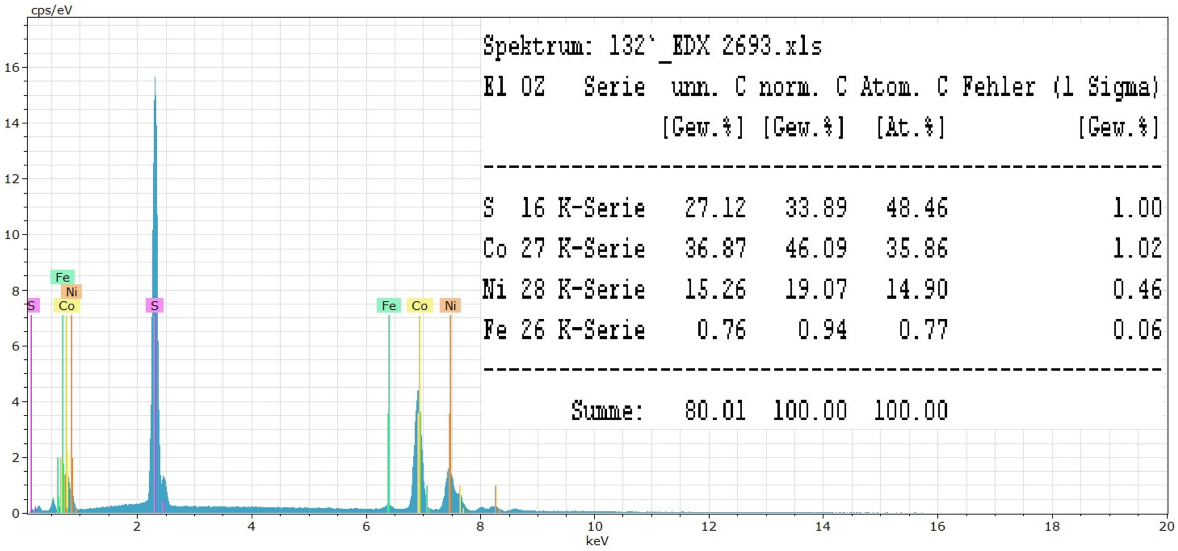

```
Spektrum: 132`_EDX 2693.xls
El OZ    Serie  unn. C norm. C Atom. C Fehler (1 Sigma)
                [Gew.%] [Gew.%]  [At.%]           [Gew.%]
---------------------------------------------------------
S  16 K-Serie   27.12   33.89   48.46              1.00
Co 27 K-Serie   36.87   46.09   35.86              1.02
Ni 28 K-Serie   15.26   19.07   14.90              0.46
Fe 26 K-Serie    0.76    0.94    0.77              0.06
---------------------------------------------------------
        Summe:  80.01  100.00  100.00
```

Figure S2. Energy dispersive X-ray analysis of $Fe_{0.1}Ni_{1.4}Co_{2.9}(S_{0.87}O_{0.13})_4$.

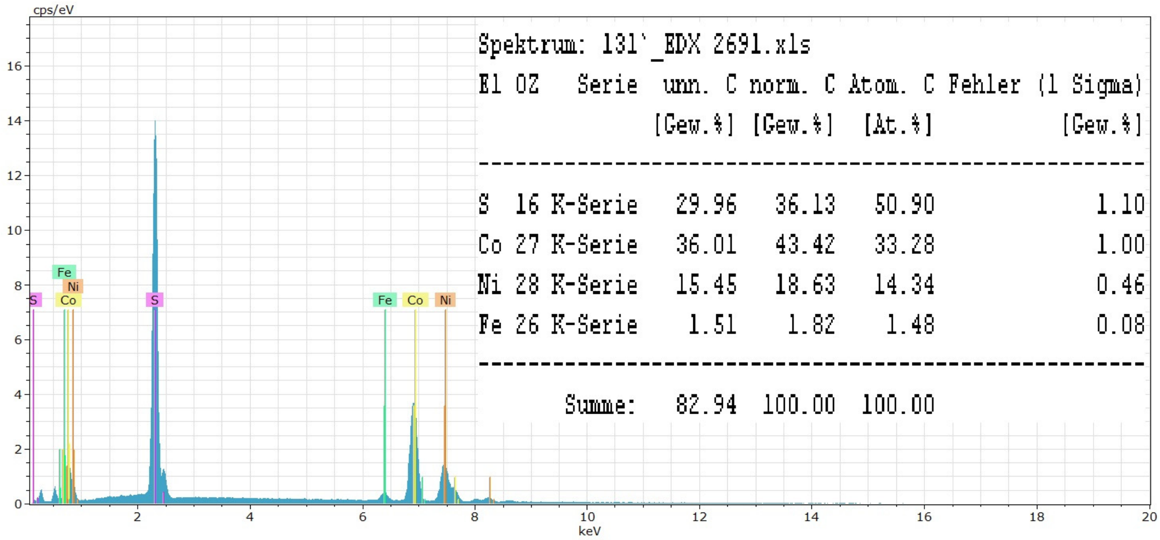

```
Spektrum: 131`_EDX 2691.xls
El OZ   Serie  unn. C norm. C Atom. C Fehler (1 Sigma)
               [Gew.%] [Gew.%] [At.%]          [Gew.%]
----------------------------------------------------
S  16 K-Serie  29.96   36.13   50.90            1.10
Co 27 K-Serie  36.01   43.42   33.28            1.00
Ni 28 K-Serie  15.45   18.63   14.34            0.46
Fe 26 K-Serie   1.51    1.82    1.48            0.08
----------------------------------------------------
      Summe:   82.94  100.00  100.00
```

Figure S3. Energy dispersive X-ray analysis of $Fe_{0.2}Ni_{1.5}Co_{2.8}(S_{0.9}O_{0.1})_4$.

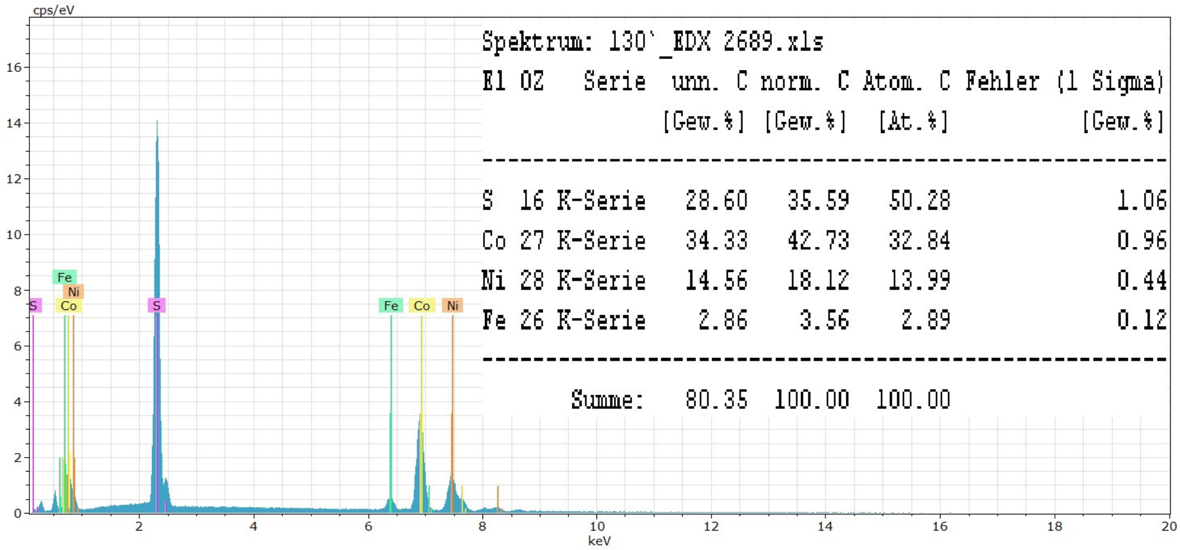

```
Spektrum: 130`_EDX 2689.xls
El OZ   Serie  unn. C norm. C Atom. C Fehler (1 Sigma)
               [Gew.%] [Gew.%] [At.%]          [Gew.%]
----------------------------------------------------
S  16 K-Serie  28.60   35.59   50.28            1.06
Co 27 K-Serie  34.33   42.73   32.84            0.96
Ni 28 K-Serie  14.56   18.12   13.99            0.44
Fe 26 K-Serie   2.86    3.56    2.89            0.12
----------------------------------------------------
      Summe:   80.35  100.00  100.00
```

Figure S4. Energy dispersive X-ray analysis of $Fe_{0.3}Ni_{1.2}Co_{2.5}(S_{0.9}O_{0.1})_4$.

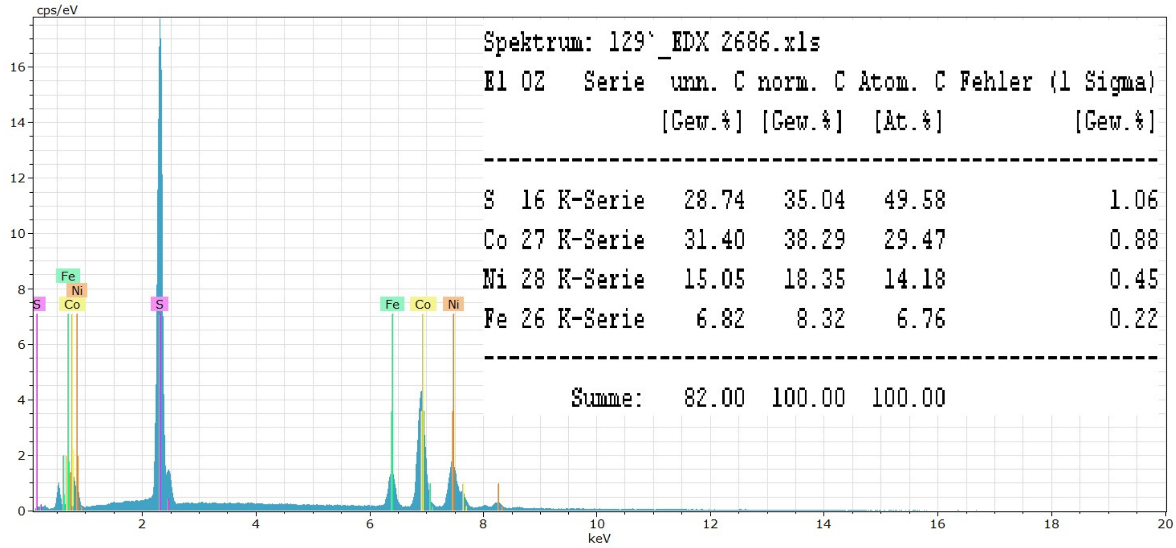

```
Spektrum: 129`_EDX 2686.xls
El OZ   Serie  unn. C norm. C Atom. C Fehler (1 Sigma)
               [Gew.%] [Gew.%]  [At.%]           [Gew.%]
-------------------------------------------------------
S  16 K-Serie   28.74   35.04   49.58               1.06
Co 27 K-Serie   31.40   38.29   29.47               0.88
Ni 28 K-Serie   15.05   18.35   14.18               0.45
Fe 26 K-Serie    6.82    8.32    6.76               0.22
-------------------------------------------------------
       Summe:   82.00  100.00  100.00
```

Figure S5. Energy dispersive X-ray analysis of $Fe_{0.6}Ni_{1.2}Co_{2.5}(S_{0.83}O_{0.17})_4$.

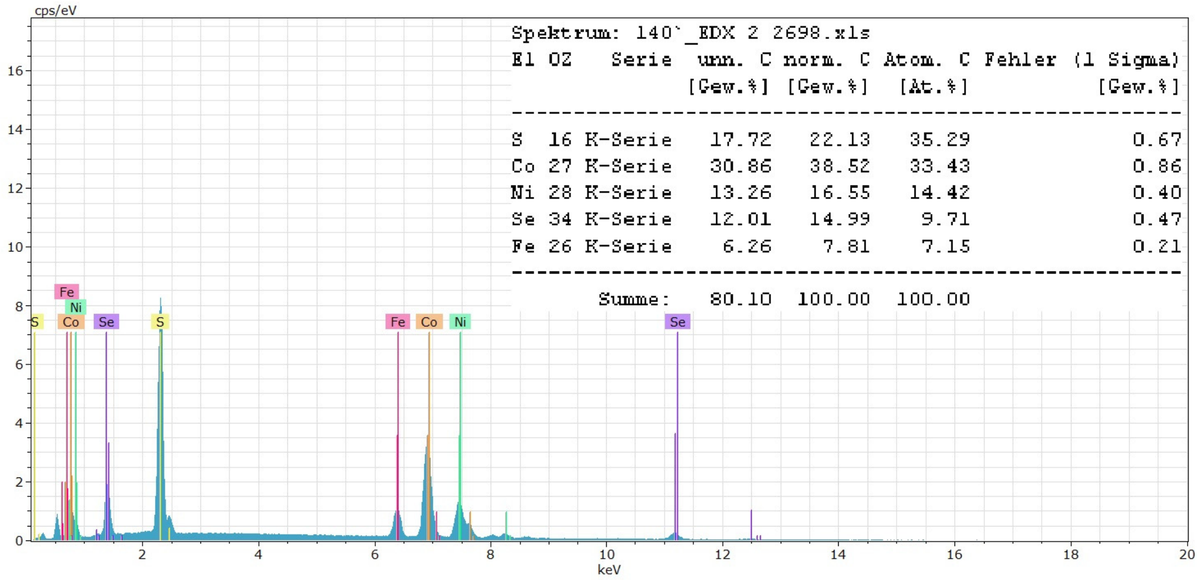

```
Spektrum: 140`_EDX 2 2698.xls
El OZ   Serie  unn. C norm. C Atom. C Fehler (1 Sigma)
               [Gew.%] [Gew.%]  [At.%]           [Gew.%]
-------------------------------------------------------
S  16 K-Serie   17.72   22.13   35.29               0.67
Co 27 K-Serie   30.86   38.52   33.43               0.86
Ni 28 K-Serie   13.26   16.55   14.42               0.40
Se 34 K-Serie   12.01   14.99    9.71               0.47
Fe 26 K-Serie    6.26    7.81    7.15               0.21
-------------------------------------------------------
       Summe:   80.10  100.00  100.00
```

Figure S6. Energy dispersive X-ray analysis of $Fe_{0.5}Ni_{1.0}Co_{2.0}(S_{0.57}Se_{0.25}O_{0.18})_4$.

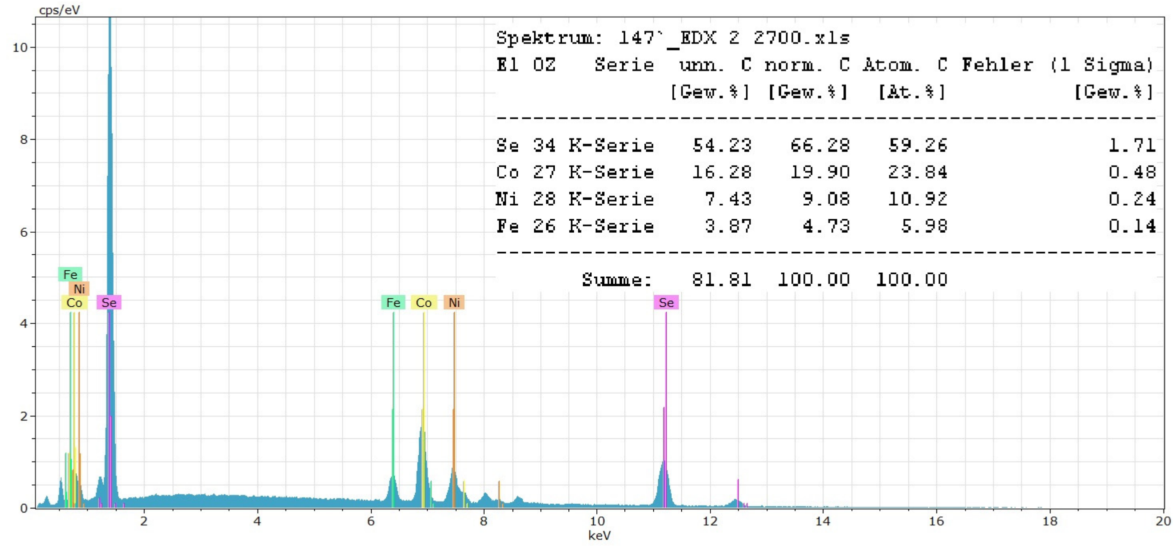

```
Spektrum: 147`_EDX 2 2700.xls
El OZ    Serie   unn. C norm. C Atom. C Fehler (1 Sigma)
                 [Gew.%] [Gew.%]  [At.%]           [Gew.%]
-------------------------------------------------------------
Se 34 K-Serie   54.23   66.28   59.26              1.71
Co 27 K-Serie   16.28   19.90   23.84              0.48
Ni 28 K-Serie    7.43    9.08   10.92              0.24
Fe 26 K-Serie    3.87    4.73    5.98              0.14
-------------------------------------------------------------
       Summe:   81.81  100.00  100.00
```

Figure S7. Energy dispersive X-ray analysis of $Fe_{0.4}Ni_{0.7}Co_{1.6}(Se_{0.81}O_{0.19})_4$.

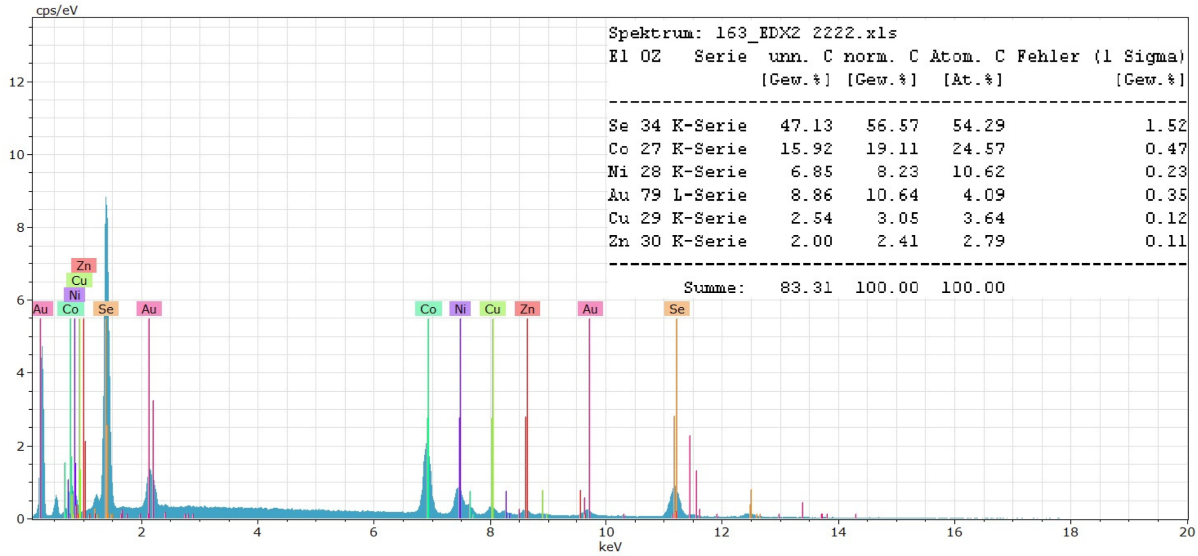

```
Spektrum: 163_EDX2 2222.xls
El OZ    Serie   unn. C norm. C Atom. C Fehler (1 Sigma)
                 [Gew.%] [Gew.%]  [At.%]           [Gew.%]
-------------------------------------------------------------
Se 34 K-Serie   47.13   56.57   54.29              1.52
Co 27 K-Serie   15.92   19.11   24.57              0.47
Ni 28 K-Serie    6.85    8.23   10.62              0.23
Au 79 L-Serie    8.86   10.64    4.09              0.35
Cu 29 K-Serie    2.54    3.05    3.64              0.12
Zn 30 K-Serie    2.00    2.41    2.79              0.11
-------------------------------------------------------------
       Summe:   83.31  100.00  100.00
```

Figure S8. Energy dispersive X-ray analysis of $Ni_{0.7}Co_{1.4}(Se_{0.85}O_{0.15})_4$. The Se and Au peaks do not overlap. Hence, EDX analysis with Au sputtering was not performed for this specific sample.

Figure S9 shows the EDX-mapping of $Fe_{0.5}Ni_{1.0}Co_{2.0}(S_{0.57}Se_{0.25}O_{0.18})_4$ and indicates the uniform distribution of the elements.

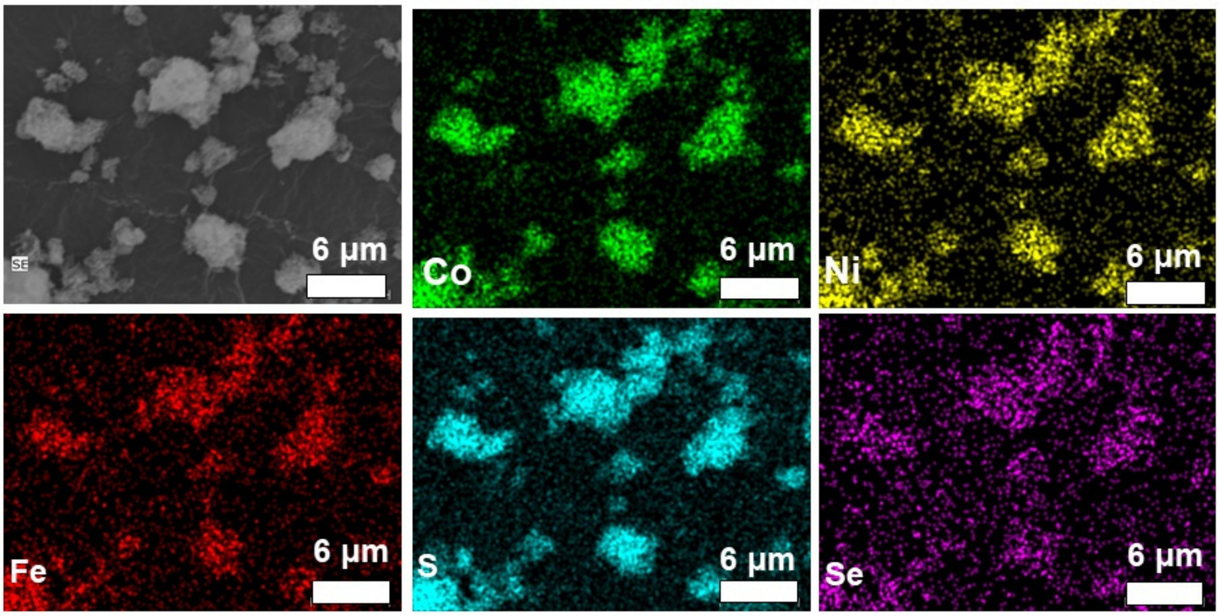

Figure S9. SEM and EDX mapping images of the $Fe_{0.5}Ni_{1.0}Co_{2.0}(S_{0.57}Se_{0.25}O_{0.18})_4$.

Table S1. TEM-EDX analysis of $Fe_{0.5}Ni_{1.0}Co_{2.0}(S_{0.57}Se_{0.25}O_{0.18})_4$.[a)]

Element	**Weight%**	**Atom%**
S (K)	14.0	11.9
Fe (K)	4.6	2.3
Co (K)	20.8	9.6
Ni (K)	9.2	4.3
Se (K)	9.3	3.2

[a)] Values for C, O and Cu which stem from the sample holder are not given, hence the values do not add up to 100%.

Section S4 Elemental analysis and atomic absorption spectroscopy measurements

Table S2. Metal concentration derived from AAS and sample mass used for AAS analysis.[a)]

Sample	Fe conc. (mg/L)	Ni conc. (mg/L)	Co conc. (mg/L)	Sample mass (mg)
$Ni_{1.0}Co_{2.1}(S_{0.9}O_{0.1})_4$	--------	13.17	28.5	3.5
$Fe_{0.1}Ni_{1.4}Co_{2.9}(S_{0.87}O_{0.13})_4$	1.196	16.04	34.3	3.8
$Fe_{0.2}Ni_{1.5}Co_{2.8}(S_{0.9}O_{0.1})_4$	1.980	18.10	33.4	3.9
$Fe_{0.3}Ni_{1.2}Co_{2.5}(S_{0.9}O_{0.1})_4$	3.371	14.59	30.8	3.7
$Fe_{0.6}Ni_{1.2}Co_{2.5}(S_{0.83}O_{0.17})_4$	6.728	13.63	29.5	3.7
$Fe_{0.5}Ni_{1.0}Co_{2.0}(S_{0.57}Se_{0.25}O_{0.18})_4$	5.506	11.40	23.9	3.8
$Fe_{0.4}Ni_{0.7}Co_{1.6}(Se_{0.81}O_{0.19})_4$	4.302	8.57	20.2	4.5
$Ni_{0.7}Co_{1.4}(Se_{0.85}O_{0.15})_4$	-------	9.19	20.8	5.0

a) Sample volume 50 mL (0.05 L).

Table S3. Weight percent (wt%) of the elements based on AAS for Fe, Ni, and Co, CHNS for S, and EDX.

Sample	Fe wt%	Ni wt%	Co wt%	Fe+Ni+Co wt%	S wt%	Se wt%	Sum of Fe,Co,Ni,S,Se wt% [a]	O wt [a]
$Ni_{1.0}Co_{2.1}(S_{0.9}O_{0.1})_4$ (304.81 g/mol) (theor.)	….	18.8 (19.25)	40.71 (38.67)	59.51 (57.92)	38.08 (42.08)		97.53	2.47
$Fe_{0.1}Ni_{1.4}Co_{2.9}(S_{0.87}O_{0.13})_4$	1.57	21.10	45.13	67.80	30.88		98.81	1.19
$Fe_{0.2}Ni_{1.5}Co_{2.8}(S_{0.9}O_{0.1})_4$	2.53	23.20	42.82	68.55	29.79		98.60	1.40
$Fe_{0.3}Ni_{1.2}Co_{2.5}(S_{0.9}O_{0.1})_4$	4.55	19.70	41.62	65.87	32.22		97.90	2.10
$Fe_{0.6}Ni_{1.2}Co_{2.5}(S_{0.83}O_{0.17})_4$	9.10	19.47	39.86	68.43	28.46		96.50	3.50
$Fe_{0.5}Ni_{1.0}Co_{2.0}(S_{0.57}Se_{0.25}O_{0.18})_4$	7.24	16.28	31.45	54.97	19.80	22	97.00	3.0
$Fe_{0.4}Ni_{0.7}Co_{1.6}(Se_{0.81}O_{0.19})_4$	4.78	9.96	22.44	37.18	….	60	97.20	2.80
$Ni_{0.7}Co_{1.4}(Se_{0.85}O_{0.15})_4$ (492.39 g/mol) (theor.)		9.77 (11.92)	20.80 (23.94)	30.57 (35.86)	…..	67 (64.14)	97.60	2.40

[a] The difference to 100% is assumed to be oxygen weight percent.

It is noteworthy that the AAS, CHNS determination and EDX(Se) for metal, S and Se, respectively, add up to almost 100%, which also indicates that the determinations, even from different methods seem to be reliable.

If we divide the wt% values in Table S3 by the relative atomic weight, we get the atom content in mol/g. These values are given in Table S4:

Table S4. Weight percent (wt%) and atom content (mol/g) of the elements based on AAS for Fe, Ni, and Co, CHNS for S, and EDX for Se.

Sample **wt%:A_r**	**Fe** **wt%** **(mol/g)**	**Ni** **wt%** **(mol/g)**	**Co** **wt%** **(mol/g)**	**S** **wt%** **(mol/g)**	**Se** **wt%** **(mol/g)**	**O** **wt [a]** **(mol/g)**	**S+Se+O**
$Ni_{1.0}Co_{2.1}(S_{0.9}O_{0.1})_4$ (theor.) wt% : A_r	….	18.8 (19.25) 0.32	40.71 (38.67) 0.69	38.08 (42.08) 1.185		2.47 0.15	1.335
$Fe_{0.1}Ni_{1.4}Co_{2.9}(S_{0.87}O_{0.13})_4$ wt% : A_r	1.57 0.028	21.10 0.36	45.13 0.766	30.88 0.967		1.19 0.074	1.041
$Fe_{0.2}Ni_{1.5}Co_{2.8}(S_{0.9}O_{0.1})_4$ wt% : A_r	2.53 0.045	23.20 0.395	42.82 0.727	29.79 0.936		1.40 0.087	1.023
$Fe_{0.3}Ni_{1.2}Co_{2.5}(S_{0.9}O_{0.1})_4$ wt% : A_r	4.55 0.081	19.70 0.336	41.62 0.706	32.22 0.998		2.10 0.13	1.128
$Fe_{0.6}Ni_{1.2}Co_{2.5}(S_{0.83}O_{0.17})_4$ wt% : A_r	9.10 0.163	19.47 0.332	39.86 0.676	28.46 0.873		3.50 0.22	1.093
$Fe_{0.5}Ni_{1.0}Co_{2.0}(S_{0.57}Se_{0.25}O_{0.18})_4$ wt% : A_r	7.24 0.129	16.28 0.277	31.45 0.534	19.80 0.624	22 0.279	3.0 0.187	1.09
							Se+O
$Fe_{0.4}Ni_{0.7}Co_{1.6}(Se_{0.81}O_{0.19})_4$ wt% : A_r	4.78 0.086	9.96 0.170	22.44 0.381	….	60 0.760	2.80 0.175	0.935
$Ni_{0.7}Co_{1.4}(Se_{0.85}O_{0.15})_4$ (theor.) wt% : A_r		9.77 (11.92) 0.166	20.80 (23.94) 0.353	…..	67 (64.14) 0.848	2.40 0.15	0.998

[a] The difference to 100% is assumed to be oxygen weight percent.

From the atom content in mol/g the atom ratio per gram, that is the formula unit is derived. The combined S, Se and O content is set to 4, the metal content referenced accordingly and rounded to one decimal digit – these formula units are summarized in Table S5.

Table S5. AAS, CHNS and EDX (for Se) derived formula units.

Atom ratio	**Atom ratio with (S,Se,O) set to 4**	**Atom ratio rounded to one decimal digit**
$Ni_{0.32}Co_{0.69}(S,O)_{1.33}$	$Ni_{0.96}Co_{2.07}(S,O)_4$	$Ni_{1.0}Co_{2.1}(S,O)_4$
$Fe_{0.028}Ni_{0.36}Co_{0.766}(S,O)_{1.04}$	$Fe_{0.11}Ni_{1.4}Co_{2.9}(S,O)_4$	$Fe_{0.1}Ni_{1.4}Co_{2.9}(S,O)_4$
$Fe_{0.045}Ni_{0.395}Co_{0.727}(S,O)_{1.02}$	$Fe_{0.17}Ni_{1.5}Co_{2.8}(S,O)_4$	$Fe_{0.2}Ni_{1.5}Co_{2.8}(S,O)_4$
$Fe_{0.081}Ni_{0.336}Co_{0.706}(S,O)_{1.13}$	$Fe_{0.29}Ni_{1.2}Co_{2.5}(S,O)_4$	$Fe_{0.3}Ni_{1.2}Co_{2.5}(S,O)_4$
$Fe_{0.163}Ni_{0.332}Co_{0.676}(S,O)_{1.09}$	$Fe_{0.60}Ni_{1.2}Co_{2.5}(S,O)_4$	$Fe_{0.6}Ni_{1.2}Co_{2.5}(S,O)_4$
$Fe_{0.129}Ni_{0.277}Co_{0.534}(S,Se,O)_{1.09}$	$Fe_{0.47}Ni_{1.0}Co_{2.0}(S,Se,O)_4$	$Fe_{0.5}Ni_{1.0}Co_{2.0}(S,Se,O)_4$
$Fe_{0.086}Ni_{0.170}Co_{0.381}(Se,O)_{0.935}$	$Fe_{0.37}Ni_{0.73}Co_{1.6}(Se,O)_4$	$Fe_{0.4}Ni_{0.7}Co_{1.6}(Se,O)_4$
$Ni_{0.166}Co_{0.353}(Se,O)_{0.998}$	$Ni_{0.67}Co_{1.4}(Se,O)_4$	$Ni_{0.7}Co_{1.4}(Se,O)_4$

A comparison between the AAS, CHNS and EDX (for Se) derived formula units and the formula unit from EDX alone is given in Table S6.

We note that in the literature on mixed-metal sulfides almost no metal analyses seem to be carried out by AAS and no sulfur weight percent analyses by CHNS. We did not find any literature which used a combination of AAS and CHNS to derive at the formula units of mixed-metal sulfides.

Instead, the mostly used method to determine the atomic ratios in mixed-metal sulfides is SEM-EDX. In rare cases, ICP-Mass MS or ICP-OES has been used to determine the Ni:Co ratios between Ni and Co

However, one has to keep in mind that X-ray spectroscopy needs standards for peak identification and quantification. Due to matrix effects a combination of elements can give different emission intensities compared to the individual constituent elements in neat form. Such matrix effects originate because the other elements in the sample can absorb the emitted X-rays. This then enhances the X-ray emission of these other elements. These matrix effects of X-ray spectroscopies are well-known but are often not taken into account. Hence, a quantification by EDX has always the risk that the composition of the sample is different than expected and different when compared to other methods. Consequently, the sample composition from EDX analysis will not be very accurate without certified standards and atom percent values from EDX should be given with at the most one decimal digit.

Further, it should be considered that in EDX the emitted X-rays derive from a 1-2 μm surface layer of the sample which can be different due to oxidation from the bulk of the sample.

It is also important to note that EDX gives only the element ratio but not the absolute content of an element because the lighter elements (atomic number smaller 9 (fluorine)) are not quantified well. The absolute metal content and also the metal atom ratio is given by AAS where a concentration in mmol/g (or mg/g) of the element is measured from the solution of a exactly weighed sample.

Table S6. Comparison between chemical formula derived from SEM-EDX and AAS +CHNS.

Chemical formula based on SEM-EDX analysis	**AAS-CHNS-EDX(Se) derived formula unit from Table S5**
$Ni_{1.2}Co_{2.5}S_4$	$Ni_{1.0}Co_{2.1}(S_{0.9}O_{0.1})_4$
$Fe_{0.06}Ni_{1.2}Co_{3.0}S_4$ [a]	$Fe_{0.1}Ni_{1.4}Co_{2.9}(S_{0.87}O_{0.13})_4$
$Fe_{0.12}Ni_{1.1}Co_{2.6}S_4$ [a]	$Fe_{0.2}Ni_{1.5}Co_{2.8}(S_{0.9}O_{0.1})_4$
$Fe_{0.2}Ni_{1.1}Co_{2.6}S_4$	$Fe_{0.3}Ni_{1.2}Co_{2.5}(S_{0.9}O_{0.1})_4$
$Fe_{0.5}Ni_{1.1}Co_{2.4}S_4$	$Fe_{0.6}Ni_{1.2}Co_{2.5}(S_{0.83}O_{0.17})_4$
$Fe_{0.6}Ni_{1.3}Co_3(S_{0.78}Se_{0.22})_4$	$Fe_{0.5}Ni_{1.0}Co_{2.0}(S_{0.57}Se_{0.25}O_{0.18})_4$
$Fe_{0.4}Ni_{0.7}Co_{1.6}Se_4$	$Fe_{0.4}Ni_{0.7}Co_{1.6}(Se_{0.81}O_{0.19})_4$
$Ni_{0.9}Co_{1.9}Se_4$	$Ni_{0.7}Co_{1.4}(Se_{0.85}O_{0.15})_4$

[a] In EDX analysis the element stoichiometric values should be rounded to only one decimal digit. Here we kept two digits for Fe in two of the samples as rounding would otherwise make the values identical.

From Table S6 it is evident that the chemical formulae from SEM-EDX and from AAS-CHNS-EDX(Se) analysis are not very far off. The trend is the same. For reasons given above AAS was taken as the more reliable analysis and combined with CHNS and EDX for Se.

Section S5 Nitrogen sorption measurement

Potential porosities of the samples were checked by nitrogen sorption measurements (Figure S10). The specific surface area (BET) of the samples is listed in Table S7. The BET surface areas are slightly above the outer surface area of 20-50 m^2 g^{-1}, which would be expected for a fine powder, and reached 71 m^2 g^{-1} in $Fe_{0.6}Ni_{1.2}Co_{2.5}(S_{0.83}O_{0.17})_4$.

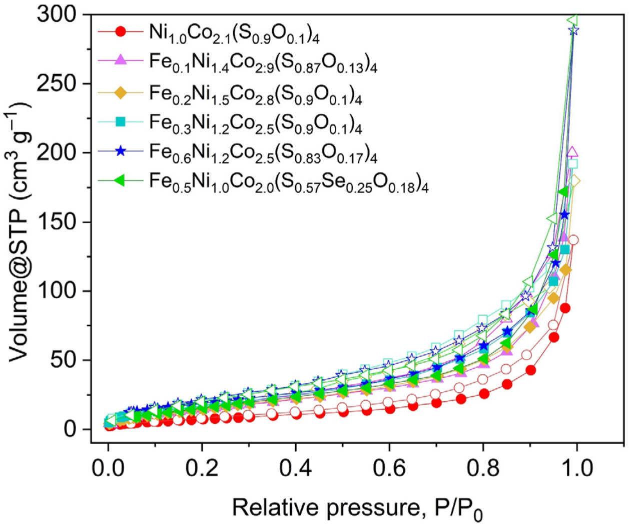

Figure S10. Nitrogen adsorption-desorption isotherms (adsorption: filled symbols; desorption: empty symbols of the sulfide and sulfoselenide samples.

Table S7. Specific **surface** area (BET) of as-prepared samples.

Sample	**BET [a] (m^2 g^{-1})**
$Ni_{1.0}Co_{2.1}(S_{0.9}O_{0.1})_4$	31
$Fe_{0.1}Ni_{1.4}Co_{2.9}(S_{0.87}O_{0.13})_4$	58
$Fe_{0.2}Ni_{1.5}Co_{2.8}(S_{0.9}O_{0.1})_4$	60
$Fe_{0.3}Ni_{1.2}Co_{2.5}(S_{0.9}O_{0.1})_4$	67
$Fe_{0.6}Ni_{1.2}Co_{2.5}(S_{0.83}O_{0.17})_4$	71
$Fe_{0.5}Ni_{1.0}Co_{2.0}(S_{0.57}Se_{0.25}O_{0.18})_4$	63
$Fe_{0.4}Ni_{0.7}Co_{1.6}(Se_{0.81}O_{0.19})_4$	56
$Ni_{0.7}Co_{1.4}(Se_{0.85}O_{0.15})_4$	21

[a] Brunauer, Emmett, and Teller

Section S6 X-ray photoelectron spectroscopy

The survey spectra of the compounds (Figure S11) confirmed the presence of Ni, Co, S, and O for $Ni_{1.0}Co_{2.1}(S_{0.9}O_{0.1})_4$ and Fe, Ni, Co, S, Se, and O for $Fe_{0.5}Ni_{1.0}Co_{2.0}(S_{0.57'}Se_{0.25}O_{0.18})_4$ with also oxygen. The oxygen content can both derive from the synthesis using metal carbonate hydroxides as precursors and from surface oxidation. Note that in XPS analysis the detected photoelectrons can only escape from a 70-110 Å thin surface layer of the sample, rendering XPS a surface analysis technique.

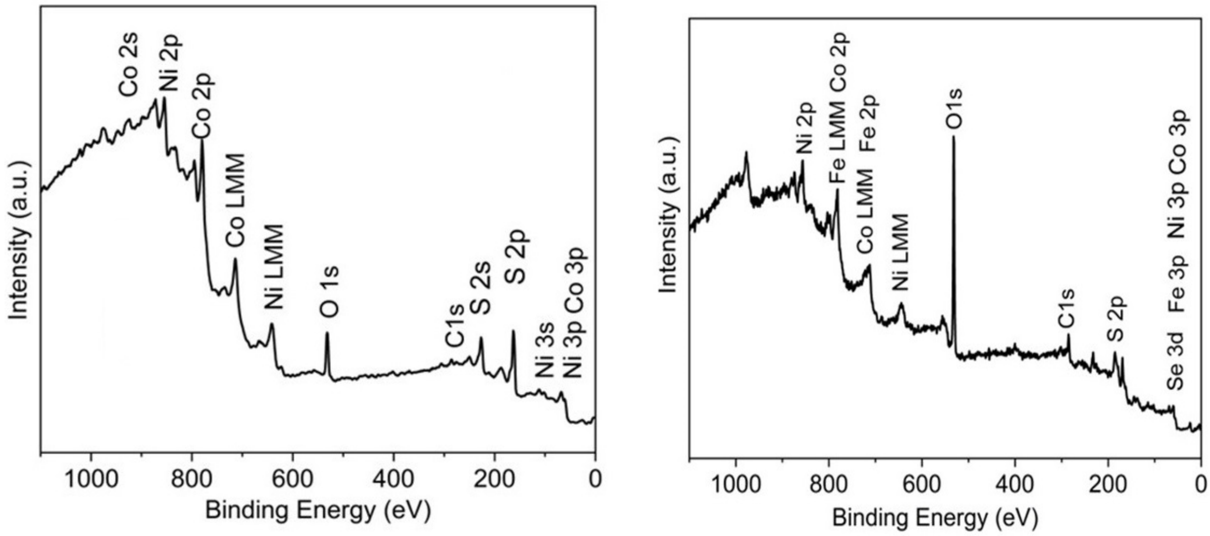

(a) (b)

Figure S11. XPS survey spectrum of (**a**) $Ni_{1.0}Co_{2.1}(S_{0.9}O_{0.1})_4$ (**b**) $Fe_{0.5}Ni_{1.0}Co_{2.0}(S_{0.57}Se_{0.25}O_{0.18})_4$.

$Ni_{1.0}Co_{2.1}(S_{0.9}O_{0.1})_4$:

The deconvolution of the Ni $2p_{3/2}$ band resulted in two peaks at 853.3 and 856.0 eV, ascribed to Ni^{2+} and Ni^{3+}. The Ni $2p_{1/2}$ region is comprised of two peaks centered at 871.8 and 875.4 eV corresponding to Ni^{2+} and Ni^{3+} respectively [1]. The Co $2p_{3/2}$ signal consists of two peaks centered at 778.7 and 780.3 eV, which can be attributed to Co^{3+} and $Co^{2+,}$ respectively, and Co $2p_{1/2}$ is comprised of two peaks at 793.6 and 796.5 eV, which can be ascribed to Co^{3+} and Co^{2+}, respectively [2, 3].

$Fe_{0.5}Ni_{1.0}Co_{2.0}(S_{0.57}Se_{0.25}O_{0.18})_4$:

The Ni $2p_{3/2}$ region can be deconvoluted into two peaks, a prominent one at 856.5 eV and a small one at 854.5 eV, which can be assigned to Ni^{3+} and Ni^{2+}, respectively. The binding energy of the Ni 2p$_{1/2}$ region can be deconvoluted into two peaks, the main one at 875.0 eV and a small one at 871.3 eV, corresponding to Ni^{3+} and Ni^{2+}, respectively [4]. The Co 2p$_{3/2}$ region consists of two peaks, the more prominent one centered at 782eV is attributed to Co^{2+}, while a smaller peak located at 779.1 can be ascribed to Co^{3+} [5]. Two fitted peaks at 798.0 and 795.2 eV in the Co 2p$_{1/2}$ signal region can be ascribed to Co^{2+} and Co^{3+} respectively [6].

S 2p XPS spectrum of $Ni_{1.0}Co_{2.1}(S_{0.9}O_{0.1})_4$ and $Fe_{0.5}Ni_{1.0}Co_{2.0}(S_{0.57}Se_{0.25}O_{0.18})_4$:

The binding energies of S 2p in $Ni_{1.0}Co_{2.1}(S_{0.9}O_{0.1})_4$ (Figure S12a) located at 161.5 eV and 162.7 eV can be assigned to S 2p$_{3/2,}$ and S 2p$_{1/2}$ from to metal-bound sulfur while the peak located at 169 eV can be ascribed to oxidized sulfur species (SO_4^{2-}, HSO_4^-) on the surface [7].

The S 2p region overlaps with the Se 3p region. As illustrated in Figure S12b for $Fe_{0.5}Ni_{1.0}Co_{2.0}(S_{0.57}Se_{0.25}O_{0.18})_4$, the S 2p bands are deconvoluted into peaks located at 160.7 and 166.3 eV, which can be attributed to the Se 3p$_{3/2}$ and Se 3p$_{1/2}$ binding energies, respectively. Additionally, two peaks observed at 162.5 and 164.8 eV correspond to the S 2p$_{3/2}$ and S 2p$_{1/2}$ binding energies [8, 9, 10]. The broad peak at 169 eV can be attributed to oxidized sulfur species (SO_4^{2-}, HSO_4^-) on the surface [7]. A certain amount of oxidized sulfur species is always observed in the XPS spectra of metal sulfides and selenides [11].

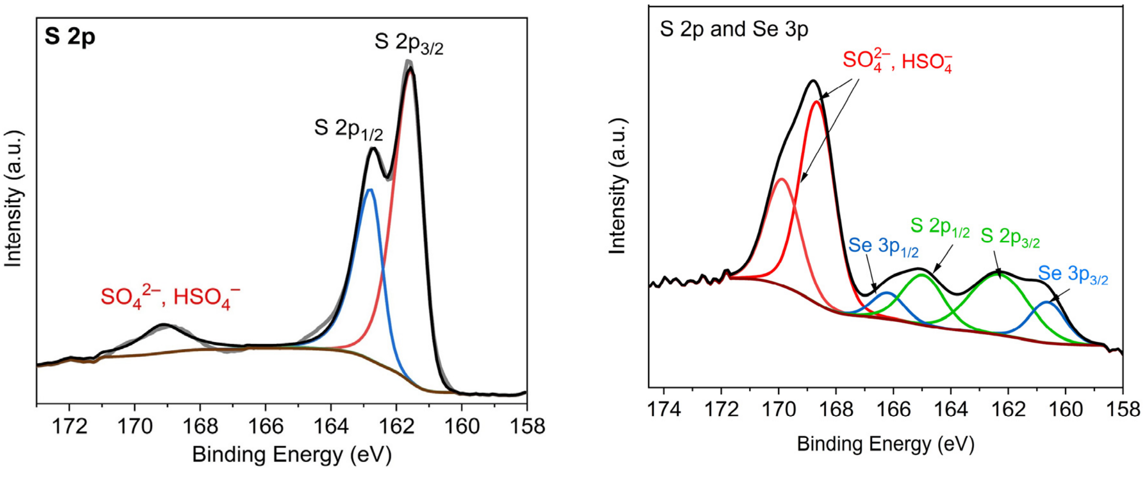

(a) **(b)**

Figure S12. X-ray photoelectron spectrum of S 2p in (**a**) $Ni_{1.0}Co_{2.1}(S_{0.9}O_{0.1})_4$, and (**b**) $Fe_{0.5}Ni_{1.0}Co_{2.0}(S_{0.57}Se_{0.25}O_{0.18})_4$ (overlapping with Se 3p)

O 1s spectra of $Ni_{1.0}Co_{2.1}(S_{0.9}O_{0.1})_4$ and $Fe_{0.5}Ni_{1.0}Co_{2.0}(S_{0.57}Se_{0.25}O_{0.18})_4$:

To further evaluate the presence of oxygen in the samples of $Ni_{1.0}Co_{2.1}(S_{0.9}O_{0.1})_4$ and $Fe_{0.5}Ni_{1.0}Co_{2.0}(S_{0.57}Se_{0.25}O_{0.18})_4$ the O 1s spectra have been deconvoluted in two peaks (Figure S13). The prominent peaks observed at 531.8 eV for $Ni_{1.0}Co_{2.1}(S_{0.9}O_{0.1})_4$ and 531.7 eV for $Fe_{0.5}Ni_{1.0}Co_{2.0}(S_{0.57}Se_{0.25}O_{0.18})_4$ are attributed to the presence of OH^- groups. These groups may arise from surface hydroxylation or the substitution of S^{2-} by OH^-. Additionally, these peaks can also be attributed to the presence of defective oxides [12,13]. In addition, the O 1s spectrum shows small signal contributions at 533.4 eV for $Ni_{1.0}Co_{2.1}(S_{0.9}O_{0.1})_4$ and 532.9 eV for $Fe_{0.5}Ni_{1.0}Co_{2.0}(S_{0.57}Se_{0.25}O_{0.18})_4$, which can be assigned to oxygen from SO_4^{2-} on the surface of samples [14,15].

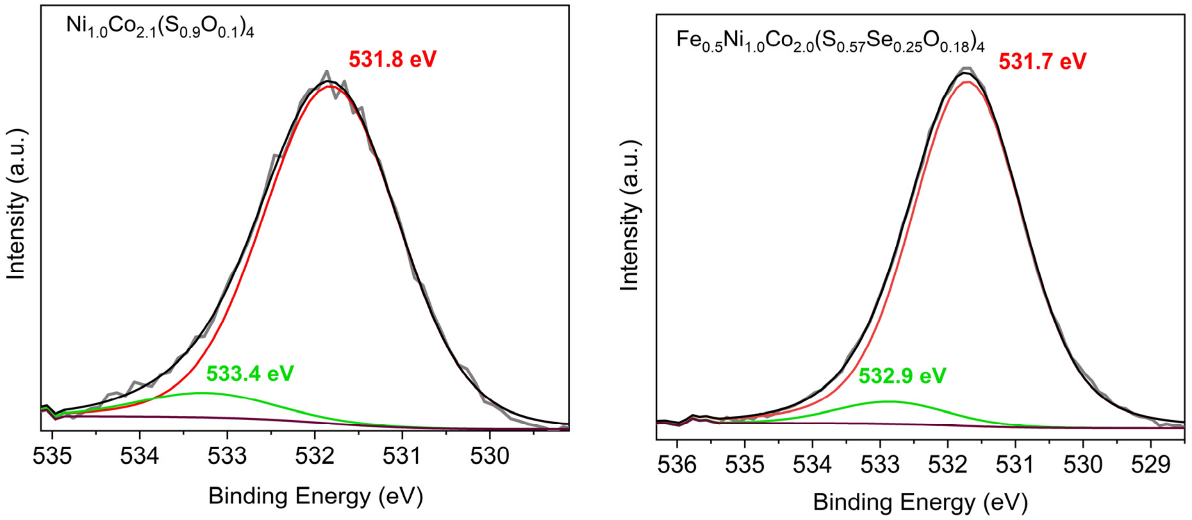

(a) **(b)**

Figure S13. XPS O 1s spectrum of (**a**) $Ni_{1.0}Co_{2.1}(S_{0.9}O_{0.1})_4$, (**b**) $Fe_{0.5}Ni_{1.0}Co_{2.0}(S_{0.57}Se_{0.25}O_{0.18})_4$.

Table S8 and S9 summarize the binding energies in the XPS spectra of $Ni_{1.0}Co_{2.1}(S_{0.9}O_{0.1})_4$ and $Fe_{0.5}Ni_{1.0}Co_{2.0}(S_{0.57}Se_{0.25}O_{0.18})_4$.

Table S8. Binding energies of the element components in $Ni_{1.0}Co_{2.1}(S_{0.9}O_{0.1})_4$.[a)]

Sample						
$Ni_{1.0}Co_{2.1}(S_{0.9}O_{0.1})_4$	**Ni $2p_{3/2}$**			**Ni $2p_{1/2}$**		
	Peak	Binding energy/eV	Sat.	Peak	Binding energy/eV	Sat.
	Ni^{2+}	853.3	860.5	Ni^{2+}	871.8	880.2
	Ni^{3+}	856.0		Ni^{3+}	875.4	
	Co $2p_{3/2}$			**Co $2_{1/2}$**		
	Peak	Binding energy/eV	Sat.	Peak	Binding energy/eV	Sat.
	Co^{2+}	780.3	784.5	Co^{2+}	796.5	801.5
	Co^{3+}	778.7		Co^{3+}	793.6	
	O 1s			**S 2p**		
	Peak	Binding energy/eV		Peak	Binding energy/eV	
	OH^- or defective oxides	531.8		S^{2-}, $2p_{3/2}$	161.5	
	O from SO_4^{2-}	533.4		S^{2-}, $2p_{1/2}$	162.7	
				SO_4^{2-}, HSO_4^-	169	

[a)] Sat. = satellite peak.

Table S9. Binding energies of the elements components in $Fe_{0.5}Ni_{1.0}Co_{2.0}(S_{0.57}\,Se_{0.25}O_{0.18})_4$.[a)]

Sample						
$Fe_{0.5}Ni_{1.0}Co_{2.0}(S_{0.57}Se_{0.25}O_{0.18})_4$	**Ni 2p$_{3/2}$**			**Ni 2p$_{1/2}$**		
	Peak	Binding energy/eV	Sat.	Peak	Binding energy/eV	Sat.
	Ni^{2+}	854.5	864	Ni^{2+}	871.3	882.4
	Ni^{3+}	856.5		Ni^{3+}	875.0	
	Co 2p$_{3/2}$			**Co 2p$_{1/2}$**		
	Peak	Binding energy/eV	Sat.	Peak	Binding energy/eV	Sat.
	Co^{2+}	782.0	787.1	Co^{2+}	798.0	803.30
	Co^{3+}	779.1		Co^{3+}	795.2	
	Fe 2p$_{3/2}$			**Fe 2p$_{1/2}$**		
	Peak	Binding energy/eV	Sat.	Peak	Binding energy/eV	Sat.
	Fe^{3+}	712.5	717.5	Fe^{3+}	725.0	734.5
	Se 3d$_{5/2}$			**Se 3d$_{3/2}$**		
	Peak	Binding energy/eV	Sat.		Binding energy/eV	Sat
	Se^{2-}	55.0	----	Se^{2-}	57.0	59.5
	O1s		**S 2p**		**Se 3p**	
	Peak	Binding energy/eV	Peak	Binding energy/eV	Peak	Binding energy/eV
	OH$^-$ or defective oxides	531.7	S^{2-}, 2p$_{3/2}$	162.5	Se 3p3/2	160.7
	O from adventitious carbon or O from SO$_4^{2-}$	532.9	S^{2-}, 2p$_{1/2}$	164.8	Se 3p1/2	166.3
			SO$_4^{2-}$, HSO$_4^-$	169		

[a)] Sat. = satellite peak.

Section S7 Electrochemical characterization

The linear sweep voltammetry polarization curve and Tafel curve of (Fe_xNi_{1-x})CoCH-(1.0) were shown in Figures S 14a and S 14b, respectively. The overpotential for generating 50 mA.cm^{-2} was 330 mV, and the calculated Tafel slope was 98 mV dec^{-2}. (Fe_xNi_{1-x})CoCH-(1.0) showed lower OER performance compared to $Fe_{0.6}Ni_{1.2}Co_{2.5}(S_{0.83}O_{0.17})_4$ (η_{50} = 294 mV, Tafel slope = 87 mV dec^{-2}), $Fe_{0.4}Ni_{0.7}Co_{1.6}(Se_{0.81}O_{0.19})_4$ (η_{50} = 306 mV, Tafel slope = 84 mV dec^{-2}) and $Fe_{0.4}Ni_{0.7}Co_{1.6}(Se_{0.81}O_{0.19})_4$ (η_{50} = 277 mV, Tafel slope = 75 mV dec^{-2}) at the same condition. This result indicates that, although (Fe_xNi_{1-x})CoCH-(1.0) was used as the precursor for the synthesis $Fe_{0.6}Ni_{1.2}Co_{2.5}(S_{0.83}O_{0.17})_4$, $Fe_{0.4}Ni_{0.7}Co_{1.6}(Se_{0.81}O_{0.19})_4$, and $Fe_{0.5}Ni_{1.0}Co_{2.0}(S_{0.57}Se_{0.25}O_{0.18})_4$ with the same transition metal content, the absence of chalcogens (S, Se) in its structure dramatically reduces its OER performance compared to related sulfide, selenide, and sulfoselenides.

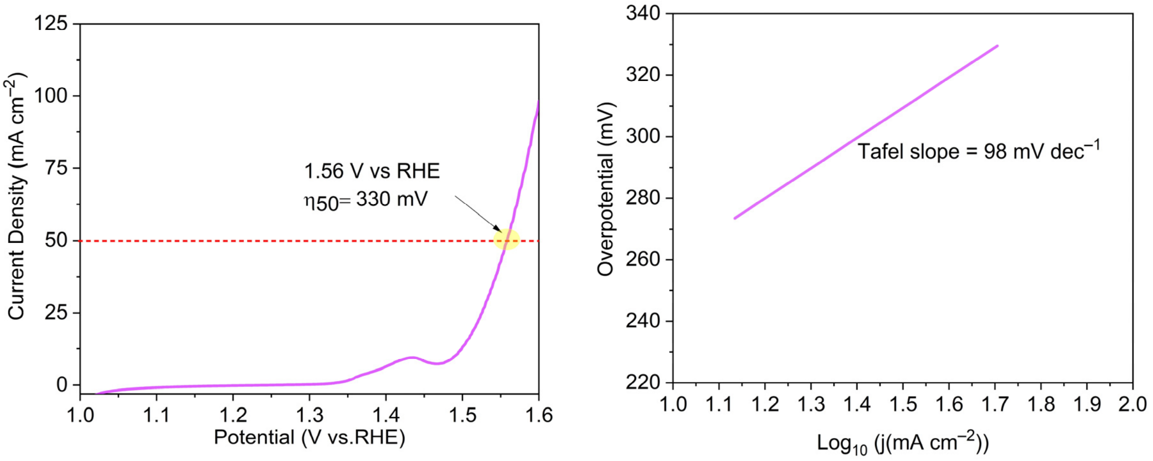

(a) **(b)**

Figure S14. (**a**) LSV polarization curve of and (**b**) Tafel slope of (Fe_xNi_{1-x})CoCH-(1.0).

The Nyquist plots of (Fe_xNi_{1-x})CoCH-(1.0) in Figure S15 also showed a bigger semicircle radius than for $Fe_{0.6}Ni_{1.2}Co_{2.5}(S_{0.83}O_{0.17})_4$, $Fe_{0.4}Ni_{0.7}Co_{1.6}(Se_{0.81}O_{0.19})_4$ and $Fe_{0.5}Ni_{1.0}Co_{2.0}(S_{0.57}Se_{0.25}O_{0.18})_4$ which indicates higher charge transfer resistance during the OER process.

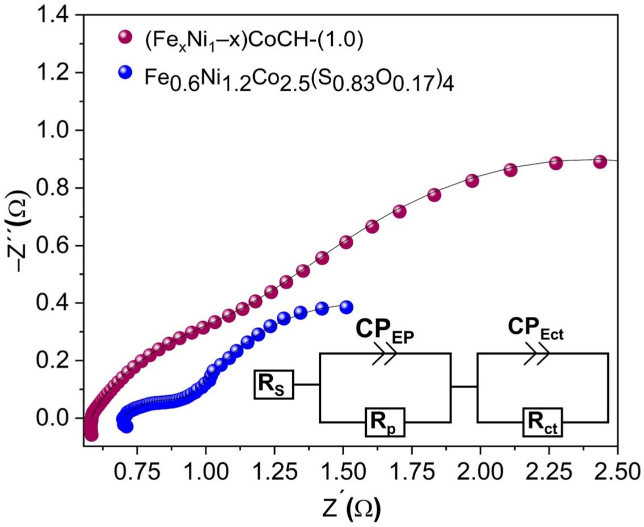

Figure S15. Nyquist plots of selected samples and Voigt circuit model of (Fe$_x$Ni$_{1-x}$)CoCH-(1.0) and Fe$_{0.6}$Ni$_{1.2}$Co$_{2.5}$(S$_{0.83}$O$_{0.17}$)$_4$.

Section S7.1 Oxygen evolution reaction conditions

We ensured the utilization of fresh commercial KOH solution for each voltammetric experiment in our study. We followed similar OER reaction conditions, particularly in terms of the characteristic properties of the KOH solution, in order to compare our results with those published by others. Therefore, we employed fresh and degassed KOH solution, consistent with the approach adopted in the field [16,17,18,19,20,21,22]. Immediately after injecting the KOH solution into the reaction vessel, we purged the system with N_2 for a duration of 10 minutes to eliminate any potential interfering gases, including CO_2, that could affect the OER. It is worth mentioning that we replaced the KOH solution after each experiment to maintain consistent OER conditions across all individual samples and to minimize the presence of extraneous dissolved gases. Furthermore, throughout the OER reaction, the electrocatalyst cell employed in our experiment was hermetically sealed, thus minimizing the exposure of the KOH solution to atmospheric gases. Consequently, the presence of dissolved CO_2 and resulted carbonates in the KOH solution in our study is expected to be negligible.

In nickel foam electrode systems, particularly when transition metal sulfides are employed as catalysts for OER, the intensity of the Ni^{2+}/Ni^{3+} redox peak is significantly higher compared to using glassy carbon electrodes. As a result, in practical applications, the LSV curve after the Ni^{2+}/Ni^{3+} peak does not fully return to baseline, making it an accepted approach to select a higher current density beyond the Ni^{2+}/Ni^{3+} peak as the reference point to compare the catalyst performance.

In the literature, researchers commonly choose higher current densities, such as 50, 100, or 200 mA cm^{-2}, to report the OER performance of the samples, when a nickel foam electrode is used, to take into account this phenomenon [23,24,25,26,27,28,29,30,31,32,33]. In all of these reports, LSV curves after the Ni^{2+}/Ni^{3+} peak did not fully return to 0 mA cm^{-2}, indicating that the onset overpotential of the OER reaction occurs at higher current densities. Figure 5 clearly illustrates that the summit point of the Ni^{2+}/Ni^{3+} peak is below 50 mA cm^{-2}. Therefore, we have selected 50 mA cm^{-2} as the reference current density to compare the performance of the samples.

In order to select the optimal region for calculating the Tafel slope, we thoroughly reviewed relevant papers that investigated the same material and focused on the identical current density range. These studies also utilized the nonlinear region of the Tafel plot to extract the Tafel slopes accurately [33,28,34,35,36,37,38].

Section S7.2 The role of iron and selenium in improving the oxygen evolution reaction

There are several reasons behind the improvement in charge transfer when introducing iron into the structure of an electrocatalyst:

The role of iron:

Iron can promote adsorption and activation of reactants during OER reaction leading to enhancement of OER reaction [39].

Iron incorporation can improve the electrical conductivity of the electrocatalysts, leading to better charge transfer during the OER. This helps to reduce energy losses and improve overall efficiency [40]. It has been reported that the presence of Fe incorporation or doping can enhance the electrical conductivity of nickel-based catalysts and triggers a partial-charge-transfer activation effect on Ni based material, consequently leading to an enhanced OER activity

Fe doping can induce changes in the surface morphology in nickel and cobalt based electrocatalysts, resulting in an increase in the number of electroactive sites and a reduction in charge transfer resistance [40].

The incorporation or doping of iron can result in the creation of new phases or the modification of the existing crystal lattice within the structure of electrocatalysts. This structural alteration can effectively promote faster charge transfer kinetics and subsequently contribute to a reduction in charge transfer resistance [41].

The role of Se:

The incorporation of larger Se atoms in transition metal sulfides leads to a modification in the lattice spacing. This alteration facilitates electron conduction at the solution interface which can reduce charge transfer resistance, ultimately enhancing the catalytic performance [42].

The doping of selenium in the structure of metal sulfides has the potential to modify the catalyst surface and create additional active sites. This modification can significantly enhance the adsorption and activation of reactant species, resulting in a decrease in charge transfer resistance and improving OER performance [43].

Selenium incorporation in metal sulfides can lead to the formation of a SeO_2 oxidation layer on the catalyst's surface, which is believed to enhance the stability and durability of the electrocatalyst during the oxygen evolution reaction (OER) [44].

Based on our experimental observations and a review of the literature, we have reached a conclusive finding that the incorporation of both iron and selenium in transition metal sulfides plays a crucial role in enhancing the performance of the oxygen evolution reaction (OER) in $Fe_{0.5}Ni_{1.0}Co_{2.0}(S_{0.57}Se_{0.25}O_{0.18})_4$. The experimental data and existing research collectively support the notion that the presence of both iron and selenium yields significant improvements in OER efficiency and catalytic activity.

Section S8 Theoretical orthogonal experiment design

Section S8.1 Direct synthesis without precursor

- Suggested orthogonal experiment design for producing iron-containing nickel cobalt sulfides.

The orthogonal experiment includes the following factors and levels:

Factor 1: $(NH_4)_2Fe(SO_4)_2·6H_2O$ with 6 levels: 0.025 mmol, 0.05 mmol, 0.075 mmol, 0.1 mmol, 0.15 mmol, 0.2 mmol; Factor 2: $NiCl_2·6H_2O$ with 1 level: 2 mmol; Factor 3: $CoCl_2·6H_2O$ with 1 level: 4 mmol; Factor 4: $Na_2S·9H_2O$ with 3 levels: 1.5 mmol, 3 mmol, 6 mmol.

Table S10. Factors and levels in the orthogonal experiment for synthesis iron containing nickel cobalt sulfide samples.[a)]

Run	Factor 1 $(NH_4)_2Fe(SO_4)_2·6H_2O$ (mmol)	Factor 2 $NiCl_2·6H_2O$ (mmol)	Factor 3 $CoCl_2·6H_2O$ (mmol)	Factor 4 $Na_2S·9H_2O$ (mmol)
1	0.025	2	4	1.5
2	0.050	2	4	3.0
3	0.075	2	4	6.0
4	0.100	2	4	1.5
5	0.150	2	4	3.0
6	0.200	2	4	6.0
7	0.025	2	4	1.5
8	0.050	2	4	3.0
9	0.075	2	4	6.0
10	0.100	2	4	1.5
11	0.150	2	4	3.0
12	0.200	2	4	6.0
13	0.025	2	4	1.5
14	0.050	2	4	3.0
15	0.075	2	4	6.0
16	0.100	2	4	1.5
17	0.150	2	4	3.0
18	0.200	2	4	6.0

[a)] The temperature (120 °C), volume of solvent (30 mL ultrapure water) and time of reaction (6 h) is kept constant. We have chosen to incorporate 1 level for both factors " $NiCl_2·6H_2O$ " and " $CoCl_2·6H_2O$ " in order to simplify the experiment and ensure a more uniform product with similar characterization of $NiCo_2Se_4$.

- Suggested orthogonal experiment design for producing iron-containing nickel cobalt selenides.

The orthogonal experiment includes the following factors and levels:

Factor 1: $(NH_4)_2Fe(SO_4)_2 \cdot 6H_2O$ with 6 levels: 0.025 mmol, 0.05 mmol, 0.075 mmol, 0.1 mmol, 0.15 mmol, 0.2 mmol; Factor 2: $NiCl_2 \cdot 6H_2O$ with 1 level: 2 mmol; Factor 3: $CoCl_2 \cdot 6H_2O$ with 1 level: 4 mmol; Factor 4: SeO_2 with 3 levels: 1.5 mmol, 3 mmol, 6 mmol.

Table S11. Factors and levels in the orthogonal experiment for synthesis iron containing nickel cobalt selenide samples.[a)]

Run	Factor 1 $(NH_4)_2Fe(SO_4)_2 \cdot 6H_2O$ (mmol)	Factor 2 $NiCl_2 \cdot 6H_2O$ (mmol)	Factor 3 $CoCl_2 \cdot 6H_2O$ (mmol)	Factor 4 SeO_2 (mmol)
1	0.025	2	4	1.5
2	0.050	2	4	3.0
3	0.075	2	4	6.0
4	0.100	2	4	1.5
5	0.150	2	4	3.0
6	0.200	2	4	6.0
7	0.025	2	4	1.5
8	0.050	2	4	3.0
9	0.075	2	4	6.0
10	0.100	2	4	1.5
11	0.150	2	4	3.0
12	0.200	2	4	6.0
13	0.025	2	4	1.5
14	0.050	2	4	3.0
15	0.075	2	4	6.0
16	0.100	2	4	1.5
17	0.150	2	4	3.0
18	0.200	2	4	6.0

[a)] The temperature (160 °C), volume of solvent (30 mL ultrapure water) and time of reaction (12 h) is kept constant. We have chosen to incorporate 1 level for both factors " $NiCl_2 \cdot 6H_2O$ " and " $CoCl_2 \cdot 6H_2O$ " in order to simplify the experiment and ensure a more uniform product with similar characterization of $NiCo_2S_4$.

- Suggested orthogonal experiment design for producing iron-containing nickel cobalt sulfoselenides

The orthogonal experiment includes the following factors and levels:

Factor 1: $(NH_4)_2Fe(SO_4)_2·6H_2O$ with 4 levels: 0.025 mmol, 0.05 mmol, 0.075 mmol, and 0.1 mmol; Factor 2: $NiCl_2·6H_2O$ with 1 level: 2 mmol; Factor 3: $CoCl_2·6H_2O$ with 1 level: 4 mmol; Factor 4: $Na_2S·9H_2O$ with 4 levels: 1.5 mmol, 3 mmol, 6 mmol, and 9 mmol; Factor 5: SeO_2 with 5 levels: 0.3 mmol, 0.6 mmol, 0.9 mmol, and 1.2 mmol.

Table S12. Factors and levels in the orthogonal experiment for synthesis iron containing nickel cobalt sulfoselenide samples.[a)]

Run	Factor 1 $(NH_4)_2Fe(SO_4)_2.6H_2O$ (mmol)	Factor 2 $NiCl_2.6H_2O$ (mmol)	Factor 3 $CoCl_2.6H_2O$ (mmol)	Factor 4 $Na_2S.9H_2O$ (mmol)	Factor 5 SeO_2 (mmol)
1	0.025	2	4	1.5	0.30
2	0.050	2	4	3.00	0.60
3	0.075	2	4	6.00	0.90
4	0.100	2	4	9.00	1.20
5	0.025	2	4	1.50	0.60
6	0.050	2	4	3.00	0.90
7	0.075	2	4	6.00	1.20
8	0.100	2	4	9.00	0.30
9	0.025	2	4	3.00	1.20
10	0.050	2	4	6.00	0.30
11	0.075	2	4	9.00	0.60
12	0.100	2	4	1.50	0.90
13	0.025	2	4	6.00	0.90
14	0.050	2	4	9.00	1.20
15	0.075	2	4	1.50	0.30
16	0.100	2	4	3.00	0.60
17	0.025	2	4	9.00	0.60
18	0.050	2	4	1.50	0.90

[a)] The temperature (160 °C), volume of solvent (30 mL ultrapure water) and time of reaction (12 h), kept constant. We have chosen to incorporate 1 level for both factors " $NiCl_2·6H_2O$ " and " $CoCl_2·6H_2O$ " in order to simplify the experiment and ensure a more uniform product with similar characterization of $NiCo_2S_4$.

Section S8.2 Two-step synthesis involves the production of precursors, followed by sulfidation, selenization, and sulfoselenization.

Orthogonal experiment design for iron containing nickel cobalt precursors synthesis:

The orthogonal experiment includes the following factors and levels: Factor 1: $(NH_4)_2Fe(SO_4)_2{\cdot}6H_2O$ with 6 levels: 0.025 mmol, 0.05 mmol, 0.075 mmol, 0.1 mmol, 0.15 mmol; Factor 2: $NiCl_2{\cdot}6H_2O$ with 1 level: 2 mmol; Factor 3: $CoCl_2{\cdot}6H_2O$ with 1 level: 4 mmol; Factor 4: Urea with 1 levels: 19.5 mmol.

Table S13. Factors and levels in the orthogonal experiment for synthesis iron containing nickel cobalt precursors.

Run	Factor 1 $(NH_4)_2Fe(SO_4)_2{\cdot}6H_2O$ (mmol)	Factor 2 $NiCl_2{\cdot}6H_2O$ (mmol)	Factor 3 $CoCl_2{\cdot}6H_2O$ (mmol)	Factor 4 Urea (mmol)
1	0.025	2	4	19.5
2	0.050	2	4	19.5
3	0.075	2	4	19.5
4	0.100	2	4	19.5
5	0.150	2	4	19.5

[a] The temperature (120 °C), volume of solvent (30 mL ultrapure water) and time of reaction (6 h), kept constant. We have chosen to incorporate 1 level for both factors " $NiCl_2{\cdot}6H_2O$ " and " $CoCl_2{\cdot}6H_2O$ " in order to simplify the experiment and ensure a more uniform product with similar characterization of $NiCo_2S_4$.

Orthogonal experiment design for iron containing nickel cobalt sulfides:

Orthogonal experiment includes the following factors and levels: Factor 1: precursor type with 5 levels; Factor 2: $Na_2S{\cdot}9H_2O$ with 3 levels 1.5 mmol, 3 mmol, 6 mmol.

Table S14. Factors and levels in the orthogonal experiment for synthesis iron containing nickel cobalt sulfidels.

Run	Factor 1 precursor type	Factor 2 $Na_2S.9H_2O$ (mmol)
1	1	1.5
2	2	1.5
3	3	1.5
4	4	1.5
5	5	1.5
6	1	3.0
7	2	3.0
8	3	3.0
9	4	3.0
10	5	3.0
11	1	6.0
12	2	6.0
13	3	6.0
14	4	6.0
15	5	6.0

[a] The temperature (160 °C), volume of solvent (30 mL ultrapure water) and time of reaction (12 h), and amount of precursors kept constant. We have chosen to incorporate 1 level for both factors " $NiCl_2{\cdot}6H_2O$ " and " $CoCl_2{\cdot}6H_2O$ " in order to simplify the experiment and ensure a more uniform product with similar characterization of $NiCo_2S_4$.

Orthogonal experiment design for iron containing nickel cobalt selenides:

Orthogonal experiment includes the following factors and levels: Factor 1: precursor type with 5 levels, Factor 2: $Na_2S{\cdot}9H_2O$ with 3 levels 1.5 mmol, 3 mmol, 6 mmol.

Table S15. Factors and levels in the orthogonal experiment for synthesis iron containing nickel cobalt selenides.

Run	Factor 1 precursor type	Factor 2 SeO_2 (mmol)
1	1	1.5
2	2	1.5
3	3	1.5
4	4	1.5
5	5	1.5
6	1	3.0
7	2	3.0
8	3	3.0
9	4	3.0
10	5	3.0
11	1	6.0
12	2	6.0
13	3	6.0
14	4	6.0
15	5	6.0

[a] The temperature (160 °C), volume of solvent (30 mL ultrapure water) and time of reaction (12 h), and amount of precursors kept constant. We have chosen to incorporate 1 level for both factors " $NiCl_2 \cdot 6H_2O$ " and " $CoCl_2 \cdot 6H_2O$ " in order to simplify the experiment and ensure a more uniform product with similar characterization of $NiCo_2S_4$.

Orthogonal experiment design for iron containing nickel cobalt sulfoselenides

Orthogonal experiment includes the following factors and levels: Factor 1: precursor type with 1 level; Factor 2: $Na_2S \cdot 9H_2O$ with 3 levels 1.5 mmol, 3 mmol, 6 mmol. Factor 3: SeO_2 with 0.3 levels 0.6 mmol, 0.9 mmol.

Table S16. Factors and levels in the orthogonal experiment for synthesis iron containing nickel cobalt sulfoselenides.

Run	Factor 1: precursor type	Factor2: $Na_2S.9H_2O$	Factor 3: SeO_2
1	4	1.5	0.3
2	4	1.5	0.6
3	4	1.5	0.9
4	4	3.0	0.3
5	4	3.0	0.6
6	4	3.0	0.9
7	4	6.0	0.3
8	4	6.0	0.6
9	4	6.0	0.9

[a] The temperature (160 °C), volume of solvent (30 mL ultrapure water) and time of reaction (12 h), and amount of precursor and type kept constant (i.e produced from precursor type 4) as its sulfide exhibited the best performance compared to the other sulfides. Therefore, precursor type 4 was selected for the preparation of sulfoselenides). We have chosen to incorporate 1 level for both factors " $NiCl_2 \cdot 6H_2O$ " and " $CoCl_2 \cdot 6H_2O$ " in order to simplify the experiment and ensure a more uniform product with similar characterization of $NiCo_2S_4$.

References

---

1. Mohamed, S.G.; Hussain, I.; Shim, J.-J. One-Step Synthesis of Hollow C-$NiCo_2S_4$ Nanostructures for High-Performance Supercapacitor Electrodes. *Nanoscale* **2018**, *10*, 6620–6628, doi:10.1039/C7NR07338K.

2. Pu, J.; Cui, F.; Chu, S.; Wang, T.; Sheng, E.; Wang, Z. Preparation and Electrochemical Characterization of Hollow Hexagonal $NiCo_2S_4$ Nanoplates as Pseudocapacitor Materials. *ACS Sustain. Chem. Eng.* **2014**, *2*, 809–815, doi:10.1021/sc400472z.

3. Zou, J.; Xie, D.; Zhao, F.; Wu, H.; Niu, Y.; Li, Z.; Zou, Q.; Deng, F.; Zhang, Q.; Zeng, X. Microwave Rapid Synthesis of Nickel Cobalt Sulfides/CNTs Composites as Superior Cycling Ability Electrode Materials for Supercapacitors. *J. Mater. Sci.* **2021**, *56*, 1561–1576, doi:10.1007/s10853-020-05257-3.

4. Bao, Y.; Zhang, W.; Yun, T.; Dai, J.; Li, G.; Mao, W.; Guan, M.; Zhuang, Y. The Application of Transition Metal Sulfide Ni_3S_4/CNFs in Rechargeable Ni–Zn Batteries. *New J. Chem.* **2021**, *45*, 22491–22496, doi:10.1039/D1NJ03768D.

5. Min, K.; Yoo, R.; Kim, S.; Kim, H.; Shim, S.E.; Lim, D.; Baeck, S.-H. Facile Synthesis of P-Doped NiCo2S4 Nanoneedles Supported on Ni Foam as Highly Efficient Electrocatalysts for Alkaline Oxygen Evolution Reaction. *Electrochim. Acta* **2021**, *396*, 139236, doi:10.1016/j.electacta.2021.139236.

6. Kung, C.-W.; Chen, H.-W.; Lin, C.-Y.; Huang, K.-C.; Vittal, R.; Ho, K.-C. CoS Acicular Nanorod Arrays for the Counter Electrode of an Efficient Dye-Sensitized Solar Cell. *ACS Nano* **2012**, *6*, 7016–7025, doi:10.1021/nn302063s.

7. Khani, H.; Wipf, D.O. Iron Oxide Nanosheets and Pulse-Electrodeposited Ni–Co–S Nanoflake Arrays for High-Performance Charge Storage. *ACS Appl. Mater. Interfaces* **2017**, *9*, 6967–6978, doi:10.1021/acsami.6b11498.

8. Matoba, M.; Anzai, S.; Fujimori, A. Thermal Expansion, Thermoelectric Power, and XPS Study of the Nonmetal-Metal Transition in $Ni_{1-x}S_{1-y}Se_y$. *J. Phys. Soc. Jpn.* **1991**, *60*, 4230–4244, doi:10.1143/JPSJ.60.4230.

9. Shi, Z.-T.; Kang, W.; Xu, J.; Sun, L.-L.; Wu, C.; Wang, L.; Yu, Y.-Q.; Yu, D.Y.W.; Zhang, W.; Lee, C.-S. In Situ Carbon-Doped $Mo(Se_{0.85}S_{0.15})_2$ Hierarchical Nanotubes as Stable Anodes for High-Performance Sodium-Ion Batteries. *Small* **2015**, *11*, 5667–5674, doi:10.1002/smll.201501360.

10. Danilson, M.; Altosaar, M.; Kauk, M.; Katerski, A.; Krustok, J.; Raudoja, J. XPS Study of CZTSSe Monograin Powders. *Thin Solid Films* **2011**, *519*, 7407–7411, doi:10.1016/j.tsf.2010.12.165.

11. Zou, X.; Wu, Y.; Liu, Y.; Liu, D.; Li, W.; Gu, L.; Liu, H.; Wang, P.; Sun, L.; Zhang, Y. In Situ Generation of Bifunctional, Efficient Fe-Based Catalysts from Mackinawite Iron Sulfide for Water Splitting. *Chem* **2018**, *4*, 1139–1152, doi:10.1016/j.chempr.2018.02.023.

12. Sahoo, M.K.; Samantara, A.K.; Behera, J.N. In Situ Transformed Cobalt Metal–Organic Framework Electrocatalysts for the Electrochemical Oxygen Evolution Reaction. *Inorg. Chem.* **2020**, *59*, 12252–12262, doi:10.1021/acs.inorgchem.0c01300.

13. Biesinger, M.C.; Payne, B.P.; Grosvenor, A.P.; Lau, L.W.M.; Gerson, A.R.; Smart, R.St.C. Resolving Surface Chemical States in XPS Analysis of First Row Transition Metals, Oxides and Hydroxides: Cr, Mn, Fe, Co and Ni. *Appl. Surf. Sci.* **2011**, *257*, 2717–2730, doi:10.1016/j.apsusc.2010.10.051.

14. Beamson, G.; Briggs, D. High Resolution XPS of Organic Polymers: The Scienta ESCA300 Database Wiley: New York, NY, 1992.

---

15. Shen, Y.; Zhu, Y.; Sunarso, J.; Guan, D.; Liu, B.; Liu, H.; Zhou, W.; Shao, Z. New Phosphorus-Doped Perovskite Oxide as an Oxygen Reduction Reaction Electrocatalyst in an Alkaline Solution. *Chem. Eur. J*. **2018**,24,6950–6957, https://doi.org/10.1002/chem.2017056

16. Yang, H.; Li, F.; Zhan, S. Intramolecular hydroxyl nucleophilic attack pathway by a polymeric water oxidation catalyst with single cobalt sites. *Nat. Catal.* **2022,** *5*, 414–429, https://doi.org/10.1038/s41929-022-00783-6.

17. Feng, C.; Wang, F.; Liu, Z.A. self-healing catalyst for electrocatalytic and photoelectrochemical oxygen evolution in highly alkaline conditions. *Nat. Commun*. **2021**, 12, 5980, https://doi.org/10.1038/s41467-021-26281-0.

18. Garcés-Pineda, F.A.; Blasco-Ahicart, M.; Nieto-Castro, D. Direct magnetic enhancement of electrocatalytic water oxidation in alkaline media. *Nat. Energy* **2019**, 4, 519–525, https://doi.org/10.1038/s41560-019-0404-4.

19. Zhang, S.L.; Guan, B.Y.; Lu, X.F.; Xi, S.; Du, Y.; Lou, X.W.D. Metal Atom-Doped Co_3O_4 Hierarchical Nanoplates for Electrocatalytic Oxygen Evolution. *Adv. Mater*. **2020**, 32, 2002235, https://doi.org/10.1002/adma.202002235.

20. Sundivich, J.; May, K.J.; Gasteiger, H.A.; Goodenough, G.B.; Horn, Y.S. A Perovskite Oxide Optimized for Oxygen Evolution Catalysis from Molecular Orbital Principles. *Science.* **2011**, *334*, 1383-1385, DOI: 10.1126/science.1212858.

21. Shan, Z.; Archana, P. S.; Shen, G.; Gupta, A.; Bakker, M.G.; Pan, S. NanoCOT: Low-Cost Nanostructured Electrode Containing Carbon, Oxygen, and Titanium for Efficient Oxygen Evolution Reaction. *J. Am. Chem. Soc*. **2015**, *137*, 11996–12005, https://doi.org/10.1021/jacs.5b05367

22. Lee, S.; Ji, L.; De Palma, A.C. Scalable highly stable Si-based metal-insulator-semiconductor photoanodes for water oxidation fabricated using thin-film reactions and electrodeposition. *Nat. Commun.* **2021**, *12*, 3982, https://doi.org/10.1038/s41467-021-24229-y.

23. Chen, R.; Zhang, Z.; Wang, Z.; Wu, W.; Du, S.; Zhu, W.; Lv, H.; Cheng, N. Constructing Air-Stable and Reconstruction-Inhibited Transition Metal Sulfide Catalysts via Tailoring Electron-Deficient Distribution for Water Oxidation. *ACS Catal*. **2022**, *12*, 13234–13246, https://doi.org/10.1021/acscatal.2c03338.

24 Shit, S.; Chhetri, S.; Jang, W.; Murmu, N. C.; Koo, H.; Samanta, P.; Kuila, T. Cobalt Sulfide/Nickel Sulfide Heterostructure Directly Grown on Nickel Foam: An Efficient and Durable Electrocatalyst for Overall Water Splitting Application. *ACS Appl. Mater. Interfaces*. **2018**, *10*, 27712–27722, https://doi.org/10.1021/acsami.8b04223.

25. Zhang, K.; Min, X.; Zhang, T.; Si, M.; Jiang, J.; Chai, L.; Shi, Y. Biodeposited Nano-CdS Drives the In Situ Growth of Highly Dispersed Sulfide Nanoparticles during Pyrolysis for Enhanced Oxygen Evolution Reaction. *ACS Appl. Mater. Interfaces* **2020**, *12*, 49, 54553–54562, https://doi.org/10.1021/acsami.0c14388.

26. Tiwari, A.; Yoon, Y.; Novak, T.G.; An, K.S.; Jeon, S. Continuous Network of Phase-Tuned Nickel Sulfide Nanostructures for Electrocatalytic Water Splitting. *ACS Appl. Nano Mater*. **2019,** *2*, 5061–5070, https://doi.org/10.1021/acsanm.9b00985.

27. Ji, Q.; Kong, Y.; Tan, H.; Duan, H.; Li, N.; Tang, B.; Wang, Y.; Feng, S.; Lv, L.; Wang, C.; Hu, F.; Zhang, W.; Cai, L.; Yan, W. Operando Identification of Active Species and Intermediates on Sulfide Interfaced by Fe3O4 for Ultrastable Alkaline Oxygen Evolution at Large Current Density. *ACS Catal.* **2022**, *12*, 4318–4326, https://doi.org/10.1021/acscatal.2c01090.

---

28. Xie, M.; Ai, S.; Yang, J.; Yang, Y.; Chen, Y.; Jin, Y. In-Situ Generation of Oxide Nanowire Arrays from AgCuZn Alloy Sulfide with Enhanced Electrochemical Oxygen-Evolving Performance. *ACS Appl. Mater. Interfaces* **2015**, *7*, 17112–17121, https://doi.org/10.1021/acsami.5b03805.

29. Shit, S.; Bolar, S.; Murmu, N.C.; Kuila, T. Design Principle of Monoclinic NiCo2Se4 and Co3Se4 Nanoparticles with Opposing Intrinsic and Geometric Electrocatalytic Activity toward the OER. *ACS Sustainable Chem. Eng.* **2019**, *7*, 18015–18026, https://doi.org/10.1021/acs.inorgchem.1c00649.

30. Swathi, S.; Yuvakkumar, R.; Ravi, G.; Thambidurai, M.; Nguyen, H.D.; Velauthapillai, D. Ternary Copper Iron Sulfide Microflowers Anchored on Reduced Graphene Oxide for Water Splitting. *ACS Appl. Nano Mater.* **2023**, *6*, 6538–6549, https://doi.org/10.1021/acsanm.3c00056.

31. Waqas, M.; Younis, J.; Awais, M.; Nazar, N.; Hussain, S.; Murtaza, S.; Yasmin, N.; Ashiq, M.N.; Mirza, M.; Safdar, M. CrS2-Modulated Enhanced Catalytic Properties of CdS/MoS_2 Heterostructures Toward Photodegradation and Electrochemical OER Kinetics. *Energy Fuels*. **2022**, *36*, 8391–8401, https://doi.org/10.1021/acs.energyfuels.2c01821.

32. Jayaramulu, K.; Masa, J.; Tomanec, O.; Peeters, D.; Ranc, V.; Schneemann, A.; Zboril, R.; Schuhmann, W.; Fischer, R.A. Nanoporous Nitrogen-Doped Graphene Oxide/Nickel Sulfide Composite Sheets Derived from a Metal-Organic Framework as an Efficient Electrocatalyst for Hydrogen and Oxygen Evolution. *Adv. Funct. Mater*. **2017**, *27*, 1700451, https://doi.org/10.1002/adfm.201700451.

33. Ganesan, P.; Sivananthama, A.; Shanmugam, S. Inexpensive electrochemical synthesis of nickel iron sulphides on nickel foam: super active and ultra-durable electrocatalysts for alkaline electrolyte membrane water electrolysis. *J. Mater. Chem. A* **2016**, *4*, 16394-16402, https://doi.org/10.1039/C6TA04499A .

34. Gervas, C.; Khan, M. D.; Zhang, C.; Zhao, C.; Gupta, R. K.; Carleschi, E.; Doyle, B. P.; Revaprasadu, N. Effect of cationic disorder on the energy generation and energy storage applications of $Ni_xCo_{3-x}S_4$ thiospinel. *RSC Adv*. **2018**, *8*, 24049-24058, https://doi.org/10.1039/C8RA03522A.

35. Wu, H.; Lu, Q.; Zhang, J. Thermal Shock-Activated Spontaneous Growing of Nanosheets for Overall Water Splitting. *Nano-Micro Lett*. **2020** *12*, 162 https://doi.org/10.1007/s40820-020-00505-2.

36. Wang, X.; Yang, Y.; Wang, R.; Li, L.; Zhao, X.; Zhang, W. Porous Ni_3S_2–Co_9S_8 Carbon Aerogels Derived from Carrageenan/NiCo-MOF Hydrogels as an Efficient Electrocatalyst for Oxygen Evolution in Rechargeable Zn–Air Batteries. *Langmuir* **2022**, *38*, 7280–7289, https://doi.org/10.1021/acs.langmuir.2c00805.

37. Li, M.; Xu, Z.; Li, Y.; Wang, J.; Zhong, Q. In situ fabrication of cobalt/nickel sulfides nano hybrid based on various sulfur sources as highly efficient bifunctional electrocatalysts for overall water splitting. *Nano Select* **2022**, *3*, 147–156, https://doi.org/10.1002/nano.202100155.

38. Guo, M.-L.; Wu, Z.-Yu.; Zhang, M.-M.; Huang, Z.-J.; Zhang, K.-X.; Wang, B.-R.; Tu, J.-C. Coupling interface constructions of FeOOH/NiCo2S4 by microwave-assisted method for efficient oxygen evolution reaction. *Rare Met.* **2023**, *42*, 1847–1857, https://doi.org/10.1007/s12598-022-02239-z.

39. Anantharaj, S.; Kundu, S.; Noda, S. The Fe Effect": A review unveiling the critical roles of Fe in enhancing OER activity of Ni and Co based catalysts. *Nano Energy* **2021**, *80*, 105514, https://doi.org/10.1016/j.nanoen.2020.105514

40. Jin, C.; Hou, M.; Li, Liu, X. D.; Qu, D.; Dong, Y.; Xie, Z.; Zhang, C. Rapid electrodeposition of Fe-doped nickel selenides on Ni foam as a bi-functional electrocatalyst for water splitting in alkaline solution. *J. Electroanal*. **2022**, *906*, 116014, https://doi.org/10.1016/j.jelechem.2022.116014

41. Guo, Y.; Zhou, X.; Tang, J.; Tanaka, S.; Kaneti, Y. V.; Na, J.; Jiang, B.; Yamauchi, Y.; Bando, Y.; Sugahara, Y. Multiscale structural optimization: Highly efficient hollow iron-doped metal sulfide

---

heterostructures as bifunctional electrocatalysts for water splitting. *Nano Energy* **2020**, *75*, 104913, https://doi.org/10.1016/j.nanoen.2020.104913.

42. Shi, Z.; Qi, X.; Zhang, Z.; Song, Y.; J. Zhang, J.; Guo, C.; Zhu, Z. Porous Cobalt Sulfide Selenium Nanorods for Electrochemical Hydrogen Evolution. *ACS Omega* **2021**, *6*, 23300–23310, https://doi.org/10.1021/acsomega.1c03019

43. Wang, C-Y.; Dong, W.-D.; Zhou, M.-R.; Wang, L.; Hu, Z-Y.; Chen, L.; Li, Y.; Su, B.-L. Gradient selenium-doping regulating interfacial charge transfer in zinc sulfide/carbon anode for stable lithium storage. *J. Colloid Interface Sci*., **2022**, *619*, 42-50, https://doi.org/10.1016/j.jcis.2022.03.085.

44. Shang, X.; Chen, W.; Jiang, Z.-J.; Song, C.; Jiang, Z. In Situ Growth of SeO_x Films on the Surface of Ni–Fe–Selenide Nanosheets as Highly Active and Stable Electrocatalysts for the Oxygen Evolution Reaction*. Mater. Adv.* **2022**, *3*, 2546–2557, https://doi.org/10.1039/D1MA01208H.

3.2 Bimetallic CPM-37 (Ni, Fe) precatalyst for electrochemical oxygen evolution reaction in aqueous alkaline medium

Soheil Abdpour, Marcus N.A. Fetzer, István Boldog, Robert Oestreich, Thi Hai Yen Beglaua and Christoph Janiak

J. Mater. Chem. A, **2023**, submitted.

Mixed metal nickel-iron materials have garnered significant attention in the realm of electrocatalysis due to their remarkable performance and cost-effectiveness in the oxygen evolution reaction (OER). This reaction is pivotal in energy conversion technologies, including fuel cells and electrolyzers. In the pursuit of enhancing OER catalysis, the synthesis of bimetallic CPM-37(Ni,Fe) materials with varying iron content (Ni/Fe ~ 2, 1, 0.5, denoted as CPM-37(Ni_2Fe), CPM-37(NiFe), and CPM-37($NiFe_2$)) has been undertaken for the first time, positioning these materials as promising precursors for OER electrode materials.

The synthesized bimetallic CPM-37(Ni,Fe) materials exhibit a considerable increase in specific surface area (BET), with values of 2039, 1955, and 2378 $m^2\,g^{-1}$ for CPM-37(Ni_2Fe), CPM-37(NiFe), and CPM-37($NiFe_2$), respectively. In stark contrast, the monometallic CPM-37(Ni) and CPM-37(Fe) materials display considerably lower specific surface areas, with values of only 87 and 368 $m^2\,g^{-1}$, respectively. This notable difference underscores the unique characteristics of the mixed metal compositions.

The resulting mixed-phase nickel and iron hydroxide/oxides derived from CPM-37(Ni,Fe) during OER, primarily comprising α-$Ni(OH)_2$, γ-NiO(OH), and γ-FeO(OH) phases, exhibit superior OER performance. Notably, derived materials from CPM-37(Ni_2Fe) with a Ni/Fe ratio of approximately 2 stands out as a superior catalyst, boasting a minimal overpotential of 290 mV at 50 mA cm^{-2}, a low Tafel slope of 39 mV dec^{-1}, and excellent electrochemical performance stability, surpassing even the benchmark catalyst RuO_2 after 20 hours of chronopotentiometry at 50 mA cm^{-2}. These findings underline the potential of bimetallic CPM-37(Ni,Fe) materials as highly efficient precatalysts for the OER.

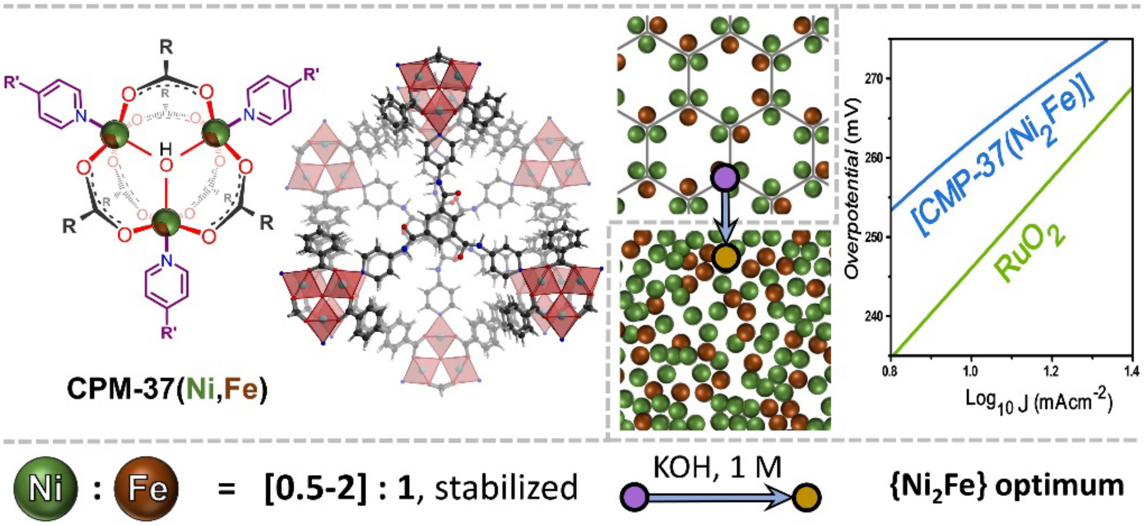

Author`s contribution to the publication:

- Concept and fabrication process.
- Synthesize all materials, encompassing all CPM-37 samples.
- Characterization of the materials (except EDX-SEM)
- Illustration of all figures, charts, and tables (except for the MOFs visualization, conducted by Dr. Istvan Boldog).
- Assessment of all findings and the initial composition of the manuscript's preliminary draft.
- Revising the manuscript in response to the reviewer's feedback.
- The initial manuscript and its subsequent revised version were rectified and formally submitted to the international journal "Journal of Material Chemistry A" under the auspices of Prof. Dr. Christoph Janiak.

Bimetallic CPM-37(Ni,Fe) metal-organic framework: enhanced porosity, stability and tunable composition†

igureReceived 00th January 20xx,
Accepted 00th January 20xx

DOI: 10.1039/x0xx00000x

Soheil Abdpour, Marcus N. A. Fetzer, Robert Oestreich, Thi Hai Yen Beglau, István Boldog* and Christoph Janiak*

A newly synthesized series of bimetallic CPM-37(Ni,Fe) metal-organic frameworks with different iron content (Ni/Fe ≈ 2, 1, 0.5, named CPM-37(Ni_2Fe), CPM-37(NiFe) and CPM-37($NiFe_2$)) demonstrated high N_2-based specific S_{BET} surface areas of 2039, 1955, and 2378 m^2 g^{-1} for CPM-37(Ni_2Fe), CPM-37(NiFe), and CPM-37($NiFe_2$), having much higher values compared to the monometallic CPM-37(Ni) and CPM-37(Fe) with 87 and 368 m^2 g^{-1} only. It is rationalized that the mixed-metal nature of the materials increases the structural robustness due to the better charge balance at the coordination bonded cluster, which opens interesting application-oriented possibilities for mixed-metal CPM-37 and other less-stable MOFs. In this work, the CPM-37-derived α,β-$Ni(OH)_2$, γ-NiO(OH), and, plausibly, γ-FeO(OH) phases obtained via decomposition in the alkaline medium demonstrated a potent electrocatalytic activity in the oxygen evolution reaction (OER). The ratio Ni:Fe ≈ 2 from CPM-37(Ni_2Fe) showed the best OER activity with a small overpotential of 290 mV at 50 mA cm^{-2}, low Tafel slope of 39 mV dec^{-1}, and more stable OER performance compared to RuO_2 after 20 h chronopotentiometry at 50 mA cm^{-2}.

Introduction

Metal-organic frameworks (MOFs) are known for their tuneability stimulating both the fundamental- and the applied research dimensions. The variability of MOFs, which are predominantly crystalline porous cordination polymers (PCPs), are usually, but not exclusively, associated with the tailorability of the organic ligand. The high-surface area, the variable size-, shape-, and nature of the pore surface are excellent prerequisite for applications. such as gas storage and separation, catalysis, as well as energy conversion.[1]

An interesting aspect of MOF-tuneability is the mixed-metal MOF approach towards functional materials,[2,3] with such recent representative reported examples as luminescence-based temperature-sensing in a mixed lanthanide $[(CH_3)_2NH_2][(Eu_x/Tb_{1-x})$(biphenyl-3,3′,5,5′-tetracarboxylate)] complex,[4] benzene oxidation by a mixed-metal MOF-derived CeO_2-Cr_2O_3 catalyst, and CO_2 reduction to MeOH by a MOF-74(Cu, Zn) catalyst,[5] water stability and/or adsorption tuning in UiO-66 and MOF-808(Zr,Ce),[6] MOF-74(Mg, M) (M = Mg,[7] Co, Ni,[8] HKUST-1(Cu, M) M= Ca, Mg, Co, Zn,[9] as well as, proton conductance in MOF-808(Zr,Ce).[10] Noteworthy, an increased stability of mixed-metal MOFs is sometimes emphasized.[2,3] For example Mg-MOF-74 gains water stability by incorporation of Ni^{2+} or Co^{2+}.[7,8] Bimetallic Ce/Zr-UiO-66 and -MOF-808 have higher thermal stability and acid resistance.[6]

In the absolute majority of published cases the metal distribution corresponds to a solid solution, *i.e.* it is governed statistically. However, the non-contiguous coordination clusters, which are often constituting the secondary building units, are potentially well-suited for a defined mixed-metal composition. The latter is equivalent to a uniform distribution of the metals on the nano-level. Electrode materials, which are represented or derived from MOFs, are particularly interesting objects, due to the synergy of uniformly distributed two or more metal ion types. Current research also investigates electrode materials that rely on solid-solution type MOFs, *e.g.* the $[Cd_4CuO(calix[4]resorcinarene)(H_2O)_4] \cdot 4DMF \cdot 5H_2O$ for electrocatalytic oxidation of uric acid,[11] mixed-metal MOF derived CeO_2-Cr_2O_3 oxides for catalytic benzene oxidation,[12] and others, mentioned below.

Our interest in this contribution is also on electrocatalysts for the oxygen-evolution reaction (OER) as a test area for optimization of mixed-metal MOF-based synergy. The focus is highly topical in the context of hydrogen economy, as electrochemical water splitting is practically the only readily available means to generate green hydrogen in large quantities.[13].

During the past decades, nickel-based materials — as a cost-effective alternative to the benchmark iridium and ruthenium oxides (IrO_2 and RuO_2) — including sulfides,[14] oxides,[15] phosphides,[16] selenides,[17] metal oxide/(oxy)hydroxides,[18] received significant attention for developing high-performance anodic electrocatalysts. The potential porosity of the electrode materials alleviates diffusion limitations and increases the apparent surface area, which was proven to be beneficial for

---

Institut für Anorganische Chemie und Strukturchemie, Heinrich-Heine-Universität Düsseldorf, 40204 Düsseldorf, Germany. Email: boldogi@hhu.de, Janiak@hhu.de

† Electronic Supplementary Information (ESI) available: synthesis and ^1H NMR spectrum of TPAMA ligand, additional details regarding the AAS, PXRD, SEM-EDX, TGA and XPS, as well as comparison of the OER performance of different materials. See DOI: 10.1039/x0xx00000x

improving the electrocatalytic performance.[19] Hence, MOFs are among promising candidates for precatalysts of electrode materials.[20]

Interestingly, the decomposition of MOFs during the OER in an alkaline aqueous medium sometimes leads to *in-situ* formed structured (also seemingly hierarchically porous) stable residues, typically represented by metal hydroxides/oxides.[21] In this case, the MOF is regarded as a 'precatalyst', which influences the nature of the catalyst actually formed during the electrochemical process.[22,23] This 'conversion' approach, which does not demand any special additional treatment, such as an energetically demanding pyrolysis, is particularly attractive, even if there is no general reliable way to predict the activity of the catalyst from the exact nature- and treatment method of the precatalyst. Some examples of mixed-metal MOF-derived materials were also reported recently, e.g. the MOF-derived $Ni_xCo_{3-x}O_4$ spinels for enhanced oxygen evolution,[24] or Fe/Co MOF derived electrocatalysts for water splitting.[25,26] It is worth mentioning again that the MOF precursors represents solid solutions with statistical distribution of metals, as discussed above.

In this work, the highly porous CPM-37 MOF platform – which is a permanently porous derivative of the well-known flexible MIL-88 MOF with a 'pore-space-partitioning' trigonal structure ligand –was tested for its stability enhancement upon incorporation of iron as monometallic of CPM-37(Ni) features a not readily understandable low surface area, low crystallinity and stability.[27] A series of bimetallic CPM-37(Ni,Fe) represented by CPM-37(Ni_2Fe), CPM-37(NiFe) and CPM-37($NiFe_2$) with different molar ratios between nickel and iron were synthesized for the first time (Fig. 1a-c; Fig. S16†). The novel mixed-metal CPM-37(Ni,Fe) MOFs with enhanced stability compared to the single-metal analogues due to the stabilization of certain metal ratios in the cluster were evaluated regarding the synergy between iron and nickel for the intended use as an electrode precatalyst (or precursor) material for the OER reaction.

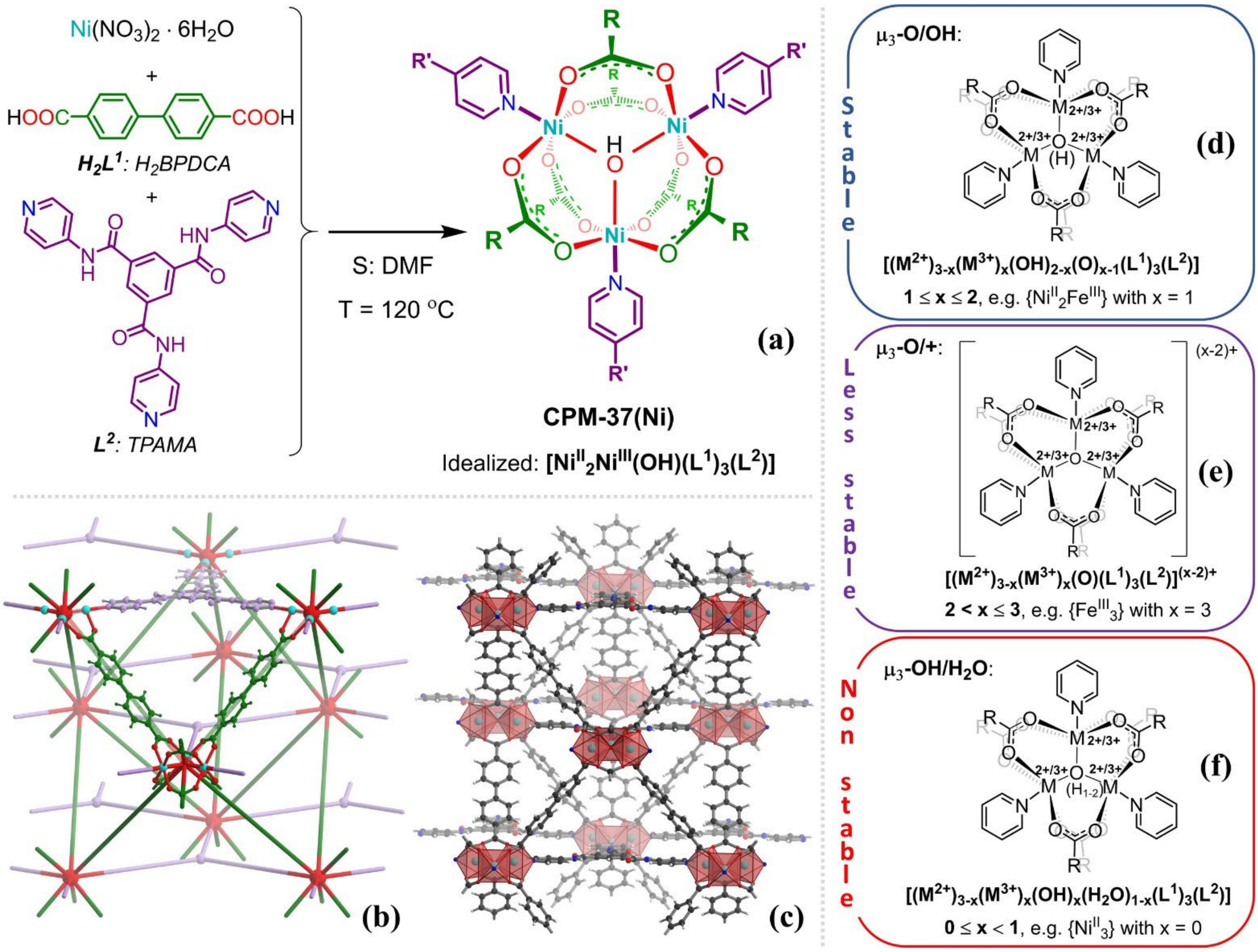

Fig. 1 (a) Synthesis of CPM-37(Ni). (b) Network level representation of the CPM-37(Ni) structure with the green edges representing the MIL-88 sub-topology with the space-partitioning nodes and edges shown in violet. (c) Structure of CPM-37(Ni_2Fe) with polyhedral representation of the Ni atom with the octahedral {NiO_5N} environment. (d) Expected stable mixed-valence metal-based CPM-37 variants with the M^{III} metal content in the range of one to two ions per cluster with the general formula of the material given. (e,f) Conceived instable CPM-37 variants with too much or too scarce amount of M^{III} content compared to the expected optimum.

Experimental

Materials and methods

All chemicals were purchased from commercial vendors and used as received: nickel nitrate hexahydrate, $Ni(NO_3)_2{\cdot}6H_2O$ (98.5% , Merck GmbH); iron sulfate heptahydrate, $FeSO_4{\cdot}7H_2O$ (ACROS GmbH); biphenyl-4,4'-dicarboxylic acid, H_2BPDCA (98%, Abcr GmbH); N,N-dimethylformamide, DMF (p.a., Fisher chemical GmbH); N-methyl-2-pyrrolidone, NMP (p.a., Fisher Scientific); dichloromethane, CH_2Cl_2 (p.a., Fisher Chemical GmbH); potassium hydroxide, KOH (1 mol L^{-1}, Roth), hydrazine monohydrate $N_2H_4{\cdot}H_2O$ (Thermo Scientific), polyvinylidene fluoride, PVDF (CAS: 24937-79-9, Sigma Aldrich); nickel foam, NF (99.5%, average Porosity 95.2%, relative average density 4.8%, thickness 1.6 mm, Recemat BV, Cell Material Engineering), and conductive Carbon Black (type Vulcan XC-72R, Fuelcellstore, product code 590106-1). Ultrapure water was produced using a Sartorius Arium Mini water purifier.

Powder X-ray diffraction (PXRD) analysis was carried out at ambient temperature on a Rigaku Miniflex 600 powder diffractometer (Rigaku, Tokyo, Japan) using Cu $K\alpha_{1,2}$ radiation with average λ = 1.5406 Å (40 kV, 15 mA, 600 W) and a flat silicon low background sample holder in the range of 2θ 5°–100°. Scanning electron microscopy (SEM) with a Jeol JSM-6510LV QSEM Advanced electron microscope equipped with a Bruker Xflash 410 silicon drift detector for energy-dispersive X-ray (EDX) spectroscopy was used to determine the morphology and establish the metal ratios in the samples. Independent quantification of the metal content of the samples was performed using a Perkin-Elmer PinaAcle 900T atomic absorption spectrometer. The Microtrac MRB Belsorp MAX II analyzer was used to record the nitrogen adsorption isotherms of the samples at 77 K. The solvent-exchanged samples were degassed at 60 °C and ~5×10^{-2} mbar for 16 h before the gas adsorption measurements (the details on the solvent exchange with CH_2Cl_2 see in Section 2.3, ESI†). Thermogravimetry analysis (TGA) was conducted using a Netzsch TG 209 F3 Tarsus instrument with a 5 K min^{-1} heating rate using nitrogen as a carrier gas. Fourier transform infrared spectroscopy (FT-IR) measurements were conducted by a Bruker TENSOR 37 IR spectrometer in the range of 4000–400 cm^{-1}. X-ray photoelectron spectroscopy (XPS) data were collected using a ULVAC-PHI Versa Probe II microfocus X-ray photoelectron spectrometer. The spectra were recorded using a polychromatic aluminum Kα X-ray source (1486.8 eV) and referenced to the carbon 1s orbital with a binding energy of 284.8 eV. The XPS spectra were processed using the CasaXPS 2.3.19PR1.0 software.

Electrochemical experiments

The nickel foam (NF), used as a support material for the electrode, was prepared as follows. A flat NF pad was accurately cut in 1×1 cm pieces. The NF pieces were washed with ultrasonic assistance using acetone (10 min, followed by drying in air) and cold (0 °C, intermediary ice-water bath) 2 mol L^{-1} HCl for 5 min to remove the surface nickel oxide (the very slow dissolution of nickel metal in cold HCl was implicitly employed). The treatment was followed by rinsing with ultra-pure water, further ultrasonication in ultra-pure water for 10 min, and finally in absolute EtOH for 10 min. The washed nickel foam pieces were then vacuum-oven dried for 15 min and used freshly as a substrate for the precatalyst-containing slurry.

The electrochemical measurements were carried out at room temperature using a three-electrode cell setup of a Gamry Interface 1010E Potentiostat. A Pt foil- and a reversible hydrogen electrode (RHE) were used as a counter and a reference electrode, respectively. Nickel foam (NF) coated by the investigated electrode material was used as a working electrode (see below for a single exception). The coating was performed using a slurry in N-methyl-2-pyrrolidone (NMP), containing 5 mg precatalyst, 0.6 mg carbon black and 0.6 mg polyvinylidene fluoride (PVDF). The slurry was carefully distributed on one side of the NF piece, and then the precatalyst-coated NF was dried at 60 °C for 12 h in a vacuum oven. Before conducting the electrochemical measurement, the 1 mol L^{-1} KOH electrolyte was freed from oxygen by bubbling an N_2 gas stream through the solution, which was maintained during the measurement. The RuO_2 electrode as a benchmark was prepared using the same method. The Faradaic efficiency (FE) was calculated according to the method described in Section 2.10.1, ESI†.

The linear sweep voltammetry (LSV) at 5 mV s^{-1} was conducted to determine the electrocatalytic performance of the as-prepared samples. Before that, cyclic voltammetry was performed at 100 mV s^{-1} (20 cycles) between 1-1.7 V vs. RHE to stabilize the catalyst performance. All of the LSV polarization curves were corrected by iR compensation.[28] The electrochemical impedance spectroscopy (EIS) was performed to determine the charge transfer resistance of the as-prepared samples in the frequency range of 1-100 kHz at 1.5 V vs. RHE. The stability of selected electrocatalysts was evaluated by chronopotentiometry at a fixed current density of 50 mA cm^{-2} for 20 h.

The tests regarding the conversion of CPM-37 in an aqueous alkaline medium without applying current were done by soaking ~30 mg of a sample in ~ 5 mL of 1 mol L^{-1} aqueous KOH for 20 h at room temperature. The obtained solid residue was separated by centrifugation and washed with 2×5 mL of water.

For post-mortem analysis after OER of the material derived from CPM-37(Ni_2Fe), a special Ni-support was prepared from a standard piece of nickel foam (see above). The foam was compressed using an IR press to form a foil-like support, which was then loaded with the slurry of 5 mg precatalyst and 0.6 mg polyvinylidene fluoride using the standard approach described above, however without the addition of carbon black. This procedure decreased the conductivity as well as the contact between the support surface and the deposited electrode material, and changed the properties of the electrode. However, it allowed an easy separation of the deposited electrode material after the OER, which was the sole goal of the procedure. The specially prepared electrode was subjected to OER in the form of standard 20-hour chronopotentiometry (see above). The converted electrode material was removed by sonication directly in the electrochemical cell and separated by centrifugation in a quantity, sufficient for small-scale PXRD and XPS analyses (this method ensured virtually no admixture of nickel metal and a decreased carbon content).

Synthesis of the N,N',N''-tris-(pyrid-4-yl)-trimesamide (TPAMA) ligand

The TPAMA ligand was synthesized according to the literature procedure[29] with slight modifications (Supporting information, Fig. S1†).

Synthesis of CPM-37(Ni), CPM-37(Fe), and the bimetallic CPM-37(Ni,Fe) materials

CPM-37(Ni), with the idealized framework formula of $[Ni_3(OH)(BPDCA)_3(TPAMA)]$, was synthesized according to the procedure reported by Feng *et al.* with some modifications (Fig. 1a).[27] In a typical experiment, 0.15 mmol (43.6 mg) of $Ni(NO_3)_2 \cdot 6H_2O$, 0.15 mmol (36.33 mg) of H_2BPDCA, and 0.05 mmol (21.92 mg) of TPAMA were dissolved in 12 mL of DMF within a thick wall 20 mL crew cap glass vial. After stirring the mixture for two hours, the sealed glass vial was placed in a preheated oven and kept at 120 °C for three days. The formed pale green hexagonal crystals of the product were isolated by gravity filtration and washed four times with DMF (20 mL per washing). The different iron-containing CPM-37(Ni,Fe) materials and CPM-37(Fe) were synthesized using the same procedure, except employing different molar ratios of nickel and iron, while keeping the combined concentration of the metal ions constant (0.15 mmol in 12 mL of DMF). The bimetallic CPM-37(Ni,Fe) series were synthesized using 0.1 mmol (29.1 mg) $Ni(NO_3)_2 \cdot 6H_2O$ and 0.05 mmol (14 mg) $FeSO_4 \cdot 7H_2O$; 0.075 mmol (21.8 mg) $Ni(NO_3)_2 \cdot 6H_2O$ and 0.075 mmol (20.8 mg) $FeSO_4 \cdot 7H_2O$; 0.05 mmol (14.5 mg) $Ni(NO_3)_2 \cdot 6H_2O$ and 0.1 mmol (27.8 mg) $FeSO_4 \cdot 7H_2O$ for CPM-37(Ni_2Fe), CPM-37(NiFe), and CPM-37($NiFe_2$), respectively. The CPM-37(Fe) was synthesized using 0.15 mmol (47 mg) $FeSO_4 \cdot 7H_2O$. The concentrations (and hence also the molar ratios) of H_2BPDCA and TPAMA were kept the same for all syntheses. The yield of the products was as follows 30 mg for CPM-37(Ni), 60 mg for CPM-37(Ni_2Fe), 65 mg for CPM-37(NiFe), 63 mg CPM-37($NiFe_2$), and 58 mg for CPM-37(Fe).

Results and discussion

Synthesis and characterization of the CPM-37 materials

The synthesis of the MOF materials was carried out under the same low-temperature solvothermal conditions as reported for the single already known representative, the prototypal CPM-37(Ni).[27] The latter was crystallizing as well-formed rods or small blocks, in the latter case with a tendency to adapt the shape of hexagonal platelets, consistent with the reported $P6_3/mmc$ crystallographic symmetry (Fig. S5†). The morphology of the crystals finely depended on the selected conditions; the conditions reported here led mostly to the latter case of the small platelets. The identity of the two morphologies to the published phase was proven either by cell measurements for selected crystals using single crystal XRD and PXRD techniques. The new CPM-37(Ni,Fe) and CPM-37(Fe) were only obtained in a form of microcrystalline powders. All attempts to obtain them in single crystalline form by variation of temperature and solvent, using N,N-diethylformamide and N,N-dimethylacetamide as DMF-analogues, were not successful. It is worth noting the good tuneability of the metal ratio in the mixed-metal CPM-37(Ni,Fe) materials by varying the ratio of the reactant salts. The 2:1, 1:1, and 0.5:1 Ni:Fe reactant molar ratios yielded very similar experimentally verified metal ratios in the products (see the AAS analysis below).

The PXRD patterns of CPM-37(Ni), CPM-37(Fe), and the bimetallic CPM-37(Ni,Fe) compounds are very similar, featuring the first five intensive peaks at 6.4°, 7.8°, 8.5°, 11.5°, and 12.5°. The experimental PXRDs correspond very well to the simulated pattern based on the single crystal XRD structure of CPM-37(Ni) reported by the Feng group,[27] confirming the isostructural nature of the compound family. An important difference is the apparently lower crystallinity of CPM-37(Ni), which features broader peaks compared to the bimetallic CPM-37(Ni,Fe) compounds and CPM-37(Fe). The CPM-37(Ni) is less stable and the deterioration was seemingly aggravated by the prolonged multiple washings with DMF (4×20 mL). In the original report of the CPM-37(Ni) synthesis,[27] the experimental PXRD pattern and N_2-sorption measurement have not been reported, so the data regarding the relatively low observed stability and non-robust permanent porosity of CPM-37(Ni) (87 $m^2 g^{-1}$) are new and somewhat unexpected. The activation involving solvent exchange with CH_2Cl_2 and degassing at 60 °C for 16 h under vacuum (~5×10^{-2} mbar) was mild, yet, it evidently was an appreciable stress factor in terms of the material's permanent porosity. While CPM-37(Fe) (368 $m^2 g^{-1}$) demonstrated similar low-stability issues after degassing, the same treatment of the bimetallic CPM-37(Ni,Fe) samples did not compromise the stability according to the PXRD (Fig. S2†) and N_2-adsorption data. The surface area of three bimetallic CPM-37(Ni,Fe) samples was 2039, 1955 and 2378 $m^2 g^{-1}$ for CPM-37(Ni_2Fe), CPM-37(NiFe), and CPM-37($NiFe_2$), respectively.

FT-IR spectroscopy was used for accessing the presence of the characteristic functional groups (Fig. 1b). The spectra imply high similarity regarding the chemical composition (the assignments of FT-IR bands of the resulted catalysts are provided in Table S1†). The broad peak around 3300-3500 cm^{-1} can be ascribed to stretching and bending vibrations of hydroxyl groups from coordinated and adsorbed water molecules, associated by H-bonds.[30,31] The asymmetric vibration of carboxylate at 1598-1513 cm^{-1} and the respective symmetric counterpart are located at 1398-1330 cm^{-1}. The band at 460-580 cm^{-1} can be attributed to the metal-oxygen stretching vibrational mode.[32]

Scanning electron microscopy of the samples is represented in Fig. 3. The three bimetallic samples CPM-37(Ni_2Fe), CPM-37(NiFe) and CPM-37($NiFe_2$) consist of aggregated nano-platelet crystals. The monometallic CPM-37(Ni) features large single crystals with a trigonal symmetry (>0.2 mm; Fig. S5†), while the monometallic CPM-37(Fe) is composed of similar, but significantly smaller plates (Fig. S6g†). The EDX elemental mapping of CPM-37(Ni_2Fe) in Fig. 3e,f reveals the uniform distribution of nickel and iron in the sample. The EDX elemental mapping of CPM-37(NiFe), CPM-37($NiFe_2$), and CPM-37(Fe) are shown in Fig. S6†, the SEM-EDX spectra in Fig. S7† (see also Table S3†).

Atomic absorption spectroscopy (AAS; see section 2.2 ESI†) was used to determine the absolute nickel and iron content in the CPM-37(Ni,Fe) samples. EDX analyzes a thin surface layer of approx. 1-2 µm,[33] and provides only a relative element content. The two methods are complementary with expected minor discrepancies between them; the results are compared in Table 1.

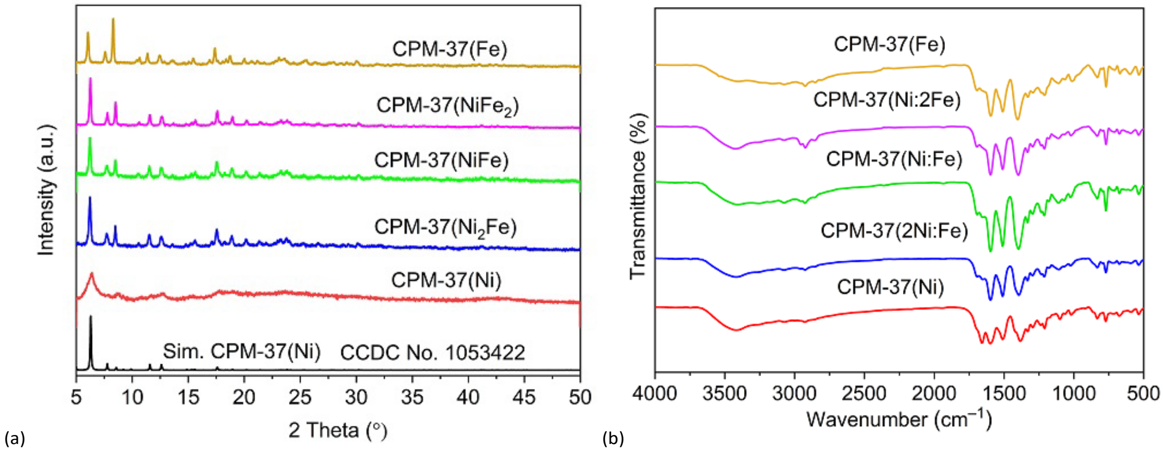

Fig. 2 (a) PXRD patterns of the as-prepared samples, (b) FT-IR spectra of the as-prepared samples.

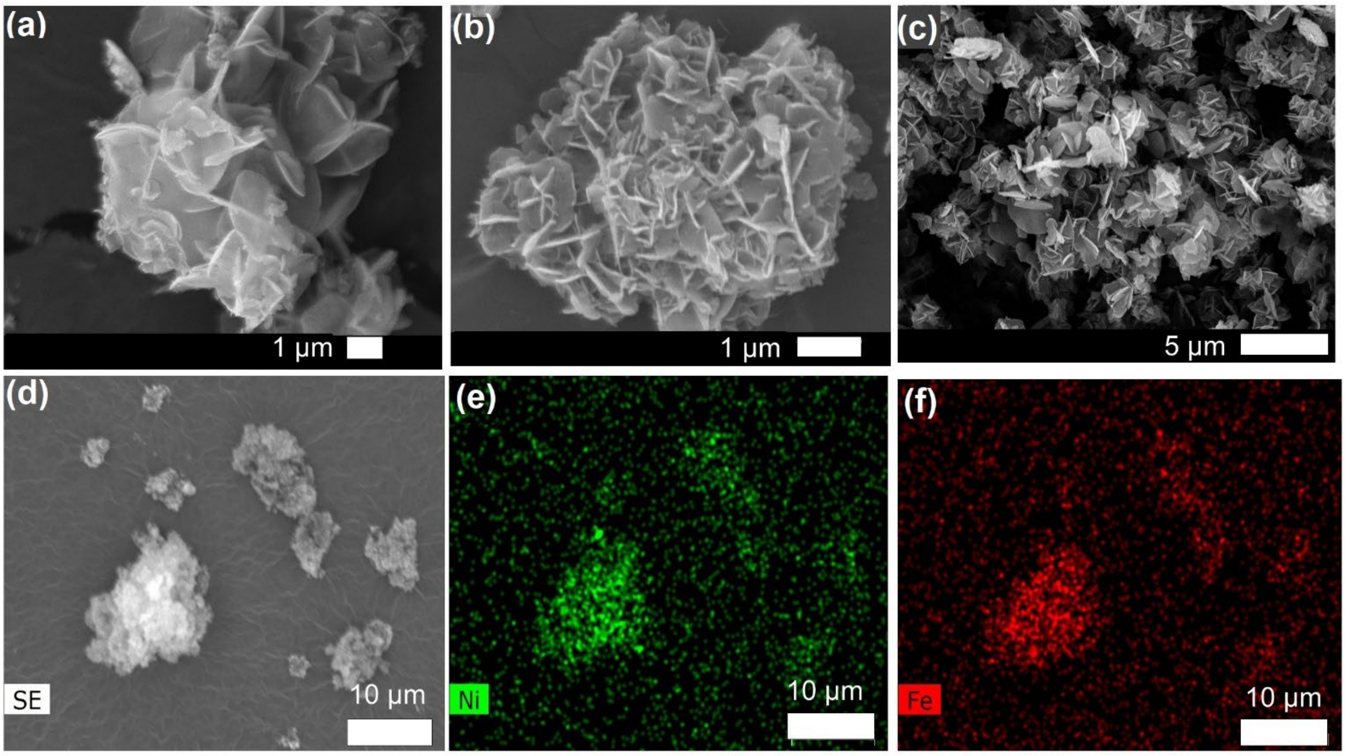

Fig. 3 SEM images of (a,d) CPM-37(Ni2Fe), (b) CPM-37(NiFe), (c) CPM-37(NiFe2). EDX elemental mappings for (e) Ni and (f) Fe.

Table 1 Ni and Fe content in the bimetallic CPM-37 materials according to SEM-EDX and AAS.

Sample	SEM-EDX	AAS			Expected Ni and Fe contents [a] and their molar ratios		
	Ni/Fe mol. ratio	*Ni wt%*	*Fe wt%*	*Ni/Fe mol. ratio*	*Ni wt%*	*Fe wt%*	*Ni/Fe mol. ratio*
CPM-37(Ni_2Fe)	1.58	7.90	3.90	1.91	8.40	4.20	2.00
CPM-37(NiFe)	0.96	4.80	4.90	1.11	6.40	6.10	1.00
CPM-37($NiFe_2$)	0.45	3.56	7.10	0.54	4.20	8.20	0.50

[a] For the theoretical Ni and Fe weight % content, the idealized formula $[Ni_3(OH)(C_{14}H_8O_4)_3(C_{24}H_{18}N_6O_3)]$ with the molecular weight of 1352.18 g mol^{-1} was used in all cases. The slight molecular weight differences due to the different content of the constituting metal ions and counter-anions X were not accounted due to low significance. The expected content and molar ratio correspond to the molar metal ratios, which were used in the synthesis.

The quantification of the metal content confirmed that the Ni:Fe ratio in the samples is close to their initial ratio in the reaction medium (*i.e.* there is no strong observed preference for the incorporation of Ni or Fe, which is somewhat unexpected, due to different expected oxidation states of +2 and +3, respectively, and hence different affinities).

The thermogravimetry analysis (TGA) under N_2 as a carrier gas was performed on the CPM-37 samples after a solvent exchange with CH_2Cl_2 (Section 2.2 and Fig. S12, ESI†). Two major weight-loss steps were registered: the first, at 50-350 °C, represents ~16-24% weight loss resulting from the desorption of the solvent guest molecules (CH_2Cl_2, water and residual DMF). Even prolonged exchange does not remove the DMF completely, which means that the found surface areas for the degassed samples are not the optimal values, but rather the best ones, we were able to achieve.[34] The second step at 350-550 °C shows a ~57-66% weight loss, which is attributed to the decomposition (decarboxylation and carbonization) of the constituting organic ligands.[35]

The porosity of the as-prepared catalysts was studied by N_2-adsorption measurement (Fig. 4a). The observed IUPAC Type IB isotherms indicate microporous structures of the materials,[36] while the porosities are radically different: the monometallic CPM-37(Ni) and CPM-37(Fe), which are assumed to have lower stability, demonstrate much lower uptakes and Brunauer-Emmett-Teller (BET) surface areas compared to the bimetallic CPM-37(Ni,Fe) materials (Table 2).

The NLDFT-based calculated pore size distribution in Fig. 4b shows a trimodal distribution of the CPM-37(Ni,Fe) materials in the microporous 0.5-2.0 nm pore diameter range, which slightly exceeds the maximum below 1.0 nm for the expected unimodal distribution (the absolute values for the mode-maxima are of low precision, i.e. indicative only, as no matching MOF model for the DFT kernel is available).[36] On the contrary, CPM-37(Ni) showed a broad pore size distribution with dominantly represented mesoporous and microporous ranges,[36] which is attributed to the partial structural collapse as a result of the solvent exchange and the subsequent degassing procedure. The corresponding total pore volumes of the catalysts derived from N_2-adsorption isotherms at 77 K are summarized in Table 2.

Table 2 N_2-sorption results, BET surface area (m^2 g^{-1}), and samples' total pore volume (cm^3 g^{-1}).

Sample	BET surface area (m^2 g^{-1})	Total pore volume (cm^3 g^{-1}) [a]
CPM-37(Ni)	87	0.11
CPM-37(Ni_2Fe)	2039	2.25
CPM-37(NiFe)	1955	1.50
CPM-37($NiFe_2$)	2378	1.30
CPM-37(Fe)	368	0.58

[a] The total pore volumes were determined at $p/p_0 = 0.90$ of the adsorption branch.

X-ray photoelectron spectroscopy (XPS) was conducted to determine the principal question regarding the oxidation state of the metal ions in the synthesized CPM-37, namely in CPM-37(Ni_2Fe), which was proven to be the best material for OER, and in the monometallic CPM-37(Fe) and CPM-37(Ni) for comparison. It is important to note that XPS has a relatively shallow penetration depth, approximately one order of magnitude less than EDX.[33] Therefore, the elemental composition obtained through XPS analysis (Fig. S13a†), as shown in Table S6†, was considered to have lower precision regarding the average values compared to EDX analysis (the determined distribution of oxidation states features the same surface-specific error, however, it gives a valuable semi-quantitative insight, which is not readily accessible by other means).

The high-resolution Ni 2p spectrum of CPM-37(Ni) and CPM-37(Ni_2Fe) (Fig. 5a) reveals a mixed Ni^{2+}/Ni^{3+} oxidation state for nickel in both the monometallic CPM-37(Ni) and bimetallic CPM-37(Ni_2Fe) samples. In the case of the CPM-37(Ni) sample, two distinct peaks observed at 856.0 and 873.6 eV can be attributed to Ni $2p_{3/2}$ and Ni $2p_{1/2}$ transitions for Ni^{2+}, respectively. The deconvolution of those peaks allows to detect the respective transitions for Ni^{3+} at 857.5 eV and 875.0 eV as well. The two peaks at 861.8 and 879.7 eV are ascribed to Ni 2p satellites.[37-39]

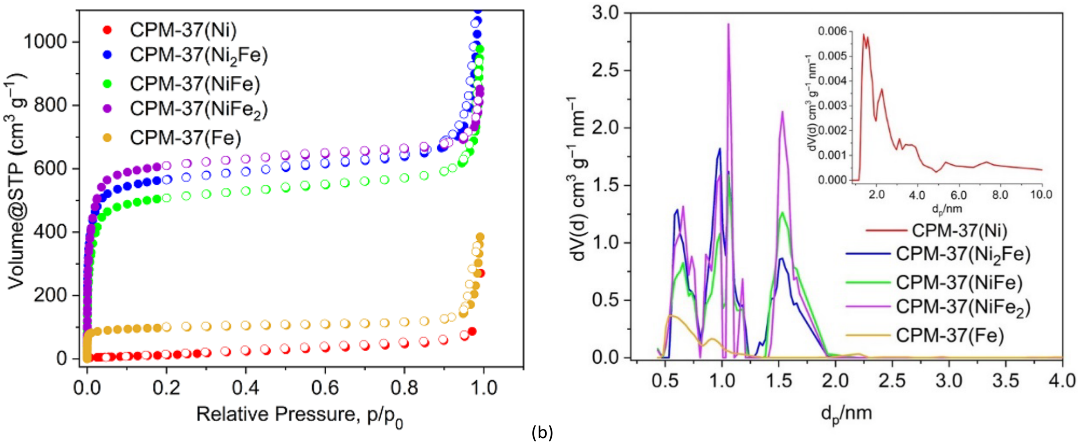

(a) (b)

Fig. 4 (a) Nitrogen adsorption isotherms of the CPM-37 samples at 77 K (adsorption: filled circles; desorption: empty circles), (b) NLDFT-based pore size distributions for the CPM-37 samples.

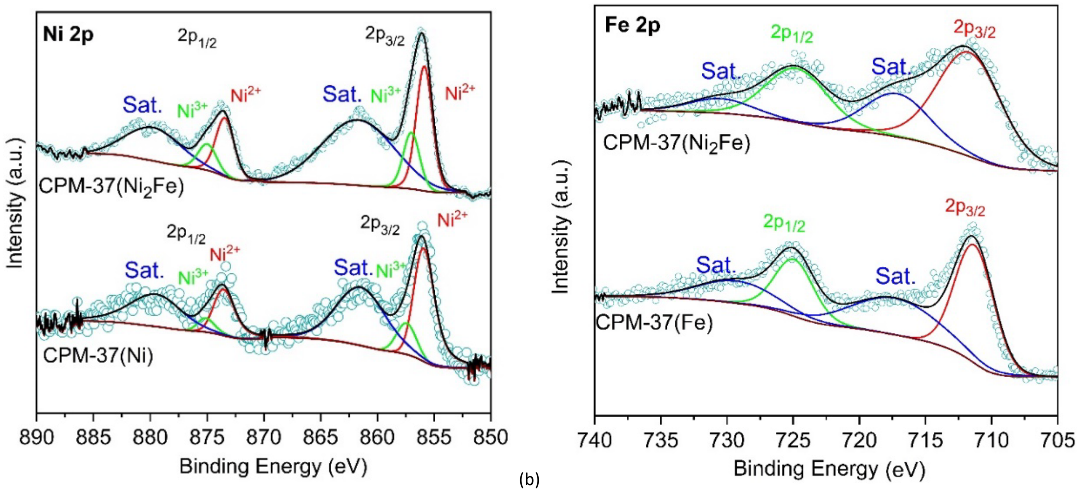

(a) (b)

Fig. 5 High-resolution XPS spectrum of (a) Ni 2p in CPM-37(Ni) and CPM-37(Ni$_2$Fe), (b) Fe 2p in CPM-37(Fe) and CPM-37(Ni$_2$Fe).

The calculated ratio of Ni^{2+}:Ni^{3+} for CPM-37(Ni) was 4.9 (Table S10†), indicating that the dominant oxidation state of nickel is Ni^{2+}, which aligns with the reported [Ni$_3$(OH)(BPDCA)$_3$(TPAMA)] framework formula.[27] Interestingly, the deconvolution analysis of the Ni 2p spectrum of CPM-37(Ni$_2$Fe) also confirms the presence of a mixed Ni oxidation state. Specifically, the peaks observed at 855.9 and 873.5 eV were assigned to Ni^{2+}, the peaks at 857.1 and 875 eV to Ni^{3+}. The two satellite peaks are detectable at 861.9 and 880.2 eV.[38,39] The calculated ratio of Ni^{3+}:Ni^{2+} for CPM-37(Ni$_2$Fe) is 2.4 (Table S10†).

The deconvolution analysis of the Fe 2p high-resolution XPS spectrum consistently indicated only an Fe^{3+} oxidation state for both CPM-37(Fe) and CPM-37(Ni$_2$Fe) (Fig. 5b). For CPM-37(Fe), two peaks located at 711.5 and 725.1 eV were observed, while for CPM-37(Ni$_2$Fe), there are two peaks centered at 711.9 and 725 eV, both characteristic for Fe^{3+}.[40,41,42] A pair of satellite peaks at 717.9 and 729.8 eV and 717.5 and 730.5 eV were observed for CPM-37(Fe) and CPM-37(Ni$_2$Fe), respectively.[43] The high-resolution XPS spectrum of Fe 3p also confirmed the nearly only Fe^{3+} state in both CPM-37(Fe) and CPM-37(Ni$_2$Fe) samples (Fig. S14†).

An interesting separate point in the question of the composition is the presence of minor amounts of sulfur in the XPS spectra of the investigated iron-containing CPM-37, namely the CPM-37(Fe) and CPM-37(Ni$_2$Fe) (S 2p peaks in Fig. S13a†), which is attributable to the residual SO$_4^{2-}$ ions from FeSO$_4$·7H$_2$O, used for their synthesis. At least Li *et al.* have also reported the incorporation of SO$_4^{2-}$ in the structure of analogous MOFs and suggested its charge-balancing role.[44] We could confirm only a minor role of the sulfate, which amounts to ~1 mol% of the total metal content (note, that the XPS analysis of sulfur is not precise due to low content, aggravated by the inherent surface nature of the analysis, which could be affected by surface defects and the associated variation of charge balancing counter-anions. Hence the given content is semi-qualitative). It seems that the role of the sulfate is not fundamental and the content depends on the method of preparation. As for the C, O, and N elements, the respective XPS peaks of C 1s, O 1s, and N 1s are shown in Fig. S13b-d†, with the corresponding peak assignments listed in Table S7†, Table S8†, and Table S9†, respectively.

The proposed final composition is based on the single-crystal structure of the reported CPM-37(Ni) (CCDC No.1053422; Fig. 1a-c),[27] which is confirmed by us via comparison of the simulated and experimental PXRDs, as well as by SCXRD-based cell-determination. The formerly ascribed composition based on the SCXRD data corresponds to the idealized formula of $[(Ni^{2+})_2(Ni^{3+})(\mu_3\text{-}OH)(BPDCA)_3(TPAMA)]$ implying a Ni^{2+}:Ni^{3+} ratio of 2:1 (Fig. 1d; stable composition with x = 1). Our XPS data suggest though, a deficiency of Ni^{3+} compared to this formula, showing a Ni^{2+}:Ni^{3+} ratio of ~5:1 (note that the precision of XPS, which is surface-relevant only, is limited, but still, the deflection is too high to be ignored). The Ni^{3+} oxidation state, normally unstable under the given conditions, is stabilized by its necessary counterbalancing role of the charged μ_3-OH central ligand, which in turn stabilizes the cationic environment. If only Ni^{2+} were present, the role of the central atom could have been played only by μ_3-H_2O (Fig. 1f), which is evidently an unstable configuration, where three cations are close to each other without an anionic counterbalance in-between. The observed structural instability of CPM-37(Ni) during direct degassing as well as the results of the XPS suggests, that some, or even a substantial amount of the framework-constituting clusters might indeed be constituted by Ni^{2+} only. It is reasonable to suggest, that while the freshly prepared CPM-37(Ni) might be closer to the ideal formula given above, a part of Ni^{3+} could reduce to Ni^{2+} upon storage, solvent exchange, and degassing (and/or upon strong local heating during the XPS measurement) thereby destabilizing the framework. The general formula in this case could be expressed as $[(Ni^{2+})_{3-x}(Ni^{3+})_x(\mu_3\text{-}OH)_x(\mu_3\text{-}OH_2)_{1-x}(BPDCA)_3(TPAMA)]$, where x is rather closer to 0.5 than to 1 (Fig. 1f), as in the idealized formula. Degassing at elevated temperatures should further destabilize the structure.

In CPM-37(Ni_2Fe) one-third of Ni atoms are substituted by Fe atoms, as confirmed by the found Ni:Fe ≈ 2.0 ratio by the AAS analysis, while the found oxidation states by XPS were $Ni^{2+}$and Ni^{3+} with a 0.4 ratio and Fe^{3+} only. Thus, the CPM-37(Ni_2Fe) is enriched by M^{3+} ions even more than minimally necessary to charge-balance the central μ_3-OH ligand. The framework formula could be expressed as $[(Ni^{2+})_{3-x}(Ni^{3+}{}_{\sim 0.33}Fe^{3+}{}_{\sim 0.66})_x(\mu_3\text{-}OH)_{2-x}(\mu_3\text{-}O)_{x-1}(BPDCA)_3(TPAMA)]$ with x ≈ 1.5 (the content of the central oxido ligand might be slightly less, namely by ~z/2, where z~0.03 is the amount of the SO_4^{2-} present. The difference is smaller than the precision of the XPS, so it could be neglected, particularly while a part of the sulfate might also be simply trapped/occluded as well). Thus, the composition corresponds to the expected stability range with M^{II} content of $x \in [1\text{-}2]$ in the three-metal cluster (Fig. 1d). The presence of the Ni^{3+} is somewhat unexpected, but it is in line with the expected additional stabilizing effect of the charge-balancing central μ_3-O ligand instead of the μ_3-OH (in other words there is a factor-equilibrium between the added stabilizing effect of the μ_3-O ligand and instability of the Ni^{3+} oxidation state).

CPM-37(Ni_2Fe), as well as the other mixed-metal CPM-37(Ni,Fe) compounds investigated in this work demonstrate good stability allowing direct degassing without strong deterioration of the expected high surface areas (in stark contrast to CPM-37(Ni)). In addition, the discussion above allows to suggest, why the CPM-37(Fe) is also less stable than the mixed-metal counterparts (even if to a lesser extent compared to CPM-37(Ni)). Formally, the situation is unexpected as MIL-88(Fe) or MIL-100(Fe) based on the $\{Fe^{III}{}_3O(OH)\}$ cluster core are stable. The possible reason is that in CPM-37(Fe) (cf. Fig. 1e) there are no free coordination sites at the iron ions, which could accept the additional charge-balancing terminal hydroxido-ligands, unlike in the case of the parent MIL-88(Fe). It is not a fundamental problem, as the charge-balancing counteranions could also be localized in the pores (as the bromide ion in NH_2-MIL-88D(Fe), according to the crystal structure with KOKKOL CSD code.[45] In the current case of CPM-37(Fe) the sulfate ions could play the same role. However, MOFs with cationic frameworks (cf. Fig. 1e) do not receive full Coulombic stabilization and hence are less stable than the analogues with fully charge-compensated frameworks. The observation that the mixed-metal CPM-37, at least for the examples of Ni and Fe materials, are much more stable than their single-metal peers regarding their high attainable permanent porosity and easy preparation is of high practical importance.

Electrocatalytic oxygen evolution reaction (OER) performance

Among the two electrochemical processes constituting the water splitting, namely the (cathodic) hydrogen evolution reaction (HER) and (anodic) oxygen evolution reaction (OER),[46] the latter requires, as a rule, higher overpotentials, and is hence less efficient.[47] The optimization of the OER, primarily via finding electrocatalytic materials with low overpotentials at high current densities, is one of the evident challenges.

The work focuses on a comparative study, and the success criterion is based on comparison of the CPM-37 materials with the RuO_2 benchmark. The OER performance of the samples was evaluated using a three-electrode setup (RHE as a reference and Pt foil as a counter electrode) in 1.0 mol L^{-1} KOH (pH=13.3) solution, degassed by constant bubbling of N_2 gas. The linear sweep voltammetry (LSV) polarization curve (Fig. 6a), confirmed that the presence of both iron and nickel in the CPM-37 samples remarkably increases the OER performance of the electrocatalyst compared to monometallic CPM-37(Ni) and CPM-37(Fe) (here and further it is implied that the CPM-37 MOFs are precursor material to the catalytic species actually formed in the alkaline medium).

Despite promising prerequisites, the usage of MOFs as electrode materials also meets strong inherent obstacles. The two most important ones are the low conductivity (which is to some extent amendable by the use of conductive additives constituting a composite) and generally low stability of MOFs in acidic, but particularly in basic conditions.[48,49] However, MOFs have been proven to be at least good precursors for electrode materials.[50,51,52] Pyrolysis (carbonization) of MOFs under an inert atmosphere is the most utilized way to produce electrocatalytic materials from MOFs. The resulting porous carbon materials with much-improved conductivity feature relatively uniformly distributed metal nanoparticles or reduced metal-based species, which could serve as electrocatalytic active sites.[20] Typical problems are low yield, poor reproducibility and/or scalability, as well as limitations regarding local uniformity and purity of the ensuing electrode materials.[53,54]

The OER enhancement of the bimetallic CPM-37(Ni,Fe) compounds can be attributed to the electrochemical Ni-Fe synergism in alkaline media,[55] and the introduction of additional structural vacancies in nickel-based MOFs.[56] Among all CPM-37 materials, the bimetallic CPM-37(Ni_2Fe) has the best performance regarding the OER reaction – namely, it has the lowest overpotential for current densities above 50 mA cm^{-2} (Fig. 6a), suggesting a Ni:Fe ratio optimum at ~2. The advantage increases with current densities, reflected by the lowest Tafel slope of ~39 mV dec^{-1} for CPM-37(Ni_2Fe) compared to the other CPM-37 materials. At a low current density of 25 mA cm^{-2}, the well-known benchmark material, RuO_2, demonstrates a slightly lower overpotential compared to CPM-37(Ni_2Fe), namely at 274 vs 278 mV respectively, but already at 50 mA cm^{-2} the order reversed to be 300 vs 290 mV.

At current densities above 80 mA cm^{-2}, all iron-containing CPM-37 materials outperform the RuO_2 benchmark, however, the CPM-37(Fe) is the worst performer. Therefore, the synergistic presence of Ni is important, and the ratio optimization led to an appreciable overpotential decrease with an optimum for CPM-37(Ni_2Fe) at >50 mA cm^{-2} currents (Fig. 6b).[37] As can be seen from Fig. 6a, in the bimetallic CPM-37(Ni,Fe) samples the oxidation of Ni^{2+} is hindered, inferred from a positive shift of the $Ni^{2+/3+}$ peaks to >1.4 V compared to <1.4 V for CPM-37(Ni).

Tafel analysis was conducted to assess the intrinsic kinetics of the OER process. The resulting Tafel slope, obtained from the plot, is commonly used to semi-quantitatively determine the reaction rate at the electrode-electrolyte interface using the following equation:[57]

$$\eta = b \log(j) + a \qquad (1)$$

where η is the iR-corrected potential (also denoted as $i_{cell}R_u$ 'ohmic' drop, which is the difference between the applied potential and the actual potential at the interface), b is the Tafel slope, j is the current density, and a is a Tafel y-intercept.[28]

The calculated Tafel slopes for CPM-37(Ni), CPM-37(Ni_2Fe), CPM-37(NiFe), CPM-37($NiFe_2$), CPM-37(Fe) were, respectively, 67, 39, 44, 47, 49 mV dec^{-1} against 57 mV dec^{-1} for RuO_2 (Fig. 6c). The lowest Tafel slope for the CPM-37(Ni_2Fe)-derived material signifies the lowest energy losses associated with the overpotential. Speaking in kinetic terms, electrons transfer is faster improving the catalytic performance.[58]

The electrochemical impedance spectroscopy (EIS) measurement was conducted to find correlations with the catalytic activity trend of the materials.[59] Fig. 6d represents the Nyquist plots of the selected samples derived from EIS measurements at 1.5 V vs. RHE. The smaller semicircle radius of the plot for the CPM-37(Ni_2Fe)-derived material infers lower charge transfer resistance on the electrode-electrolyte interface, which means accelerated kinetics of the OER.[60]

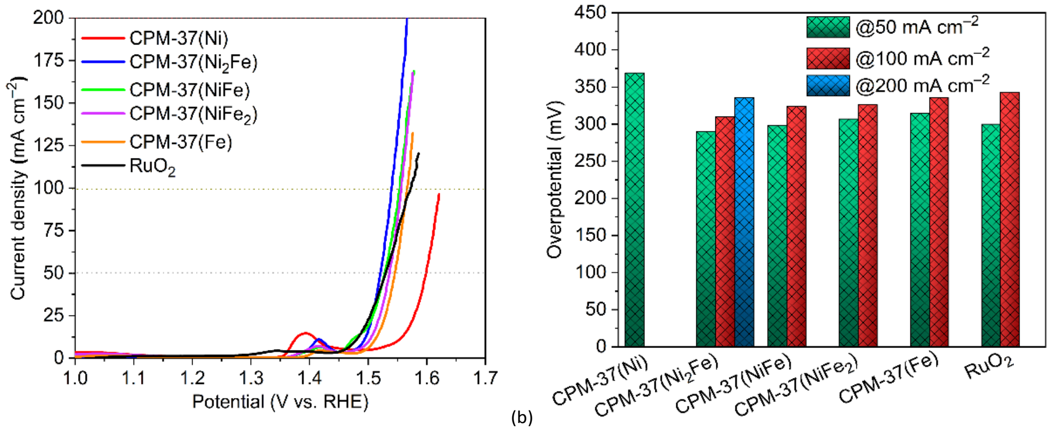

(a) (b)

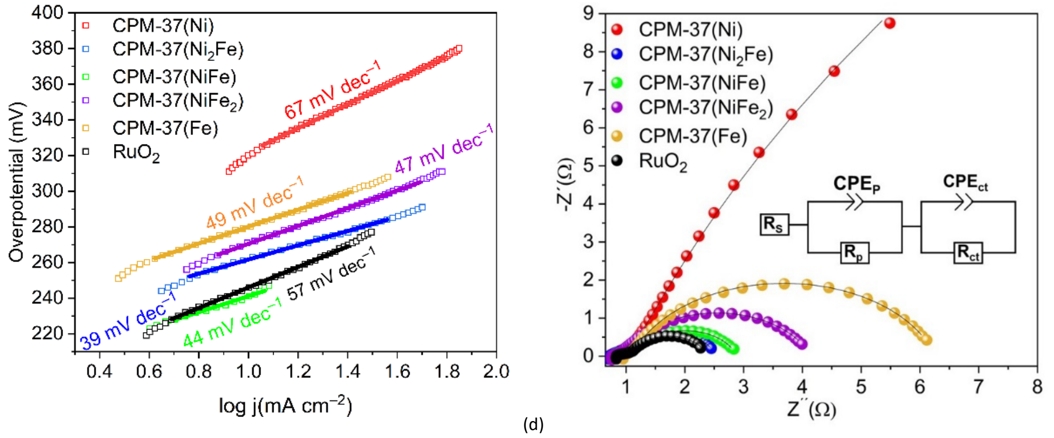

(c) (d)

Fig. 6 (a) OER polarization curves for the converted CPM-37 precatalysts, i.e. derived electrode materials. (b) Overpotentials determined at 50, 100, and 200 mA cm^{-2} for the derived materials. (c) Tafel plot of the derived materials determined in 1 mol L^{-1} KOH solution. (d) Nyquist plots for the selected samples at 1.5 V vs. RHE. The Voigt circuit model (black lines) was used to fit the data, where R$_s$ represents the electrolyte resistance, R$_p$ is the resistance associated with the electrode's porosity, and R$_{ct}$ with the charge transfer, respectively. Constant phase elements (CPE) were used to show double-layer capacitance.

The Nyquist plots were fitted using a Voigt-type circuit (Fig. 6d) to determine the charge transfer resistance, R_{ct} (Table 3). The lowest (1.45 Ω) and highest (66 Ω) R_{ct} values were observed for the CPM-37(Ni$_2$Fe)- and CPM-37(Ni)-derived materials, respectively. These findings correlate with the observed trend in catalytic activity as evaluated by the linear sweep voltammetry (LSV) polarization curves, indicating that CPM-37(Ni$_2$Fe) showcased superior OER performance in comparison to the other CPM-37-derived materials. The smaller (R_{ct}) for CPM-37(Ni$_2$Fe) (1.45 Ω) signifies higher electrode-electrolyte ion transport speed compared to the analogs, which is a prerequisite for more favorable OER kinetics.[61] Furthermore, the catalyst that was derived from CPM-37(Ni$_2$Fe) had a Faradaic efficiency of 84% (Section 2.10.1, ESI†).

Table 3 Overpotentials at 50 mA cm^{-2}, Tafel slopes, and the estimated charge transfer resistances, R_{ct}, for the CPM-37-derived materials at 1.5 V vs RHE.

Sample	Overpotential at 50 mA cm^{-2} (mV)	Tafel slope (mV dec^{-1})	Charge transfer resistance, R_{ct} (Ω)
CPM-37(Ni)	369	67	66.0
CPM-37(Ni$_2$Fe)	290	39	1.45
CPM-37(NiFe)	298	44	1.66
CPM-37(NiFe$_2$)	307	47	3.15
CPM-37(Fe)	316	49	5.15
RuO$_2$	300	57	1.23

Long-term stability is one of the most important practical performance-defining qualities of an electrocatalyst.[62] The stability of the CPM-37(Ni$_2$Fe)-derived material and RuO$_2$ as a reference material was investigated by chronopotentiometric analysis (CP) at a fixed current density of 50 mA cm^{-2} over 20 h (Fig. 7a). The results of the OER stability test confirmed the superiority of CPM-37(Ni$_2$Fe) compared to RuO$_2$ regarding the long-term performance. The overpotential needed to achieve a current density of 50 mA cm^{-2} experienced a relatively modest increase, from 290 mV to 304 mV, for the electrode material derived from CPM-37(Ni$_2$Fe). Conversely, the OER performance of RuO$_2$ exhibited a substantial decline after 20 hours, resulting in a significant overpotential rise from 300 mV to 387 mV.

To investigate more in-depth the conversion of the initial CPM-37 materials in aqueous alkali, dedicated tests were performed on larger scales of the material without the involvement of electrochemical processes (this test is not equivalent to the investigation of the actual electrode material after the OER – see below – but it gives an interesting insight to an approximation of its initial composition). A sample of CPM-37 was soaked in 1 mol L^{-1} an aqueous KOH for 20 h, and the recovered material was analyzed by means of PXRD analysis (Fig. S3†). In line with the known low stability of carboxylate MOFs in alkaline aqueous media,[63] complete decomposition of the CPM-37 MOFs was observed, together with microscopically witnessed loss of initial morphology (Fig. S8† and Table S4†). As a result, a mixed-phase residue of metal (oxy)hydroxides was formed (Fig. S3†). It is worth noting here the purposefulness of the TPAMA ligand choice, unlike the acidic H$_2$BPDCA, the former has relatively low solubility in aqueous alkaline solutions, but it is chemically labile under the given conditions and the products of hydrolysis are well soluble.

Thus, in the case of CPM-37(Ni$_2$Fe) (Fig. 7b), most interesting in the context of OER, four phases were identified: α-Ni(OH)$_2$ (ICDD 38-0715),[64] β-Ni(OH)$_2$ (ICDD14-0117),[65] α-FeO(OH) (ICDD 29-0713),[66] and β-FeO(OH) (ICDD 01-080-1770).[67] For CMP-37(NiFe) and CPM-37(NiFe$_2$) the same phases, except β-Ni(OH)$_2$ were observed (Fig. S3†). The conversion of the monometallic CPM-37(Ni) and CPM-37(Fe) led to a mixture of hydroxides, dominantly to β-Ni(OH)$_2$ and β-FeO(OH), respectively (see Fig. S4† and Table S2† for the IR spectra of the formed residues and the respective assignments).

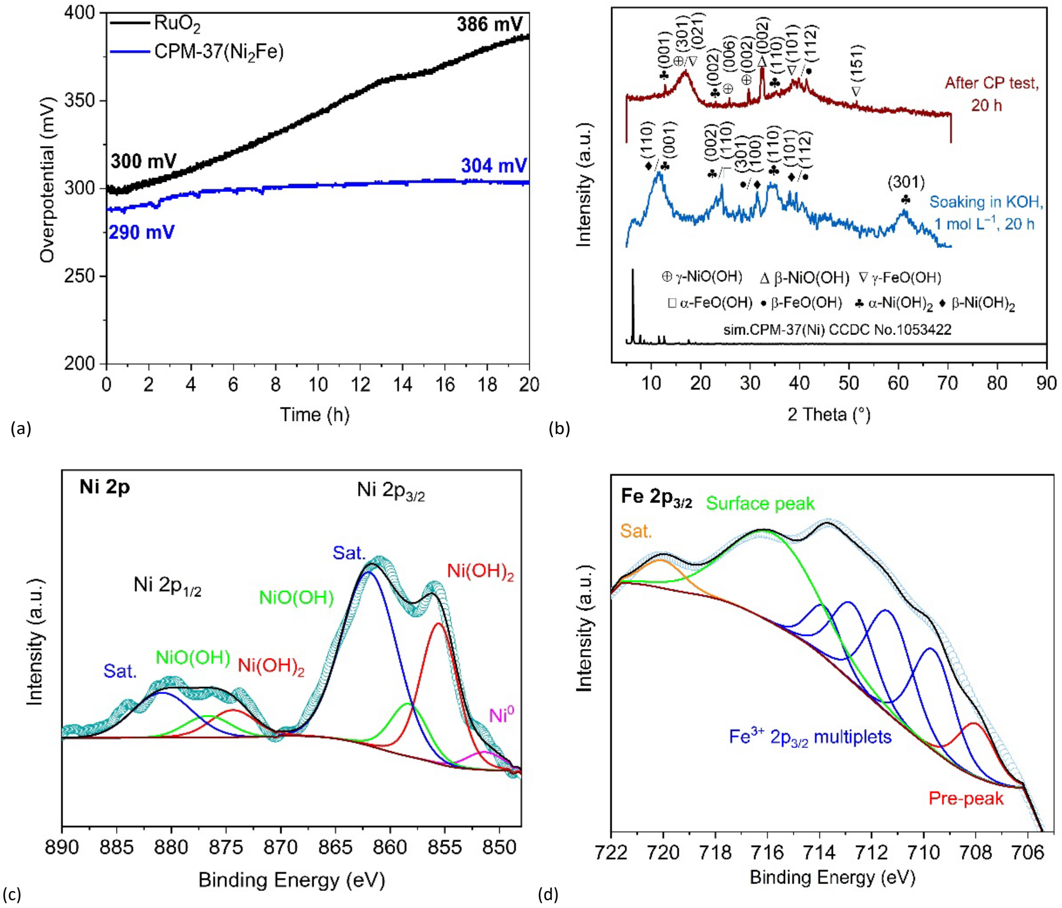

Fig. 7 (a) Chronopotentiometry (CP) analysis of CPM-37(Ni_2Fe) and RuO_2 at 50 mA cm^{-2} for 20 h. (b) PXRD patterns of CPM-37(Ni_2Fe) after CP test in 1 mol L^{-1} KOH for 20 h, and soaking in 1 mol L^{-1} KOH for 20 h. (c) High-resolution XPS spectrum of Ni 2p in CPM-37(Ni_2Fe) after CP test in 1 mol L^{-1} KOH for 20 h. (d) High-resolution XPS spectrum of Fe 2p in CPM-37(Ni_2Fe) after CP test in 1 mol L^{-1} KOH for 20 h.

It is worth noting that the residues derived from CPM-37(Ni_2Fe) in an aqueous alkaline solution without the application of current contains an intermediary quantity of β-$Ni(OH)_2$ compared to its dominant content for CPM-37(Ni)- and near absence for other more iron-rich CPM-37-derived materials. The conversion of the β-phase to the α-$Ni(OH)_2$ might be stimulated by a phenomenon known as 'interstratification', caused by the presence of charge-imbalancing Fe^{3+} cations.[68] The latter creates defects by substituting the Ni^{2+} ions in β-$Ni(OH)_2$, causing an excess of positive charge, which is compensated by anions localized between the β-$Ni(OH)_2$ layers. This arrangement stimulates the formation of α-$Ni(OH)_2$ via conversion of the β-$Ni(OH)_2$ phase.[69–71] The layered striated morphology with tightly incorporated iron ions, whose synergistic presence is crucial,[66] might play a role in increased efficiency. On the other hand, there is a formal contradiction, as α-$Ni(OH)_2$ itself has a higher catalytic activity in OER than β-$Ni(OH)_2$ (according to the Bode model,[72] the α-$Ni(OH)_2$ more readily oxidizes to γ-NiO(OH) during the OER reaction, which in turn takes part in the catalytic cycle).[73,74] Accordingly, it was suggested that the derived material after the OER could have a different composition.

Therefore, the best-performing actual electrode material derived from CPM-37(Ni_2Fe) was also analyzed by means of PXRD, using a sample collected after the application of the current, i.e. after the OER. This type of test is generally cumbersome as it is hard to separate the non-metal part of the electrode material from the nickel foam without introducing nickel metal and/or separating the material non-uniformly. Hence a specially prepared 'flattened' Ni electrode was loaded (see the materials and method section), processed under the same conditions as the other samples, and then a simple separation of the deposited non-metal part of the electrode material was achieved by ultrasonication. Such modification of the electrode comes at a cost of higher overpotential due to worse contact with the metal support. Hence, the standard and modified electrodes could be compared only regarding the qualitative composition of the electrode material's outcome. The comparison of the initial metal oxide/hydroxide mixed phase residue (previous tests), and the electrode material after the OER allows to observe the result of the evolution of the material during the process.

The PXRD of the CPM-37(Ni_2Fe)-derived material after the OER on the special electrode revealed the presence α-$Ni(OH)_2$ (ICDD 38-0715),[64] γ-NiO(OH) (ICCD 06-0075),[65] β-FeO(OH) (ICDD 01-080-1770),[67] and γ-FeO(OH) (JCPDS No. 76-2301)[75], and possibly minor amounts of β-$Ni(OH)_2$ (Fig. 7b, Fig. S10†). During the OER the latter converted to other Ni-containing phases, while a part of the Ni(II) was oxidized to nickel(III) oxide hydroxide phases.

According to the generally accepted theoretical model, the nickel oxy(hydroxide) species play a crucial role in the oxygen evolution reaction (OER) in alkaline aqueous medium due to the electrocatalytic role of the Ni^{3+}/Ni^{2+} redox pair. γ-NiO(OH) and γ-FeO(OH) are usually identified as synergistic active sites for the OER process.[37,76,77] The role of Fe could be at least partially postulated as catalyst for the decomposition of the peroxy-species and, hence, the mixture, tight at the nano-scale, of nickel and iron is viewed as advantageous. The mechanism of the OER reaction is usually given by equation 2–5,[78] where the Σ and Σ^+ symbols represent the active centers associated with the Ni^{2+} and Ni^{3+} catalyst:

$$\Sigma\text{-}OH^- \rightarrow \Sigma^+\text{-}OH + e^- \qquad (2)$$

$$\Sigma^+\text{-}OH + OH^- \rightarrow \Sigma^+\text{-}O^{\cdot} + H_2O + e^- \qquad (3)$$

$$\Sigma^+\text{-}O^{\cdot} + OH^- \rightarrow \Sigma\text{-}OOH + e^- \qquad (4)$$

$$\Sigma^+\text{-}OOH + OH^- \rightarrow \Sigma + O_2 + H_2O + e^- \qquad (5)$$

The XPS analysis of the CPM-37(Ni_2Fe)-derived material recovered from the special electrode after the OER (Fig. S15a†) shows the presence of both Ni^{2+} and Ni^{3+} (Fig. 7c,d and Section 2.8.2, ESI†). Thus the Ni 2p peaks are found both for Ni^{2+} (at 855.7 eV for Ni $2p_{3/2}$ and 874.8 eV for Ni $2p_{1/2}$) and Ni^{3+} (at 858.7 eV for Ni $2p_{3/2}$ and 876.7 eV for Ni $2p_{1/2}$), which should be associated with $Ni(OH)_2$ and NiO(OH) phases respectively, also identified by PXRD (Fig. 7b). The two further peaks located at 862.2 and 881.4 eV are attributed to satellite peaks of Ni $2p_{3/2}$ and Ni $2p_{1/2}$ respectively, while the small peak at 852 eV can be ascribed to metallic nickel, which is produced by Ar sputtering during XPS analysis.[37,79]

Regarding iron, practically only Fe^{3+} is expectedly detected in the CPM-37(Ni_2Fe)-derived material. Unlike in the case of the Fe in the parent MOF, where the $2p_{3/2}$ envelope was fitted by a single peak (which is a strong simplification), it was attempted to make a more precise fit using the four strongest 'Gupta and Sen' (GS) multiplet components (the four-peak fitting is a practical simplification as the two further weaker peaks at ~714.1 and ~719.5 are not taken in account because it is hard to fit them reliably. The simplification could underestimate the content of iron up to ~17%, but due to peak overlap the value tends to be lower). The obtained values 709.7 (32.5%), 711.4 (32.3%), 712.8 (22.7%), and 713.7 eV (12.5%) are fully consistent with the average Fe(III) (except that a small 'pre-peak' at 707.4 eV could be interpreted as minor amounts of iron in lower oxidation states formed during Ar sputtering).[80] However, the result does not allow to distinguish, for example, α-FeO(OH) and γ-FeO(OH), which are overall the closest candidates. Thus, the reference values for the latter are 710.3 (31.9%), 711.3(32.2%), 712.3 (23.5%), 713.9 (12.2%),[80] while the difference from α-FeO(OH) is within 0.2 eV(2.5%) max., and those values are somewhat closer than those are from α-Fe_2O_3 and β-Fe_2O_3).[81–83] The dominant role of γ-FeO(OH) was rather postulated, based on generally higher stability under similar conditions and the available low-quality PXRD.

Among the further observed elements, including the evident potassium from KOH solution, carbon, oxygen, and sulfur, represented by K 2p, C 1s, O 1s, and S 2p bands, the residual sulfur is interesting as demonstrating the presence of a small amount of SO_4^{2-} in the CPM-37(Ni_2Fe) introduced during the synthesis of the precursor MOF as discussed above. No N 1s signal was detected, confirming that the CPM-37(Ni_2Fe) structure underwent complete decomposition during the OER reaction.

Conclusions

A series of newly developed bimetallic CPM-37(Ni,Fe) metal-organic frameworks showed much better stability and surface areas after activation than the monometallic Ni- or Fe-based peers. This observation is easily rationalizable: the low stability of CPM-37(Ni) is due to the relative instability of the Ni^{3+} state, which should be present to allow the μ_3-OH cluster-supporting central ligand. On the other hand, the CPM-37(Fe), featuring exclusively the stable Fe^{3+} state, should have some of the counter-anions to be localized in the pores. The cationic framework should have comparatively lesser stability. The observation of increased stability of mixed-metal CPM-37(Ni,Fe) coupled with easiness of preparation, high surface areas (~2000 $m^2\,g^{-1}$) and variability of metal content are important for the application-oriented MOF-field and calls for in-depth investigations of similar mixed-metal MOFs (due to the relative novelty of the analogous CPM materials, their prospects are somewhat obscured; it could be indirectly inferred from the absence of reports on permanent porosity of some representatives, e.g. CPM-37(Ni)). In this contribution, the uniform distribution of the two constituent metals down to the nano-scale, stipulated by the increased stability of the constituent coordination-bonded cluster, was inherently employed for the preparation of a nano-structured composite of metal oxides and oxo hydroxides, yielding the core functional part of the electrode material, by hydrolytic decomposition of the parent MOF.

Among the electrode materials derived from the CPM-37(Ni,Fe) precursors, the CPM-37(Ni_2Fe) material had the highest OER performance, with a low overpotential of 290 mV at 50 mA cm^{-2}, a low charge transfer resistance (R_{ct}) of 1.45 Ω and a low Tafel slope of 39 mV dec^{-1}, implying favorable OER kinetics. This is better than for the benchmark RuO_2 material (300 mV overpotential at 50 mA cm^{-2} but with a significantly higher Tafel slope at 57 mV dec^{-1}). The long-term performance is also better as witnessed by the results of the chronopotentiometry performance (CP) test after 20 h: the CPM-37(Ni_2Fe)-derived material with the overpotential increase from 290 to 308 mV outperformed the RuO_2 with the overpotential increased from 300 to 386 mV. The comparison of the materials derived by soaking CPM-37(Ni_2Fe) in 1 mol L^{-1} KOH solution and the material derived after the OER reaction showed the formation of γ-NiO(OH) phase during the electrochemical process, supporting the expected electrocatalytic role of Ni^{3+} species.

In general, the CPM-37(Ni_2Fe) derived material, where an optimized Ni:Fe content was established, performs comparably or better also in comparison with $Ni(OH)_2$ (in various forms), Fe-doped $Ni(OH)_2$, and other materials derived from bimetallic Ni,Fe-MOF precatalysts (Table S12†), suggesting the advantages of the highly porous CPM-37(Ni_2Fe) precatalyst and the morphology of the derived material, as well as of the optimized Ni/Fe ratio. The low Tafel-slope for the CPM-37(Ni_2Fe), which is a prerequisite for the use at high current-densities, demonstrates the room, which still exists for optimization of advanced electrode materials with improved ion transport kinetics based on analogous microporous MOF precursors with adjustable composition, being uniform on the nanoscale.

Author contributions

Conceptualization: S.A (Soheil Abdpour), I.B. (István Boldog); Methodology: S.A; Validation: S.A; Formal analysis: S.A, M.N.A.F. (Marcus. N. A. Fetzer), I.B., R.O. (Robert Oestreich), T.H.Y.B. (Thi Hai Yen Beglau): Investigation, S.A; Resources: C.J. (Christoph Janiak); Writing original draft: S.A; Writing-review & editing: I.B., C.J.; Supervision: C.J.; Project administration: C.J.; Funding acquisition, C.J. All authors have read and agreed to the published version of the manuscript.

Conflicts of interest

There are no conflicts to declare.

Acknowledgements

The authors thank Mr. Takin H.H. Sohi for single crystal XRD-based unit cell parameter checking for the known CPM-37(Ni) phase and Ms. Annette Ricken for the AAS measurements. This research was funded by a joint National Natural Science Foundation of China–Deutsche Forschungsgemeinschaft (NSFC-DFG) project (DFG JA466/39-1).

Notes and References

1 Y. Cui, B. Li, H. He, W. Zhou, B. Chen and G. Qian, *Acc. Chem. Res.,* 2016, **49**, 483–493.

2 S. Abednatanzi, P. Gohari Derakhshandeh, H. Depauw, F.-X. Coudert, H. Vrielinck, P. Van Der Voort, K Leus, *Chem. Soc. Rev.* 2019, **48**, 2535-2565.

3 L. Chen, H.-F. Wang, C. Li, Q. Xu, *Chem. Sci.* 2020, **11**, 5369-5403.

4 Y. Pan, H. Q. Su, E. L. Zhou, H. Z. Yin, K. Z. Shao and Z. M. Su, *Dalton Trans.*, 2019, **48**, 3723-3729.

5 T. Stolar, A. Prasnikar, V. Martinez, B. Karadeniz, A. Bjelic, G. Mali, T. Friscic, B. Likozar and K. Uzarevic, *ACS Appl. Mater. Interfaces*, 2021, **13**, 3070-3077.

6 M. Lammert, C. Glissmann and N. Stock, *Dalton Trans.*, 2017, **46**, 2425-2429.

7 J. D. Howe, C. R. Morelock, Y. Jiao, K. W. Chapman, K. S. Walton and D. S. Sholl, *J. Phys. Chem. C*, 2016, **121**, 627-635.

8 Y. Jiao, C. R. Morelock, N. C. Burtch, W. P. Mounfield, J. T. Hungerford and K. S. Walton, *Ind. Eng. Chem. Res.* 2015, **54**, 12408-12414

9 I. Jahan, M. A. Islam, T. H. Rupam, M. L. Palash and B. B. Saha, *Therm. Sci. Engin. Progress*, 2022, **35**, 101453.

10 W. H. Ho, S. C. Li, Y. C. Wang, T. E. Chang, Y. T. Chiang, Y. P. Li and C. W. Kung, *ACS Appl. Mater. Interfaces*, 2021, **13**, 55358-55366.

11 Y.-X. Ma, C. Liu, J.-F. Ma and Y. Zhao, *ACS Mater. Lett.*, 2022, **4**, 2522-2527.

12 N. Ye, J. Zheng, K. Xie, B. Jiang and S. Zuo, *J. Rare Earths*, 2023, **41**, 889-895

13 X. Wang, H. Xiao, A. Li, Z. Li, S. Liu, Q. Zhang, Y. Gong, L. Zheng, Y. Zhu, C. Chen, D. Wang, Q. Peng, L. Gu, X. Han, J. Li and Y. Li, *J. Am. Chem. Soc.,* 2018, **140**, 15336–15341.

14 A. P. Tiwari, Y. Yoon, T. G. Novak, K.S. An and S. Jeon, *ACS Appl. Nano Mater.,* 2019, **2**, 5061–5070.

15 F. E. S. Oztuna, T. Beyazay and U. Unal*, J. Phys. Chem. C,* 2019*,* **123**, 28131–28141.

16 J. Zhou, C. Huang, Q. Zhou, Y. Xie, L. Yang, L. Yu and Y. Yu, *Inorg. Chem.*, 2022, **61**, 9318–9327.

17 S. Abdpour, L. Rademacher, M. N. A. Fetzer, T.H.Y. Beglau and C. Janiak, *Solids*, 2023, **4**, 181–200.

18 D. Y. Chung, P. P. Lopes, P. F. B. D. Martins, H. He, T. Kawaguchi, P. Zapol, H. You, D. Pkovic, D. Strmcnik, Y. Zhu, S. Seifert, S. Lee, V. R. Stamenkovic and N. M. Markovic, *Nature*, 2020, **5**, 222-230.

19 T. H. Y. Beglau, L. Rademacher, R. Oestreich and C. Janiak, *Molecules,* 2023, **28,** 4464.

20 J. Liu, D. Zhu, C. Guo, A. Vasileff and S. Z. Qiao, *Adv. Energy Mater*., 2017, ***7***, 1700518.

21 G. Lee, W. Na, J. Kim, S. Lee and J. Jang, *J. Mater. Chem. A*, 2019, **7**, 17637-17647.

22 L. Gao, Z. Lin, X. Cui, C. D. Sewell, J. Li and Z. Lin, *Chem. Soc. Rev.,* 2021, **50**, 8428-8469.

23 S. Chen, L.Ma, Z. Huang, G. Liang and C. Zhi, *Cell Rep.,* 2022, ***3*,** 100729.

24 D. K. Singha, T. Ping and B. K. Jena, *ACS Appl. Energy Mater.*, 2023, **6**, 9963-9974.

25 S. Dai, Y. Liu, Y. Mei, J. Hu, K. Wang, Y. Li, N. Jin, X. Wang, H. Luo and W. Li, *Dalton Trans.*, 2022, **51**, 15446-15457.

26 Y. Dang, P. Han, Y. Li, Y. Zhang and Y. Zhou, *J. Mater. Sci.*, 2020, **55**, 13951-13963.

27 X. Zhao, X. Bu, Q. Zhai, H. Tran and P. Feng, *J. Am. Chem. Soc.,* 2015, **137**, 1396–1399.

28 S. Anantharaj and S. Noda, *J. Mater. Chem. A*, 2022, **10**, 9348-9354.

29 S. Hasegawa, S. Horike, R. Matsuda, S. Furukawa, K. Mochizuki, Y. Kinoshita, and S. Kitagawa, *J. Am. Chem. Soc.,* 2007, **129**, 2607–2614.

30 P. Maniam and N. Stock, *Inorg. Chem.,* 2011, **50**, 5085–5097.

31 L. Sondermann, W. Jiang, M. Shviro, A. Spieß, D. Woschko, L. Rademacher and C. Janiak, *Molecules,* 2022, **27**, 1241.

32 T. Zhang, N. Zhao, J. Li, H. Gong, T. An, F. Zhao and H. Ma, *RSC Adv.,* 2017, **7**, 23583–23590.

33 D. Titus, E. J. J. Samuel and S. M. Roopan, Nanoparticle characterization techniques in: Green Synthesis, Characterization and Applications of Nanoparticles (Eds.: A. K. Shukla, S. Iravani), Elsevier, Amsterdam, 2019, Ch. 12, pp. 303-319.

34 W. Zhang, H. Yin, Z. Yu, X. Jia, J. Liang, G. Li, Y. Li and K. Wang, *Nanomaterials*, 2022, **12**, 2062.

35 H. Yang, F. Peng, C. Dang, Y. Wang, D. Hu, X. Zhao, P. Feng and X. Bu, *J. Am. Chem. Soc.,* 2019, **141**, 9808–9812.

36 M. Thommes, K. Kaneko, A. V. Neimark, J. P. Olivier, F. R.-Reinoso, J Rouquerol and K. S. W. Sing, *Pure Appl. Chem.*, 2015, **87**, 1051–1069.

37 Y. Jia, Z. Xu, L. Li and S. Lin, *Dalton Trans.,* 2022, **51**, 5053-5060.

38 Y. Zhang, J. Wang, L. Ye, M. Zhang and Y. Gong, *Dalton Trans.*, 2021, **50**, 4720-4726.

39 Y. Wang, C. Wang, H. Shang, M. Yuan, Z. Wu, J. Li and Y. Du, *J. Colloid Interface Sci*., 2022, **605**, 779-789.

40 F. Li, Du, X. Li, J. Shen, Y. Wang, Y. Zhu and L. Sun, *Adv. Energy Mater*., 2018, **8**, 1702598.

41 B. Wang, D. Chen, S. Jiao, Q. Zhang, W. Wang, M. Lu, Z. Fang, G. Pang and S. Feng, *New J. Chem*., 2021, **45**, 19646-19650.

42 N. Geng, W. Chen, H. Xu, M. Ding, T. Lin, Q. Wu and L. Zhang, *Ultrason. Sonochem.,* 2021, **72**, 105411.

43 Y. Lin, L. Zhao, L. Wang and Y. Gong, *Dalton Trans.,* 2021, **50**, 4280-4287.

44 F. L. Li, P. Wang, X. Huang, D. J. Young, H.F. Wang, P. Braunstein and J. P. Lang, *Angew. Chem. Int. Ed.*, 2019, **58**, 7051–7056.

45 S. Bauer, C. Serre, T. Devic, P. Horcajada, J. Marrot, G. Férey and N. Stock, *Inorg. Chem*., 2008, **47**, 7568–7576.

46 Z.P. Wu, X. F. Lu, S.Q. Zang and X. W. Lou, *Adv. Funct. Mater.*, 2020, **30**, 1910274.

47 Q. Zha, F. Yuan, G. Qin and Y. Ni, *Inorg. Chem.*, 2020, **59**, 1295–1305.

48 T. Zhang, J. Du, P. Xi and C. Xu, *ACS Appl. Mater. Interfaces* 2017, **9**, 362–370.

49 J. Huo, Y. Wang, L. Yan, Y. Xue, S. Li, M. Hu, Y. Jiang and Q-G. Zhai, *Nanoscale,* 2020, **12**, 14514-14523.

50 A. Radwan, H. Jin, D. He and S. Mu, *Nanomicro Lett.,* 2021, **13**, 132.

51 L. Yang, G. Zhu, H. Wen, X. Guan, Xun Sun, H. Feng, W. Tian, D. Zheng, X. Cheng and Y. Yao, *J. Mater. Chem. A*, 2019, **7**, 8771-8776.

52 F. Sun, G. Wang, Y. Ding, C. Wang, B. Yuan and Y. Lin, *Adv. Energy Mater.,* 2018, **8**, 1800584.

53 J. Tian, F. Jiang, D. Yuan, L. Zhang, Q. Chen and M. Hong, *Angew. Chem. Int. Ed.,* 2020, **59**, 13101–13108.

54 M. K. Sahoo, A. K. Samantara and J. N. Behera, *Inorg. Chem.,* 2020, **59,** 12252−12262.

55 D. Li, H. Liu, and L. Feng, *Energy Fuels.,* 2020, **34**, 13491−13522.

56 J. Duan, S. Chen and C. Zhao, *Nat. Commun*., 2017, **8**, 15341.

57 S. Anantharaj, S. R. Ede, K. Karthick, S. Sam Sankar, K. Sangeetha, P. E. Karthik and S. Kundu, *Energy Environ. Sci.,* 2018, **11**, 744-771.

58 S. Öztürk, G. H. Moon, A. Spieß, E. Budiyanto, S. Roitsch, H. Tüysüz and C. Janiak, *ChemPlusChem*, 2021, **86**, 1106–1115.

59 S. Anantharaj and S. Noda, *ChemElectroChem,* 2020, **7**, 2297–2308.

60 M. Chauhan, K. Prabhakar Reddy, C. S. Gopinath and S. Deka, *ACS Catal.,* 2017, **7**, 5871–5879.

61 X. Cheng, Z. Pan, C. Lei, Y. Jin, B. Yang, Z. Li, X. Zhang, L. Lei, C. Yuan and Y. Hou, *J. Mater. Chem. A,* 2019, **7**, 965-971.

62 A. Tahira, Z. Hussain, M. Vagin, U. Aftab, M. I. Abro, M. Willander and O. Nur, *Catal. Sci. Technol.,* 2019, **9**, 2879-2887.

63 M. Ding, X. Cai and H.-L. Jiang, *Chem. Sci.,* 2019, **10**, 10209-10230.

64 D. S. Hall, D. J. Lockwood, C. Bock and B. R. MacDougall, *Proc. R. Soc. A,* 2015, **471**, 20140792.

65 Y. F. Yuan, X. H. Xia, J.B. Wu, J. L. Yang, Y. B. Chen and S. Y. Guo, *Electrochim. Acta*., 2011, **56** 2627–2632.

66 X. Zhang, Y. Qiu, W. Zhang, X. Ji and J. Liu, *Sustain. Energy Fuels,* 2021, **5**, 2228-2233.

67 G. Kasparis, A. S. Erdocio, J. M. Tuffnell and N. T. K. Thanh, *CrystEngComm,* 2019, **21**, 1293-1301.

68 S. Krehula, M. Ristić, C. Wu, X. Li, L. Jiang, J. Wang, G. Sun, T. Zhang, M. Perović, M. Bošković, B. Antić, L. Kratofil Krehula, B. Kobzi, S. Kubuki and S. Musić, *J. Alloys Compd*., 2018, **750**, 687-695.

69 M. Rajamathi, P. V. Kamath and R. Seshadri, *J. Mater. Chem.,* 2000, **10**, 503-506.

70 L. Guerlou-Demourgues, C. Denage and C. Delmas, *J. Power Sources,* 1994, **52**, 269-274.

71 K. Lawson, S. P. Wallbridge, A. E. Catling, C. A. Kirk and S. E. Dann, *J. Mater. Chem. A.,* 2023, **11**, 789-799.

72 H. Bode, K. Dehmelt and J. Witte, *Electrochim. Acta.,* 1996, **11**, 1079-1084.

73 J. Yu, S. Pan, Y. Zhang, Q. Liu and B. Li, *Front. Mater.,* 2019, **6**, 1-11.

74 M. Gao, W. Sheng, Z. Zhuang, Q. Fang, S. Gu, J. Jiang and Y. Yan, *J. Am. Chem. Soc.,* 2014, **136**, 7077–7084.

75 J-Q. Xie, Y-Q. Ji, J-H. Kang, J-L. Sheng, D-S. Mao, X-Z. Fu, R. Sun and C-P. Wong, *Energy Environ. Sci.,* 2019, **12**, 194-205.

76 J. Zhao, J.-J. Zhang, Z.-Y. Li and X-H. Bu, *Small,* 2020, **16**, 2003916.

77 M. K. Adak, L. Mallick, K. Samanta and B. Chakraborty, *J. Phys. Chem. C,* 2023, **127**, 154–168.

78 Z. W. Seh, J. Kibsgaard, C. F. Dickens, I. Chorkendorff, J. K. Nørskov and T. F. Jaramillo, *Science,* 217, **335**, 6321.

79 M. C. Biesinger, L. W. M. Lau, A. R. Gerson, and R. S. C. Smart, *Phys. Chem. Chem. Phys.,* 2012**, 14**, 2434–2442.

80 A. P. Grosvenor, B. A. Kobe, M. C. Biesinger and N. S. McIntyre, *Surf. Interface Anal.*, 2004, **36**, 1564–1574.

81 R. P. Gupta and S. K. Sen, *Phys. Rev. B.*, 1975, **12**, 15-19.

82 X. Han, Y. Niu, C. Yu, Z. Liu, H. Huang, S. Li, W. Guo, X. Tan and J. Qiu, *Nano Energy.,* 2020, **69**, 104367.

83 G. T. Vuong, M.-H. Phama and T. O. Do, *CrystEngComm*, 2013, **15**, 9694-9703.

Bimetallic CPM-37(Ni,Fe) metal-organic framework: enhanced porosity, stability and tunable composition

Soheil Abdpour, Marcus. N. A. Fetzer, Robert Oestreich, Thi Hai Yen Beglau, István Boldog* and Christoph Janiak*

Institut für Anorganische Chemie und Strukturchemie, Heinrich-Heine-Universität Düsseldorf, 40204 Düsseldorf, Germany

soheil.abdpour@hhu.de, marcus.fetzer@uni-duesseldorf.de, robert.oestreich@uni-duesseldorf.de, beglau@uni-duesseldorf.de, boldogi@hhu.de, janiak@hhu.de

Contents

Section 1 Synthesis

Section 1.1 Synthesis of N,N',N''-tris-(pyrid-4-yl)-trimesamide (TPAMA)

Materials used

3A molecular sieves (CAS: 308080-99-1), tetrahydrofuran, THF (CAS: 109-99-9, anhydrous, ⩾99.9%), 1,3,5-benzene tricarboxytrichloride (CAS: 4422-95-1, 98%), and triethylamine (CAS:121-44-8, 99.5%) were purchased from Merck GmbH, 4-aminopyridine (CAS: 504-24-5, 98%), dimethylsulfoxide, DMSO (CAS: 67-68-5 99%), and acetone (CAS: 67-64-1, ACS reagent, ⩾99.5%) from Thermo Fisher Scientific. All solvents were dried over molecular sieves. Prior to use, THF and triethylamine were freshly distilled. Unless otherwise described, all reactions were carried out under nitrogen atmosphere.

Synthesis

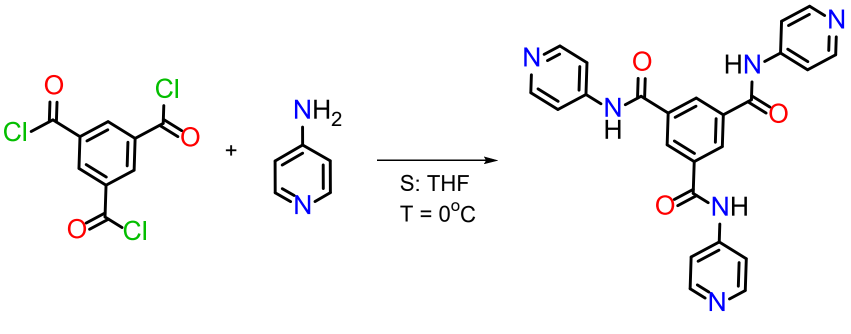

TPAMA

The TPAMA ligand was synthesized according to the literature with slight modifications.[1]

4-Aminopyridine (3.5 g, 37.2 mmol) was dissolved in a mixture of triethylamine (7.3 mL, 52.7 mmol) and THF (40 mL) and added dropwise to a solution of 1,3,5-benzene tricarboxytrichloride (3.3 g, 12.4 mmol) in THF at 0 °C under stirring. The reaction mixture was stirred for 8 h and allowed to warm up to room temperature. The crude product was filtered off, washed with THF (4x30 mL) and recrystallized from a mixture of H_2O (300 mL) and DMSO (140 mL). The pale yellowish precipitate was filtered off and washed with acetone (3×30 mL). The obtained product was dried under high vacuum (~ 5×10^{-2} mbar) at 30 °C overnight (4.0 g, 9.1 mmol, 73%).

Section 2 Analytics

Section 2.1 Nuclear magnetic resonance spectroscopy analysis

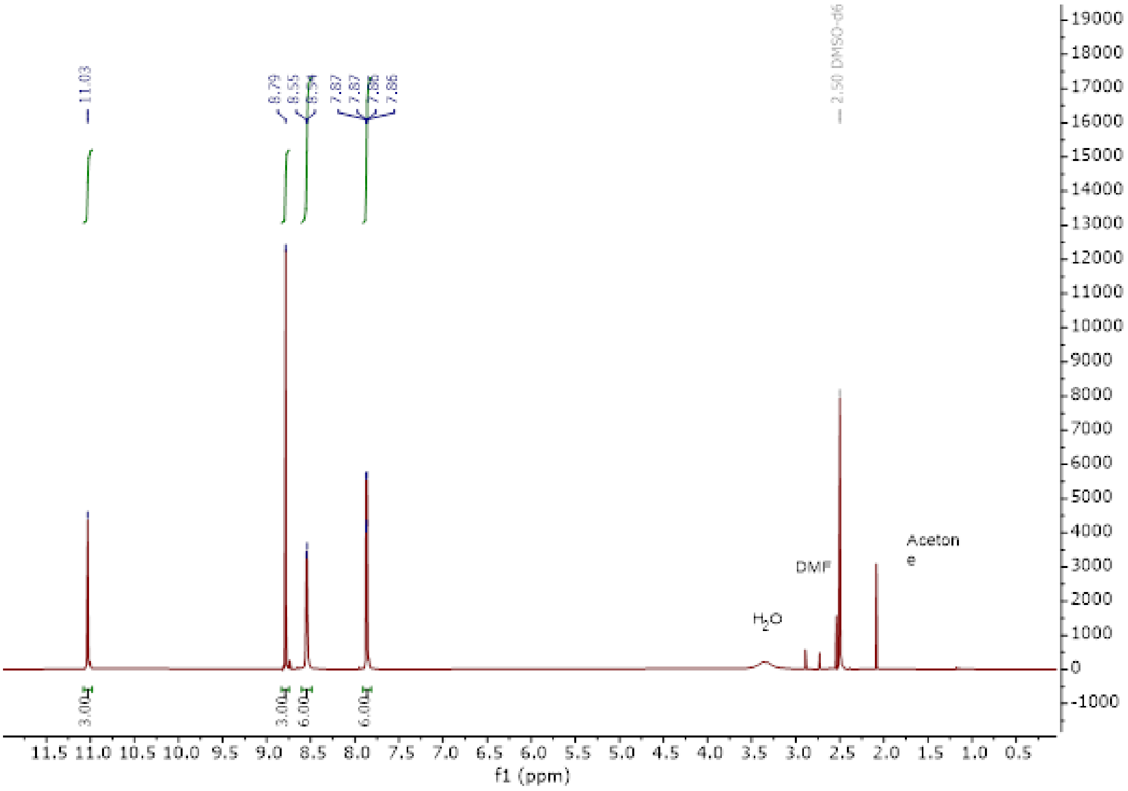

Fig. S1 NMR spectrum of N,N',N''-tris-(pyrid-4-yl)-trimesamide (TPAMA).
^{1}H NMR (DMSO-d_6, 300 MHz) δ: 11.03 (s, 3H), 8.79 (s, 3H), 8.55 (d, J = 5.6 Hz, 6H), 7.89-7.82 (m, 6H).

Section 2.2 Sample preparation for atomic absorption spectroscopy (AAS)

Analyte preparation method: a precisely weighted dried (*i.e.* degassed in vacuum until no guest molecules were present) sample of approx. 5 mg was suspended in *aqua regia* solution (3:1 conc. HCl and HNO_3 mixture) and the liquid was slowly boiled under stirring in a fume-hood until near complete evaporation of the liquid. The treatment by aqua regia solution was repeated two times, which yielded a clear solution prior to final evaporation. Finally, the obtained residue was dissolved in a fresh portion of diluted *aqua regia* (5 mL *aqua regia* + 10 mL ultra-pure water) and stirred overnight. The solution was filtered, the filter was carefully washed multiple times with ultra-pure water, and the filtrate was diluted precisely to 50 mL in a volumetric flask to yield the solution used for the determination of Ni and Fe content in the samples.

Section 2.3 Sample preparation for powder X-ray diffraction (PXRD) and additional information regarding the measurements

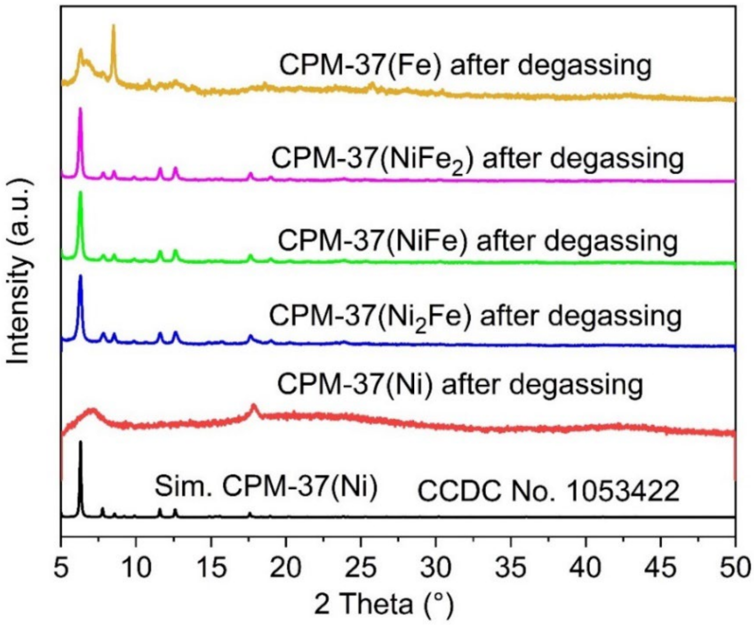

Fig. S2 PXRD patterns of the samples after the degassing in vacuum (5 10^{-2} Torr) at 60 °C for 16 h.

The CPM-37 samples were treated by CH_2Cl_2 in order to exchange the less-volatile guest molecules. For that ~30 mg of a sample was soaked in 30 mL CH_2Cl_2 for 5 days, while the CH_2Cl_2 was refreshed every day by accurate decantation and refilling the vial and degassing in vacuum (~5 10^{-2} Torr) at 60 °C for 16 h.

The PXRD of CPM-37(Ni) exhibited broad peaks, particularly well-recognizable around 6.4°, showing partial loss of crystallinity (note that the as-synthesized material consists of well-formed single crystals, whose identity were confirmed by single crystal structure determination, thereby demonstrating the excellent crystallinity). Similarly, the CPM-37(Fe) has also suffered partial loss of crystallinity. In contrary, all the bimetallic CPM-37(Ni,Fe) samples showed sharp PXRD peaks and high surface areas after degassing, indicating that the improved stability evidently stems from the presence of both iron and nickel, i.e. their synergism in the context of structural stability.

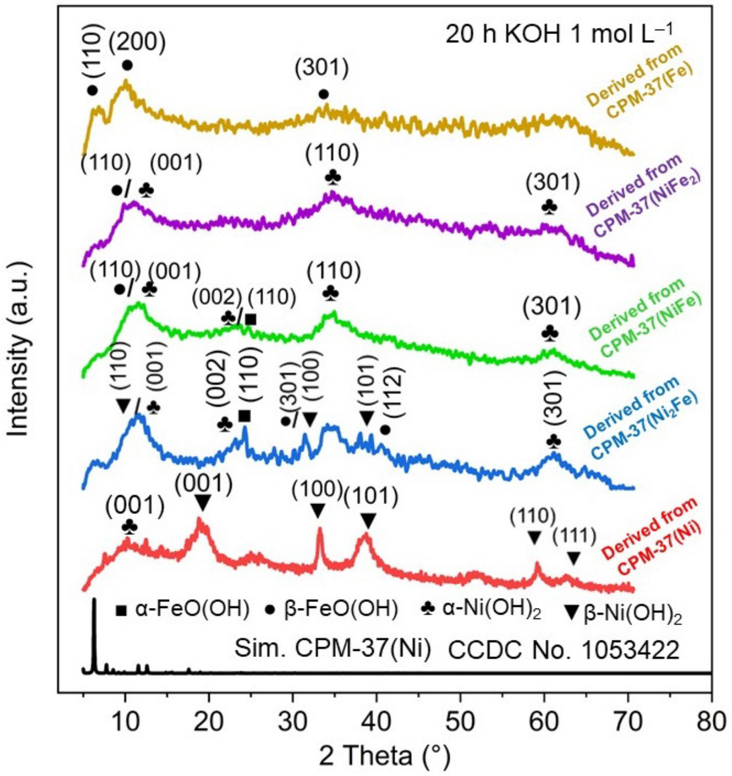

Fig. S3 PXRD patterns of the CPM-37(Ni), CPM-37(NiFe), CPM-37(Ni_2Fe) CPM-37($NiFe_2$) and CPM-37(Fe) after 20 h in 1 mol L^{-1} KOH solution.

Section 2.4 Infrared spectroscopy (IR)

Section 2.4.1 Sample preparation

Fourier transform infrared spectroscopy (FT-IR) measurements were conducted by a Bruker TENSOR 37 IR spectrometer in the range of 4000–400 cm^{-1}. About 0.1 mg of the sample was mixed with dried KBr (the mass percentage of sample per KBr was about 1-2%) and grinded to fine powder. The resulted fine powder was pressed between two stainless steel disks to form a pellet, which was the actual subject of the measurement.

Table S1 FT-IR band assignment for as-synthesized CPM-37(Ni), CPM-37(Fe), and the bimetallic CPM-37(Ni,Fe) series (cm^{-1}).

Vibration	**CPM-37(Ni) (cm^{-1})**	**CPM-37(Ni$_2$Fe) (cm^{-1})**	**CPM-37(NiFe) (cm^{-1})**	**CPM-37(NiFe$_2$) (cm^{-1})**	**CPM-37(Fe) (cm^{-1})**
ѵ (OH)[2]	3434	3421	3401	3421	3434
ѵ (C_{Ar}H)[3]	2923	2962 2921	2970 2929	2962 2917	2929
ѵ (N–H)[4] (amide)	3085	3078	3083	3087	3074
v(C=O) (of the residual DMF) / δ(O–H)[5]	1664	1699	1691	1699	1695
ѵ$_{as}$ (OCO)[6]	1602 1506	1598 1513	1600 1512	1600 1515	1600 1613
ѵ$_s$(OCO) [7]	1384 1332	1394 1338	1402 1336	1392 1324	1398 1332
C–N amide[8]	1290	1292	1294	1292	1294
ѵ (C–N)(of DMF)[9]	1209	1296	1215	1216	1207
ѵ (C–N) (of DMF)/ѵ(C–C)$_{Ar}$[10] and	1101	1110	1112	1113	1107
ρ(C–H)$_{Ar}$, ɣ(C–H)$_{Ar}$[11]	1062 1020	….. 1027	1066 1027	…… 1020	….. 1014
δ(C–H)$_{Ar}$ /ѵ (C–C)$_{Ar}$ [6]	837 769	831 771	825 770	837 767	831 769
Ni–O, Fe–O[12]	536	538	536	537	537
Fe–O[13]	-	447	455	468	464

v = stretching vibration (vas= asymmetric, vs = symmetric vibration), δ = bending vibration (ρ = in plane, γ = out of plane vibration), Ar: the moiety belongs to an aryl group.

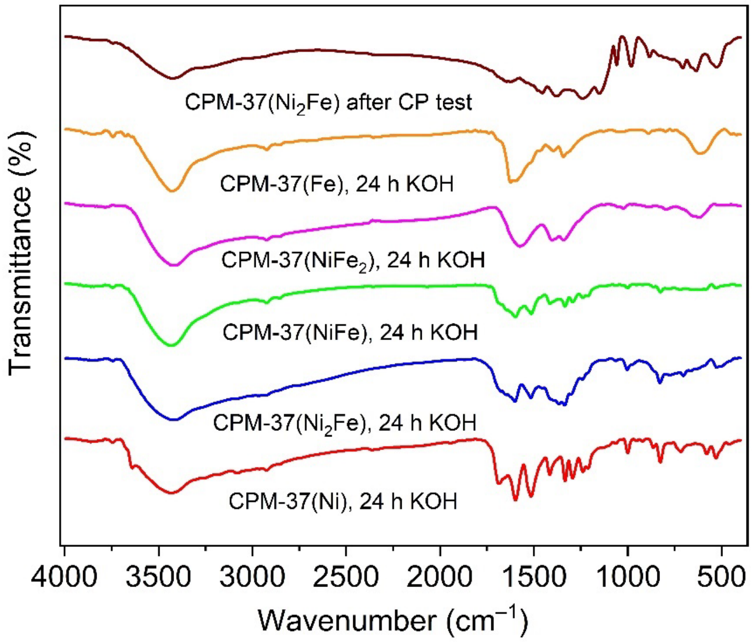

Fig. S4 FT-IR spectra of the CPM-37 after 20 h immersing in KOH 1 mol L^{-1}.

Table S2 Assignments of FT-IR-bands in the spectra of CPM-37(Ni), CPM-37(Fe), and the bimetallic CPM-37(Ni,Fe) series after treatment of the sample by 1 mol L^{-1} KOH aqueous solution during 20 h and after CP test for 20 h.

Allocation	**CPM-37(Ni) (cm^{-1})**	**CPM-37(Ni_2Fe) (cm^{-1})**	**CPM-37(NiFe) (cm^{-1})**	**CPM-37($NiFe_2$) (cm^{-1})**	**CPM-37(Fe) (cm^{-1})**	**CPM-37(Ni_2Fe) (cm^{-1}) after CP test**
ν (OH)[2]	3433	3437	3438	3425	3431	3444
O–H bend layered in H_2O [14]	1600	1606	1601	1587	1618	----
O–H freely rotating water molecules [15]	1510 1330	1523 1361	1508 1379	---- 1378	---- 1379	---- 1363
Combination of lattice modes[15]	1000 827	1008 823	1012 828	1022 813	1043 877	1058 981
Translation modes of OH,[16] influenced by Fe^{3+}	----	----	----	611	597	634
ν(Ni–O)[17]	528	516	530	----	----	518

Section 2.5 Optical microscopy

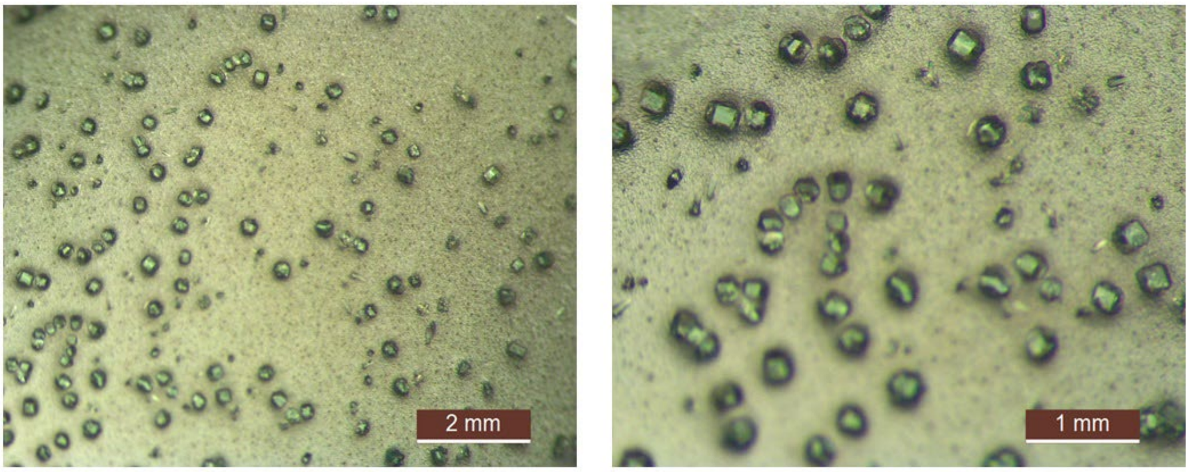

Fig. S5 Light microscopic images of the synthesized CPM-37(Ni) sample.

Section 2.6 Scanning electron microscopy (SEM) and energy dispersive X-ray analysis (EDX)

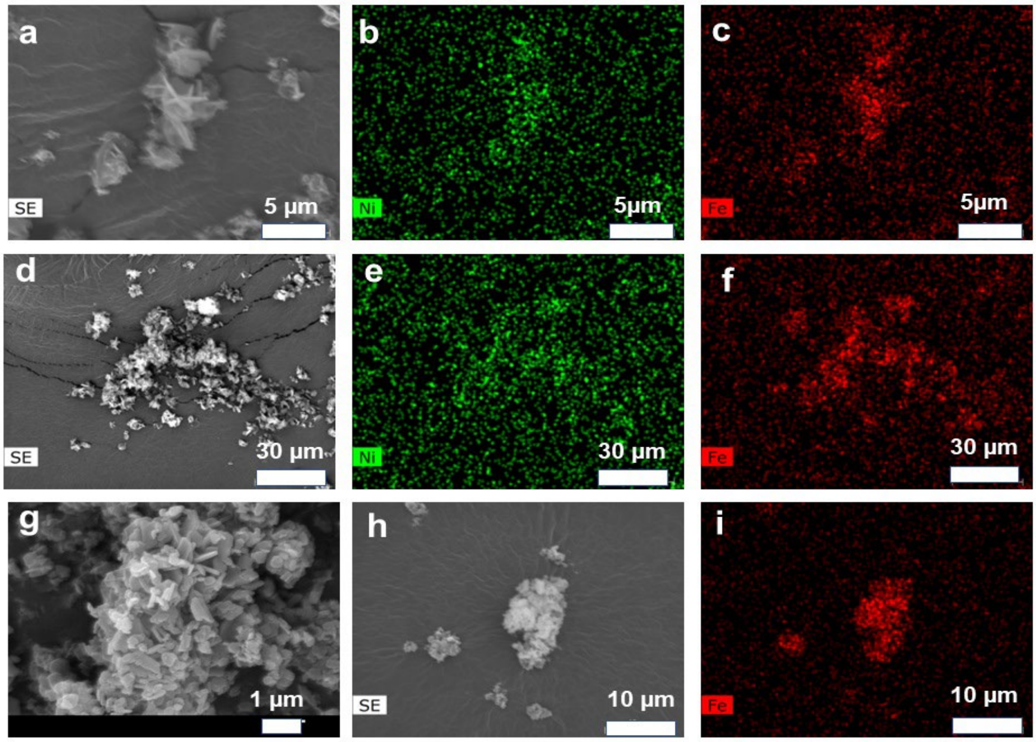

Fig. S6 SEM-EDX mapping images: (a-c) CPM-37(NiFe); (c-f) CPM-37(NiFe2); (f-i) CPM-37(Fe).

Table S3 Raw SEM-EDX data for the CPM-37 samples [a)].

Element / **Sample**	**Fe**		**Ni**	
	Wt%(raw)	**At%(raw)**	**Wt%(raw)**	**At%(raw)**
CPM-37(Fe)	11.6	3.5	----	-----
CPM-37(Ni$_2$Fe)	7.7	2.5	12.7	4.0
CPM-37(NiFe)	8.8	2.9	8.8	2.8
CPM-37(NiFe$_2$)	12.2	3.9	5.5	1.7
CPM-37(Ni)	----	----	15.0	4.5

a) Values for C, O, N and Au, Cu which stem from the sample holder are not given, hence the given values do not add up to 100%.

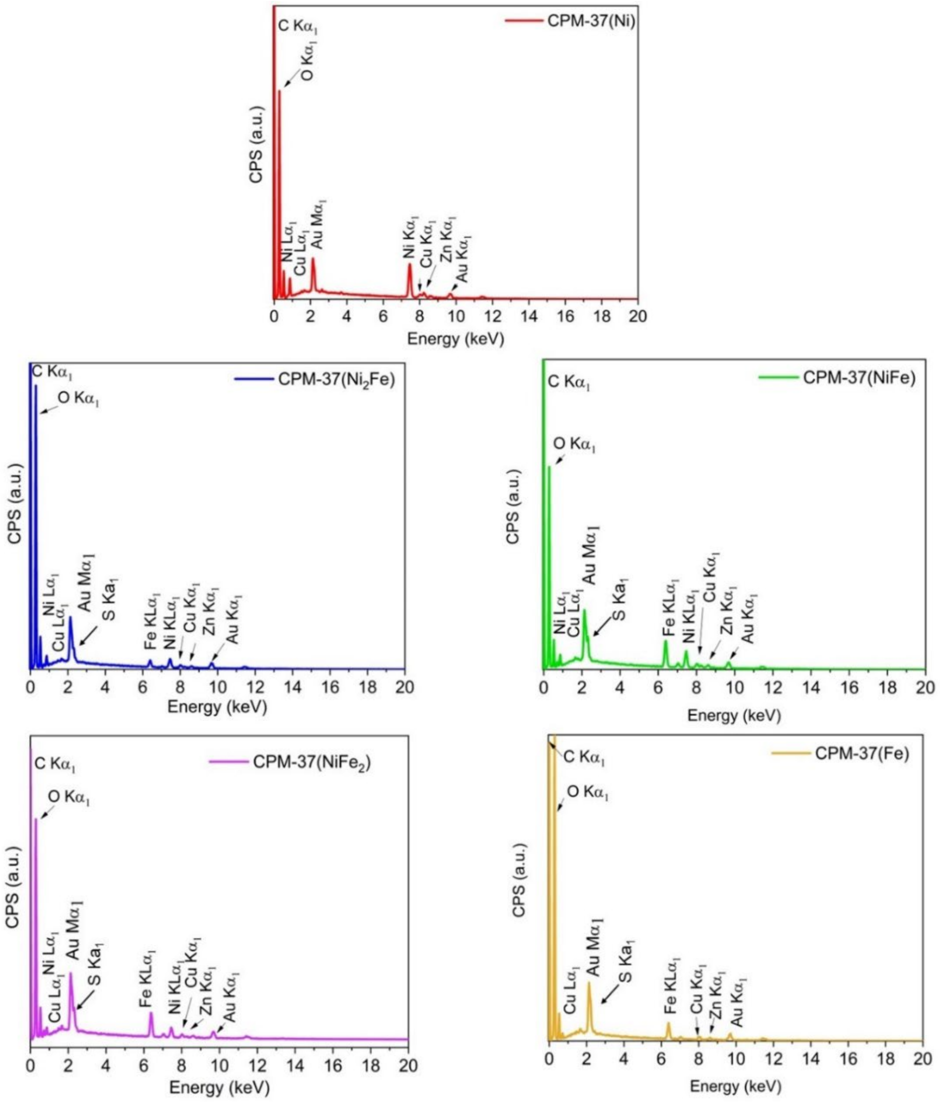

Fig. S7 SEM-EDX spectra of the CPM-37 samples.

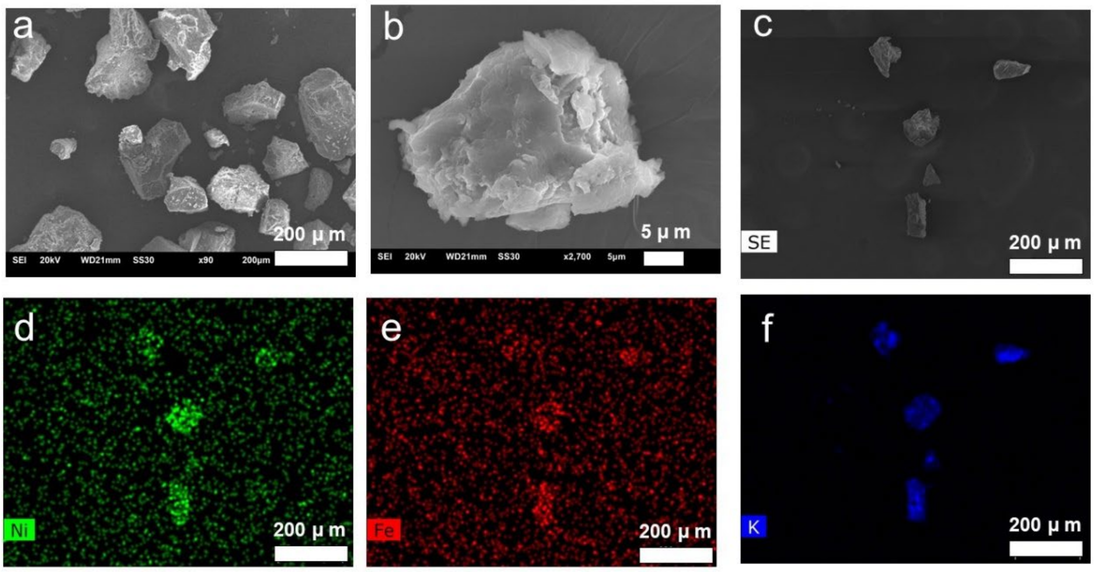

Fig. S8 SEM-EDX mapping of CPM-37(Ni_2Fe) after treatment of the sample by 1 mol L^{-1} KOH aqueous solution during 20 h.

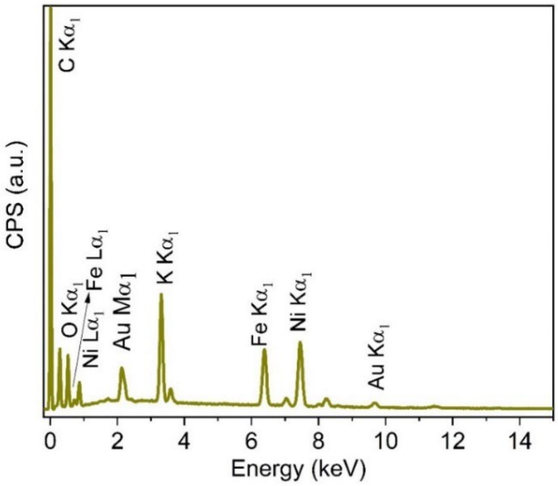

Fig. S9 SEM-EDX spectrum of CPM-37(Ni_2Fe) after treatment of the sample by 1 mol L^{-1} KOH aqueous solution during 20 h.

Table S4 SEM-EDX result of CPM-37(Ni_2Fe) soaking in 1 mol L^{-1} KOH aqueous solution for 20 h.

Element [a)]	Weight%(raw)	Atomic% (raw)	Relative ratio
Ni	5.4	4.7	2.04
Fe	2.5	2.3	1

[a)] Values for C, O, K, Au and Cu which stem from the sample holder are not given, hence the given values do not add up to 100%.

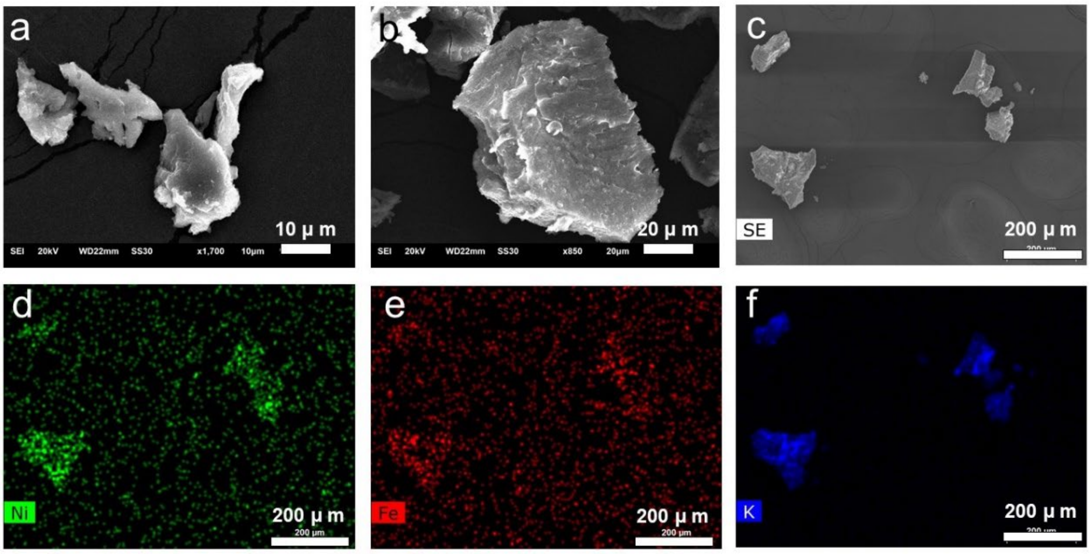

Fig. S10 SEM-EDX mapping of CPM-37(Ni_2Fe) after chronopotentiometry analysis (CP) in 1 mol L^{-1} KOH aqueous solution for 20 h.

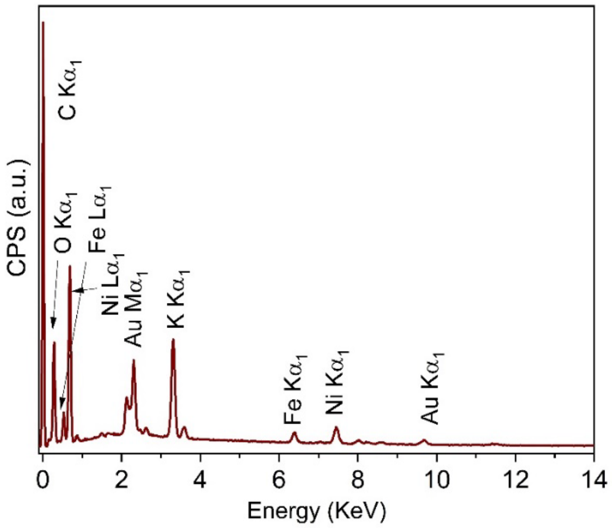

Fig. S11 SEM-EDX spectrum of CPM-37(Ni_2Fe) after CP in 1 mol L^{-1} KOH aqueous solution for 20 h.

Table S5 SEM-EDX result of CPM-37(Ni_2Fe) after CP in 1 mol L^{-1} KOH aqueous solution for 20 h.

Element [a)]	**Weight% (raw)**	**Atomic% (raw)**	**Relative ratio**
Ni	15.5	15.1	1.7
Fe	6.7	8.9	1

[a)] Values for C, O, Au, K and Cu which stem from the sample holder are not given, hence the values do not add up to 100%.

Section 2.7 Thermogravimetry analysis (TGA)

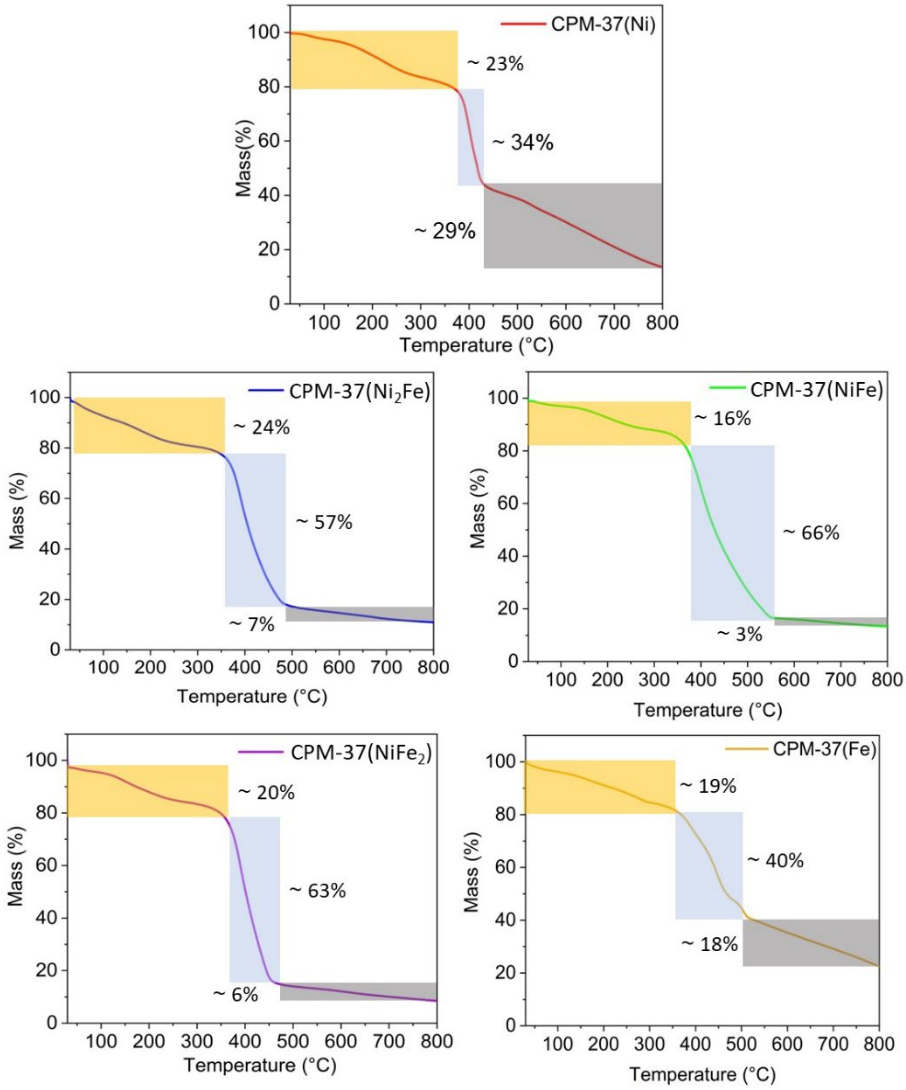

Fig. S12 TGA curves for CPM-37(Ni), CPM-37(Ni_2Fe), CPM-37(NiFe), CPM-37($NiFe_2$), and CPM-37(Fe) samples. The measurements were done using N_2 as a carrier gas with a heating rate of 5 K min^{-1}.

Section 2.8 X-ray photoelectron spectroscopy (XPS)

Section 2.8.1 X-ray photoelectron spectroscopy (XPS) of CPM-37(Ni), CPM-37(Fe), and CPM-37(Ni_2Fe)

The XPS spectra of CPM-37(Ni), CPM-37(Fe), and CPM-37(Ni_2Fe) are presented in Fig. S13a, confirming the presence of Ni, C, O, and N in CPM-37(Ni); Fe, C, O, and N in CPM-37(Fe); and Ni, Fe, C, O, and N in CPM-37(Ni_2Fe). The high-resolution XPS spectrum of C1s for all samples was subjected to deconvolution, resulting in four distinct peaks attributed to (C–C, C–H), (C–N), (C–O–C, C–OH), and (O–C=O) bands.[18] The position of each peak is assigned in Table S8. The high-resolution spectrum of O1s can be deconvoluted into three main peaks corresponding to M–O, O=C–O, and O–H functionalities.[19,20] The positions of these peaks are provided in Table S9. Moreover, N 1s in the samples can be deconvoluted to two peaks (amidic N) and (pyridinic N) [21] Fig. S13 d. It should be considered that the pyridinic nitrogen are located almost at the same binding energy (399.5) independently on whether it is coordinated or not. The binding energy peaks of N1s are listed in Table S10.

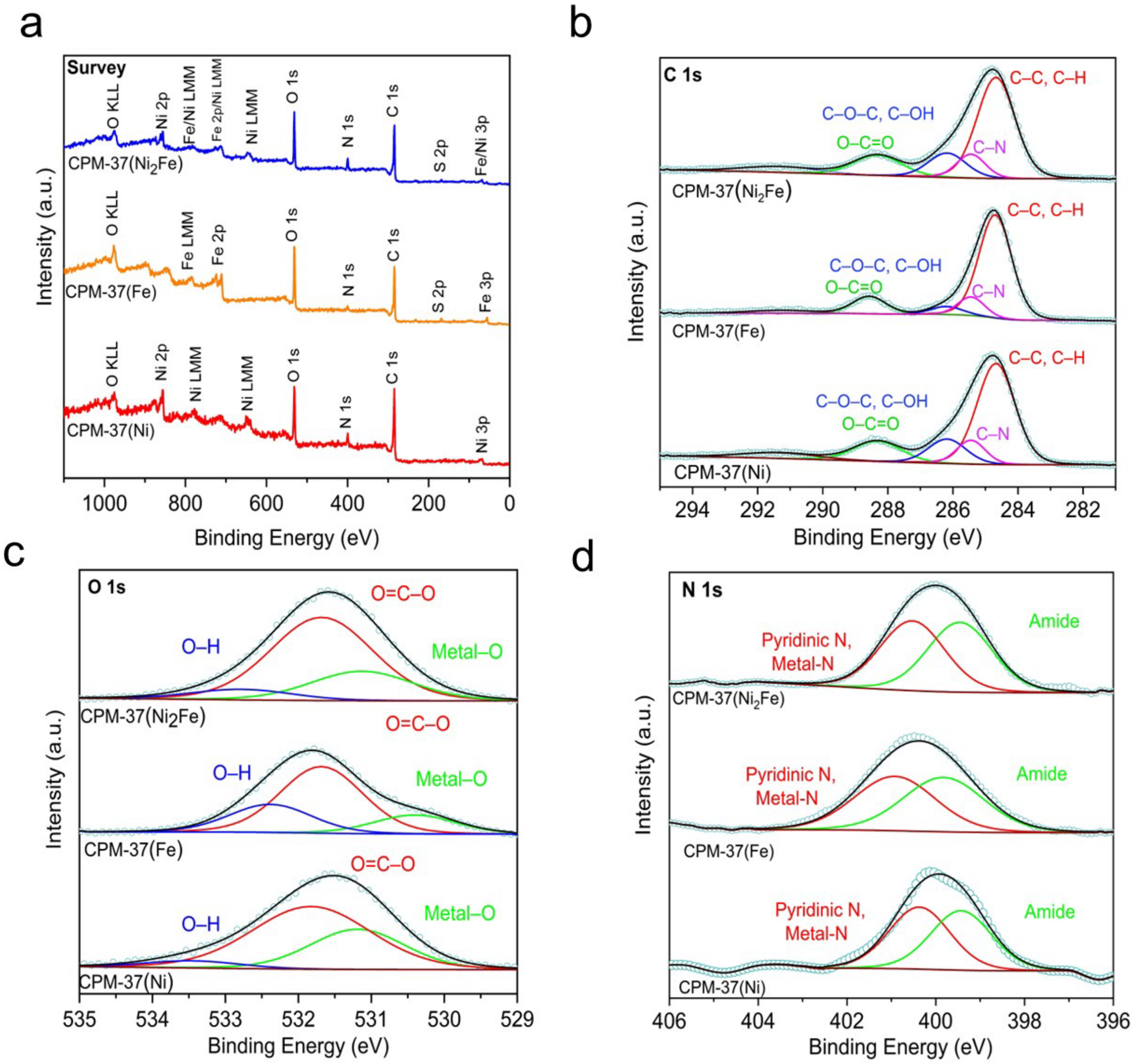

Fig. S13 XPS survey and high-resolution spectra of CPM-37(Ni), CPM-37(Fe) and CPM-37(Ni$_2$Fe).(a) Survey spectra of CPM-37(Ni), CPM-37(Fe) and CPM-37(Ni$_2$Fe); (b) C 1s high-resolution spectra of CPM-37(Fe) and CPM-37(Ni$_2$Fe); (c) O 1s high-resolution spectra of CPM-37(Fe) and CPM-37(Ni$_2$Fe); (d) N 1s high-resolution spectra of CPM-37(Fe) and CPM-37(Ni$_2$Fe).

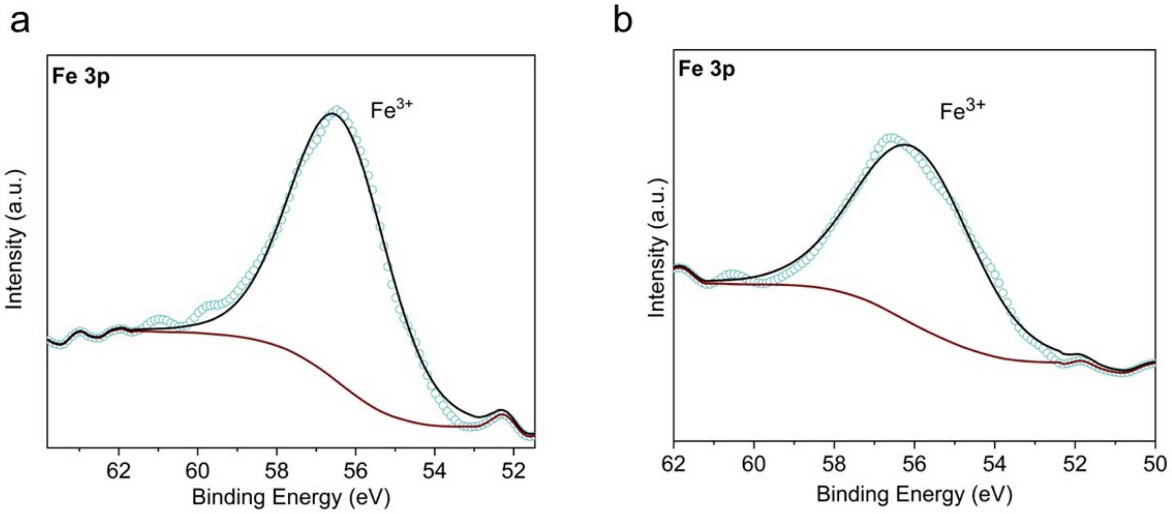

Fig. S14 High-resolution spectrum of Fe 3p: a) CPM-37(Fe), b) CPM-37(Ni_2Fe).

Fig. S14 illustrates the deconvolution of the high-resolution spectrum of Fe 3p, revealing main peaks at 56.4 and 56.3 eV for CPM-37(Fe) and CPM-37(Ni_2Fe), respectively. These results confirm the presence of Fe^{3+} as the predominant oxidation state of Fe in both CPM-37(Fe) and CPM-37(Ni_2Fe).[22]

Table S6 XPS quantitative elemental analysis of CPM-37(Ni), CPM-37(Fe), and CPM-37(Ni_2Fe).

Catalyst	Ni (At%)	Fe (At%)	O (At%)	N (At%)	S (At%)	C (At%)
CPM-37(Ni)	3.76	-----	18.27	5.65	-----	72.32
CPM-37(Fe)	-----	4.01	17.34	8.15	2.27	68.23
CPM-37(Ni_2Fe)	3.11	1.74	16.08	6.82	1.25	71.00

Table S7 XPS peak types and corresponding binding energies of carbon in CPM-37(Ni), CPM-37(Fe) and CPM-37(Ni_2Fe).

Element	Characteristic peak	Catalyst	C–C,C–H (eV)	C–N (eV)	C–O–C, C–OH (eV)	O–C=O (eV)
C	C 1s	CPM-37(Ni)	284.7	285.4	286.2	288.5
		CPM-37(Fe)	284.7	285.5	286.2	288.6
		CPM-37(Ni_2Fe)	284.7	285.5	286.2	288.5

Table S8 XPS peak types and corresponding binding energies of oxygen in CPM-37(Ni), CPM-37(Fe) and CPM-37(Ni_2Fe).

Element	Characteristic peak	Catalyst	Metal–O (eV)	O=C–O (eV)	O–H (eV)
O	O 1s	CPM-37(Ni)	531.1	531.8	533.2
		CPM-37(Fe)	530.4	531.7	532.4
		CPM-37(Ni_2Fe)	531.2	531.7	532.8

Table S9 XPS peak types and corresponding binding energies of nitrogen in CPM-37(Ni), CPM-37(Fe) and CPM-37(Ni_2Fe).

Element	Characteristic peak	Catalyst (eV)	N_{amide} (eV)	$N_{Pyridine}$–Metal (eV)
N	N1s	CPM-37(Ni)	399.4	400.3
		CPM-37(Fe)	399.8	400.9
		CPM-37(Ni_2Fe)	399.5	400.6

Table S 10 XPS-based metal ratios and the ratios between different oxidation states of nickel and iron in CPM-37(Ni), CPM-37(Fe) and CPM-37(Ni_2Fe).

Sample		At% a)	Ni/Fe		At% b)	Position (eV)	M^{2+}/M^{3+}
CPM-37(Ni)	Ni	3.76	-----	Ni^{3+}	4.6	857.5	4.9
				Ni^{2+}	22.4	856.0	
	Fe	-----		Fe^{3+}	-----	-----	----
				Fe^{2+}	-----	-----	
CPM-37(Fe)	Ni	----	-----	Ni^{3+}	-----	-----	----
				Ni^{2+}	-----	-----	
	Fe	4.01		Fe^{3+}	36.3	711.6	----
				Fe^{2+}	-----	-----	
CPM-37(Ni_2Fe)	Ni	3.11	1.8	Ni^{3+}	10.1	857.1	2.4
				Ni^{2+}	24.0	855.9	
	Fe	1.74		Fe^{3+}	43.8	711.9	----
				Fe^{2+}	-----	-----	

a) From XPS survey spectrum, b) Based on the Ni $2p_{3/2}$ and Fe $2p_{3/2}$ regions in XPS, At% Ni 2p1/2 and the satellites are not given, hence the values do not add up to 100%.

Section 2.8.2 X-ray photoelectron spectroscopy (XPS) of 37(Ni2Fe) after OER

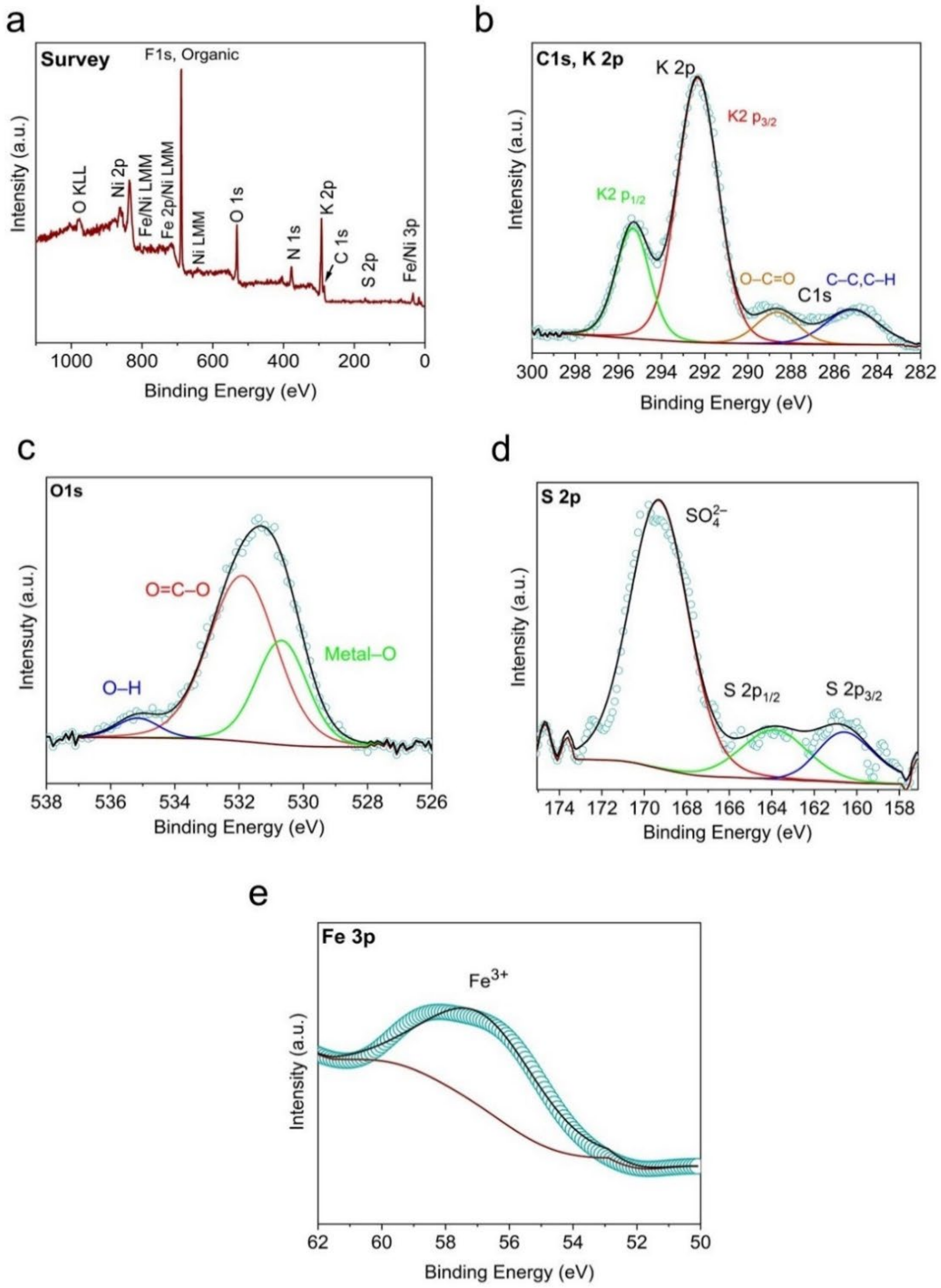

Fig. S15 XPS survey and high-resolution spectra of CPM-37(Ni_2Fe) after CP in 1 mol L^{-1} for 20 h.(a) Survey spectra of CPM-37(Ni_2Fe) CPM-37(Ni_2Fe) after CP in 1 mol L^{-1} for 20 h ; (b) C 1s and K 2p high-resolution spectra of CPM-37(Ni_2Fe) after CP in 1 mol L^{-1} for 20 h; (c) O 1s high-resolution spectra of CPM-37(Ni_2Fe) after CP in 1 mol L^{-1} for 20 h; (d) S 2p high-resolution spectra of CPM-37(Ni_2Fe) after CP in 1 mol L^{-1} for 20 h.

The XPS spectra of derived electrode materials from CPM-37(Ni_2Fe) after the CP test are presented in Fig. S15a, confirming the presence of and Ni, Fe, C, O, N, K, and F in CPM-

37(Ni_2Fe). Note that the presence of potassium is due to the treatment by the 1 mol L^{-1} KOH alkaline solution, while the fluorine is present in the residues of polyvinylidene fluoride (PVDF), which is used as a binder to for the electrode coating. Fig. S15b presents the high-resolution spectrum of K 2p (K $2p_{1/2}$ at 295.3 eV and K $2p_{2/3}$ at 292.3 eV), along with C1s (C–C, C–H at 284.9 eV, associated with the binder) and (O–C=O at 288.5 eV, associated with adventitious carbon, e.g. in the form of metal (hydroxo)carbonates forming due to anodic oxidation of carbon containing species).[23] The high-resolution spectrum of O1s can be deconvoluted into three main peaks which are assumed to be corresponding to M–O (531.8 eV), O=C–O (532.5 eV) and O–H (535.5 eV) (originating from adventitious carbon or residual organic linkers.[19] Fig. 15d exhibits a sharp peak located at 169.4 eV, which can be attributed to the sulfate groups originating from $FeSO_4 \cdot 7H_2O$. Additionally, two smaller peaks at 163.7 and 160.5 correspond to S $2p_{1/2}$ and S$2p_{3/2}$, respectively.[24] Deconvolution of the high-resolution spectrum of Fe 3p revealed main peaks at 57.3 eV, confirming the presence of Fe^{3+} as the predominant oxidation state of Fe in the derived electrode materials from CPM-37(Ni_2Fe) after the OER.

Table S11 The metal ratios and the ratios between different oxidation states of Derived electrode materials from CPM-37(Ni_2Fe) after CP test.

Sample		**At% a)**	**Ni/Fe**		**At% b)**	**Position (eV)**	**M^{3+}/M^{2+}**
Derived electrode materials from CPM-37(Ni_2Fe) after the CP test	Ni	2.61	1.78	Ni^{3+} c)	10	858.7	0.42
				Ni^{2+} d)	24	855.7	
	Fe	1.46		Fe^{3+}	42.6	709.9 e) 711.2 712.7 713.9	----
				Fe^{2+}	-----		
a) From XPS survey spectrum, b) Based on the Ni $2p_{3/2}$ and Fe $2p_{3/2}$ regions in XPS. b) derived from NiO(OH) d) derived from $Ni(OH)_2$, e) Gupta and Sen (GS) multiplets fitting method.							

Section 2.9 Crystal structure of the CPM-37(Ni)

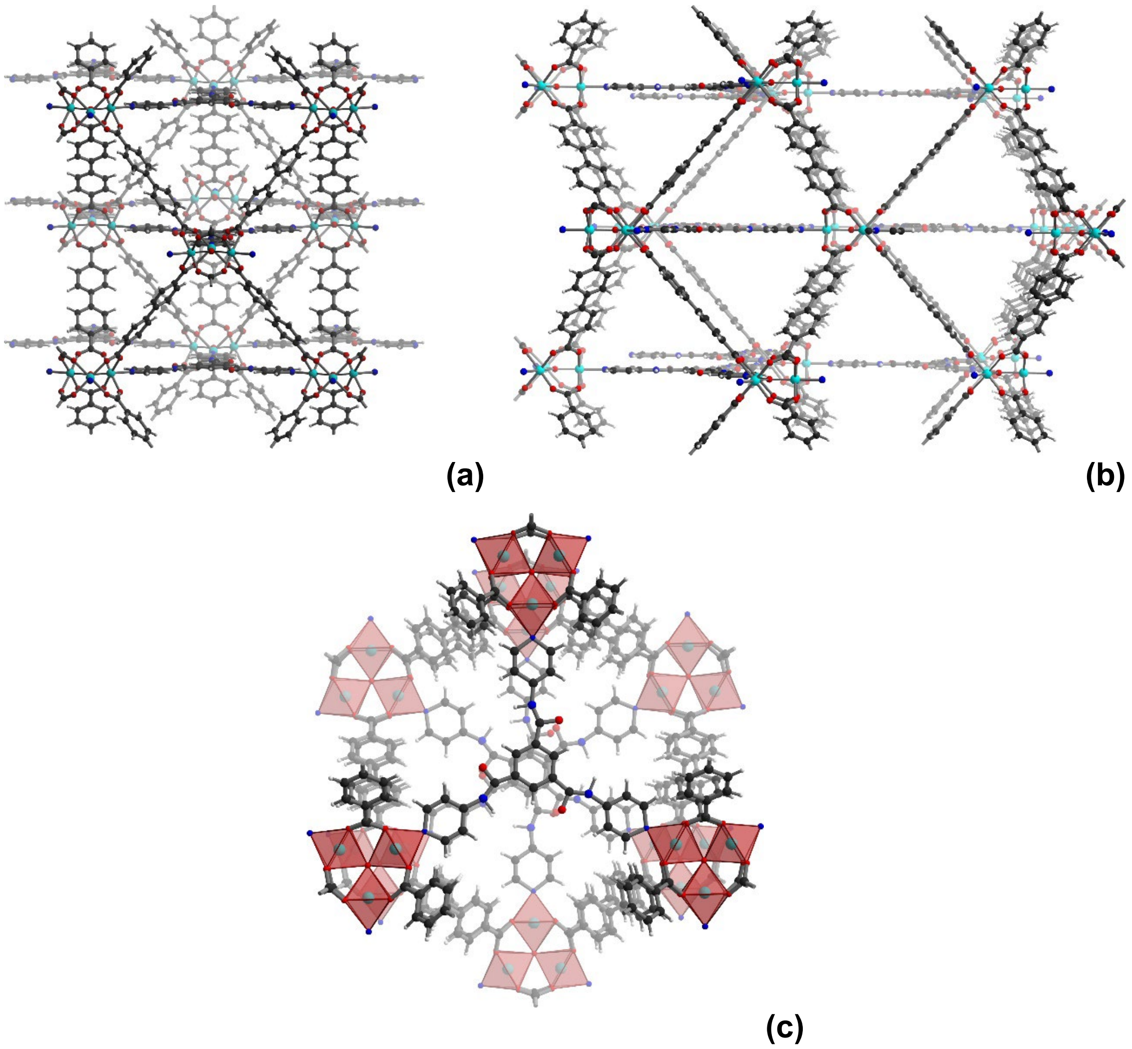

Fig. S16 Views on the CPM-37(Ni) structure:[25] a) along the (-110) direction demonstrating the pore-enclosures; b) the view on the structure along the *a*-axis with the well-visible triangular pore-channels; c) the view on the structure along the 6_3 axis.

Section 2.10 Electrochemical section

Section 2.10.1 Faradaic Efficiency

To assess the Faradaic efficiency regarding oxygen generation, the method reported by Mascaros et al. was used,[26] using, in our case, a constant current of 50 mA cm^{-2}. The oxygen level in the electrochemical cell was monitored during the process using the Ocean Optics NeoFOX sensor system coupled with a FOSPOR probe. The FOSPOR probe was calibrated using a two-point method using nitrogen atmosphere (0% O_2) and in ambient air (21% O_2). The electrolyte was thoroughly freed from the initially dissolved oxygen by continuous bubbling of nitrogen gas for at least one hour before commencing the chronopotentiometric test.

The number of oxygen molecules produced during the electrolysis was determined using the subsequent formula, which assumes the applicability of the ideal gas law for the analysed gas mixture at atmospheric pressure:

$$n_{O2,exp} = x_{O2,frac}\, P_{total}\, V_{gas}\ \ R^{-1}\, T^{-1}$$

where $x_{O2,frac}$ is the fraction of oxygen in the evolved gaseous mixture as detected by the FOSPOR probe; P_{total} is the pressure of gas mixture (1 atm); V_{gas} (L) is the evolved gas volume at atmospheric pressure; R is the gas constant, 0.082 (atm L K^{-1} mol^{-1}); and T is the temperature (293 K).

The theoretical evolved Faradaic oxygen is given by:

$$n_{O2,far} = Q.n_e^{-1}F^{-1}$$

where, Q (measured in C, coulombs) represents the total electric charge transferred within the system; n_e signifies the molar amount of electrons for the production of one mole of oxygen (equals to 4), and F designates the Faraday constant (equal to 96485 C mol^{-1}). The Faradaic efficiency (expressed in percentage), denoted as FE, is determined using the following equation:

$$FE = \frac{n_{O2,exp}}{n_{O2,far}} * 100$$

Section 2.10.2 Comparison of the OER performance for different reported materials)

Table S12 Comparison of OER performance for the previously reported bimetallic nickel and iron MOF precatalysts and nickel-based catalysts in aqueous alkaline medium, KOH 1 mol L^{-1}, at 50 mA cm^{-2}.

Material	**η (mV)**	**Tafel slope (mV dec^{-1})**	**Electrode type**	**Ref.**
CPM-37(Ni_2Fe)	290	39	NF	This work
NiSe@NiOOH	300	162	NF	27
Ni–Fe -MOF	270	49	NF	28
CD/$NiCo_2O_4$	390	91	NF	29
(Co/Ni/Cu) hydroxyphosphate	370	88	NF	30
Co_3O_4/$NiCo_2O_4$	407	84	NF	31
Porous Nickel–Iron Oxide	420	42	NF	32
FeNi-DOBDC	270	49	GC	28
$Ni(OH)_2$	330	140	NF	33
NiFeSe	300	80	NF	34
NiFeMoSe	253	36	NF	34
P-containing $NiCo_2S_4$	300	70	NF	35
Fe-Ni_3S_2	287	120	NF	36
NiCo-MOF	270	35.4	NF	37
Hierarchical Porous Ni_3S_4	300	40	NF	38
NCF/Ni-BDC	350	39.5	NF	39
Defective-CeO_{2}-x decorated MOF(Ni/Fe)	254	34	NF	40

References

---

1 S. Hasegawa, S. Horike, R. Matsuda, S. Furukawa, K. Mochizuki, Y. Kinoshita and S. Kitagawa, *J. Am. Chem. Soc.,* 2007, **129**, 2607–2614.
2 P. Maniam and N. Stock, *Inorg. Chem.,* 2011, **50**, 5085-5097.
3 C. R. Wade and M. Dincă, *Dalton Trans.,* 2012, **41**, 7931-7938.
4 Y. Li, A. Hammoud, L. Bouteiller and M. Raynal, *J. Am. Chem. Soc.,* 2020, **142**, 5676−5688.
5 K. I. HadjiivanoV, D. A. Panayotov, M. Y. Mihaylov, E, Z. Ivanova, K. K. Chakarova, S. M. Andonova and N. L. Drenchev, *Chem. Rev.,* 2021, **121**, 1286−1424.
6 Y. Wu, X. Song, S. Li, J. Zhang, X. Yang, P. Shen, L. Gao, R. Wei, J. Zhang and G. Xiao, *J. Ind. Eng. Chem.,* 2018, **58**, 296-303.
7 O. M. Yaghi, H. Li, and T. L. Groy, *J. Am. Chem. Soc.,* 1996, **118**, 9096–9101.
8 A. Modrow, D. Zargarani, R. Herges and N. Stock, *Dalton. Trans.,* 2012, **41**, 8690-8696.
9 F. Israr, D. Chun, Y. Kim and D. K. Kim, *Ultrason. Sonochem.,* 2016, **31**, 93-101.
10 C. Lucarelli, S. Galli, A. Maspero, A. Cimino, C. Bandinelli, A. Lolli, J. V. Ochoa, A. Vaccari, F. Cavani and S. Albonetti, *J. Phys. Chem. C.,* 2016, **120**, 15310–15321.
11 A. Awadallah, F. Hillman, S. A. Al-Muhtaseb and H-K. Jeong, *J. Mater. Sci.,* 2019, **54**, 5513–5527.
12 G. T. Vuong, M. H. Phama and T-O. Do, *CrystEngComm,* 2013, **15**, 9694-9703.
13 X. Zheng, L. Zhang, Z. Fan, Y. Cao, L. Shen, C. Au and L. Linag, *J. Chem. Eng*., 2019, **374**, 793–801.
14 D. S. Hall, D. J. Lockwood, C. Bock and B. R. MacDougall, *Proc. R. Soc. A.,* 2015, **471**, 20140792.
15 C.W. Hu, Y. Yamada and K. Yoshimura, *J. Mater. Chem. C.,* 2016, **4**, 5390-5397.
16 S. Abelló, F. Medina, D. Tichit, J. P. Ramírez, J. C. Groen, J. E. Sueiras, P. Salagre and Y. Cesteros, *Eur. J. Chem.,* 2005, **11**, 728-739.
17 F. B. D. Saiah, B.L. Su and N. Bettahar, *J. Hazard. Mater.,* 2009, **165**, 206-217.
18 M. C. Biesingera, B. P. Payne, A. P. Grosvenord, L. W. M. Lau, A. R. Gerson and R. S. C. Smart, *Appl. Surf. Sci*., 2011, **257,** 2717-2730.
19 L. Zhou, Z. Niu, X. Jin, L. Tang and L. Zhu, *ChemistrySelect,* 2018, **3**, 12865–12870.
20 J. Zhou, Z. Han, X. Wang, H. Gai, Z. Chen, T. Guo, X. Hou, L. Xu, X. Hu, M. Huang, S. V. Levchenko and H. Jiang, *Adv. Funct. Mater.,* 2021, **31**, 2102066.
21 R.J.J. Jansen and H. V. Bekkum, *Carbon*,1995, **33**, 1021-1027.
22 A. Punnoose, K. Dodge, J. J. Beltrán, K. M. Reddy, N. Franco, J. Chess, J. Eixenberger and C. A. Barrero, *J. Appl. Phys*. 2014, **115**, 2012-2015.
23 Q. Li, G. Li, C. Fu, D. Luo, J. Fan and L. Li, *ACS Appl. Mater. Interfaces,* 2014, **6**, 13, 10330–10341.
24 S. Abdpour, L. Rademacher, M. N. A. Fetzer, T. H. Y. Beglau and C. Janiak, *Solids,* 2023, **4**, 181–200.
25 X. Zhao, X. Bu, Q. Zhai, H. Tran, and P. Feng, *J. Am. Chem. Soc.,* 2015**, 137**, 1396−1399.
26 J.Yu, S.Giancola, B. Khezri, D.N. Castro, J. Redondo, F. Schiller, S. Barja, M. C. Spadaro, J. Arbiol, F.A. Garce´s-Pineda, and J. R. G. Mascaro´s, *EES Catal.,* 2023, **1**, 765.
27 X. Li, G.-Q. Han, Y.-R. Liu, B. Dong, W.-H. X. Y.-M. Chai and C-G. Liu, *ACS Appl. Mater.Interfaces,* 2016, **8**, 20057–20066.
28 F. Zheng, D. Xiang, P. Li, Z. Zhang, C. Du, Z. Zhuang, X. Li and W. Chen, *ACS Sustain. Chem. Eng.,* 2019**, 7**, 9743–9749.
29 A. Kundu, B. Ryplida and S. Y.Park, *Electroanalysis,* 2020, **32**, 2090–2100.
30 Y. Zhang, T. Qu, F. Bi, P. Hao, M. Li, S. Chen, X. Guo, M. Xie and X. Guo, *ACS Sustain. Chem. Eng.,* 2018, **6**, 16859–16866.
31 M. Yang, W. Lu, R. Jin, X.-C, Liu, S. Song and Y. Xing, *ACS Sustain. Chem. Eng.,* 2019, **14**, 12214–12221.
32 J. Qi, W. Zhang, R. Xiang, K. Liu, H.-Y. Wang, M. Chen, Y. Han and R. Cao, *Adv. Sci*., 2015, **2**, 1500199.
33 Y. Rao, Y. Wang, H. Ning, P. Li and M. Wu, *ACS Appl. Mater. Interfaces,* 2016, **8**, 33601–33607.
34 Z. Yin, J. Liang, H. Xu, H. Luo, D. Deng, W. Luand and S. Long *J. Electroanal. Chem.,* 2021, **895**, 115501.
35 K. Min, R. Yoo, S. Kim, H. Kim, S.E. Shim, D. Lim and S.-H. Baeck, *Electrochim. Acta*., 2021, **396**,
36 Y. Yang, F. Guo, L. Zhang, X. Guo, D. Wang, R. Niu, H. Yang, J. Li, G. Ma and Z. Lei, *Dalton Trans.,* 2022, **51**, 17283-17291.
37 P. Thangasamy, S. Shanmuganathan and V. Subramanian, *Nanoscale Adv.,* 2020, **2**, 2073-2079.

---

38 K. Wan, J. Luo, C. Zhou, T. Zhang, J. Arbiol, X. Lu, B.-W. Mao, X. Zhang and J. Fransaer, *Adv. Funct. Mater.,* 2019, **29**, 1900315.

39 E. Sadeghi, N.S. Peighambardoust, S. Chamani and U. Aydemir, *ACS Mater. Au,* 2023, **3**, 143–163.

40 M. Wu, Y. Zhang, R. Zahng, J. Ma and N. A. Vante, *Electrochim. Acta.,* 2022, **403**, 139630.

4 Conclusion

The primary objective of this study was to synthesize earth-abundance mixed metal materials specifically tailored for application in the electrochemical oxygen evolution reaction (OER). This endeavor explored diverse material classes, including mixed metal sulfides, selenides, sulfoselenides, and mixed metal metal-organic frameworks (MOFs). To this end, three transition metals, namely iron (Fe), nickel (Ni), and cobalt (Co), were judiciously chosen due to their well-established prevalence, high catalytic activity, and abundance within the Earth's crust. The outcomes of this study have been organized into two distinct sections. The first section focuses on the synthesis of mixed metal chalcogenides for OER, while the second section pertains to the synthesis of mixed metal metal-organic frameworks (MOFs) for the OER.

In the initial phase of this investigation, $NiCo_2S_4$, a renowned electrocatalyst, was deliberately chosen as the foundational material for further enhancement, involving the incorporation of a third metal species (Fe) and the introduction of selenium, aimed at augmenting its electrocatalytic performance. The investigation showcased the heightened OER efficacy of iron-incorporated nickel-cobalt sulfides and selenides compared to their iron-deficient counterparts, as evidenced by lower overpotentials. This underlines the substantial influence of iron in enhancing the electrocatalytic attributes of nickel cobalt materials, as illustrated by the following exemplars: $Fe_{0.1}Ni_{1.4}Co_{2.9}(S_{0.87}O_{0.13})_4$, (318 mV at 50 mA cm^{-2}); $Fe_{0.2}Ni_{1.5}Co_{2.8}(S_{0.9}O_{0.1})_4$, (310 mV at 50 mA cm^{-2}); $Fe_{0.3}Ni_{1.2}Co_{2.5}(S_{0.9}O_{0.1})_4$, (294 mV at 50 mA cm^{-2}); $Fe_{0.6}Ni_{1.2}Co_{2.5}(S_{0.83}O_{0.17})_4$, (294 mV at 50 mA cm^{-2}); $Fe_{0.4}Ni_{0.7}Co_{1.6}(Se_{0.81}O_{0.19})_4$, (306 mV at 50 mA cm^{-2}) exhibit superior OER performance compared to iron-free counterparts, $Ni_{1.0}Co_{2.1}(S_{0.9}O_{0.1})_4$, (346 mV at 50 mA cm^{-2}) and $Ni_{0.7}Co_{1.4}(Se_{0.85}O_{0.15})_4$, (355 mV at 50 mA cm^{-2}) which highlighted the significant role of iron in enhancing OER nickel cobalt electrocatalysts.

Furthermore, the iron-incorporated nickel cobalt sulfoselenide, denoted as $Fe_{0.5}Ni_{1.0}Co_{2.0}(S_{0.57}Se_{0.25}O_{0.18})_4$, exhibited remarkable performance in the OER (277 mV at 50 mA cm^{-2}), notably surpassing the performance of the benchmark RuO_2 electrode (299 mV at 50 mA cm^{-2}). The exceptional electrocatalytic performance of the $Fe_{0.5}Ni_{1.0}Co_{2.0}(S_{0.57}Se_{0.25}O_{0.18})_4$ can be attributed to its notably low charge transfer resistance (Rct) of 0.8 Ω recorded at 1.5 V vs. RHE. Furthermore, during a prolonged 20 h chronopotentiometry test, the sulfoselenide demonstrated remarkable stability, as evidenced by a marginal increase in overpotential from (277 mV to 279 at 50 mA cm^{-2}). These findings collectively reveal the potential of trimetallic iron, nickel, and cobalt-based sulfide, selenide, and particularly sulfoselenide materials as highly efficient, economically viable, and durable electrocatalysts for sustainable OER applications. This research contributes significantly to developing efficient electrocatalytic materials, thereby advancing the field of renewable energy technologies.

The second part of the thesis embarked on a parallel exploration, focusing on the development of bimetallic CPM-37(Ni,Fe) metal-organic frameworks (MOFs) and their potential as precursors for advanced electrocatalysts. In this study, a series of bimetallic metal-organic frameworks denoted as CPM-37(Ni,Fe) with varying iron content (Ni/Fe ratios approximately 2, 1, and 0.5, designated as CPM-37(Ni_2Fe), CPM-37(NiFe), and CPM-37($NiFe_2$) respectively), were synthesized for the first time to serve as precursors for OER electrode materials.

All bimetallic CPM-37(Ni,Fe) samples showed substantial N_2-based specific surface areas (BET) of 2039, 1955, and 2378 $m^2\ g^{-1}$ for CPM-37(Ni_2Fe), CPM-37(NiFe), and CPM-37($NiFe_2$), respectively. In contrast, the monometallic CPM-37(Ni) and CPM-37(Fe) exhibited significantly lower surface areas of 87 and 368 $m^2\ g^{-1}$, respectively. This increase in surface area is attributed to enhancing structural robustness through improved charge balance within the coordination-bonded clusters. This characteristic offers intriguing application prospects for mixed-metal MOFs.

Moreover, the electrode materials derived from CPM-37(Ni_2Fe) via alkaline decomposition exhibited heightened electrocatalytic activity in the OER. The initially formed nanostructured mixed-phase nickel and iron hydroxide/oxides evolved during the OER process, primarily comprising α,β-$Ni(OH)_2$, γ-NiO(OH), and possibly γ-FeO(OH) phases. Particularly, CPM-37(Ni_2Fe) with a Ni/Fe ratio of approximately 2 demonstrated superior OER activity, manifesting a minor overpotential of (290 mV at 50 mA cm^{-2}), a low Tafel slope of 39 mV dec^{-1}, and sustained OER performance over 20 h of chronopotentiometry (overpotential increase from 290 to 304 mV at 50 mA cm^{-2}), outperforming RuO_2 (overpotential increase from 300 to 386 mV at 50 mA cm^{-2}).

References

---

1. B. M. Hunter, H. B. Gray, A. M. Müller, Earth-abundant heterogeneous water oxidation catalysts, *Chem. Rev.,* **2016**, *116*, 14120−14136.

2. B. You, Y. Sun, Innovative strategies for electrocatalytic water splitting, *Acc. Chem. Res.,* **2018**, *51*, 1571−1580.

3. S. Chu, A. Majumdar, Opportunities and challenges for A sustainable energy future, *Nature*, **2012**, *488*, 294−303.

4. Y. P. Zhu, C. Guo, Y. Zheng, S. Z. Qiao, Surface and interface engineering of noble-metal-free electrocatalysts for efficient energy conversion processes, *Acc. Chem. Res.*, **2017**, *50*, 915−923.

5. R. D. Levie, The electrolysis of water, *J. Electroanal. Chem.*, **1999**, *476*, 92–93.

6. R. D. Levie, Industrial water electrolysis: present and future, *Int. J. Hydrog. Energy,* **1983**, *8*, 401–417.

7. G. Li, L. Anderson, Y. Chen, M. Pan, P.Y. A. Chuang, new insights into evaluating catalyst activity and stability for oxygen evolution reactions in alkaline media, *Sustain. Energy Fuels.,* **2018**, *2*, 237–251.

8. M. E. G. Lyons, L. D. Burke, Mechanism of oxygen reactions at porous oxide electrodes. Part 1.—Oxygen evolution at RuO_2 and $Ru_xSn_1–xO_2$ electrodes in alkaline solution under vigorous electrolysis conditions, *J. Chem. Soc., Faraday Trans.1*, **1987**, *83*, 299–321.

9. X. Zhou, H. Dong, A.-M. Ren, The mechanism of hydrogen and oxygen evolution reaction in Ni–NiO/β-Ga_2O_3 photocatalyst, *Int. J. Hydrog. Energy*, **2016**, *41*, 5670–5681.

10. J. O. Bockris, T. Otagawa, Mechanism of oxygen evolution on perovskites, *J. Phys. Chem.,* **1983**, *87*, 2960–2971.

11. N. Jiang, B. You, M. Sheng, Y. Sun, Electrodeposited cobalt-phosphorous-derived films as competent bifunctional catalysts for overall water splitting, *Angew. Chem. Int. Ed.,* **2015**, *54*, 6251−6254.

12. B. Rausch, M.D. Symes, G. Chisholm, L. Cronin, Decoupled catalytic hydrogen evolution from a molecular metal oxide redox mediator in water splitting, *Science*, **2014**, *345*, 1326−1330.

13. G. Han, G. Jin, Y. H. Burgess, R. A. Dickenson, N. E. Cao, X. M. Sun, Y. Visible-light-driven valorization of biomass intermediates integrated with H_2 production catalyzed by ultrathin Ni/CdS nanosheets, *J. Am. Chem. Soc.,* **2017**, *139*, 15584−15587.

14. V. V. Struzhkin, B. Militzer, W.L. Mao, H. Mao, R.J. Hemley, Hydrogen storage in molecular clathrates, *Chem. Rev.,* **2007**, *107*, 4133−4151.

15. X. Xie, L. Du, L. Yan, S. Park, Y. Qiu, J. Sokolowski, W. Wang, Y. Shao, Oxygen evolution reaction in alkaline environment: material challenges and solutions, *Adv. Funct. Mater.*, **2022**, *32*, 2110036.

16. N. T. Suen, S. F. Hung, Q. Quan, N. Zhang, Y.J. Xu, H. M. Chen, Electrocatalysis for the oxygen evolution reaction: recent development and future perspectives, *Chem. Soc. Rev.,* **2017**, *46*, 337– 365.

17. D. J. Chen, C. Chen, Z. M. Baiyee, Z. P. Shao, F. Ciucci, Nonstoichiometric oxides as low-cost and highly-efficient oxygen reduction/evolution catalysts for low-temperature electrochemical devices, *Chem. Rev.,* **2015**, *115*, 9869–9921.

18. W. T. Hong, M. Risch, K. A. Stoerzinger, A. Grimaud, J. Suntivich, Y. Shao-Horn, Toward the rational design of non-precious transition metal oxides for oxygen electrocatalysis, *Energy Environ. Sci.,* **2015**, *8*, 1404–1427.

19. I. C. Man, H. Y. Su, F. Calle-Vallejo, H. A. Hansen, J. I. Martínez, N. G. Inoglu, J. Kitchin, T. F. Jaramillo, J. K. Nørskov, J. Rossmeisl, Universality in oxygen evolution electrocatalysis on oxide surfaces, *ChemCatChem*, **2011**, *3*, 1159–1165.

20. Z. Xu, J. Rossmeisl, J. R. Kitchin, A linear response DFT+U study of trends in the oxygen evolution Activity of transition metal rutile dioxides, *J. Phys. Chem. C,* **2015**, *119*, 4827–4833.

21. J. S. Kim, B. Kim, H. Kim, K. Kang, Recent progress on multimetal oxide catalysts for the oxygen evolution reaction, *Adv. Energy Mater.*, **2018**, *8*, 1702774.

22. H. Chen, L. Shi, X. Liang, L. Wang, T. Asefa, X. Zou, Optimization of active sites via crystal phase, composition, and morphology for efficient low-Iridium oxygen evolution catalysts, *Angew. Chem. Int. Ed.,* **2020**, *59*, 19654–19658.

23. Z.P. Wu, X. F. Lu, S.Q. Zang, Xi. W, Lou, Non-noble-metal-based electrocatalysts toward the oxygen evolution reaction, *Adv. Funct. Mater.*, **2020**, *30*, 1910274.

24. P. Xiao, W. Chen and X. Wang, A review of phosphide-based materials for electrocatalytic hydrogen evolution, *Adv. Energy Mater.*, **2015**, *5*, 1500985.

25. A. J. Bard and L. R. Faulkner, Electrochemical methods: fundamentals and applications, *Wiley*, **1980**.

26. T. R. Cook, D. K. Dogutan, S. Y. Reece, Y. Surendranath, T. S. Teets, D. G. Nocera, Solar energy supply and storage for the legacy and nonlegacy worlds, *Chem. Rev.,* **2010***,* *110,* 6474–6502.

27. Y. P. Zhu, T. Y. Ma, M. Jaroniec, S. Z. Qiao, Self-templating synthesis of hollow Co_3O_4 microtube arrays for highly efficient water electrolysis, *Angew. Chem. Int. Ed.,* **2017***,* *56,*1324–1328.

28. K. Fominykh, J. M. Feckl, J. Sicklinger, M. Döblinger, S. Böcklein, J. Ziegler, L. Peter, J. Rathousky, E. W. Scheidt, T. Bein, D. Fattakhova-Rohlfing, Ultrasmall dispersible crystalline nickel oxide nanoparticles as high-performance catalysts for electrochemical water splitting, *Adv. Funct. Mater.,* **2014***,* *24,* 3123–3129.

29. T. Shinagawa, A. T. Garcia-Esparza, K. Takanabe, Insight on Tafel slopes from a microkinetic analysis of aqueous electrocatalysis for energy conversion, *Sci. Rep.,* **2015**, *5*, 13801–13821.

30. S. Anantharaj, S. R. Ede, K. Karthick, P. E. Karthikc, S. Kundu, Precision and correctness in the evaluation of electrocatalytic water splitting: revisiting activity parameters with a critical assessment, *Energy Environ. Sci.,* **2018**, *11*, 744–771.

31. S. Anantharaj, H. Sugime, S. Noda, Why shouldn't double-layer capacitance (Cdl) be always trusted to justify Faradaic electrocatalytic activity differences?, *J. Electroanal. Chem.*, **2021**, *903*, 115842.

32. S. Anantharaj, P. E. Karthik, S. Kundu, E. K. Pitchiah, S. Kundu, P. E. Karthik, S. Kundu, Self-assembled IrO_2 nanoparticles on a DNA scaffold with enhanced catalytic and oxygen evolution reaction (OER) activities, *J. Mater. Chem. A,* **2015**, *3*, 24463–24478.

33. S. Anantharaj, P. E. Karthik, K. Subrata*,* Petal-like hierarchical array of ultrathin $Ni(OH)_2$ nanosheets decorated with $Ni(OH)_2$ nanoburls: a highly efficient OER electrocatalyst, *Catal. Sci. Technol.*, **2017**, *7*, 882–893.

34. T. N. Kumar, S. Sivabalan, N. Chandrasekaran, K. L. Phani*,* Synergism between polyurethane and polydopamine in the synthesis of Ni–Fe alloy monoliths*, ChemComm*, **2015**, *51*, 1922–1925.

35. S. Anantharaj, S. Rao Ede, K. Sakthikumar, K. Karthick, S. Mishra, S. Kundu, Recent trends and perspectives in electrochemical water splitting with an emphasis on sulfide, selenide, and phosphide catalysts of Fe, Co, and Ni: A review, *ACS Catal.*, **2016**, *6*, 8069−8097.

36. S. Anantharaj, S. Noda, Appropriate use of electrochemical impedance spectroscopy in water splitting electrocatalysis, *ChemElectroChem*, **2020**, *7*, 2297–2308.

37. Y. Shi, B. Zhang, Recent advances in transition metal phosphide nanomaterials: synthesis and applications in hydrogen evolution reaction, *Chem. Soc. Rev.,* **2016**, *45*, 1529–1541.

38. E. Fabbri, A. Habereder, K. Waltar, R. Kötz, T. J. Schmidt, Developments and perspectives of oxide-based catalysts for the oxygen evolution reaction, *Catal. Sci. Technol.,* **2014**, *4*, 3800–3821.

39. T. Weber, H. Prins, R. A. van Santen, Transition metal sulphides: chemistry and catalysis, *Springer Science & Business Media*, **2013**.

40. S. Chandrasekaran, C. Bowen, P. Zhang, Z. Li, Q. Yuan, X. Ren, L. Deng, Spinel photocatalysts for environmental remediation, hydrogen generation, CO_2 reduction and photoelectrochemical water splitting, *J. Mater. Chem. A,* **2018**, *6*, 11078–11104.

41. Q. Zhao, Z. Yan, C. Chen, J. Chen, Spinels: Controlled preparation, oxygen reduction/evolution reaction application, and beyond, *Chem. Rev.,* **2017**, *117*, 10121–10211.

42. S. Chandrasekaran, L. Yao, L. Deng, C. Bowen, Y. Zhang, S. Chen, Z. Lin, F. Peng, P. Zhang, Recent advances in metal sulfides: from controlled fabrication to electrocatalytic, photocatalytic and photoelectrochemical water splitting and beyond, *Chem. Soc. Rev.,* **2019**, *48*, 4178-4280.

43. J. Hauck and K. Mika, Ordering of metal atoms in wurtzite and sphalerite structures, *J Solid State Chem,* **1998**, *138*, 334–341.

44. S. Wang, B. Y. Guan, Y. Lu, X. W. Lou, Formation of hierarchical In_2S_3–$CdIn_2S_4$ hetero structured nanotubes for efficient and stable visible light CO_2 reduction, *J. Am. Chem. Soc.,* **2017**, *139*, 17305–17308.

45. L. R. Benco, J. L. Barras, M. Atanasov, C. Daul, E. Deiss, First principles calculation of electrode material for lithium intercalation batteries: TiS_2 and $LiTi_2S_4$ cubic spinel structures, *J Solid State Chem*, **1999**, *145*, 503–510.

46. H. Enokiya, M. Yamaguchi, T. Hihara, Spin wave contribution to the nuclear spin-lattice relaxation in ferromagnetic $CuCr_2S_4$ and β_1-MnZn, *J. Phys. Soc. Japan,* **1977**, *42*, 805–807.

47. X. Rui, H. Tan, Q. Yan, Nanostructured metal sulfides for energy storage, *Nanoscale*, **2014**, *6*, 9889–9924.

48. M. R. Gao, Y. F. Xu, J. Jiang, S. H. Yu, Nanostructured metal chalcogenides: synthesis, modification, and applications in energy conversion and storage devices, *Chem. Soc. Rev.,* **2013**, *42*, 2986– 3017.

49. Y. Zheng, Y. Jiao, M. Jaroniec, S. Z. Qiao, Advancing the electrochemistry of the hydrogen-evolution reaction through combining experiment and theory, *Angew. Chem. Int. Ed.,* **2015**, *54*, 52−65.

50. H. Chen, J. Jiang, L. Zhang, H. Wan, T. Qi, D. Xia, Highly conductive $NiCo_2S_4$ urchin-like nanostructures for high-rate pseudocapacitors, *Nanoscale,* **2013**, *5*, 8879–8883.

51. L. Shen, L. Yu, H. B. Wu, X. Y. Yu, X. Zhang, X. W. Lou, Formation of nickel cobalt sulfide ball-in-ball hollow spheres with enhanced electrochemical pseudocapacitive properties, *Nat. Commun.,* **2015**, *6*, 6694.

52. J. Staszak-Jirkovsky, C. D. Malliakas, P. P. Lopes, N. Danilovic, S. S. Kota, K. C. Chang, B. Genorio, D. Strmcnik, V. R. Stamenkovic, M. G. Kanatzidis, N. M. Markovic, Design of active and stable Co–Mo–Sx chalcogels as pH-universal catalysts for the hydrogen evolution reaction, *Nat. Mater.*, **2016**, *15*, 197.

53. T. L. Tamang, S, Sahoo, J.-J. Shim, Triple-shelled nickel-cobalt-manganese sulfides hollow spheres for advanced hybrid supercapacitors, *J. Power Sources,* **2023**, *572*, 233107.

54. C.-L. Huang, Z-F. He, J-Y. Pai, Y-H. Yang, W-Y. Jao, C-Y. Lai, Y-T Lu, H-Y. Ku, C-C. Hu, Atomically well-mixed quad-metallic sulfide as multi-functional electrocatalyst for overall water electrolysis and zinc-air battery, *Chem. Eng. J.,* **2023**, *469*, 143855.

55. M. Wang, L. Zhang, Y. Hec, H. Zhu, Recent advances in transition-metal-sulfide-based bifunctional electrocatalysts for overall water splitting, *J. Mater. Chem. A*, **2021**, *9*, 5320–5363.

56. B. Bornamehr, V. Presser, S. Husmann, Mixed Cu−Fe sulfides derived from polydopamine-coated Prussian blue analogue as a lithium-ion battery electrode, *ACS Omega,* **2022**, *7*, 38674–38685.

57. Y. Fang, D. Luan, X. W. Lou, Recent advances on mixed metal sulfides for advanced sodium-ion batteries, *Adv.Mater.,* **2020**, *32*, 2002976.

58. A. S. Arico, P. Bruce, B. Scrosati, J. M. Tarascon, W. V. S. Wijk, Nanostructured materials for advanced energy conversion and storage devices, *Nat. Mater.,* **2005**, *4*, 366.

59. Y. J. Kang, P. D. Yang, N. M. Markovic, V. R. Stamenkovic, Shaping electrocatalysis through tailored nanomaterials, *Nano Today*, **2016**, *11*, 587–600.

60. J. Jiang, Y. Y. Li, J. P. Liu, X. T. Huang, C. Z. Yuan, X. W. Lou, Recent advances in metal oxide-based electrode architecture design for electrochemical energy storage, *Adv. Mater.,* **2012**, *24*, 5166.

61. J. M. Tarascon, T. P. Orlando, M. J. Neal, Rechargeable lithium batteries based on the ternary chevrel phase $AgMo_6S_8$ as the cathode, *J. Electrochem. Soc.,* **1988**, *135*, 804.

62. M. Wakihara, T. Uchida, K. Suzuki, M. Taniguchi, A rechargeable lithium battery employing iron Chevrel phase compound ($Fe_{1.25}Mo_6S_{7.8}$) as the cathode, *Electrochim. Acta*, **1989**, *34*, 867– 869.

63. S. L. Zhao, Y. Wang, Q. H. Zhang, Y. F. Li, L. Gu, Z. H. Dai, S. L. Liu, Y. Q. Lan, M. Han, J. C. Bao, Two-dimensional nanostructures of non-layered ternary thiospinels and their bifunctional electrocatalytic properties for oxygen reduction and evolution: the case of $CuCo_2S_4$ nanosheetsInorg, *Inorg. Chem. Front.,* **2016**, *3*, 1501–1509.

64. J. Yang, Y. Zhang, C. C. Sun, G. L. Guo, W. P. Sun, W. Huang, Q. Y. Yan, X. C. Dong, Controlled synthesis of zinc cobalt sulfide nanostructures in oil phase and their potential applications in electrochemical energy storage, *J. Mater. Chem. A,* **2015**, *3*, 11462–11470.

65. D. Y. Wang, M. Gong, H. L. Chou, C. J. Pan, H. A. Chen, Y. P. Wu, M. C. Lin, M. Y. Guan, J. Yang, C. W. Chen, Y. L. Wang, B. J. Hwang, C. C. Chen, H. J. Dai, Highly active and stable hybrid catalyst of cobalt-doped FeS_2 nanosheets–carbon nanotubes for hydrogen evolution reaction, *J. Am. Chem. Soc.,* **2015**, *137*, 1587–1592.

66. M. Guo, J. Balamurugan, T. D. Thanh, N. H. Kim, J. H. Lee, Facile fabrication of Co_2CuS_4 nanoparticle anchored N-doped graphene for high-performance asymmetric supercapacitors, *J. Mater. Chem. A,* **2016**, *4*, 17560–17571.

67. W. Chen, C. Xia, H. N. Alshareef, One-step electrodeposited nickel cobalt sulfide nanosheet arrays for high-performance asymmetric supercapacitors*, ACS Nano*, **2014**, *8*, 9531–9541.

68. X. Y. Yu, X. W. Lou, Mixed metal sulfides for electrochemical energy storage and conversion, *Adv. Energy Mater.,* **2018**, *8*, 1701592.

69. Q. Liu, J. T. Jin, J. Y. Zhang, $NiCo_2S_4$@graphene as a bifunctional electrocatalyst for oxygen reduction and evolution reactions, *ACS Appl. Mater. Interfaces*, **2013**, *5*, 5002–5008.

70. W. M. Du, Z. Q. Zhu, Y. B. Wang, J. N. Liu, W. J. Yang, X. F. Qian, H. Pang, One-step synthesis of $CoNi_2S_4$ nanoparticles for supercapacitor electrodes, *RSC Adv.,* **2014**, *4*, 6998–7002.

71. Y. F. Tang, T. Chen, S. X. Yu, Y. Q. Qiao, S. C. Mu, S. H. Zhang, Y. F. Zhao, L. Hou, W. W. Huang, F. M. Gao, A highly electronic conductive cobalt nickel sulphide dendrite/quasi-spherical nanocomposite for a supercapacitor electrode with ultrahigh areal specific capacitance, *J. Power Sources*, **2015**, *295*, 314–322.

72. Y. Cui, C. W. Zhou, X. Z. Li, Y. Gao, J. Zhang, High performance electrocatalysis for hydrogen evolution reaction using nickel-doped CoS_2 nanostructures: experimental and DFT insights, *Electrochim. Acta*, **2017**, *228*, 428–435.

73. V. Ganesan, P. Ramasamy, J. Kim, Hierarchical $Ni_{3.5}Co_{5.5}S_8$ nanosheet-assembled hollow nanocages: Superior electrocatalyst towards oxygen evolution reaction, *Int. J. Hydrog. Energy*, **2017**, *42*, 5985–5992.

74. M. S. Faber, M. A. Lukowski, Q. Ding, N. S. Kaiser, S. Jin, Earth-abundant metal pyrites (FeS_2, CoS_2, NiS_2, and their alloys) for highly efficient hydrogen evolution and polysulfide reduction electrocatalysis, *J. Phys. Chem. C,* **2014**, *118*, 21347–21356.

75. D. S. Kong, J. J. Cha, H. T. Wang, H. R. Lee, Y. Cui, First-row transition metal dichalcogenide catalysts for hydrogen evolution reaction, *Energy Environ. Sci.*, **2013**, *6*, 3553–3558.

76. S.-Y. Huang, D. Sodano, T. Leonard, S. Luiso, P. S. Fedkiw, Cobalt-doped iron sulfide as an electrocatalyst for hydrogen evolution, *J. Electrochem. Soc.,* **2017**, *164*, F276.

77. T. Uchida, Y. Tanjo, M. Wakihara, M. Taniguchi, Nickel-molybdenum sulfide $Ni_2Mo_6\,S_{7.9}$ as the cathode of lithium secondary batteries, *J. Electrochem. Soc.,* **1990**, *137*, 7.

78. S. Yamaguchi, T. Uchida, M. Wakihara, A rechargeable lithium battery employing cobalt chevrel-phase compound as the cathode, *J. Electrochem. Soc.,* **1991**, 138, 687.

79. G. H. Li, H. Ikuta, T. Uchida, M. Wakihara, Re-examination of copper chevrel-phase sulfides as cathode in lithium secondary batteries, *J. Power Sources*, **1995**, *54*, 519–521.

80. K. Ramasamy, R. K. Gupta, H. Sims, S. Palchoudhury, S. Ivanov, A. Gupta, Layered ternary sulfide $CuSbS_2$ nanoplates for flexible solid-state supercapacitors, *J. Mater. Chem. A*, **2015**, *3*, 13263–13274.

81. K. Ramasamy, R. K. Gupta, S. Palchoudhury, S. Ivanov, A. Gupta, Layer-structured copper antimony chalcogenides ($CuSbSe_xS_{2-x}$): stable electrode materials for supercapacitors, *Chem. Mater.,* **2015**, *27*, 379–386.

82. Z. A. Zhang, C. K. Zhou, Y. K. Liu, J. Li, Y. Q. Lai, M. Jia, $CuSbS_2$ Nanobricks as Electrode materials for lithium Ion batteries, *Int. J. Electrochem. Sci.*, **2013**, *8*, 10059–10067.

83. X. Xu, W. Liu, Y. Kim, J. Cho, Nanostructured transition metal sulfides for lithium ion batteries: Progress and challenges, *Nano Today*, **2014**, *9*, 604–630.

84. Y. Xiao, S. H. Lee, Y. K. Sun, The Application of metal sulfides in sodium ion batteries, *Adv. Energy Mater.,* **2017**, *7*, 1601329.

85. S. R. Batten, N. R. Champness, X.-M. Chen, J. Garcia-Martinez, S. Kitagawa, L. Öhrström, M. O'Keeffe, M. Paik Suh, J. Reedijk, Terminology of metal–organic frameworks and coordination polymers (IUPAC Recommendations 2013), *Pure Appl. Chem.*, **2013**, *85*, 1715–1724.

86. S. Kitagawa, R. Kitaura, S.-I. Noro, Functional porous coordination polymers, *Angew. Chem. Int. Ed.*, **2004**, *43*, 2334– 2375.

87. P-Q. Liao, J-Q. Shen, J-P. Zhang, Metal–organic frameworks for electrocatalysis, *Coord Chem Rev*, **2019**, *373*, 22-48.

88. H. Furukawa, K. E. Cordova, M. O'Keeffe, O. M. Yaghi, The Chemistry and applications of metal-organic frameworks, *Science*, **2013**, *341*, 1230444.

89. U. Mueller, M. Schubert, F. Teich, H. Puetter, K. S-Arndt, J. Pastréa, Metal-organic frameworks—prospective industrial applications, *J. Mater. Chem.*, **2006**, *16*, 626–636.

90. L. E. Kreno, K. Leong, O. K. Farha, M. Allendorf, R. P. Van Duyne, J. T. Hupp, Metal–organic framework materials as chemical sensors, *Chem. Rev.,* **2012**, *112*, 1105–1125.

91. E. Adatoz, A. K. Avci, S. Keskin, Opportunities, and challenges of MOF-based membranes in gas separations, *Sep. Purif. Technol.,* **2015**, *152*, 207–237.

92. H. Xiao, Z-X Low, D. B. Gore, R. Kumar, M. Asadnia, Z. Zhong, Porous metal–organic framework-based filters: Synthesis methods and applications for environmental remediation, *Chem. Eng. J.,* **2020**, *430*, 133160.

93. H. Kummer, F. Jeremias, A. Warlo, G. Füldner, D. Fröhlich, C. Janiak, R. Gläser, S. K. Henninger, A functional full-Scale heat exchanger coated with aluminum fumarate metal–organic framework for adsorption heat transformation, *Ind. Eng. Chem. Res.,* **2017**, *56*, 8393–8398.

94. B. Xu, H. Zhang, H. Mei, D. Sun, Recent progress in metal-organic framework-based supercapacitor electrode materials, *Coord Chem Rev,* **2020**, *420,* 213438.

95. A. Morozana, F. Jaouen, Metal organic frameworks for electrochemical applications, *Energy Environ. Sci.,* **2012**, *5*, 9269–9290.

96. V. Pascanu, G. G. Miera, A. K. Inge, B. Martín-Matute, Metal–organic frameworks as catalysts for organic synthesis: A critical perspective, *J. Am. Chem. Soc.,* **2019**, *141*, 7223–7234.

97. M. Jacoby, Heading to market with MOFs, *Chem. Eng. News,* **2008**, *86*, 13–16.

98. C. Pettinari, F. Marchetti, N. Mosca, G. Tosi, A. Drozdov, Application of metal−organic frameworks, *Polym Int*, **2017**, *66*, 731–744.

99. H-C. J. Zhou, S. Kitagawa, Metal–organic frameworks (MOFs), *Chem. Soc. Rev.,* **2014**, *43*, 5415–5418.

100. A.J. Howarth, A. W. Peters, N.A. Vermeulen, T.C. Wang, J. T. Hupp, O. K. Farha, Best practices for the synthesis, activation, and characterization of metal–organic frameworks, *Chem. Mater.,* **2017**, *29*, 26–39.

101. Z. Wang, S. M. Cohen, Postsynthetic modification of metal–organic frameworks, *Chem. Soc. Rev.,* **2009**, *38*, 1315–1329.

102. S. Abednatanzi, P. Gohari Derakhshandeh, H. Depauw, F-X. Couder, H. Vrielinck, P. V. Der Voort, K. Leus, Mixed-metal metal–organic frameworks, *Chem. Soc. Rev.,* **2019**, *48*, 2535–2565.

103. N. Stock, S. Biswas, Synthesis of metal-organic frameworks (MOFs): routes to various MOF topologies, morphologies, and composites, *Chem. Rev.*, **2012**, *112*, 933–969.

104. X. Qin, D. Kim, Y. Piao, Metal-organic frameworks-derived novel nanostructured electrocatalysts for oxygen evolution reaction, *Carbon Energy.*, **2021**, *3*, 66–100.

105. W. Xia, A. Mahmood, R. Zou, Q. Xu, Metal–organic frameworks and their derived nanostructures for electrochemical energy storage and conversion, *Energy Environ. Sci.*, **2015**, *8*, 1837–1866.

106. K. Shen, X. Chen, J. Chen, Y. Li, Development of MOF-derived carbon-based nanomaterials for efficient catalysis, *ACS Catal.*, **2016**, *6*, 5887–5903.

107. A. Mahmood, W. Guo, H. Tabassum, R. Zou, Metal-organic framework-based nanomaterials for electrocatalysis, *Adv. Energy Mater.,* **2016**, *6*, 1600423.

108. Y. Jia, Z. Xue, Y. Li, G. Li, Recent progress of metal organic frameworks-based electrocatalysts for hydrogen evolution, oxygen evolution, and oxygen reduction reaction, *Energy Environ. Mater.,* **2022**, *5*, 1084–1102.

109. Q. Qian, Y. Li, Y. Liu, L. Yu, G. Zhang, Ambient fast synthesis and active sites deciphering of hierarchical foam-like trimetal–organic framework nanostructures as a platform for highly efficient oxygen evolution electrocatalysis, *Adv. Mater.*, **2019**, *31*, 1901139.

110. Y. Peng, W. Yang, Metal-organic framework nanosheets: a class of glamorous low-dimensional materials with distinct structural and chemical natures, *Sci China Chem,* **2019**, *62*, 1561–1575.

111. J. Duan, S. Chen, C. Zhao, Ultrathin metal-organic framework array for efficient electrocatalytic water splitting, *Nat. Commun.,* **2017***, 8*, 15341.

112. S. Zheng, X. Guo, H. Xue, K. Pan, C. Liu, H. Pang, Facile one-pot generation of metal oxide/hydroxide@metal–organic framework composites: highly efficient bifunctional electrocatalysts for overall water splitting, *ChemComm*, **2019**, *55*, 10904–10907.

113. Y. Zhou, R. Abazari, J. Chen, M. Tahir, A. Kumar, R. R. Ikreedeegh, E. Rani, H. Singh, A. M. Kirillov, Bimetallic metal–organic frameworks and MOF-derived composites: Recent progress on electro- and photoelectrocatalytic applications, *Coord Chem Rev,* **2022**, *451*, 214264.

114. A. Aijaz, J. Masa, C. Rösler, W. Xia, P. Weide, A. J. R. Botz, R. A. Fischer, W. Schuhmann, M. Muhler, $Co@Co_3O_4$ encapsulated in carbon nanotube-grafted nitrogen-doped carbon polyhedra as an advanced bifunctional oxygen electrode, *Angew. Chem. Int. Ed.,* **2016**, *55*, 4087–4091.

115. Y. Shi, B. Zhu, X. Guo, W. Li, W. Ma, X. Wu, H. Pang, MOF-derived metal sulfides for electrochemical energy applications, *Energy Stor. Mater.,* **2022**, *51*, 840–872.

116. J. Zhou, Y. Dou, A. Zhou, L. Shu, Y. Chen, J-R Li, Layered metal–organic framework-derived metal oxide/carbon nanosheet arrays for catalyzing the oxygen evolution reaction, *ACS Energy Lett.,* **2018**, *3*, 1655–1661.

117. X. Tang, N. Li, H. Pang, Metal–organic frameworks-derived metal phosphides for electrochemistry application, *Green Energy Environ.*, **2022**, *7*, 636–661.

118. N. Yao, T. Tan, F. Yang, G. Cheng, W. Luo, Well-aligned metal–organic framework array-derived CoS_2 nanosheets to- ward robust electrochemical water splitting, *Mater. Chem. Front.,* **2018**, *2*, 1732–1738.

119. L. Yan, H. Jiang, Y. Xing, Y. Wang, D. Liu, X. Gu, P. Dai, L. Li, X. Zhao, Nickel metal–organic framework implanted on graphene and incubated to be ultrasmall nickel phosphide nanocrystals acts as a highly efficient water splitting electrocatalyst, *J. Mater. Chem. A,* **2018**, *6*, 1682–1691.

120. J. Rong, F. Qiu, T. Zhang, Y. Fang, J. Xu, Y. Zhu, Self-directed hierarchical $Cu_3(PO_4)_2$/Cu-BDC nanosheets array based on copper foam as an efficient and durable electrocatalyst for overall water splitting, *Electrochim. Acta*, **2019**, *313*, 179–188.

121. Y. Pan, K. Sun, S. Liu, et al. Core-shell ZIF-8@ZIF-67-derived CoP nanoparticle-embedded N-doped carbon nanotube hollow polyhedron for efficient overall water splitting, *J. Am. Chem. Soc.,* **2018** ,*140*, 2610–2618.

122. X. Liang, B. Zheng, L. Chen, J. Zhang, Z. Zhuang, B. Chen, MOF–derived formation of Ni_2P-CoP bimetallic phosphides with strong interfacial effect toward electrocatalytic water splitting, *ACS Appl. Mater. Interfaces,* **2017**, *9*, 23222–23229.

123. T. Sun, S. Zhang, L. Xu, D. Wang, Y. Li, An efficient multifunctional hybrid electrocatalyst: Ni_2P nanoparticles on MOF-derived Co,N-doped porous carbon polyhedrons for oxygen reduction and water splitting, *ChemComm,* **2018**, *54*, 12101–12104.

124. W. Hong, M. Kitta, Q. Xu, Bimetallic MOF-Derived FeCo-P/C Nanocomposites as efficient catalysts for oxygen evolution reaction, *Small Methods*, **2018**, *2*, 1800214.

.

125. X. Zhao, B. Pattengale, D. Fan, Z. Zou, Y. Zhao, J. Du, J. Huang, C. Xu, Mixed-node metal–organic frameworks as efficient electrocatalysts for oxygen evolution reaction, *ACS Energy Lett.***,** **2018**, *3*, 2520–2526.

126. J. Zhou, Z. Han, X. Wang, H. Gai, Z. Chen, T. Guo, X. Hou, L. Xu, X. Hu, M. Huang, S. V. Levchenko, H. Jiang, Discovery of quantitative electronic structure-OER activity relationship in metal-organic framework electrocatalysts using an integrated theoretical-experimental approach, *Adv. Funct. Mater.,* **2021**, *31*, 2102066.

127. W. Ahn, M. Park, D. Lee, Hollow multivoid nanocuboids derived from ternary Ni-Co-Fe Prussian blue analog for dual-electrocatalysis of oxygen and hydrogen evolution reactions, *Adv Energy Mater.,* **2018**, *28*, 1802129.

128. W. Zheng, L. Y. S. Lee, Metal–organic frameworks for electrocatalysis: catalyst or precatalyst?, *ACS Energy Lett.,* **2021**, *6*, 2838–2843.

129. N. C. Burtch, H. Jasuja, K. S. Walton, Water Stability and Adsorption in Metal-Organic Frameworks, *Chem. Rev.,* **2014**, *114*, 10575−10612.

130. J. Tian, F. Jiang, D. Yuan, L. Zhang, Q. Chen, M. Hong, Electric-field assisted in situ hydrolysis of bulk metal-organic frameworks (MOFs) into ultrathin metal oxyhydroxide nanosheets for efficient oxygen evolution, *Angew. Chem., Int. Ed.,* **2020**, *59*, 13101−13108.

131. S. Zhao, C. Tan, C-T. He, P. An, F. Xie, S. Jiang, Y. Zhu, K-H. Wu, B. Zhang, H. Li, J. Zhang, Y. Chen, S. Liu, J. Dong, Z. Tang, Structural transformation of highly active metal–organic framework electrocatalysts during the oxygen evolution reaction, *Nat. Energy*, **2020**, *5*, 881–890.